Title

Developing a Fiber Optic Magnetic Field Sensor: Fiber Bragg Gratings and the Magnetorefractive Effect

Author

Strutner, Scott Strutner

Publication Date

2016

Peer reviewed|Thesis/dissertation

UNIVERSITY OF CALIFORNIA

Los Angeles

Developing a Fiber Optic Magnetic Field Sensor: Fiber Bragg Gratings and the Magnetorefractive Effect

A dissertation submitted in partial satisfaction

of the requirements for the degree

Doctor of Philosophy in Mechanical Engineering

by

Scott Michael Strutner

2016

ABSTRACT OF THE DISSERTATION

Developing a Fiber Optic Magnetic Field Sensor: Fiber Bragg Gratings and the Magnetorefractive Effect

by

Scott Michael Strutner

Doctor of Philosophy in Mechanical Engineering

University of California, Los Angeles, 2016

Professor Gregory P. Carman, Chair

Optical fiber Bragg gratings (FBGs) have been shown to provide sensing of strain and temperature at 100's of points along a fiber's path. This work extended that to 1000's of points, and added discrete sensing of magnetic field along the fiber. The first was achieved via an extension of the optical frequency domain reflectometery (OFDR) de-multiplexing method. This was done by treating FBG segments as a series of concatenated FBGs instead of one discrete FBG. Such treatment allows for the resolution of even a micro-crack's strain fields in a pressurized composite overwrapped pressure vessel (COPV), which are on the 0.5 mm scale. The second advancement of FBGs, magnetic sensing, was added via an assembly to transduce magnetic attraction into fiber strain. This assembly allowed multiplexed magnetically sensitive FBG sensors for the first time. Stringing pieces of magnetic material onto a fiber and gluing that fiber onto a structure is an easy method and largely uses off-the-shelf components. This will prove simple to expand and utilize to solve actual engineering problems. To further improve, by removing the strain transduction and thus reduce vibrational sensitivity, a new magneto-optical material is needed. An investigation into the magnetorefractive effect (MRE), and characterization of the shift of index of refraction in the material $La_{1-x}Sr_xMnO_3$ (LSMO) with magnetic field and temperature was performed. The index of refraction of the LSMO was found to shift with magnetic field. This was leveraged to create a magnetometer interferometer. That device did not function though, as the absorption of

the magneto-optic LSMO used prevented light's transmission through that active material. This highlights the complex, i.e. non-real, index of refraction of LSMO an aspect which would warrant further investigation.

The dissertation of Scott Michael Strutner is approved.

Oscar Stafsudd

Pei-Yu Chiou

Christopher Lynch

Gregory P. Carman, Committee Chair

University of California, Los Angeles

2016

For my partner through and for life,

my fellow skiing, traveling, adventuring, and engineering wife,

Monica

Table of Contents

List of figures

List of tables

Acknowledgments

First, I would like to thank Prof. Greg Carman and Dr. Lance Richards. Their generous advice, management and support of my graduate career enabled this work. It is always hard for mentors to find the right blend of supporting a budding mind without merely reshaping it in their own image. Thank you for striking that balance with me.

Next I would like to thank the rest of the AERO Institute and NASA Armstrong (Dryden) personal for their work. In particular, Jeff Bauer and Frank Pena but also, Allen Parker, Anthony (Nino) Piazza and Hon Man (Patrick) Chan. Jeff and Frank you have worked with me on the magnetics work and the strain projects, sharing many thoughts and ideas, guiding me and acting as sounding boards. Thank you both!

To my fellow lab mates present and past. First, to Mike Emmons' for his introduction to this research. Our short but excellent time of overlap was worth a year of literature reading. Next thanks to Kyle Wetzlar, Scott Keller, Paul Nordeen, Wei-Yang Sun, John Domann, John Voldovinos, Tony Barra, Auni Kundu, Andres Chavez and Chuck Liang have all been excellent sounding boards, offering insightful (and sarcastic) questions, and answering many questions I had for them. The support of my fellow graduate students, and our comradely was able to get me through the mountain of literature, and many failed experiments to find a few nuggets of new knowledge to bring into the light of our world. I think we all take turns being the ones watching shadows on the wall, and being the one who has seen the sun.

Next, thank you to the many interns which have worked on my research. You dozen have all taught me much about my research, how to explain it, and so many different views on the subject. Further, you let me learn to manage other researchers, and your work has been key in developing the research that follows. Edmundo, your COPV overview plotting videos changed the way I viewed the strain data, and allowed us for the first time to watch the pressurization of whole COPV at once. Adam, your work on the magnetic ellipsometer was excellent and enabled us to characterize the index of LSMO for the first time leading to characterizing its shift. Sabina, your work on the magnetic interferometer was wonderful and I wish we had a success in that project to publish. Further your skilled and detailed

editing of many documents is sorely missed. Thank you each, as well as many other interns for their hours in lab.

To my parents, your thirst to understand what this research is, despite it being well over your head was always inspiring. I am saddened that I am no longer going to be able to tell you what I work on... but such are the backrooms of industry. You have supported my thirst to learn and experiment since I was young, starting with helping me take apart garage sale electronics, Odyssey of the Mind, Lyceum, pushing for us to enter Harker Academy, then to support me in taking every Math and Science AP at Archbishop Mitty HS while doing FIRST robotics 6 weeks a year (and thus slicing 0.25 off my GPA at least). Thank you for continuing to support me through UCSB, allowing me to go onto graduate school un-indebted.

Finally, I would like to thank my wife Monica. You have been with me from the first graduate school tour to through the highs of microcracks, the lows of LSMO absorption, and back to the joy of magnetic beads and my defense. Your extensive support, via living near UCLA, splitting the bills, giving us vacations, and bringing out the silly side of me have all been key for me continuing this degree. I love you, and I am finally filing this thesis... for you. On to the "real world" we go together!

Vita

2006	Apprentice Researcher, CNSI, UCSB. Santa Barbara, CA.
2007	Summer Intern, Mechanical Eng. Dept., UCSB. Santa Barbara, CA.
2008	Thermal Modeler, RoboAcademy, NASA. Moffet Field, CA.
2009	Research Intern, Institute for Paper Sci. and Tech., TU Darmstadt. Darmstadt, Germany.
2010	Aqueous Foam Researcher, Trinity College Dublin. Dublin, Ireland.
2011	B.S. (Mechanical Engineering), UCSB, Santa Barbara, CA.
2012	M.S. (Mechanical Engineering), UCLA, Los Angeles, CA.
2012–2013	Instructional Assistant, Matlab workshop, UCLA. Los Angeles, CA.
2014	Summer Associate, RAND Corporation. Santa Monica, CA.
2011–2016	Graduate Student Researcher, UCLA. Los Angeles, CA.
2016	Ph.D. Candidate (Mechanical Engineering), UCLA, Los Angeles, CA.
2016	Future Technical Leader Program, Northrop Grumman Corporation

Publications and Presentations

S. M. Strutner, F. Pena, A. Piazza, A. R. Parker, W. L. Richards, and G. P. Carman,

"Recovering strain readings from chirping fiber Bragg gratings in composite overwrapped pressure vessels," *SPIE*, 2014, vol. 9059, no. 408, p. 90590F.

S. Strutner, A. Garcia, C. Adamo, L. Richards, K. Wang, D. Schlom, G. Carman, "Index of refraction changes under magnetic field observed in La0.66Sr0.33MnO3 (LSMO) correlated to the Magnetorefractive effect," (In Preparation)

S. Strutner, T. Barra, S. Ula, F. Pena, L. Richards, G. Carman, "FBG Magnetometer Array," (Paper and U.S. Patent Applications in Preparation)

S. Strutner, A. Garcia, C. Adamo, D. Schlom, and G. Carman, "Magnetorefractive based index of refraction changes under magnetic field in LSMO," *MMM*, San Diego, CA, (Presentation) Jan 12, 2016.

S. Strutner, F. Pena, A. Piazza, A. Parker, W. Richards, and G. Carman, "Recovering strain readings from chirping fiber Bragg gratings in composite overwrapped pressure vessels," *SPIE*, San Diego, CA, (Presentation) March 12, 2013.

S. Strutner, S. Ula, T. Lee, and G. Carman, "Optical magnetometer utilizing the magnetorefractive effect in LSMO," *MMM*, San Diego, CA, (Poster) Jan 14, 2016.

S. Strutner, C. Adamo, A. Garcia, L. Richards, D. Schlom, and G. Carman, "Characterizing Sensitivity of Refractive Index to Magnetic Field," *TANMS NSF Annual Review*, Los Angeles, CA, (Poster) April 28, 2015.

S. Strutner, C. Adamo, A. Garcia, L. Richards, K. Wang, D. Schlom, and G. Carman, "Characterizing Index of Refraction Changes From The Magnetorefractive Effect In LSMO," *MRS*, Cancun, Mexico, (Poster) Aug 19, 2014.

CHAPTER 1

Introduction

1.1 Structural health monitoring

"Like nerves in your arm, this will add sense to plane wings. It will let a plane know when one is damaged, and to favor the undamaged side." - Scott Strutner

High performance structures carry loads without needing as much mass and material as traditional structures. These are efficient designs, which utilize only the material needed for the load and safety factor. These safety factors reduce the efficiency of the structure by adding more material for "corner cases" of extra loading or variance in material/manufacturing quality. A simple example is a pressurized vessel, such as a compressed air tank. For pressure tanks, the classic performance metric [76] is

$$\text{Performance} = \text{Pressure} * \frac{\text{volume}}{\text{weight}} \tag{1.1}$$

Pressure tanks are designed for a variety of operating pressures with a safety factor of surviving 2 to 2.2 [18] times that pressure. Each gram the structure is reduced by makes for a higher performance vessel, but makes the system vulnerable to unexpected loads, and damage taken during such loadings. When pressure vessels fail, they may do so by leaking slowly, or by quickly and catastrophically failing. In all metallic structures, the failure is designed by ASME standards to be a slow leak. In a COPV, the failure is instead sudden, rapid, and may be akin to a small bomb. COPVs are commonly used in high performance-need places, such as satellite fuel tanks. Their failure mode is dictated by one crack in the structure reaching critical size, and precipitating a cascading failure. Thus, to greatly reduce

the material in the system while still maintaining its safety, distributed sensors monitoring structural health are needed. This would alert the operator (human or automated) that the structure is overloading or damaged. After notification, the systems may change their structure or loading configuration to accommodate the damage or extra load. To change loading in a pressure vessel, pressure may be released. To unload damaged regions of plane wings, rearranging the angles of flaps or even landing the plane and repairing the wing is needed. Systems which monitor their health and modify loads or stiffness are known as smart structures,[12] and furthering the sensor implementation of them to allow for high fidelity sensing is the first goal of this work. This will be done using optical fiber Bragg gratings, embedded and surface mounted on a COPV.

1.2 Magnetic field sensing

"Look at this poor oil-covered duck. It got coated in oil when this pipeline split open in rural America. Within this environmental disaster lays an engineering tragedy - ***the magnetic inspection system failed*** *to identify those cracks just months earlier."* - Scott Strutner

A modern sensor with wide application is the magnetometer. These measure the intensity and/or direction of magnetic field. Magnetic field monitoring is an old science, dating back to the compass and load stone of the 1000s [65]. These showed the direction of Earth's magnetic field for navigation. Analogous magnetic field navigational senses have been found in a diverse set of creatures, from birds [101, 36] to turtles [56], from fruit flies [92] to lobsters [5] and down to bacteria [39]. These organic systems utilize various methods from magneto-chemical-photon interactions [101, 56, 92, 23], to single domain magnetite particle chain alignment [39], to super paramagnetic particles [36]. Modern sensor systems for magnetic fields are single sensor or multiple sensor devices [16, 70]. Single sensor devices are still common in navigation, such as allowing smart phones to know the phone's orientation [70]. Multi-point sensing devices may be used as a gradiometer, detecting spatial changes in field strength [70]. These may be first order systems using two sensors up to nth order gradiometers with n+1 sensors [70]. Such gradient readings allow estimation of source dipole

size and distance estimation. Gradiometers play a crucial role in imaging remote areas, such as under the ground in an archaeological dig, without disturbing the site. Further arrays of sensors can be said to "image" a structure's magnetic signature to locate anomalies. In practical applications, dense, medium-sensitivity magnetometer arrays are used extensively for oil pipeline inspection on vehicles known as "Smart-Pigs" [78]. Via MFL, pipe wall thinning due to corrosion, abrasion, pin-holes or cracking may be found via 'scanning' the walls of a pipe. MFL works by magnetizing the pipe walls, and where there is a deficiency in the material the magnetic field will be seen to 'leak' out of the walls, and interact more with sensors passing along the surface.

1.3 Motivation

As technology advances systems' ability to understand data, there is the opportunity to feed more sensor data to these systems to improve the control and understanding of their performance. At its core, this work was meant to advance how future systems will sense themselves and the world they are in.

1.3.1 Strain sensing motivation

This National Air and Space Administration (NASA) funded research effort was started in response to a crash of their HELIOS aircraft. As seen in Figure 1.1, the plane failed when its wings exceeded the allowed dihedral, bending so far as to break. A post-failure investigation found that operators did not know about the already significant loading to the wing. Should they have been able to monitor that high dihedral state they would have landed the plane, averting the overloading and failure. FBG technology was identified as able to detect wing surface strain, and then integrate to define wing shape. A successful instrumentation of an Ikhana aircraft to monitor its wing shape during take-off, flight, and landing was performed in 2008 by the AERO institute and NASA Armstrong (then Dryden [100]). Following this, a further strain monitoring application was identified - COPVs fuel tanks. They are known to fail at unpredictable conditions, requiring very high safety margins when in use. Low failure

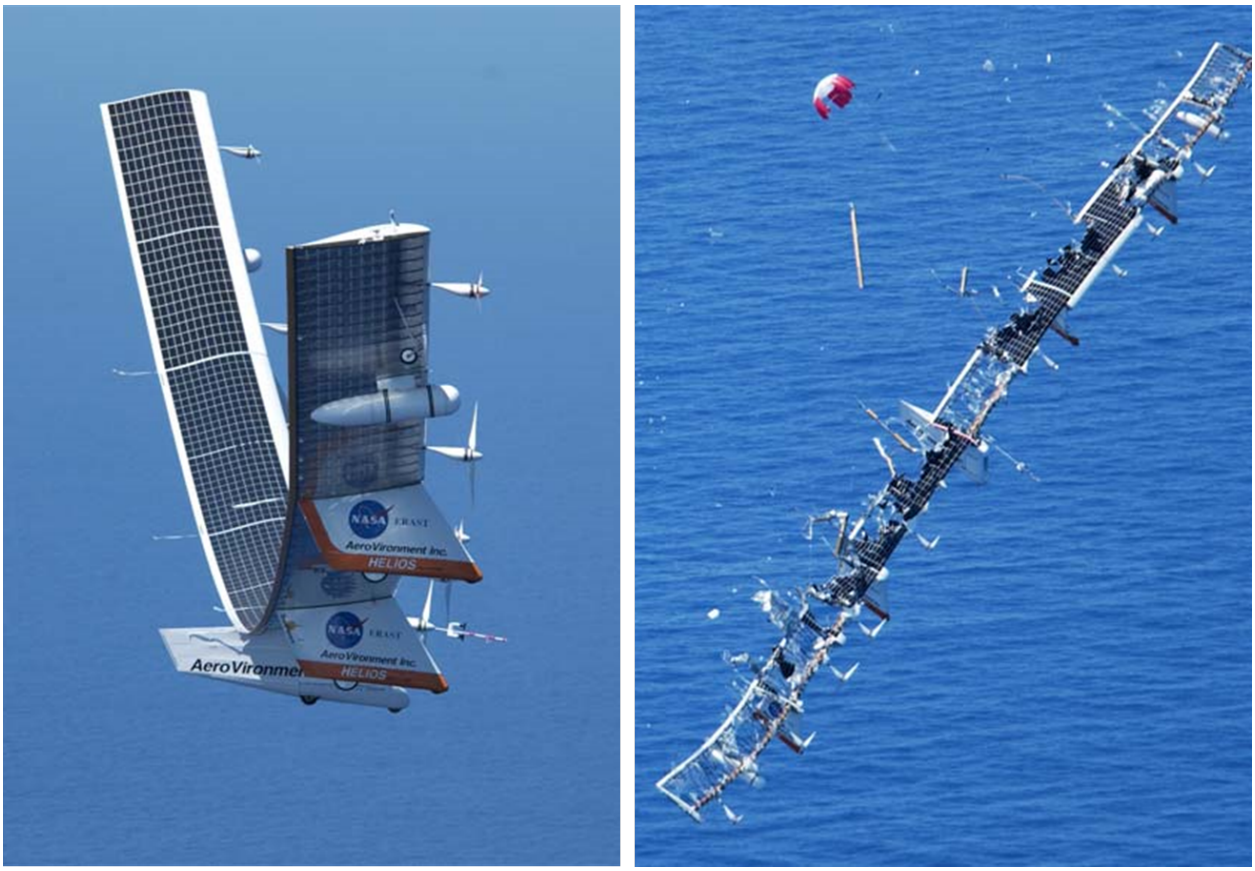

Figure 1.1: The Helios aircraft before and after catastrophe (as it was falling to the ocean).

pressures have led to space missions being launched under-fueled, such as the NASA Dawn mission [58]. As dramatically stated by the news article [114] shown in Figure 1.2, missions end when fuel in vehicles runs out. Thus, the corollary is that pressurizing systems to higher levels with more fuel would directly lengthen the useful life of the system. It is hard to find a clearer or more direct increase of a system's return on investment (ROI) than this.

1.3.2 Magnetic field sensing motivation

In our world's pursuit of energy we have drilled into the Earth and brought to the surface the compressed, bonded and stored energy of plants from eons past, in the form of petroleum and oil. While this thick, energy dense material was once green plants and healthy life, it now may pose a direct and debilitating threat to life on our surface. Take for example the poor oil-covered duck shown in Figure 1.3, section A. It was covered in oil when a pipe

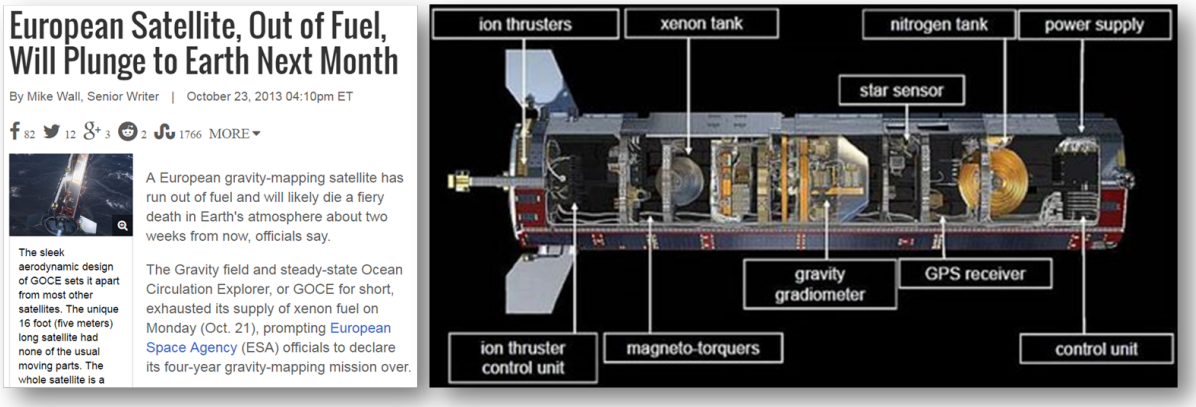

Figure 1.2: The GOCE spacecraft and an article about its end of mission, headline reproduced from [114].

crossing Alabama wetlands shown in section B split lengthwise along its weld line. Within this environmental disaster lies an engineering tragedy. As summarized in the headline from the Wall Street Journal [37] shown in section C, the inspection method used just months before to inspect that pipe did not find those cracks. This is a sad and routine story that was repeated roughly a year later in California [103].

1.4 Light

The study of light is an ancient endeavor. The use of optics go back to before recorded history, with a polished rock crystal plano-convex lens being found from 2200 BCE [104], and more lenses found in digs have been dated to later centuries. An excellent early treatise on lens design and optics was made much later, around 100 CE, by Ptolemy. Ptolemy's work [97] was largely ignored until Arabian mathematician Ibn Al-Haytham's *Book of Optics (Kitab al-Mancdir)* referenced it around 1000 CE. In this book, Al-Haytham derives and states Snell's law long before its European namesake [97] did. This literature, too, had little impact on further works, and was overlooked by the western world.

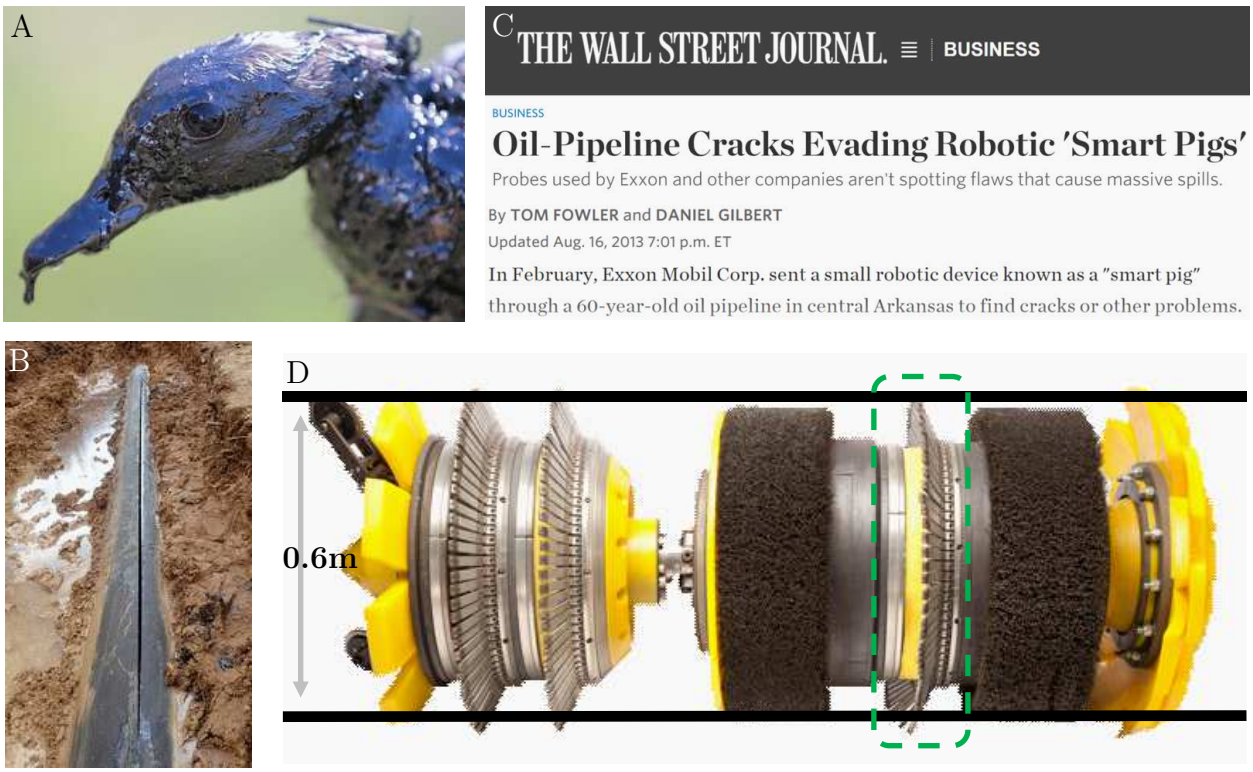

Figure 1.3: A composite figure. Section A is from Courtney Spradlin of the Log Cabin Democrats. Section B is an image from the Wall Street Journal shown in section C, of the split oil pipeline which led to the coating of the duck seen in section A. Section C is a news headline about this pipeline splitting open [37]. Section D is the DfI by Enduro, a smart pig which used MFL to detect cracks in pipes like the one shown in section B.

1.4.1 Light's nature

In the Middle Ages, theories on light were again addressed, with René Descartes stating that light had wave properties in his 4th point of the 14th chapter of the 1633 *Le Monde ou Traite de la lumiere* [22]. On the nature of light, Newton, starting in 1666 CE, discovered that white light is really many colors traveling together. He theorized that color was an aspect of "bigness" [82], and later that light was composed of particles [83]. Christiaan Huygens at the same time pushed that light was instead a propagating wave [38], allowing for polarization and interference effects to be explained. These two theories - that light was a particle of size, and that it was a wave of sorts - conflicted and were vivaciously discussed for many years.

The next great advancement in western understanding of light came in measuring the speed of light, and understanding that the speed is finite. In 1849 Fizeau estimated the speed of light at $313.000\,\mathrm{km\,s^{-1}}$ [35] using a rotating toothed wheel [38]. For the next hundred years, light's speed underwent further study, with Maxwell showing that the speed of direct current (DC) electric currents and light were connected, both being at either end of the EM frequency spectrum [38]. Finally, Evenson et al. found the speed of light to be $299\,792.456\,20(11)\,\mathrm{km\,s^{-1}}$ in 1972 [33]. In 1983 it was felt well known enough that the speed of light was used as a basic constant with the meter defined as a the distance traveled by light in a vacuum in $\frac{1}{299792458}$ s. Studying the 'speed of light' today has become the study of how light slows in materials, quantified by the index of refraction, n. Characterizing, controlling, and utilizing the indices of refraction of materials is the core physics that drove this thesis.

Finally, it should be noted that recent work throws into question whether the speed of light in a 'vacuum' is constant. Recent literature by Urban theorizes that in vacuums, the spontaneous and constant creation and destruction of matter turns the speed of light into a statistical matter on the femtometer scale [112]. It is also proposed that this universal creation and destruction of particles spontaneously is what really gives rise to the permittivity and permeability of "free space". One can then argue that this is the rediscovery of luminous ether, a concept that light travels through a massless medium, though now the theory is better characterized than it was in the 1800s. For the rest of this manuscript, however, we shall not bother with this nuance of the speed of light in a vacuum, and will treat light in a vacuum as having a constant speed, and thus the permeability and permittivity of free space as given, unchanging quantities.

Our scientific understanding needs grounding in the propagation of light. Maxwell unified the theories of Ampere and Faraday, to show that an electromagnetic wave is self-propagating in nature, as illustrated in Figure 1.4.

While free space is empty, propagation may continue unimpeded or modified, but once light interacts with matter, then we must consider the matter's permeability and permittivity, and their effect on light.

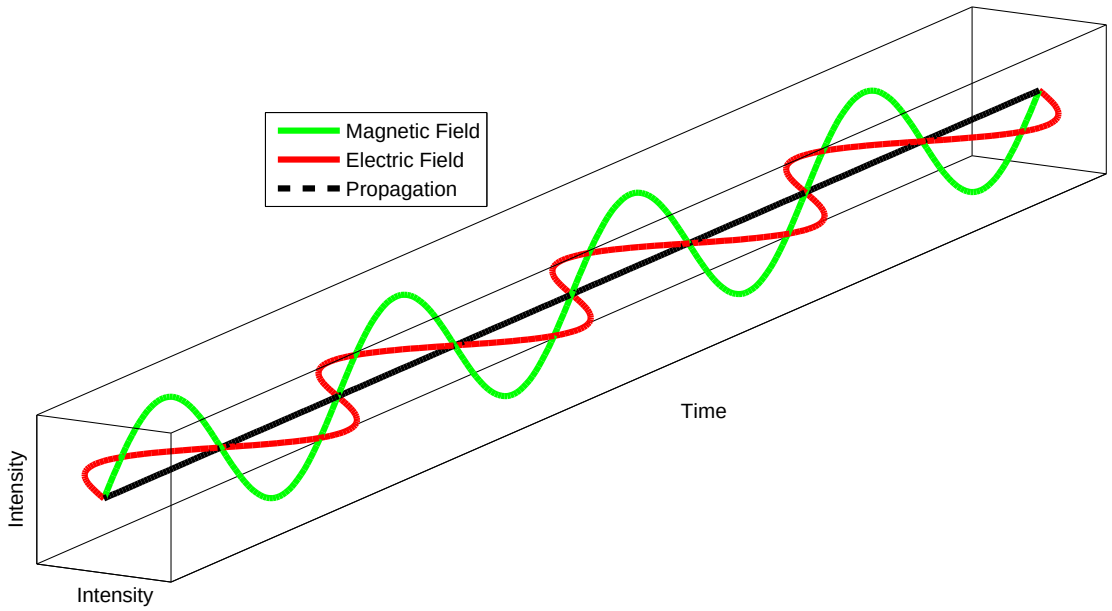

Figure 1.4: The propagation of an EM wave

1.4.2 Conduction Through Media

The permeability and permittivity of matter slow the propagation of EM waves. This is due to the electrically and magnetically polarizable dense medium responding to the wave of alternating fields of magnetic and electric charge. When a photon strikes an atom it is either absorbed, energizing an electron, or scattered, careening off in a new direction. At the spectrum we consider to be "light" for EM radiation, the magnetic permeability is considered equal to free space, as the alternating magnetic field does not stay polarized in a state long enough to rearrange the electron spins of the atom.

In a dense, homogeneous medium, the large number of close and identical scattering interactions interfere and create a coherent wave front such that light can only propagate in one direction. Lateral propagations are canceled out, and so the ray nature of light is seemingly preserved to the outside observer. The "scattering" process happens because each atoms' electrons act as dipole antennas, with the electrons' orbits being slightly polarized by the electric field of the photon and then falling back to a regular state. Such a dense array of phase-locked emitters effectively create a single intense interference of the incoming energy,

creating one bright band that continues the light's propagation in the direction it started in. Bulk scattering, such as colors milk and fog white, happens as there are particles and boundaries larger than the wavelength of light disturbing this interference condition, instead throwing light off in many directions.

When photons are instead absorbed into an atom, this energizes the atom's electrons, pushing them to a higher orbital. To return to the previous orbital, either the difference in energy must leave as another photon via re-emittance, or it must be conducted away and generally increase the thermal energy of the atom and its neighbors. Energized electron conduction generally goes on to be phonon relaxation, which yields thermal energy and is akin to joule heating. Before all dissipating as heat though, energized electrons may be conducted away and into other materials, which is how a solar cell operates.

When atomic space is non-uniform on the scale of the wavelength of the EM wave, then non-coherent scattering occurs. As the atoms, each acting as antennas, are not uniformly spaced, their re-emitted EM waves of light interfere in random ways, eventually creating a uniform propagation in all directions. This is classically called "scattering" in media, and is why clouds, milk, and clouded glass are a uniform white. Scattering from a rough surface is different, as the surface has multiple orientations at the wavelength scale, allowing small regions to reflect coherently, but preventing long-range coherent directionality due to the surface's lack of long-range common orientation.

Of the EM nature of light, this work focuses primarily on the wave's electronic nature's interaction with matter. The magnetic field of light also propagates through media though, and that must be addressed. At visible and IR wavelengths, the magnetic dipoles of atoms do not have time to reorient towards the light's magnetic field's direction. This is because the dipole of an atom is the axis of orbital spin of its unpaired electrons. It can be understood that it takes less energy to shift an electron's orbit to be more eccentric, than it does to fully reorient its axis of spin. The ability for light to magnetically polarize material quickly becomes complex for microwave frequencies and at THz frequencies as matter may orient some dipoles given the longer temporal period the field is applied for. For the matter and EM spectrum of this manuscript, the permeability *encountered by light* will be that of free

space. Still, DC magnetic field (or low frequency alternating current (AC) magnetic fields) will encounter a permeability specific to each medium and are very important to the second half of this work, which discusses the MRE.

Understanding that light is able to conduct through mediums, the question becomes what happens when light encounters a new material. In the antenna array model of matter, this is the boundary between two different antenna arrays. If light strikes this boundary at an angle then it will propagate in the new array at a different angle than before. From this we can see how light bends when it encounters a lens' surface.

1.5 Index of refraction

The speed of light is dependent on the ability of light's EM nature to charge matter both magnetically and electronically, and is represented by

$$v = \frac{1}{\sqrt{\epsilon * \mu}} \tag{1.2}$$

In free space we may use the permittivity and permeability of free space

$$c = \frac{1}{\sqrt{\epsilon_0 * \mu_0}} \tag{1.3}$$

but in materials we must use their specific values. To aid in measurement, the relative permittivity is the more common metric, presented by

$$\epsilon_r = \frac{\epsilon}{\epsilon_0}. \tag{1.4}$$

ϵ_r stays above 1 in classic materials (meta materials and other fields are focused on breaking this 'rule'). The permeability of materials falls to that of free space when the EM wave interacting with a material is at the IR or shorter spectrum. So, light's propagation in a material follows

$$v = \frac{1}{\sqrt{\epsilon_r * \epsilon_0 * \mu_0}} = \frac{c}{n}. \tag{1.5}$$

As conventional media's nature can only add to the permittivity of free space, then $\epsilon_r > 1$ for most materials. Thus, light travels fastest in free space. The speed of light in a medium is represented by the inverse ratio of its current speed to that in free space:

$$n = \frac{c}{v} \tag{1.6}$$

n is that inverse ratio, known as the index of refraction, and is equal to

$$n = \sqrt{\epsilon_r * \mu_r} \tag{1.7}$$

As visible spectrum light does not interact with the magnetic nature of materials, as explained above, μ_r is held at 1, and the index of refraction simplifies down to

$$n = \sqrt{\epsilon_r} \tag{1.8}$$

1.5.1 Complex and tensor forms of index of refraction

In many materials, a simple and real index of refraction is not sufficient to describe light's propagation. When light is absorbed by a medium (e.g. tinted sunglasses) or produced (e.g. lasing in a laser medium) then a complex index for the optical properties is needed. This expands the classic index of refraction defined in 1.6 to be $\bar{n}$:

$$\bar{n} = n - ik \tag{1.9}$$

with n being the real index, and k the complex component. The complex component is often known as the extinction coefficient (or gain value). Depending on the definition and perspective of a document, sometimes the equation is represented as $\bar{n} = n + ik$ instead. The complex component of index in optical materials arises from the complex permittivity.

$$\bar{\epsilon} = \epsilon - i\frac{\sigma}{\omega} \tag{1.10}$$

with σ the conductivity of the material (under given conditions such as magnetic field, or EM frequency,) and ω the frequency of the EM wave. As 1.8 shows index is dependent on permittivity, so too does complex index depend on the complex permittivity:

$$\bar{n} = n - ik = \sqrt{\frac{\epsilon - i\frac{\sigma}{\omega}}{\epsilon_0}} \tag{1.11}$$

$$\bar{n} = n - ik = \sqrt{\epsilon_r - i\frac{\sigma}{\omega\epsilon_0}} \tag{1.12}$$

$$n = \sqrt{\frac{1}{2}(\sqrt{\epsilon_r^2 + (\frac{\sigma}{\omega\epsilon_0})^2} + \epsilon_r)} \tag{1.13}$$

$$k = \sqrt{\frac{1}{2}(\sqrt{\epsilon_r^2 + (\frac{\sigma}{\omega\epsilon_0})^2} - \epsilon_r)} \tag{1.14}$$

However, this is insufficient to describe some materials, as not all optical mediums are isotropic. In particular, crystals - and otherwise isotropic mediums under an anisotropic strain, electric or magnetic field - shall all need tensor expansions on the complex index of refraction to properly describe the interaction of light and materials. Then, in a 'simple' non-isotropic optical medium

$$n = \begin{bmatrix} n_{11} & 0 & 0 \\ 0 & n_{22} & 0 \\ 0 & 0 & n_{33} \end{bmatrix} \tag{1.15}$$

In isotropic materials, $n_{11} = n_{22} = n_{33}$. In this manuscript, the magneto-optical (MO) discussion shall involve complex tensors to describe interaction of magnetic field gradients, crystals, material absorption, and optical conduction. Strain sensing work in FBGs often also require a tensor to describe the non-isotropic index resulting from various loading conditions and to describe the resulting birefringence. Exploring that topic is beyond the scope of this work and was well covered by Mike Emmons, the previous Ph.D. in the Active Materials Lab to work on this optics project, in his thesis [26].

1.6 Glass

The most commonly thought of optical material is glass. This material dates back to at least the Egyptian times and was first used for making beads and glazing pottery. In this manuscript, the word *glass* shall refer to amorphous materials containing silica oxide in solid solution with other atoms. Crystalline silica will be denoted as *quartz*, and glassy materials (those lacking crystalline ordering such as met-glass) as *amorphous* materials.

1.6.1 Properties of Glass

The vernacular usage of glass is to describe a clear material primarily made of silicon dioxide, where a non-crystalline matrix of silicon and oxygen is bonded together. This pure form may not have the optical, mechanical, thermal, or electrical properties desired though, and so various other oxides are added. Additionally, pure silicon sources are expensive, thus many oxides are natively present, such as iron oxide, which is the source of the green and brown colors in many glass drinking vessels, and why two mirrors facing each other fade into a dark green tunnel. These impurities are sources of scattering in glass. In the array of antennas model of solid media, these atoms may be thought of as slightly different antennas than the surrounding antennas, thus interrupting the interference-generated wavefront. Control of their presence is necessary for light to be conducted for long distances through glass.

1.6.1.1 Impurity Removal

An optical fiber may be thought of as a very thick window, through which we can shine light many kilometers. For a photon stream to be detected at the other end of such a window, nearly all sources of impurities must first be removed. The discovery that trace impurities were what hindered light's long-distance propagation is attributed to Charles Kao and Charles Hockham in the UK [106, 61]. It was Corning Glass [106] in 1970 that met this challenge, reducing the iron impurities down to the 1 ppm, and attenuation down to $20\,\mathrm{dB\,km^{-1}}$ [61]. With a glass through which light could be conducted long distances without

attenuating, fiber optic communication was made possible, and fiber production ramped up.

1.6.1.2 Photo-sensitivity

Photo-sensitivity is generally a chemical reaction driven by illumination with light. In glass, it is when the glass cross-links further, increasing the index of refraction in that area. It was at first discovered in Germanium doped glass by accident, and with it, the FBG was discovered too.

In experimenting with fibers, it was found that their indices changed when exposed to 488 nm light [47]. This was discovered by shining 488 nm light down a fiber, and observing that over time it would not transmit as intensely, but instead be reflected back. With just 9 min of 250 mW illumination, the fiber was up to reflecting back 44 % of the light. This effect was only present in low-mode fibers instead of the then popular multi-mode fibers. After this state of reflectivity to 488 nm light was reached, it would not fade, appearing permanent (it is until heated) [47]. The fiber would not reflect light that was not 488 nm, instead only being reflective to that particular wavelength. This was also the discovery of Bragg gratings, as that was what was being created in the fiber, a 488 nm Bragg grating. As light would reflect back from the end facet of the fiber optic, it would constructively interfere with the first path of light. This constructive interference was at half the wavelength of the light Δ =488 nm/$(n * 2)$.

1.6.1.3 Photo-elasticity

Using the antenna array model for a dense medium, as the medium is strained, the location and density of the antennas change slightly. This straining then changes the array's propagation speed for the EM wave. Then this propagation speed change is perceivable as a change in the index of the material. That change in the index due to strain of a material is known as photo-elasticity, and was discovered and described by David Brewster [7]. It is commonly reversible, unless the strain causes lattice movement, such as movement of dislocations. Photo-elasticity is dependent on temperature, wavelength and material. This

manuscript will mainly be concerned with silica, which has photo-elastic constants near $p_{11} = 0.126$ and $p_{12} = 0.26$ [6].

In uniaxial strain the transverse strains, ϵ_1 and ϵ_2, are equal and determined by Poisson's ratio ν and longitudinal strain ϵ_3:

$$\epsilon_1 = \epsilon_2 = -\nu\epsilon_3 \tag{1.16}$$

The strain-optic coefficient p_e is used to describe these [26]:

$$p_e = -\frac{n^2}{2}(p_{12} - \nu(p_{11} + p_{12})) \tag{1.17}$$

which will in part determine a Bragg shift $\delta\lambda_B$:

$$\frac{\delta\lambda_B}{\lambda_B} = (1 - p_e)\epsilon_3 \tag{1.18}$$

the effective uniaxial strain-optic coefficient is

$$\frac{\delta n}{n} = -p_e\epsilon_3 \tag{1.19}$$

From Emmons, $p_e = 0.1667$ [26] to Morey's characterization of $p_e = 0.22$ [80].

1.7 Reflections

Reflectivity describes the fraction of light that rebounds off of a surface of a medium. This is opposed to light that is transmitted past a boundary, generally refracted at an angle. A nominal reflection encountered daily is light shining directly onto a glass surface. The reflectivity of the air-glass interface is $\tilde{4}\%$. As each plane of glass has two interfaces, this then leaves only 92% of light to pass through a pane of glass, and 85% through energy efficient double-paned windows (which are efficient as thermal insulators, but not for blocking all light per se, though IR and UV coatings may reduce solar insolation-based home heating). This is part of why it is darker inside a building than outside: windows may be transparent, but they are reflective.

1.7.1 Reflective Fresnel equations

When light propagates from one medium into another, then its electric nature encounters a change in permittivity. This is an impedance mismatch electrically, and can be thought of as speed mismatch that a classical strain wave would encounter. If the boundary is approached directly, perpendicularly, then the direction of propagation is maintained, while the speed changes. The governing equation for reflection normal to a boundary is

$$R = \left(\frac{n_1 - n_2}{n_1 + n_2} \right)^2 \tag{1.20}$$

with n_1 being the index of the material that light is exiting or coming from, and n_2 being the index of the material that light is entering or striking. Glasses have a visible spectrum index of refraction of approximately 1.5 and so for light traveling through air, which has an index of 1.0003 or so, reflection off of the interface is about 4 %.

When light impinges on the boundary at an angle θ_1, its path is bent at the boundary. This is again due to the impedance mismatch. The new angle is then θ_2,

$$\theta_2 = asin \left(\frac{n_1}{n_2} sin(\theta_1) \right) \tag{1.21}$$

This is called Snell's law, named after its Dutch re-discoverer, Willebrod Snellius, although first stated by Ibn Al-Haytham [97].

1.7.2 Variable angle of incidence

The reflectivity at a given angle θ was studied and characterized by Fresnel, who gave the characterization equation for s-polarized light to be

$$R_s = \left(\frac{n_1 cos(\theta) - n_2 \sqrt{1 - \left(\frac{n_1}{n_2} sin(\theta) \right)^2}}{n_1 cos(\theta) + n_2 \sqrt{1 - \left(\frac{n_1}{n_2} sin(\theta) \right)^2}} \right)^2 \tag{1.22}$$

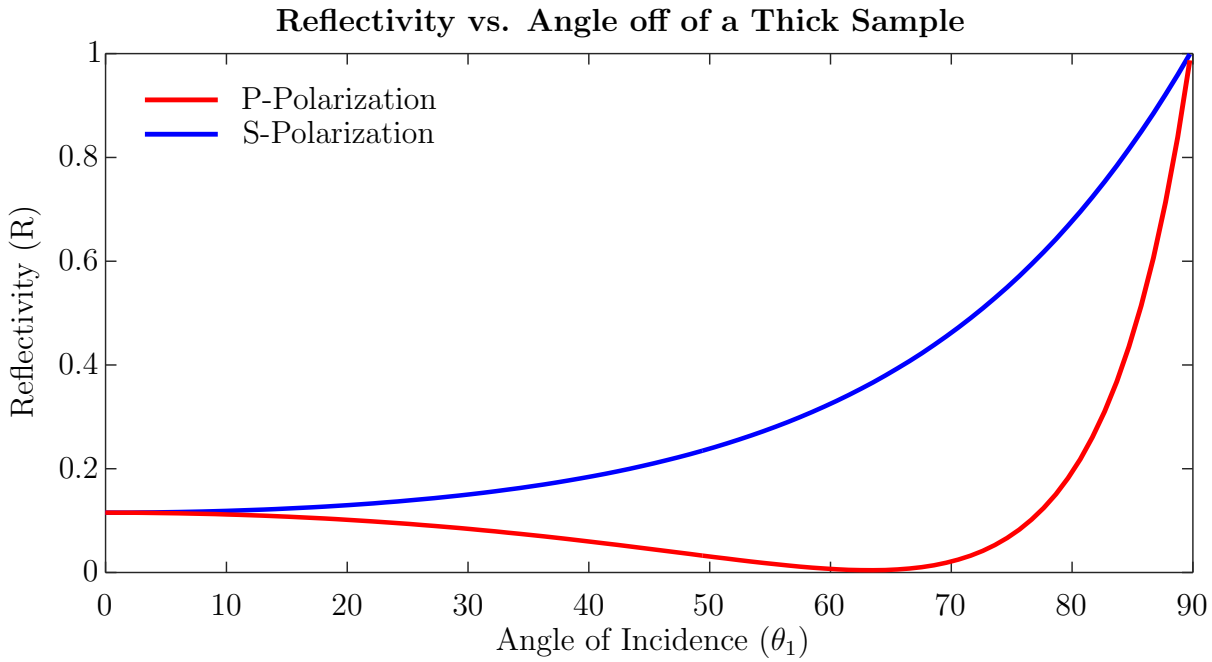

Figure 1.5: The modeled reflectivity vs. angle for two polarizations of light off of a bulk sample of index of refraction 2 in air of index of refraction 1.0003.

and p-polarized light to be

$$R_p = \left(\frac{n_1 \sqrt{1 - \left(\frac{n_1}{n_2} sin(\theta)\right)^2} - n_2 cos(\theta)}{n_1 \sqrt{1 - \left(\frac{n_1}{n_2} sin(\theta)\right)^2} + n_2 cos(\theta)} \right)^2 \tag{1.23}$$

These equations are applicable when bulk optics are being considered, as they do not account for phase interactions of reflected beams.

1.7.3 Brewster's angle

The Brewster's angle is defined as the angle at which the p-polarized light is best coupled into the material, showing a minimum of reflectivity. In Figure 1.5, this is at around 63.6°. For p-polarized light, this may be found at:

$$\theta_{\text{Brewster}} = atan(\frac{n_1}{n_2}) \tag{1.24}$$

As the reflectivity goes through an inflection point, it is a distinctive feature in the reflectivity versus angle plot. This region is useful in characterizing the index of a sample, as mathematically fitting indices' to reflectivity data around the Brewster's angle yield more consistent results than around other angles. This will be used extensively in Chapter 6.

1.7.4 Critical angle - total internal reflection

Between the boundary of two mediums of different indices, while propagating from the higher index to the lower index material, there is an angle at which reflectivity is absolute, and at any subsequent angles will continue to be fully reflective. This is known as the critical angle and exists only when $n_1 > n_2$, that is to say, only when the light encounters a boundary, transitioning between a slower medium, into a faster medium. This effect can be experienced by swimming and looking at the surface of the water while one's eyes are submerged underneath. The critical angle is found at:

$$\theta_{\text{critical}} = asin(\frac{n_2}{n_1}) \tag{1.25}$$

There is a point, at 48.75°, where it appears that the water ahead is merely a tunnel, with the pool bottom doubling as tunnel ceiling. Really it is that the light and the view it creates is being reflected off of the surface of the water. This same phenomenon occurs as light is conducted down a light pipe as shown in Figure 2.1.

1.7.5 Thin film reflectivity

When the reflectivity of thin films is considered, the phase interactions and their interference must also be considered. The general and common note is that the light normal to a thin film surface will have "Newton Lines" form due to interference effects totally constructively and destructively interacting [119]. The equations of interest are reversed depending on if the thin film coating will create a phase inversion between the two waves. Inversion of waves occurs when waves go from a fast material to a slow one, or, in optics, from a low index material to a high index material. Thus, when $n_1 < n_2$ with light of wavelength λ and a film

of thickness t

$$2t = (m + \frac{1}{2})\lambda \tag{1.26}$$

with $m = [0, 1, 2, 3, ... < \text{inf}]$ will be constructive reflection, and

$$2t = m\lambda \tag{1.27}$$

will be destructive reflection for an film of thickness t.

When $n_2 < n_1$ there is no interface driven phase inversion, then the cases reverse and

$$2t = (m + \frac{1}{2})\lambda \tag{1.28}$$

will be destructive reflection, and

$$2t = m\lambda \tag{1.29}$$

will be constructive reflection.

For off-normal reflectivity, the situation is more complex, and is instead described by thin film interactions. A general expression for this case was developed by Cook in 1948 [15]. A subset of the general case, and the one relevant to the MRE sections of this manuscript, is that of a one-film layer on a bulk substrate.

$$R = \frac{r_{12} + r_{23} * e^{i2\phi_2}}{1 + r_{12}r_{23} * e^{i2\phi_2}} \tag{1.30}$$

R is the net reflectivity off of the first boundary (e.g. that of air to a LSMO film). ϕ_k is the phase lag and defined in Eq. 6.4. r_{kk+1} is the reflectivity from k to $k+1$, k being the layer number from the top, and is dependent on the polarization of the light. For light polarized with the electric field vector in the plane of incidence (s-polarized) then

$$r_{kk+1} = \frac{n_{k+1}c_k - n_k c_{k+1}}{n_{k+1}c_k + n_k c_{k+1}} \tag{1.31}$$

should be used.

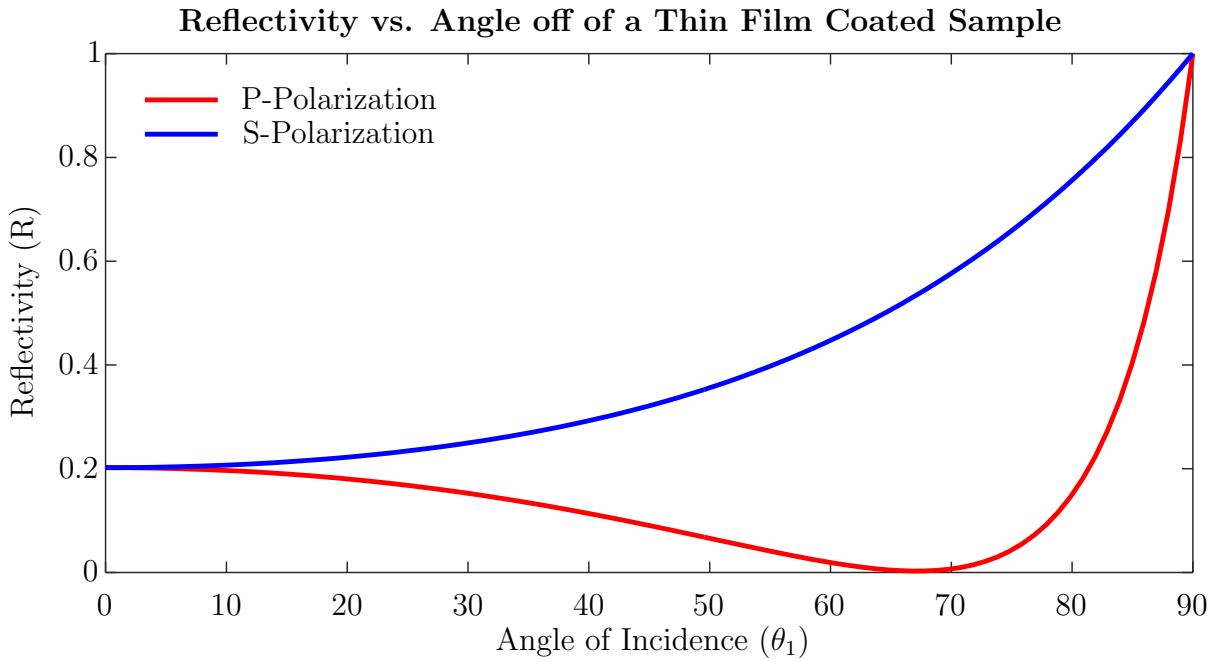

Figure 1.6: Reflectivity vs. angle for two polarizations of 633 nm light is shown off of a thin film sample in air, with index stack of [1, 2, 1.5] and thicknesses of [inf, 70 nm, inf].

For light polarized with the electric field vector perpendicular to the plane of incidence (p-polarized) then

$$r_{kk+1} = \frac{n_k c_k - n_{k+1} c_{k+1}}{n_k c_k + n_{k+1} c_{k+1}} \tag{1.32}$$

should be used with n_k as the index of the k^{th} layer, and c_k as the light's path, defined in Eq. 6.5. The ϕ_k from Eq. 6.2 is the phase lag induced in the material, defined by

$$\phi_k = -2\pi n_k c_k d_k \lambda^{-1} \tag{1.33}$$

ϕ_k also utilizes the light's path, c_k, which is angle and index dependent,

$$c_k = cos(\theta_k) \tag{1.34}$$

θ_k being the angle of the light in the material, dependent on the index of the given layer

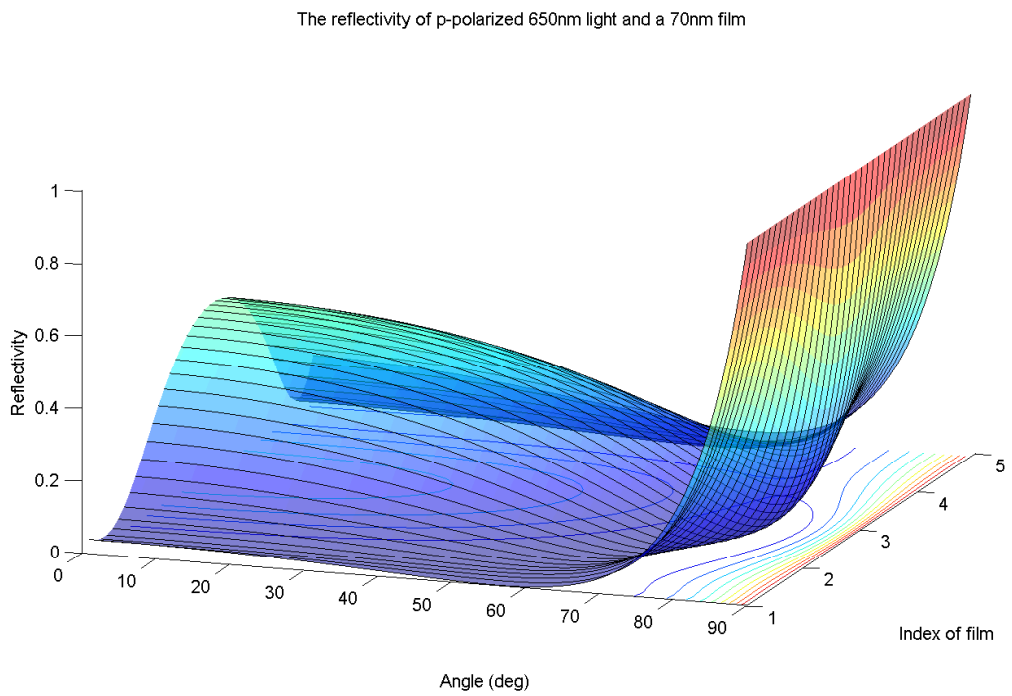

Figure 1.7: The reflectivity of a film of various indices at angles from 0 to 90 degrees

compared to that of the top layer

$$\theta_k = asin\left(\frac{n_1}{n_k}sin(\theta_1)\right) \tag{1.35}$$

$$c_k = cos(asin\left(\frac{n_1}{n_k}sin(\theta_1)\right)) = \sqrt{1-\left(\frac{n_1}{n_k}sin(\theta_1)\right)^2} \tag{1.36}$$

where k=[1,2,3] represents air, a thin film, and a substrate, while d_k are their respective thicknesses. λ is the wavelength of light, in the same units as d_k. Finally, θ_1 is the angle of incidence from air onto the sample. For a 70 nm thin film sample of index 2, in air, on a substrate of index 1.5, then the reflectivity vs. angle of 633 nm light may be calculated to be as shown in Figure 1.6.

If one were to look at reflectivity as a function of angle and index, the following surface would be given:

.

CHAPTER 2

Fiber Optics

The groundwork of optical fibers starts with the optical lens, bending and focusing light. A lens bends light at its interfaces, with the bulk merely conducting light. The actual reorienting and focusing of light is due to the index change from lens to air. Similarly, the first conduction of light from one place to another in a medium was due to boundary conditions of an abrupt change in medium. Conducting light was first demonstrated in a controlled manner using total internal reflection. It is widely credited to John Tyndall who in 1870 [106] demonstrated to the Royal Society of London that a water stream can conduct light. This can be seen in Figure 2.1. This very topic and method was previously published, in Paris by Colladon in 1842 [14]. Still, Mr. Tyndall's presentation is seen as the founding of the field of fiber optics, and would lead to the glass light pipe which utilizes total internal inflection to carry light a great distance.

The next step towards optical fibers was in 1966, when Kao and Hockham proposed that optical fibers would work as an optical data transmission line, if losses could be reduced to below 20 dB/km [61]. Their seminal paper further speculated that the then current losses at over 1000 dB/km in glass fibers were from impurities in the glass [106]. In the 1970s, Corning Glassworks removed iron impurities from the glass, achieving what Kao and Hockam proposed. The optical fiber was ready for creation [106, 1], and the fiber Bragg grating (FBG) was ready for discovery.

Since the creation of purified glass, optical fiber technology progress has not stopped. There was a commercial slump in the early 2000s after many manufacturers over-extended themselves, but further work on geometric shape, and index of refraction profile, has progressed the field. Now, optical fibers are also made of plastic [66]. These plastic optical

fiberss (POFs) are still an active field of development in raw fiber research. As a cheaper material, and with a much higher yield strain, they may allow new applications. POF currently do not perform well over long (1 km's) distances, but do work well over short ones (100 ms). POF would be a "drop-in" replacement to the magnetic fiber Bragg grating (MFBG) fiber of Chapter 9 and push a 10x improvement to the sensitivity of the MFBG sensor studied there.

2.1 History of light pipes

Colladon's first light pipe was a stream of water in air. When lit from behind, a stream of water flowing out of a tank guides light, channeling it within the water's path [14]. Seen in Figure 2.1, at each water-air boundary that the light strikes, it is reflected and continues to be guided by the stream of water. Light pipes are still in use today, now made with modern plastic for low power and glass for high power. Light pipes can be seen in many car taillights, and endoscopic illumination systems. Seen in Figure 2.2 is an example of such an endoscopic illumination system.

2.2 Fiber optics

In a sheet of glass, one can imagine looking at the edge into the thickness and seeing the view of the far edge, as well as this strip of image reflected ad-infinitum above and below due to viewing the glass-air boundary beyond its critical angle. This is an example of light conduction in a slab waveguide. Taking that glass-air boundary and wrapping it into a cylinder, we now have a glass light pipe. As light conducts down the length, it reflects off of each boundary. Not all glass works well for this purpose. Even with no light leaving the pipe via its walls, there is loss and attenuation along the length of the light path due to absorption and excessive scattering. A mile-long light pipe is akin to looking through a mile-thick window. The effect of so much glass absorption can be modeled by placing two glass coated mirrors face to face, and seeing that the "far off" reflections become green and

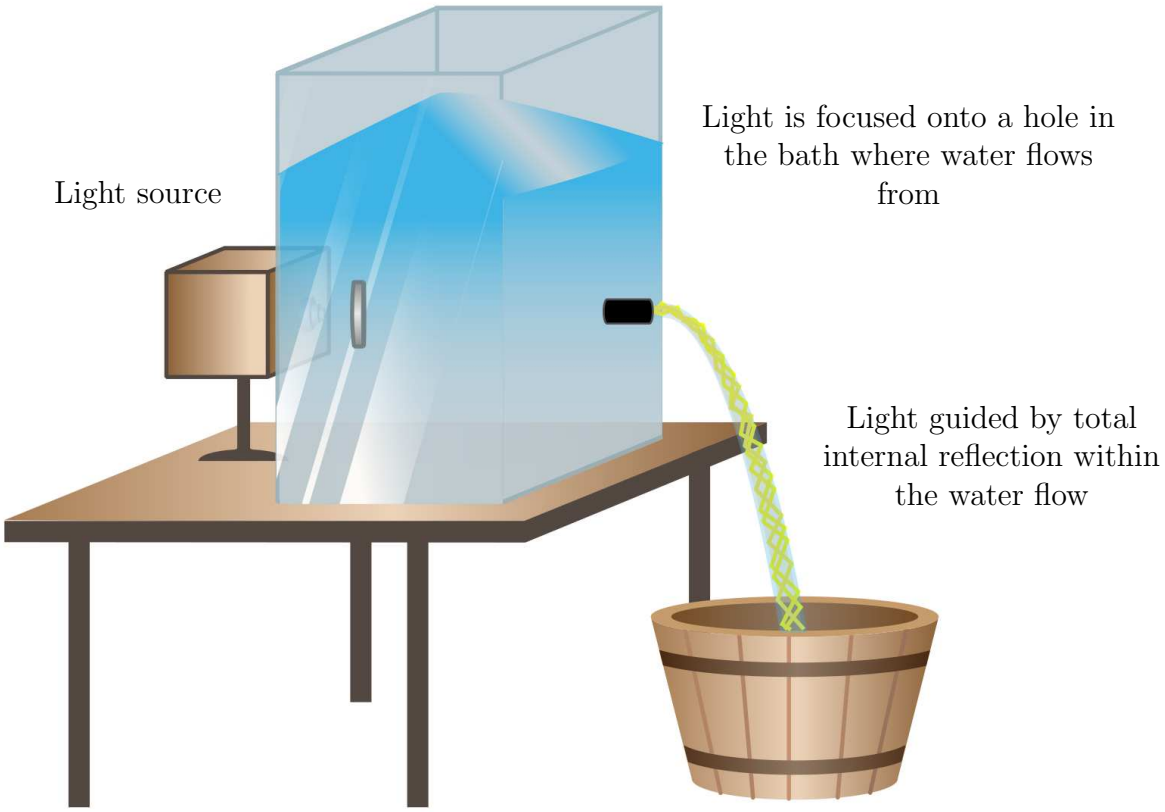

Figure 2.1: Diagram of the 1842 light pipe described by Colladon and shown in 1870 by Tyndall to the Royal Society.

Figure 2.2: A commercial endoscopic light source sold by LUT GmbH

dim. The green is the characteristic absorption due to common impurities in glass, and the general dimming is due to absorption.

To develop a functional optical fiber, it took a special effort by Corning Glassworks to remove impurities and allow glass light pipes to be more efficient, and carry light further. The push to make light pipes into optical fibers was due to a number of factors. First, material costs - a smaller diameter glass fiber takes correspondingly less glass to manufacture. Next, smaller fibers were more flexible, increasing handling durability. There are two complimentary sources of this. A: with less material, there is correspondingly less space for irregularities and imperfections. B: the strain on the surface of the fiber is less. Also important at first, and much more later, is that the thinning of the light pipe allowed light to go from being conducted in a ray manner, to a waveform nature. This contains light closer in the core, and does not make conduction of light dependent on surface roughness of the outside of the glass tube. This dramatically reduced transmission losses in the optical fiber. When light resonates within the fiber, it is said to conduct in modes. Over long distances, these modes may interact minimally, but enough to interfere. To allow for high throughput trans-oceanic cables, low-mode or single-mode fibers were developed, as well as sub-sea signal repeaters.

No matter the type of glass fiber, they are manufactured by a multi-step process. First, a glass preform is made, which mimics the layers of the eventual fiber. This is done via chemical vapor deposition (CVD) to 'grow' a solid glass core into a tube of glass of the desired fiber cladding type. Next, the preform's end is evenly heated and pulled on. This pulling process necks down the preform and draws out a single small diameter filament. This distinctive step gives the process its name of "drawing" or "pulling" fibers. The temperature and speed of drawing must be carefully controlled to control the diameter of the resulting fiber. As it is drawn it is cooled, then wrapped around a drawing roller. Then it is re-suspended, and coated with a polymer coating to protect the glass from very damaging nicks. FBGS, a Belgium FBG manufacturer, will write FBGs (see section 2.6) onto the fiber between the drawing and coating step for optimum gratings and fiber strength 10x that of stripped and recoated fiber. FBGs cannot be written through the plastic coating and it interferes with the ultraviolet (UV) writing light (see section 1.6.1.2 on photo-sensitivity). Finally, the fiber is spooled and ready to use.

2.3 Multi-mode

2.3.1 Ray vs. Evanescent field

As the optical medium for light is shrunk from a light pipe to an optical fiber, the optical conduction region then is shrunk from a diameter on the order of hundreds of wavelengths to that of a few tens. At this size, the ray nature of light begins to give way to the evanescent fields or resonant model of light conduction. Going back to the model of a solid medium being a collection of dipole antennas introduced in section 1.4.2, it can be seen that if the array has a structure (e.g. the core and cladding of an optical fiber) now the slight differences may be used to bend the light or add a phase lead in the cladding, which will push the proverbial light ray into the core of the material. The light then seems to resonate in the core of the optical fiber. Of course, with any resonance there are certain modes of appropriate propagation and conduction. These depend on the optical wavelength, medium and geometry of the fiber. Changing the wavelength or material constants, such as increasing the diameter of the core of fiber, will each increase the number of modes that can propagate within the fiber.

2.3.2 Fiber optics by modes count

Optical fibers are commonly classified into three categories:

- Single-mode fibers, which allow only one mode of conduction. (Core diameter of 5 µm to 10 µm [106])
- Low mode fibers, which allow up to a dozen modes.
- Multi-mode fibers, which may conduct upwards of thousand modes in large diameter fibers (Common core diameters are 50 µm, 62.5 µm and 85 µm [106])

2.3.3 Single mode

Due to data link length requirements, many optical fibers are single-mode. These generally have less attenuation, and no mode mixing compared to multi-mode fibers. For single-mode

fibers, the glass composition is optimized generally to one of two specific spectrums. For FBG, a single-mode fiber is needed.

2.4 1550 nm and 1300 nm fiber optics

1550 nm and 1300 nm are the standard working frequencies for optical communication channels [106]. The 1550 nm light is easy to make using a helium-neon gas laser (commonly referred to as a "HeNe"). 1550 nm is a point of minimum transmission loss in an optical fiber, as infrared absorption and ultraviolet absorption are equal and minimal. 1310 nm is also attractive, as dispersion is low, while transmission loss is at a local minimum. Separating 1310 nm and 1550 nm is an absorption hump from OH bonds, such as in water. When optical fibers are perfectly dry and desiccated then 1400 nm would be a transmittable wavelength. However, in normal operation, water intrudes slightly, and then rapidly increases transmission losses for telecommunication transmission lengths.

2.5 Basics of FBG

A FBG is a periodic series of perturbations in the index of refraction [32] of a glass or plastic optical fiber's core and/or cladding [66]. A common commercial method to produce these index of refraction perturbations of a constant pitch is side exposure to an interference pattern of UV light [77], allowing for the sensors to be quickly and consistently made. FBGs have been shown to be able to monitor strain [43, 40, 75], temperature [40, 26, 55], magnetic field [118, 86, 19, 107, 20, 115, 73, 95, 26, 30], cryogenic fuel levels, chemical composition, and electric current [120]. Literature has examples of other structural monitoring efforts for FBGs, such as a limited number of FBG on plane wings for health monitoring of UAVs by Park et al. [89].

2.5.1 Governing equation

Optical techniques can be used to both accurately quantify strains, and do so at many points on a body. This is through optical fibers and FBGs. FBGs are periodic structures in the optical fiber that have a narrow band reflectivity, dependent on the index of refraction which light encounters (usually that of the fiber), and the spacing of the periodic structure. Their governing equation is:

$$\lambda_B = 2n_{eff}\Lambda \tag{2.1}$$

with n_{eff} being the effective index which light encounters in the grating, Λ being the pitch (or spacing) of the periodic structure, and λ_B the reflected wavelength. As strain stretches the fiber, it also stretches the grating structure and so its pitch. This alone would change the peak reflected wavelength of the structure, but additionally the index of refraction of most glasses are photo-elastic (as introduced in section 1.6.1.3.) Thus, the λ_B of the structure changes due to the lengthening of the periodic structure of the grating, and a change in index of the structure's material.

2.5.2 Weak reflectivity allowing for multiple gratings

To allow for many FBG responses along a single fiber, weakly reflecting gratings may be used [41]. This is done by making δn perturbations small, which make up the total grating. To calculate the reflected intensity, one could try using 1.20, but that would only be for a single interface of a single perturbation. Instead, in a short 1 mm long grating for 1550 nm light in a nominally 1.5 RIU fiber there will be roughly 3871 such reflectivity facets. To get a nominal 0.1% reflectivity then requires that the reflected intensity at any one point need only be quite small if each reflectivity was additive. They are not additive, but it has been shown that a small index increase relative to the carrier medium is sufficient to achieve reflectivity [67].

With each FBG reflecting so little light back, subsequent FBGs are exposed to nearly the same intensity of light as a FBG at the beginning of the fiber. This allows each FBG to be treated as having the same input intensity. Also, FBGs at the end of a fiber do not have

their reflected spectrum 'screened' by FBGs near the front of the fiber.

2.5.3 Uniaxial strain sensing of a single grating

Literature often assumes a FBG is a single uniform device which reports a single strain. This viewpoint likely arises from a FBG's similarity to a strain gauge. In strain gauges, the resistance for the entire device is measured and thus a single reading is only available. For this introduction, FBGs will be continued to be treated as single quantized structures but it should be noted that each is already an analog device, and not innately quantized sensors. In subsequent sections of this thesis it will be shown that breaking the one FBG to one λ_B assumption significantly improves the understanding of a complexly strained FBG in the structure of a composite overwrapped pressure vessel (COPV).

2.5.4 Thermal sensing

It may be apparent, but any stretching of the grating results in a change reflective wavelength. Thus, elongation due to temperature change and thermal expansion is also detectable on FBG. This has been used to monitor the temperature of a furnace [98]. In a single FBG, it is in fact not mathematically possible to say whether a change in wavelength is due to a strain, or a temperature difference. There are, however, various methods to isolate mechanically induced strains and thermally induced strains on optical fibers. Temperature effects will cause a direct shift in the index of the fiber, effectively lengthening the optical path, while indirectly physically lengthening the glass via thermal expansion. Thus, the shift in λ_B may be written as

$$\Delta\lambda_B = \lambda_B[(\alpha_f + \xi_f)\Delta T + (1 - p_e)\epsilon] \tag{2.2}$$

where p_e is the photo-elastic constant, α_f the coefficient of thermal expansion (CTE), and ξ_f is a thermo-optical coefficient.

Mechanical strain on the fiber changes both the glass' index and geometry and is thus traditionally empirically measured in a combined state as a gauge factor. These factors' contribution will vary by specific fiber composition, geometry and operating wavelength.

This variation is clearly seen in the testing done by Black et al. on the gauge factor g of commercial FBGs as defined by

$$g = \frac{\delta\lambda_B}{\delta\epsilon_3} \tag{2.3}$$

FBGs may range from 1.00 pm/με to 1.28 pm/με depending on a given fiber and the wavelength that fiber is operated at [4]. For any given fiber type and wavelength, a calibration to find the gauge factor is needed for exact strain measurements.

2.5.5 Separating temperature and strain contributions in readings

There are multiple ways to separate temperature, T, and strain-based, ϵ, changes in Bragg wavelength, such as a strain isolated temperature control fiber [60, 71] or using two wavelengths of light [117]. The simpler method is to utilize the fiber as Chapter 3 does, on a structure without significant thermal gradients present. With no temperature compensation needed, the governing equation is reduced to

$$\Delta\lambda_B = \lambda_B(1 - p_e)\epsilon \tag{2.4}$$

or in another form

$$\epsilon = \frac{\Delta\lambda_B}{\lambda_B(1 - p_e)} \tag{2.5}$$

The first method is running two parallel fibers wherein one is mechanically isolated using a sleeve around the fiber and the other one is mechanically attached to a structure. The mechanically isolated one shall be assumed to only have changes due to temperature whereas the non-isolated fiber shall be assumed to have sensitivity to changes due to both temperature and mechanical loading. Subtracting the strain from the isolated fiber from the mechanically attached fiber, one can then subtract the temperature loading from the optical fiber.

Another method is using optical fiber Bragg gratings for both 1310 nm and 1550 nm light. In this system, the thermo-optic coefficient's dispersion allows that temperature changes at 1550 nm and 1310 nm are different [75]. This satisfies the two unknowns and two knowns when solving a set of equations. Equation 2.1 may be augmented for higher order gratings,

with a term N.

$$\lambda_B = 2n_{eff}\Lambda N \tag{2.6}$$

This can allow one grating to reflect multiple, but separate, spectrums at $N = 1, 2, 3....$ If 650 nm reflecting gratings were made with $N = 1$ than they would also reflect 1300 nm light with $N = 2$. If there is dispersion between the two spectrums though (as would be expected if not explicitly designed to prevent) then n_{eff} would not be the same, as it is really $n_{eff}(\lambda)$. Further, the fiber would have dispersion, as the two wavelengths would form separate modes when traveling down the fiber. A grating may be found which could simultaneously reflect 700 nm and 1310 nm light due to engineering these two factors. Conceivably, a fiber could also include reflectivity of 1550 nm light if carefully designed. This would allow for three unknowns to be separately solved for, albeit with great expense due to the triple lasers necessary for such a system to function. Such a system would allow for separately measuring strain, temperature and magnetic field using a material like Lanthanum Strontium Manganite $La_{0.66}Sr_{0.33}MnO_3$ (LSMO) with an index dependent on magnetic field.

2.5.6 Traditional uses for strain and temperature monitoring

To measure the strain that a structure is undergoing, the optical fiber is attached firmly to the surface of a structure, or embedded in it. A key factor is a very high strain rate transfer, that is, the ratio of strain in the structure to that in the optical fiber. This may not be one to one as the fiber is often much stiffer than the structure and thus a strain gradient is created in the bonding adhesive. To improve the strain transfer, fiber optics may be embedded into the structure, essentially straining it from above and below the fiber. If attached in a long section then the strain transfer issue is reduced.

A common comment when hearing that thousands of sensors may be added to a composite structure, is if these will add more weight than just reinforcing the structure, or carefully positioning a few strain gauges. The optical fibers are on the order of grams per meter. Comparably, the three wires needed for a strain gauge add tens of grams per meter. Thus, to evenly measure strain in one place, an optical fiber will weigh less than a strain gauge.

As FBGs can measure the strain at many places between that end strain placement and the originating point, the mass per sensed strain is massively reduced. The final consideration is the mass of the interrogating box compared to that of the strain gauge data acquisition unit (DAQ). The DAQ's mass scales roughly linearly with the number of strain gauges, while the interrogator hardly scales with fibers interfaced. While a strain gauge system may be lighter for a single reading, at the tens of strain readings then DAQ may have equal mass to a fiber optic interrogator.

In summary, fiber Bragg gratings are very lightweight sensors, with easy attachment and limited structural impact to systems, which can accurately quantify strain and be multiplexed along a single optical fiber.

2.5.7 Birefringence

Up to this point, it is assumed that an optical fiber is experiencing purely uniaxial loading which is due to strains along the fiber direction. A mounted optical fiber, though particularly one that is embedded in the structure, may experience transverse loading across the fiber.

In this case, there may be three different strain states present, wherein the X, Y and Z strains all experience different amounts. Due to photo-elasticity (PE), this non-isotropic strain state induces a non-isotropic index of refraction in an otherwise isotropic medium. Thus, when light propagates in an optical fiber with one linear polarization, it may experience a different index light than light in a perpendicular polarization. Further, both polarizations may be modified by the longitudinal strain Z in the fiber.

This dual index nature of material is known as birefringence. In reality, the materials become birefringent (instead of tri-refingent) as there are only two polarizations of light that are possible in the two radial dimensions of the optical structure - the third direction being the direction conducted down optical fiber. Now there are three unknowns ($\epsilon_x, \epsilon_y, \epsilon_z$) in the three cardinal strain directions, yet only two knowns - the two reflected Bragg wavelengths which must be the principle strains in the perpendicular radial directions X and Y with a Poisson's contribution from Z. This has confounded researchers, and spurred them to identify

ways to definitely state what is the strain along the axial direction and radial directions of an optical fiber with certainty, or give a range for what it may be due to, like the splitting of the two birefringent peaks [27]. Isolating transverse loading and using polarization-stabilized fibers have also been used to create/identify individual Bragg wavelengths and their strains.

2.5.8 Chirping

Chirping is the reflection of a broader spectrum of wavelengths rather than just a single peak. FBGs may be made in a chirping mode by writing the grating pitch in a non-constant manner, such as having the pitch linearly increase along the length of the grating. It may also be seen in a FBG with a constant pitch, and a non-constant index, such as one with an increasing index along the length of the FBG. This may be created by non-uniform loading in a uniaxial direction. Sometimes the interference from non-uniform chirping produces a signal confused with birefringence. Multi-peak states are often called birefringent even when they reflect more than two main peaks. This has confounded literature, but this manuscript will offer an explanation for its origin. This is from two strain states, and a continuum of strains between them.

In literature, it was found that the multi-peaks systems were due to crimping in the optical fiber due to multiple loading scenarios along the axial length of the Bragg grating. This is confirmed by researchers adding a capillary tube around the optical fiber to mechanically isolate the fiber from transverse loads and non-uniform loading. Thus, the optical fiber was loaded at two ends on either sides of Bragg grating and pulled in uniform nature, much like the tension in a rope is uniform. This manuscript instead will de-multiplex for 0.5 mm spaced and length strain measurements along the fiber. This is able to use the data from a multi-peak Bragg grating, and reveal the distributed strain state instead of hiding the occurrence of this phenomenon from detection.

2.6 Methods of writing

Originally, FBGs were detected when transmitting UV light, a Ge doped 'low mode' fiber's transmission died, but only at that exact wavelength. This was seen by Ken Hill in 1978 [47]. The reflection off of the end of the fiber was interfering with the oncoming light, and producing a standing wave in the fiber. This mode would then 'write' a grating into the glass due to the photo-sensitivity of the glass (see section 1.6.1.2.) This grating propagated up the length of the fiber. Heating the fiber would remove the grating. It was eventually found that side exposure of the fiber with UV light would allow for selective pitch writing, and thus allow for a designable Bragg spectrum via this 'holographic' technique.

2.6.1 Holographic technique

The current state-of-the-art system is holographic side writing, where the interference of the two light sources going through a series of slits creates an oscillating intensity wave. This is illustrated in Figure 2.3. By angling the incoming lights at different, equal angles from the fiber, different grating spacings may be written into the structure. This allows for Bragg gratings of different wavelengths to be written. Thus, using a 488 nm source a Bragg grating of peak reflectance 1550 nm may be made immediately followed by one of 1551 nm.

After this method was established to be an effective manner to write Bragg gratings, the process was integrated into the fiber pulling setup such that as fibers were pulled, Bragg gratings could be written into them, then the polymer coating applied. This is now done by FBGS in Belgium. Previous to this, the side writing process required taking existing fibers, stripping the polymer coating off the outside, writing the fiber, and then recoating the fiber. This stripping of the fiber often will add micro-damage to the fiber, reducing its yield strength by an order of magnitude.

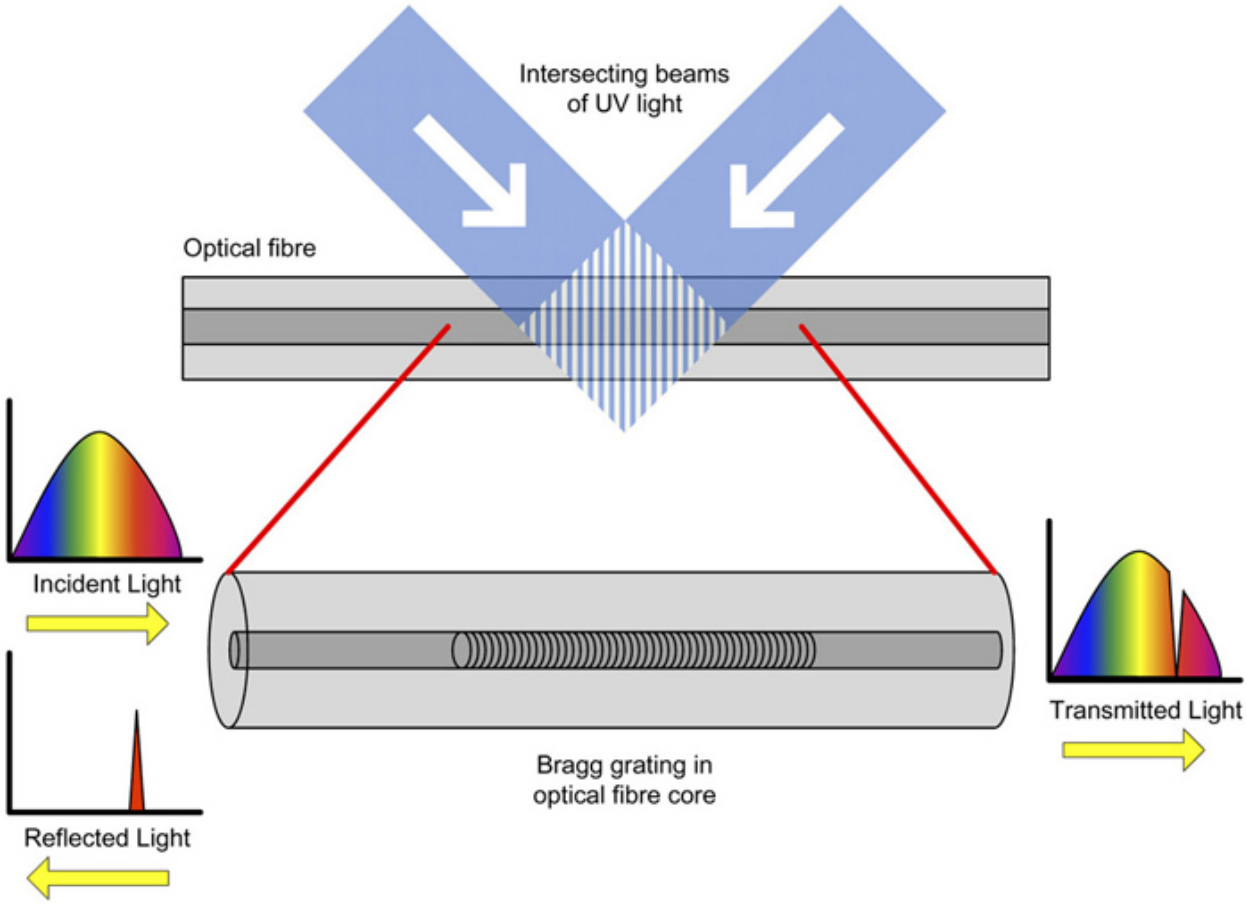

Figure 2.3: Diagram of grating writing showing UV interference based holographic FBG writing. Reproduced from Johnson [57].

2.7 WDM

With the ability to rapidly apply gratings to fiber, the question turned to how many gratings could be written on the same fiber and used. Various multiplexing methods have been produced. Wavelength and time domain multiplex are the two popular ones. Wavelength multiplex involves writing gratings at different Bragg wavelengths, such as 1540 nm, 1545 nm, 1550 nm and 1555 nm etc. Then reflected spectrum peaks are assumed to be from the closest wavelength grating. This method suffers from limitations in the range of strain able to be sensed and assigned to a given grating, as strain that pushes the grating out of its assigned spectrum disrupts the de-multiplexing system. Further, for each grating written into the fiber, there is less spectrum per grating, reducing the range of strains that can be sensed over. Finally, a broader scanning laser is required to address all the gratings.

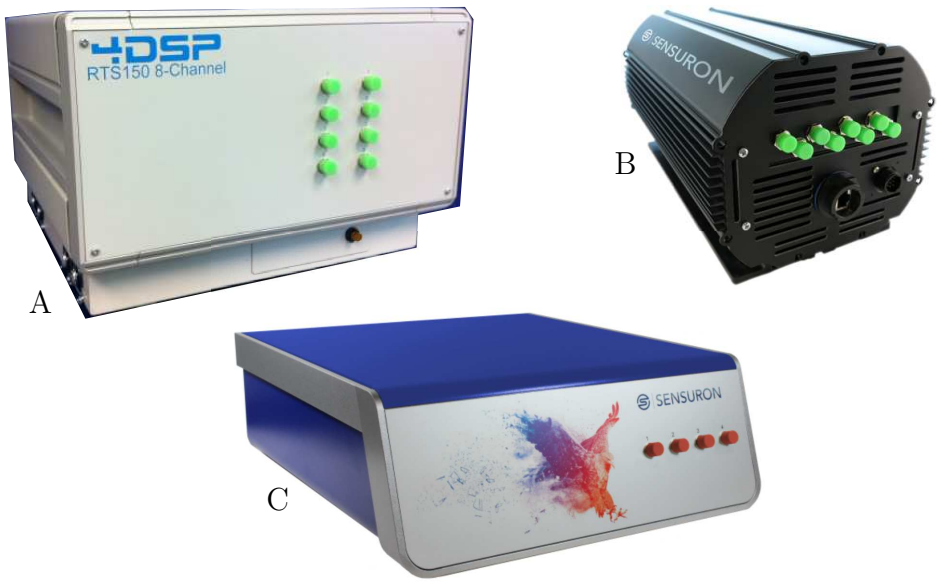

Figure 2.4: 3 OFDR based FBG systems offered by 4DSP and Sensuron, the A) RTS150, B) RTS125, C) Summit

2.8 Multiplexing using OFDR

In the optical frequency domain reflectometery (OFDR) approach, many FBGs may be written with the same central wavelength (λ_B.) A given FBG is addressed by isolating its data region on the fiber, and the time of its reflected signal. A fast Fourier transformation (FFT) of the reflectivity versus wavelength data [42] yields a plot of reflectivity vs. length along the fiber. This is essentially reflectivity vs. optical path length, as other system component's contribution to reflectivity is also seen in this data. A single reflective region, representing a FBG, may be isolated in the data set. This isolated region is padded with zeros on both sides, and then inverse FFT yielding the wavelength data of just that section of fiber. The double FFT needed makes OFDR slower than wavelength domain multiplexing (WDM) and computationally intensive, but allows for multiplexing of thousands of FBGs without a loss of strain range reading. Improvements on this method have allowed for strain reading on the order of 100 Hz for gratings. Shown in Figure 2.4 are 4DSP hardware sold by Sensuron, the Summit, RTS125 and RTS150, able to sense up to 16,300+ FBGs with 30 Hz refresh rate. These systems are based on licensed technology under further active research by the Aero Institute NASA in Palmdale, California.

CHAPTER 3

Recovering strain readings from chirping FBGs in COPVs

3.1 Summary

This chapter reports on signal recovery of optical fiber Bragg gratings (FBGs) embedded in a carbon fiber composite overwrapped pressure vessel (COPV)'s structure that had become chirped due to microcracks in the composite. COPVs are commonly used for the storage of high pressure liquids and gases. They utilize a thin metal liner to seal in contents, with a composite overwrap to strengthen the vessel with minimal additional mass. A COPV was instrumented with an array of surface mounted and embedded FBGs for structural health monitoring (SHM) via strain sensing of the material. FBGs have been studied as strain sensors for the last couple of decades and their response was thought to be understood. Yet, many of the embedded FBGs reflected a multi-peak, chirped response which was not able to be interpreted by the current monitoring algorithm used by the National Air and Space Administration (NASA) collaborators. Literature and this study found that the chirping correlated with microcracks. As loading increases, so does the number of chirped FBGs and microcracks. This study uses optical frequency domain reflectometery (OFDR) to demultiplex the array of FBGs, and then sub-divide individual FBGs. When a FBG is sub-divided using OFDR, the gratings' strain along its length is recovered. The sub-divided chirped FBGs have strain gradients along their length from microcracks. Applying this method to all chirped gratings, nearly the entirety of the embedded sensors' readings can be recovered into a series of single peak responses, which show very large local strains throughout the structure. This study reports on this success in recovering embedded FBGs signal, and the

strain gradient from microcracks. As microcracks in composites are not a significant SHM concern in many instances, future FBGs should not be embedded except in instances where such cracks do pose special concern (such as exposure to water-icing cycles).

3.2 Introduction

This chapter shows the recovery of signals from an embedded optical fiber based health monitoring array which, over the course of use, reported conventionally 'unreadable' signals from many sensors. This advances the technology of SHM of composite structures via optical FBGs.

Upon recovering the signals, high strain gradients were found in the optical fiber of FBG embedded in a carbon fiber COPV structure. The COPV is seen in Figure 3.1. These are presumed to be the strain fields from microcracks also present via visual inspection, and which have been cited in literature for causing chirping [84, 79, 113, 31, 21]. The method to recover these FBGs and process their signals is revealed. This chapter advances health monitoring by FBGs, showing strain fields from microcracks, in a General Dynamics T-1000 COPV, which is a commercial, off-the-shelf, aerospace fuel tank.

3.2.1 Motivation

High performance structures are classically characterized by being low mass and carrying high loads [18]. Composite materials, with their high strength and low mass, have become a material of choice for many high performance structures. Unfortunately, the failure of composite structures can be hard to predict, occurring with little visible damage, and with large variation in seemingly identical structures [76]. This lack of easy health monitoring inhibits replacing the components before failure, as eminent failure cannot be identified by routine visual inspections. When heavily loaded, such structures can fail catastrophically, damaging other systems around them. Thus, structural health monitoring to identify when composite structures are approaching failure is an active research field [69].

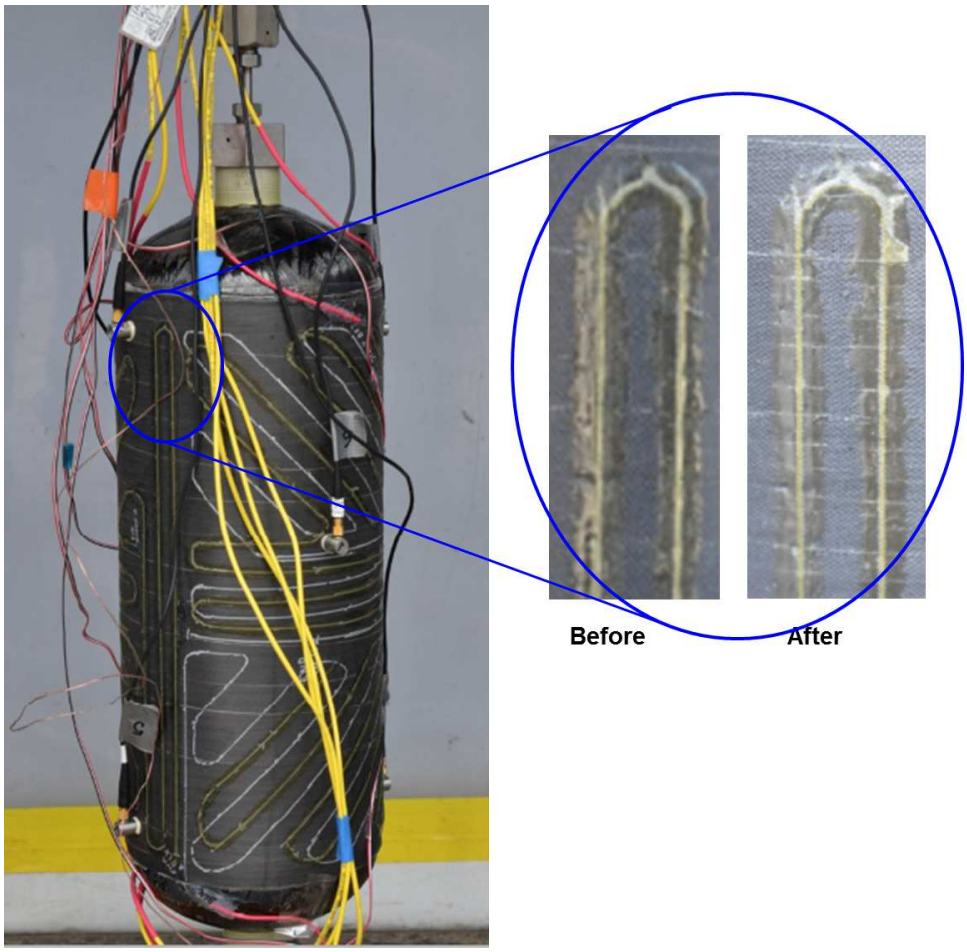

Figure 3.1: A picture of the COPV before testing, with full sensor instrumentation. On the COPV, the white traces indicate the embedded FBG fiber optics, while the light yellow traces are the paths of the surface mounted FBG fiber optics. The highlighted area shows 'before' and 'after' views of the same surface region, where a fiber strand goes along the length and doubles back down. During pressurization, microcracks formed, which may be seen as the thin, lighter lines in the epoxy of the highlighted region's 'after' view.

3.2.2 Purpose

This chapter advances the current FBG based SHM methods, by showing how multi-peak, chirped signals from FBGs are recoverable. When recovered, these show the strain fields from microcracks present in the composite. This was done in post-test data analysis, but is intended for live monitoring in further tests. The sensor array is larger than previous literature, at the 1000s sensor level instead of 10s of sensors. The recovery method is more computationally intensive, and does not need to be applied to all FBGs. Thus, metrics for

strain signal quality of an FBG are introduced and compared.

A COPV is a geometrically simple composite structure. They have widespread use from satellites to fire fighter oxygen tanks. With a simple purpose come clear failure criteria, such as leaking and bursting. Finally, their performance metric is,

$$Pressure * volume/weight \tag{3.1}$$

[76]. Thus, COPVs make an excellent case study for composite structures' health monitoring, and lessons learned may be applied to them now, and to other composite structures later. Directly applying health monitoring to a COPV may allow for higher safe pressurizations, thus increasing an individual tank's performance metric, and enabling appropriate use even after damage to the structure has been sustained.

3.3 Background

3.3.1 COPV

COPVs are commonly used for the storage of high pressure liquids and gases. They utilize a thin metal liner to seal in contents, with a composite overwrap to strengthen the vessel with minimal additional mass. When they fail, it is akin to a small kinetic blast, as the pressurized contents of the vessel rapidly leave the damaged structure, which may propel fragments of the structure as shrapnel [76]. SHM of COPVs would help prevent this and as a COPV's structure is geometrically simple, it is an easier structure to monitor the health of than many other more geometrically complex composite structures, making it an excellent entry development system.

3.3.2 FBG governing equations

FBGs have been studied as strain sensors for the last few decades [85, 91]. The FBG fibers used in this study were sourced from Luna Innovations, and are the same batch as used in

previous studies by Emmons et al. [28, 27, 29]

The signal from a FBG is a reflected wavelength, the Bragg wavelength, which is represented by λ_B. From Equation 2.6, the first order (N=1) Bragg equation is

$$\lambda_B = 2n_e\Lambda \tag{3.2}$$

with n_e as the effective index of refraction of the fiber and Λ as the pitch of the grating. Nominally, the λ_B was 1546 nm for this fiber batch. During testing, various zero states were recorded and used in the study. These were specific to each Bragg region, and recorded when the COPV was unpressurized. The photo-elastic value p_e used was set to 0.1667 as has been used previously with this fiber batch [28]. This constant was determined previously, via testing at the AERO Institute of Palmdale, to show that on an aluminum beam, strain gauges agreed with FBG fibers when a 0.1667 photo-elastic constant was used.

3.3.3 Multiplexing

To demultiplex the signal, OFDR was used. In this method, a tuning laser is scanned across the expected range of FBGs Bragg wavelengths. The total fiber's reflectivity to this varying input is recorded. After tuning up in wavelength, an optical rotator rotates the illuminating laser polarization by 90° and the laser scans down from the long wavelength to the short wavelength. This is a modification to the experimental setup detailed by Emmons et al. [29]. This dual-polarization based method is used as many gratings were found to reflect only at one polarization better than another when integrated into the total system. If only testing with one polarization, then the FBG would fade out of the data mid testing. While real time strain monitoring of the test was performed [90] utilizing a separate method, the wavelength vs. intensity data from the test was also recorded, and that is what was post-processed in this study to further develop the system.

OFDR demultiplexes in the frequency domain, where FBGs appear as square waves in the data. Reflected intensity vs. wavelength, the time domain, is Fourier transformed into an intensity vs. "length" signal, the frequency domain. The region of the fiber in

the data that an individual grating is on is copied into a zero vector, and that vector is inverse Fourier transformed back to frequency domain to determine a single grating's reflected spectrum [29, 52]. Either the peak intensity or the centroid of the spectrum may be denoted as λ_B. Commonly the centroid has been used due to speed of calculation relative to peak finding routines. An extension of this method and hardware to perform it are commercially available from 4DSP, on license from the AERO Institute [2]. This chapter extends the OFDR method in a different fashion to advance the practice of SHM. The region of frequency domain "length" treated as the "grating" was varied in this study from an entire grating of 5 mm, down to one fifteenth of one grating, revealing extra information from the sensors about the COPV's loading, which previously had been averaged out by taking a centroid of a whole FBG.

A comparable study of FBGs on a COPV was performed in 2002 by Kang et al. using only 20 sensors due to them being wavelength domain multiplexing (WDM) instead of OFDR[60]. Because WDM does not allow for arbitrary location demultiplexing it has inherent multiplexing limitations. However, it is significantly simpler to demultiplex, and is a robust method for operating a limited number of FBGs with less computation necessary, a cheaper electronics package, and the large body of literature using WDM has been key in identifying and characterizing the problem this chapter solves.

3.4 Experimental setup

Seen in Figure 3.1 is the COPV fully instrumented with optical fibers, strain gauges, and piezo acoustic pickups. This study only focuses on the optical fibers and improving their performance via adding to the demultiplexing routines.

3.4.1 Instrumenting the COPV

This General Dynamics T-1000 COPV was first instrumented with four optical fibers, with a combined count of 832 FBGs (strands 1-4). These were epoxied on with Master Bond Supreme 33 Epoxy in the rosette patterns shown in Figure 3.2. The vessel was then pres-

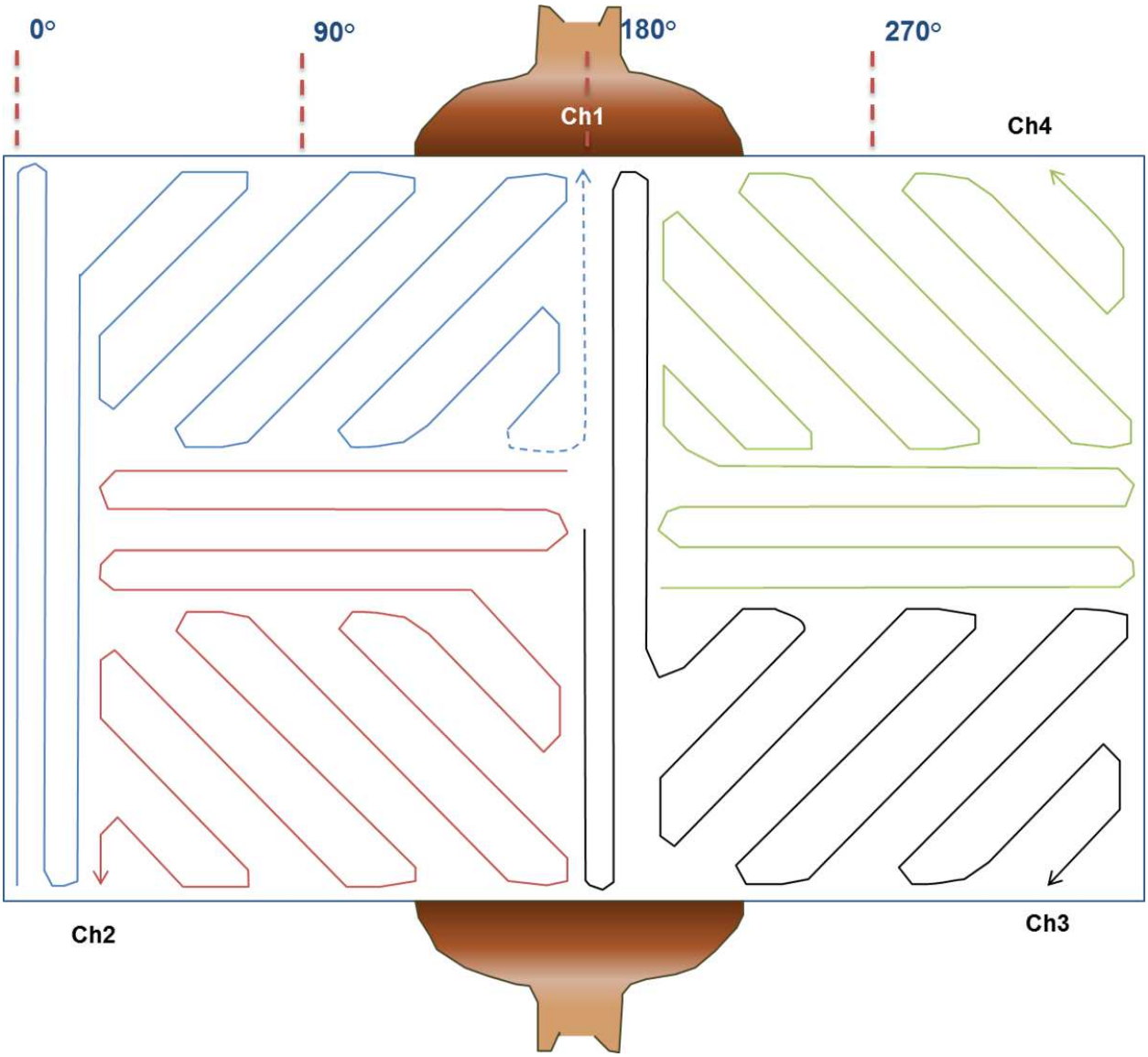

Figure 3.2: The layout for the first layer of FBG strands, showing the 4 strands. The end of each fiber coupled to the fiber optic interrogation device (FOID) is marked with an arrow. These were over-wrapped, and become the "embedded" layer. The Rosette pattern used has a roughly equal length of fiber optics for each orientation of $0°$, $-45°$, $45°$ and $90°$ directions.

surized in cycles, reaching higher pressurizations with each successive pressurization and depressurization cycle.

After this initial test, an additional composite overlay was added to the vessel, over-wrapping the FBGs so that they were embedded into the structure. This was done by first adding a layer of epoxy to the outside of the vessel and then over-wrapping with a tow of

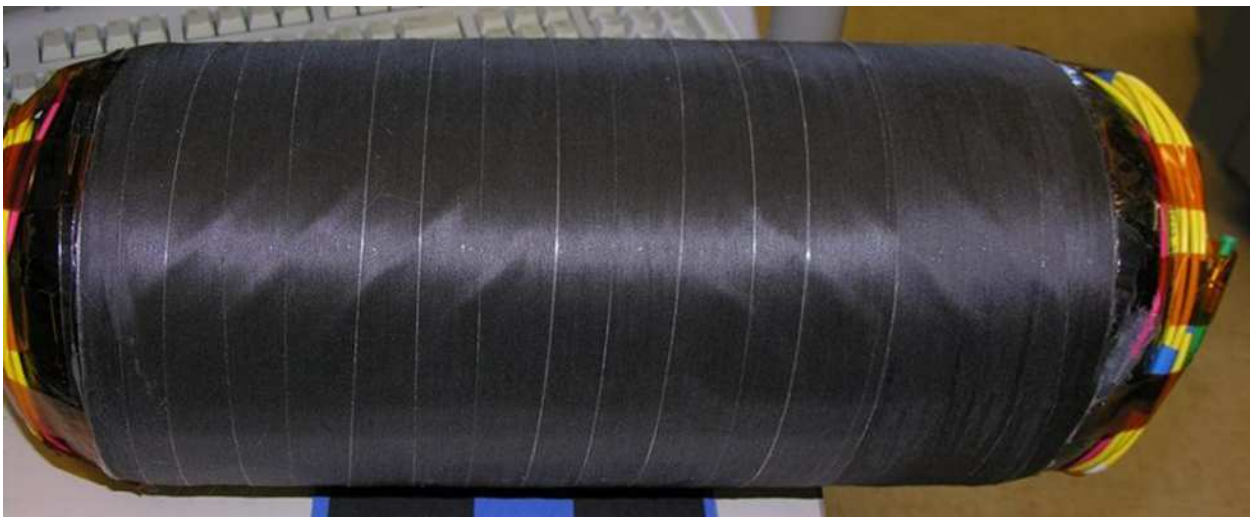

Figure 3.3: COPV with first layer of sensing fibers, over-wrapped with a layer of composite. The glare from an overhead light highlights the 45° runs' ridges from the epoxy holding the now-embedded fiber optics in place.

"Towpreg" from TCR Composites, with one hoop wrap layer, 5 sparse passes at high angle helical passes for one effective layer, and a final hoop overwrap. These three new layers resulted in the vessel shown in Figure 3.3, which now has the previously surface mounted optical fibers embedded between into the reinforced COPV's structure, with the fiber immediately adjacent to hoop oriented layers at a near 5° orientation. The now embedded optical fibers were traced with white paint for ease of locating later.

Next, four additional sensing fibers were added on to the new surface of the COPV for a total of eight optical fibers with 1537 FBGs regions of 5 mm each, spaced 5 mm apart. The two patterns can be seen in Figure 3.1, with the white paths being the embedded fibers, and the pale yellow path the surface mounted fibers. The yellow color is a result of white paint covered by the epoxy, which cures to a translucent yellow. Finally, the COPV was re-pressurize cycled as shown in Figure 3.4, now with two layers of FBG encoded optical fibers, while the whole array was monitored.

The objective of the second test was to cyclically load the vessel via increasing pressurizations until failure of the COPV. This would then be analyzed for health monitoring signals tied to the COPV's failure. Unfortunately for this goal, the vessel withstood the highest pressures able to be applied by the pressurization system, roughly 9800 psi, without suffering

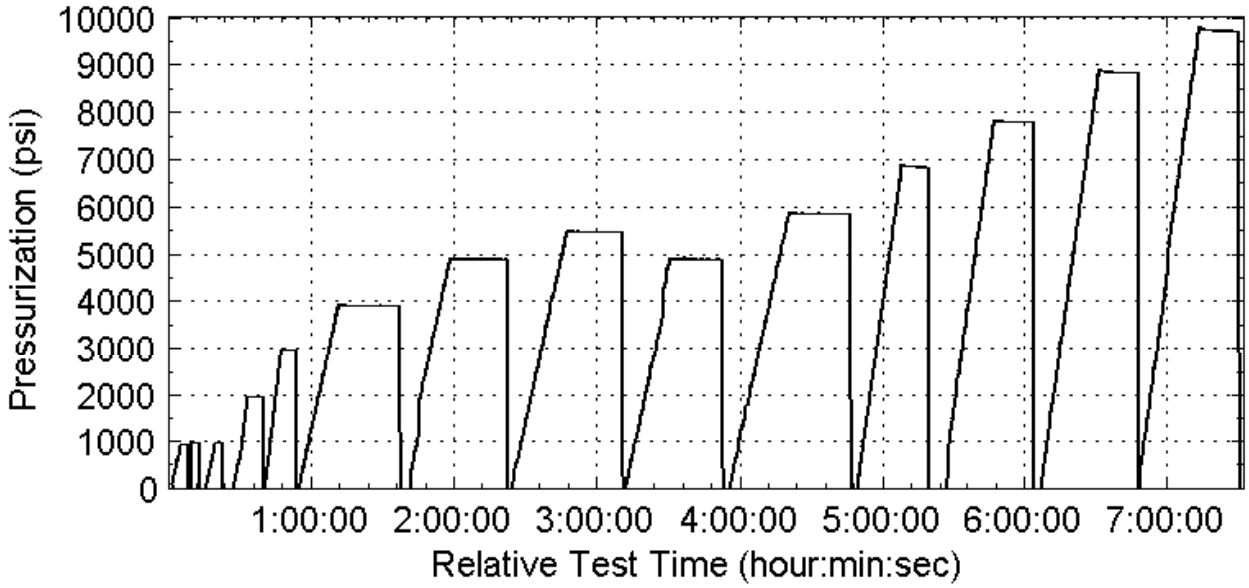

Figure 3.4: Pressurization cycles as measured by a pressure gauge on the pressurization system, when the COPV has two layers of FBG fibers, embedded and surface mounted. The time scale used here is of compiled sensor readings, and not real time. The sensing system periodically stopped recording pressure, leading to the sudden jumps in the pressure recorded on otherwise regular ramping pressurizations.

the expected failure. In the process of successive pressurizations, while the vessel did not suffer a failure, some of the sensing optical fibers did suffer individual failures. Further, individual FBGs began to jump in strains while at constant pressure giving a noisy signal [90], giving the impression that they may be malfunctioning. Post analysis of this optical data showed FBGs reporting multiple peaks in their reflectivity, thus in a state that is not able to translated back to a single known strain from basic theory. That spurred this manuscript's effort to understand and recover those sensors' signals.

3.5 Problem

The Bragg grating governing Equation 3.2 shows that there should be a single peak in the spectrum. As seen in Figure 3.5, embedded gratings may start reflecting a single peak then, while gradually loading them via steady rate vessel pressurization, suddenly change to a multi-peak, chirped response.

Literature suggests there are two explanations for multiple reflected Bragg wavelengths.

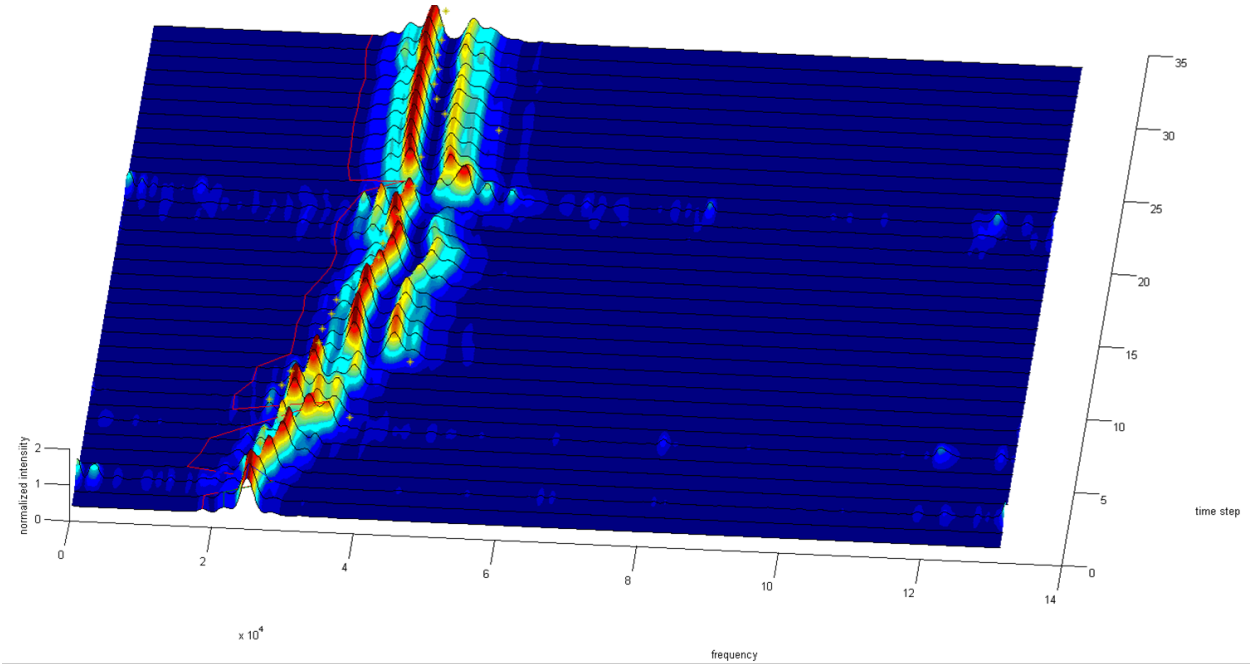

Figure 3.5: As a single embedded FBG taken as a whole was strained overtime, it became multi-peaked with this loading.

They may arise from fiber and FBG mis-fabrication, and from non-uniform or non-longitudinal loading conditions. As the gratings were not chirped at the start of the test, manufacturing issues are not the issue. Thus, there is a loading strain that induced a non-singular Bragg condition across individual gratings. The first source, and commonly cited, is birefringence from off-axial loads, such as to pinch a grating [27] and thus give separate polarizations separate Bragg wavelengths. The second potential origin is non-uniform yet longitudinal strain along the length of the Bragg grating, inducing an optical phenomenon known as chirping [88]. One way to differentiate the two phenomenon is that birefringence should only have two peak wavelengths, not more, and they can be found to occupy the same space on a FBG. Non-uniform longitudinal loading though, should be able to be separated into a series of single Bragg wavelengths.

In literature, the chirping phenomenon has been encountered before [60]. Kang et al. encountered peak splitting in 2002, and were unable to conclusively state what the strain in their COPV was in 5 of 20 sensors. They aptly concluded that peak splitting was due to high strain rates across their 10 mm FBG, and proposed that the strain gradient could be

removed by adding a small glass sleeve to each FBG, forcing uniform axial strain.

In composite coupon testing, microcracks were seen to also distort the FBG reflection [84, 79, 113, 31, 21], and so the full width half max (FWHM) of the reflected spectrum was proposed to represent the level of microcracking as a health monitoring technique [84]. This method is not quantifiable enough, despite efforts such as a "Distortion Index" [59]. This text proposes that instead of the FWHM of the reflection, treating smaller regions of the FBG as individual FBGs reveals the strain field, and allows for direct counting of microcracks and thus tracking of microcrack density. This gives a quantitative measure to replace FWHM for microcrack assessment via embedded FBGs.

The core of this chapter is to analyze these FBGs undergoing chirping and, by using OFDR, to demultiplex the strains along their length. This yields a series of single peak wavelengths, which may be equated via Equation 2.5 to the strain field from a microcrack. This proves their presence, as has been proposed is present by others, and shows that as single peaks may be found, there is not birefringence from pinching.

Regions as small as 1 mm were previously reported as able to be demultiplexed from long period gratings [52]. Here, the region to be treated as an individual sensor is reduced as a series of subdivisions were tried. Seen in Figure 3.6, this is shown by splitting a 5 mm FBG into increasing divisions through the series of 3, 7, 15 leading to sensing regions of 1.33 mm, 0.714 mm and 0.33 mm. As each subdivision requires an additional Fourier transformation, subdividing into smaller and smaller regions requires more computation. Thus, metrics were made of when to continue subdividing, vs. when there has been sufficient subdivisions made, and the signal is clear. These metrics are:

1. The half width mean of the peak wavelength reflectivity.
2. The height of side peaks normalized by the max peak.
3. The allowable difference in wavelength between the peak wavelength, and the centroid of the reflectivity.

3.6 Results

This study reports on the success in subdividing chirping FBGs to recovering single peak reflections, as shown in Figure 3.6. To do so, tracking FBGs at the 0.5 mm level in the data is performed. The chirping is shown to be from sudden onset of high strain gradients as seen in Figure 3.8 and is due to epoxy matrix microcracks as seen in Figure 3.9 and Figure 3.1. Metrics to define when single peaks have been found are qualitatively compared.

3.6.1 Subdividing

Seen in Figure 3.6 is the subdivision of an FBG into smaller regions, and subsequent refinements into further smaller regions. This leads to showing a continuous change in peak Bragg wavelength, representing a continuous strain field across the Bragg grating. While smaller subdivisions are possible, further dividing does not reveal more waveforms, merely varying in strain to show peak strains over double that of minimum strain on the grating.

3.6.2 FBGs shifting in the dataset

In practice, it was found that the straining of the fiber during the test manifested in a strain of the fiber's data as well. At the moderate pressurizations of 5.5 ksi, the final grating region shifted in the data by 10mm, meaning the data was strained an average $5000\mu\epsilon$ along the fiber. The leading edge location of the last 4 FBG regions of a strand are plotted in Figure 3.7. They are shown from pressurizations 2 ksi to 5.5 ksi. As the discretization of a FBG to finer regions made spatial strain measurements at the 0.5 mm scale, mapping data locations back to bottle locations, required identifying FBGs in the data at each strain state. Thus, to track 0.5 mm regions, full FBGs were first found and tracked over time, then each FBG was divided into regions.

As the FBGs were written onto the fiber in a 1 mm period of 5 mm grating, then 5 mm unmodified fiber, the frequency domain data has a series of highly reflective regions. These areas were identified by smoothing the data using a box-car smoothing routine. A waterfall

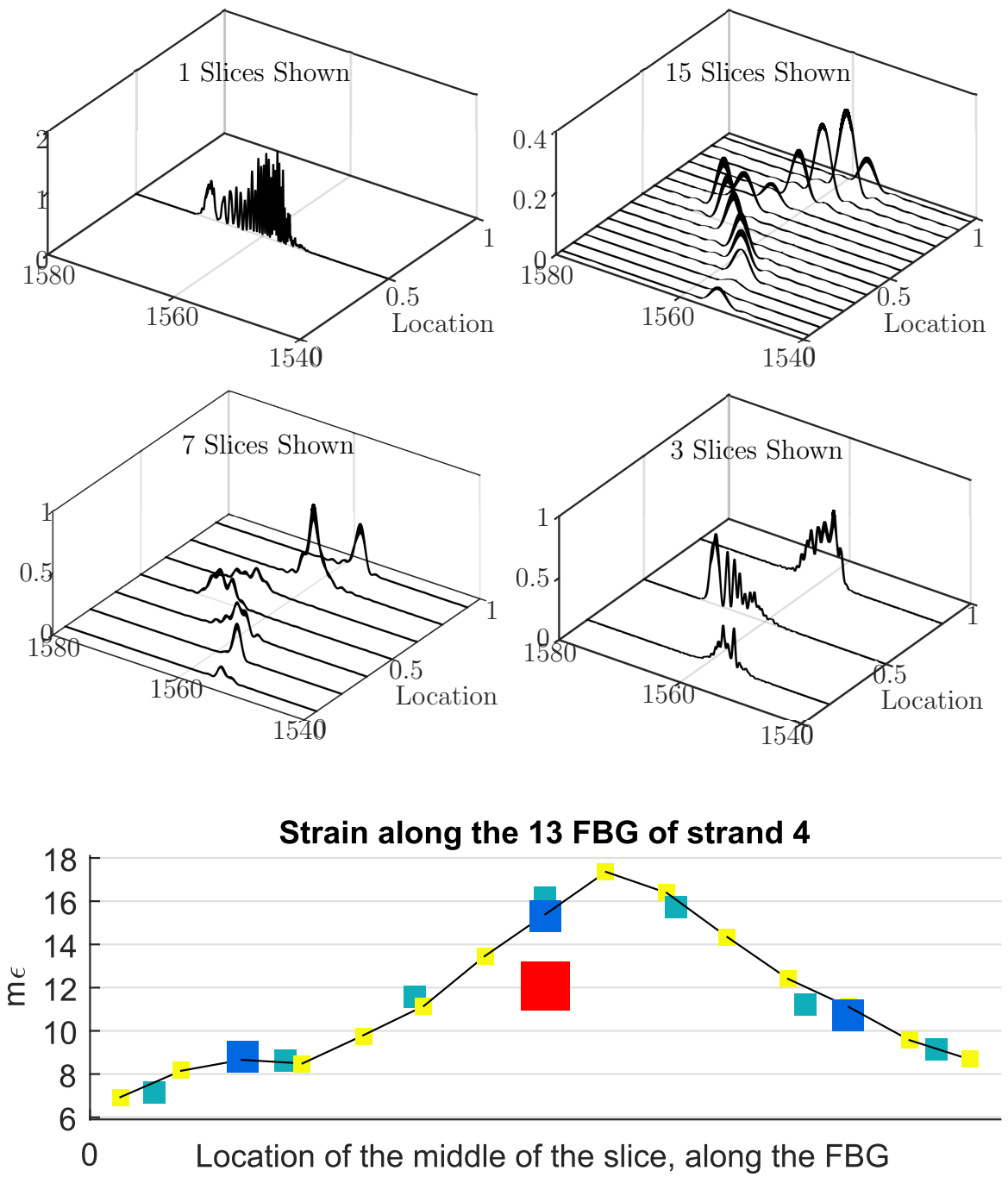

Figure 3.6: This is a demonstration of slicing a single FBG to smaller sizes. Each 3D figure shows a successively larger number of subdivisions of the FBG, plotted such that the reflected spectrum variations are visible. The strain plot at the bottom equates these spectrums' centroids to strains, and plots them. The location and orientation of the FBG in the layout is shown.

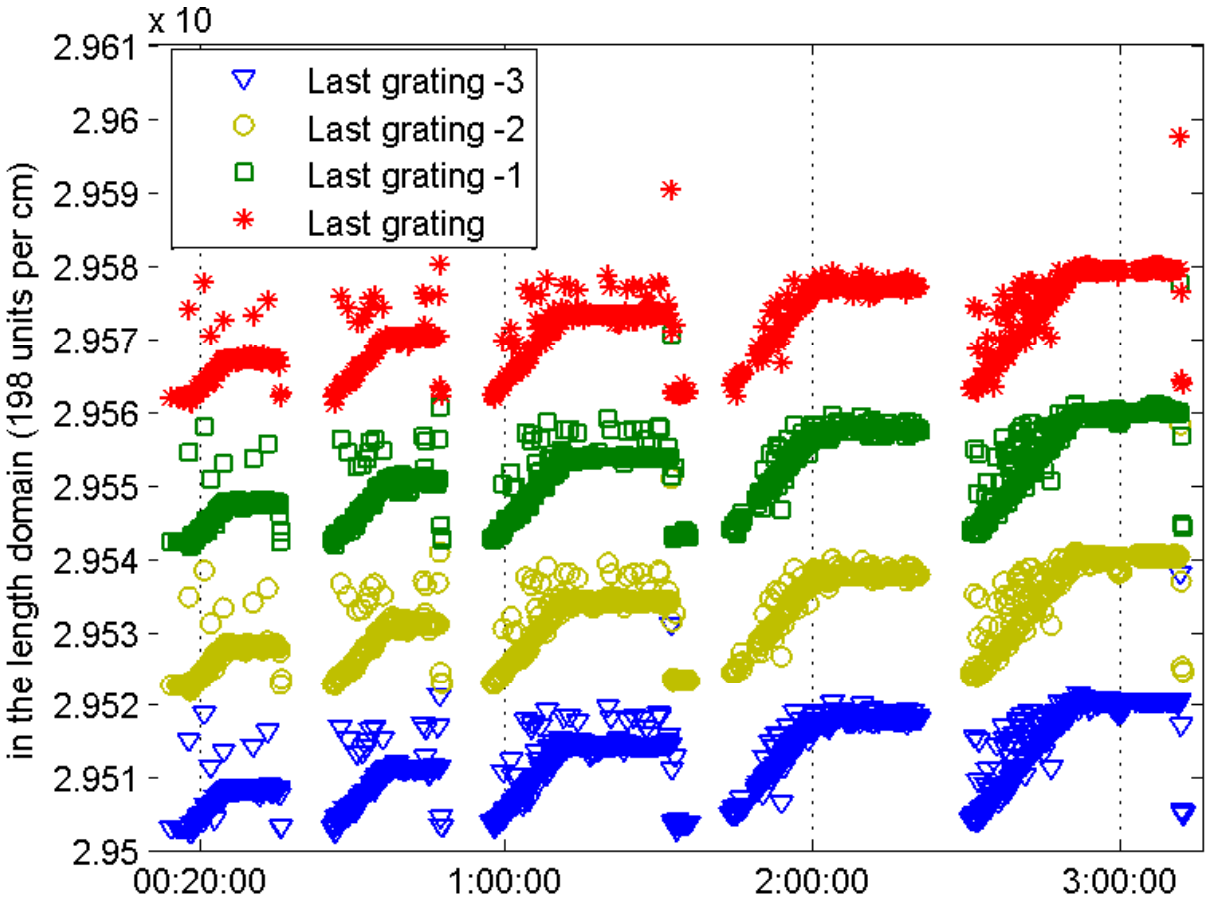

Figure 3.7: The location of the leading edges of the last FBGs of a strand undergoing pressurizations 2 ksi through 5.5 ksi. The time scale here has been marked to align with that of the pressurization plots.

routine was then performed on the data to find regions between FBGs. The center of each low region was found, and average spacing between the centers of these low regions was 198 data points (DP).

Utilizing the first low region between gratings 1 and 2 in a fiber, the centers of other regions were found by checking for low centers 198 DP further in the data, in a window of ±2 %. If a low spot was not found in the guessed location, then the function would check at 2x the expected length, 396 DP down in the data, in a window of ±2% of 396 DP. This was continued until a center of a non-reflective region was found, then the length was divided into the expected number of FBGs. Repeating this method throughout the data allowed for tracking of each FBG over time, even when sudden depressurization would drastically shift the data location.

3.6.3 Applying subdividing to the fiber changes understanding of the strain in the vessel

In all metallic structures, mm scale strain fields and nonlinearity are rare, thus a single strain gauge can represent a whole structure's strain state well. In composites though, the scales of interest strain are much smaller, on the 1 mm scale. There is global structural loading, which requires 10cm resolution, and local material loading and health, needing 1 mm resolution. Despite being known as "structural health monitoring", the health of the composite structure is dependent on material health monitoring. The material's health is revealed when looking at strain at the 1 mm scale, as that is where local cracking of both epoxy and structural fibers will be seen.

When taking the data as a whole, the microcrack events qualitatively appear to start at the 3 ksi pressurization loading, as is seen in Figure 3.6. They appear suddenly, as expected of microcracks [18] and once opened, reopen with each subsequent pressurization of the COPV. As the pressurizations increase, so do qualitatively the number of strain peaks found in the composite.

3.6.4 Metrics to show single peak status

In an attempt to conserve computational resources and determine if the signal is clean enough, multiple methods were tried to address the number of divisions a sensor should be divided into. How each method performs:

1. The half width mean of the peak wavelength reflectivity: Inherently, subdividing the data into smaller regions leaves less data for transformation into the wavelength domain, widening the waveforms that are the result of inverse Fourier transformations. Thus, measuring the half width of the main peak may show that a clean signal becomes "poorer" with subdividing. Upon realizing this, the metric was suppressed.

2. The height of side peaks normalized by the max peak: The requirement to find all peaks at least $\frac{1}{10}$ the height of the max peak was computationally intensive in itself.

Thus, in the Matlab post-processing, it was found to be more effective to always assume the fiber grade grating needed 10 slices than to find all the peaks present.

3. The allowable difference in wavelength between the peak wavelength and the centroid of the reflectivity: While computationally the simplest of the three metrics, this method was susceptible to noise in the reflectivity signal from optical components. Background optical noise at either end of the tuning spectrum would lead to a permanent bias of the centroid from the peak, creating false positives for chirping. Occasionally false negatives are also possible, as a multi-peak response may have its centroid and peak wavelength align under some circumstances.

Finally, it was concluded that while these would be useful in deployment of an efficient live demultiplexing system, further research was better served with a fixed division of 10 sub-sensors. This yields the 0.5 mm regions, and eases understanding the test's data.

3.6.5 Bragg wavelength locally exceeding set laser scan range

In sub-slicing the data, it was revealed that some high strain regions moved the Bragg wavelength to above that of the scanning laser's set range, as illustrated in Figure 3.8. As the 14th sensor experiences a microcrack event, in the 5th cycle near sample 300 it shows there is a region of the fiber experiencing high strain. In subsequent cycles, this region of the grating's Bragg wavelength surpasses that of the system's laser, leading to the peak strain not being found, and instead incorrectly reported as lower. In the frequency domain, first Fourier transformation of the data, the grating's data significantly loses its reflected intensity, with merely the noise of the optics in the system being recorded. After the 1560th reading, the system's laser scanning range was expanded, and the peak response is picked up again by the scanning laser. The same effect is seen on the left edge of the 12th FBG, and the middle of the 13th FBG.

3.6.6 Correcting for Polarization fading

The polarization of light in the fiber was found to twist. If only one polarization is tracked then the optical sensors would experience a "polarization fading" effect. This would manifest as a 20cm period of intensity perturbation in the frequency domain of the data. To correct for this, each FBG was found in each polarization, then the two polarizations of the FBG were combined, via $I = \sqrt{(P_1)^2 + (P_2)^2}$ with P_1 & P_2 being two orthogonal polarization of light, for each FBG before then discretizing the FBGs to find the strain gradients. If birefringence due to fiber pinching is expected, then the two polarizations would be expected to give separate Bragg wavelengths. With the polarizations combined it should not be possible then to reduce the reflection down to single peak Bragg wavelengths along the length of the grating.

3.7 Discussion

The high strain rate across each chirped FBGs shows strain concentrations, which may be from microcracks in the epoxy matrix. As seen in Figure 3.9, such cracking is evident to visual inspection via discolorations on the surface of the COPV, were epoxy was used to affix fiber optics and strain gauges.

The study was successful in tracking of the location of individual FBGs, to be able to track 0.5 mm regions within them over time. By combining two different polarizations, fading of the signal from using only one polarization filtering was corrected. Tracking a FBG overtime, its transition to being a multi-peaked, chirped grating is often sudden, and upon reaching a new highest loading for the structure. The chirping is most seen in 90° oriented, embedded sensing fibers.

This chirping phenomenon is proposed to be microcracks in the epoxy. Chirping is not seen in the surface mounted sensors. It may be that the microcracks are propagating along the boundary between the epoxy and the COPV surface instead of through the epoxy of the FBG, and to another layer of composite as they can in the embedded case. In the embedded

sensors, there were varying densities the microcracks. Due to the Rosette pattern in which they were laid, the sensors were at different orientations relative to the composite plies they were embedded in. Exact quantification of the microcrack density was not performed as the FBG regions were of the same length as the strain field, leading to a Smiths sampling law limitation. Instead, only qualitative descriptions from the data are possible, with future work needed for a full quantitative study.

The composite layers that all the optical fibers were directly next to were in a near hoop direction, off axis by 5°. Fiber sections laid in a hoop orientation will be referred to as 0°, with ±45° and 90° also in use. Qualitatively, the 0° saw the least microcrack appearance, with only a few < 10 events seen in the data. The 45° saw some microcrack appearance, as is evident to be present in Figure 3.9. The 90° saw the densest microcrack appearance.

3.8 Conclusions

Matrix microcracks are a precursor to more serious damage mechanisms, particularly delamination [18, p.260-266]. Due to liquid intrusion, and structure permeability, microcracks themselves may be a limiting performance factor in a structure [81]. Tracking microcrack density can be an early detection method in structural health monitoring then. Further studies may enable the use of microcrack density to be an evaluation of COPV health. Previous studies showed that FBGs can detect microcracks via coupon testing but tests on actual structures have not yet been adequately detailed [84, 88, 79]. This study is the first reporting quantifiable strain field of microcracks, and does so on an off-the-self aerospace structure, with a large population of sensors. It was limited from being able to conclusively detail the microcrack density and correlation back to COPV failure as the strain regions from the microcracks appeared to have the same scale as that of the FBG, leading to a Smiths sampling law limitation, the COPV withstood the pressurizations without failing.

3.9 Future work

Further testing using pseudo-continuous FBGs embedded in a COPV's composite structure is required to create a robust structural health metric from the recovered embedded FBGs signals. With longer FBG regions, the true density of microcracks could be quantified, and with a vessel's failure, a health metric created from tracking these microcracks.

Acknowledgments

This research was funded by AERO 615 contract from the AERO Institute and NASA Dryden (now Armstrong).

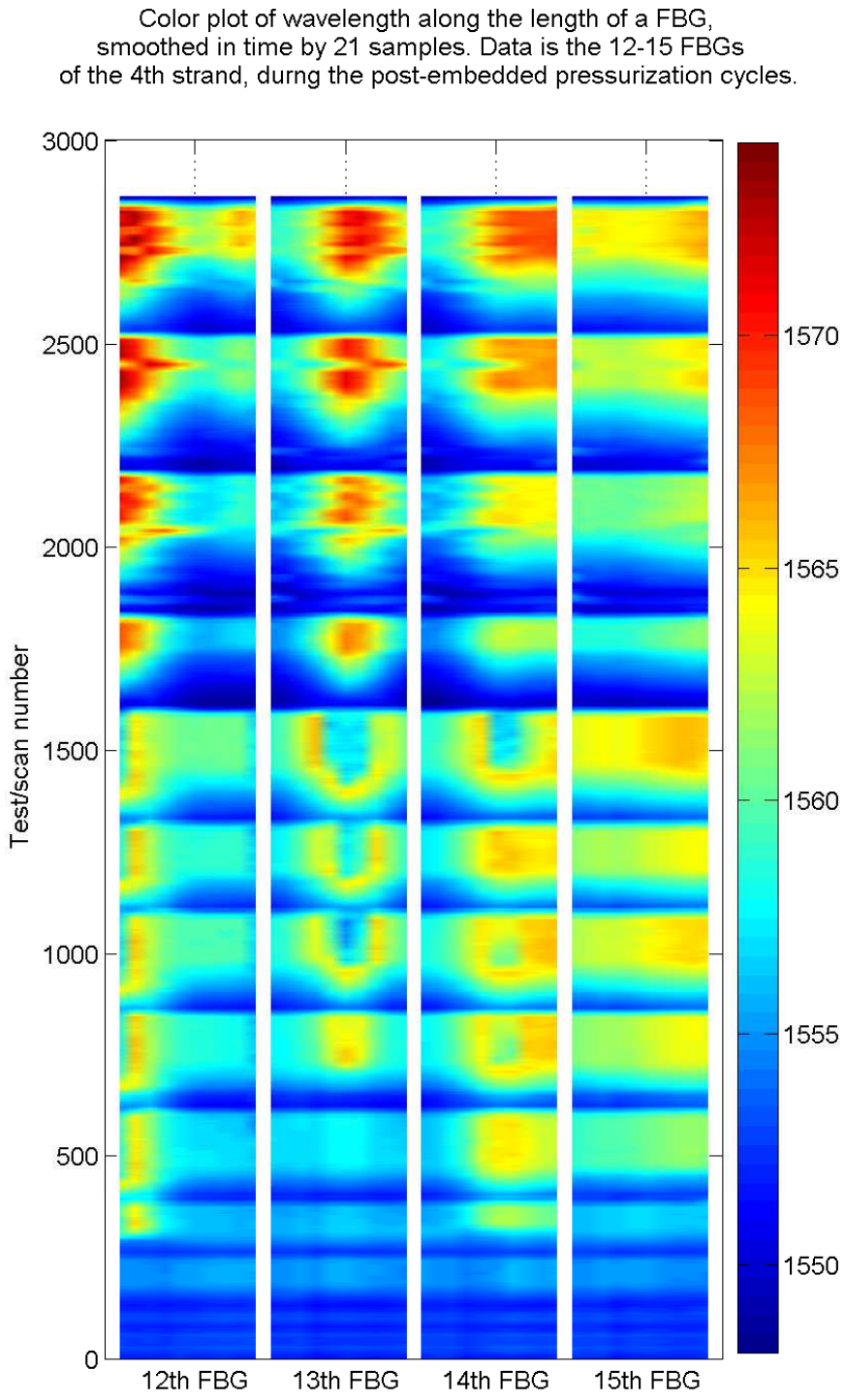

Figure 3.8: Plot of the centroid wavelength of the 10ths of FBGs concatenated together to show the strain distribution across a gradient over all the pressurization cycles. The data has been box-car averaged for 21 units to smooth the data over time. The 13th and 14th FBGs exceed the laser's scanning wavelength for cycles 8, 9, and 10. At the start of the 11th cycle, and through the 14th cycle, the tuning laser was set to scan further, again capturing the peak wavelength once more.

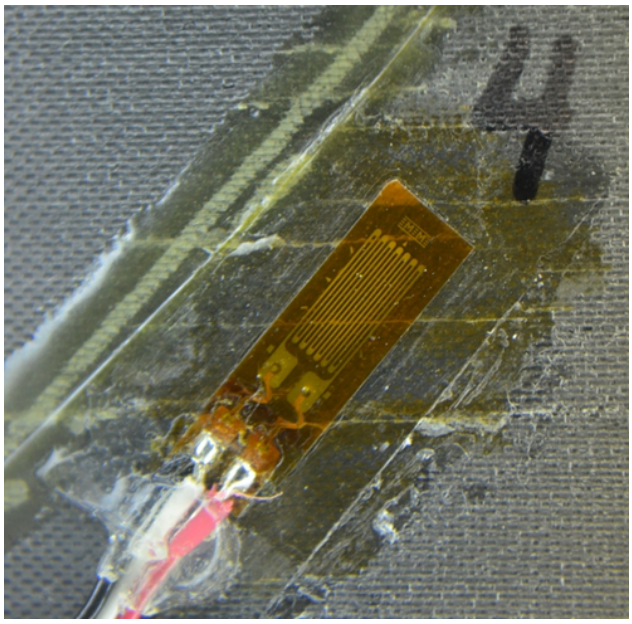

Figure 3.9: Image of the surface of the COPV after all tests were performed. The image contains an epoxied on strain gauge, showing that the cracks were of great length, propagating through the epoxy for $2\,\mathrm{cm}$ to $3\,\mathrm{cm}$.

CHAPTER 4

Magnetorefractive effect

The "Magnetorefractive effect" was coined in 1995 [54] by Jacquet and Valet to describe the change in infrared (IR) reflectivity of material under application of a magnetic field. This definition has been expanded over the last 20 years to include transmission changes. It is now known that there are multiple origins of these reflectivity changes, able to be grouped into Drude mechanisms and Jahn-Teller absorption band mechanisms. Regardless of the source, a change in reflectivity of material represents a change in the material's complex index of refraction. Such changes may be used to make interesting optical devices, a subset which may even be useful, such as magnetic fiber Bragg grating (MFBG). With a complex index though, the loss tangent in the material may be prohibitive for MFBG.

4.1 Introduction

In the last 20 years, an interaction between the reflectivity of various films and magnetic fields has been discovered and has undergone investigation. At its discovery, this was coined the "Magnetorefractive effect" [54]. It is now accepted that the change in reflectivity of a sample is due to changes in the index of refraction of the sample, though magnitude of the exact change had not been investigated previously. The effect has been found in many materials, but is most prominent in the manganite class of materials, around their individual Curie temperatures (T_Cs), and is dependent on the wavelength of light that the reflectivity is measured at [111]. This thesis focuses on one magnate in particular, Lanthanum Strontium Manganite $La_{0.66}Sr_{0.33}MnO_3$ (LSMO), due to its T_C being near 10 °C [102, 49, 51].

T_C's appearance has coincided with magnetoresistance (MR) in materials, and correlated

with the temperature and magnetic field dependencies of MR. Theory, though, only holds that changes in resistance can affect the index of refraction up to the near IR (10 µm) by MR. As light's wavelength shortens, then other theories are needed. One theory is by Kravets [63, 64], that light's interactions with dielectric optical phonon modes is effected by magnetic fields. This would affect the first term of index, the real component, instead of the second imaginary component that resistance changes influence [54]. This a similar mechanism to water's change of index under application of magnetic field [48]. As magnetorefractive effect (MRE) appears in an even shorter wavelength spectrum than IR, the visible spectrum, an additional theory is needed and that has caused large disagreement [46]. There are five theories for MRE in the visible spectrum:

1. magnetic field's influence on inter-band transitions,
2. magnetic field changing the effective mass of non-magnetic polarons,
3. magnetic field effecting magnetic polarons,
4. magnetic field suppressing the Jahn-Teller effect,
5. and even-parity magneto-optical (MO) effects.

Of these, the 4th is the leading one that explains MRE in magnates at room temperature, low magnetic field, with visible and near visible light. Jahn-Teller absorption band shifting and suppression with magnetic field, shifts absorption bands in the material under application of magnetic field [46]. Even the authors of this theory believe that the others may play a part, and that further research is certainly required for any one explanation to win out.

The first mechanism discovered for MRE was a Drude, or "high frequency impedance" mechanism caused by the resistance in the material changing. The resistance change may be giant magnetoresistance (GMR) or colossal magnetoresistance (CMR), a magnetically induced change in resistance found in many manganites around their T_C. The T_C is when the material changes from ferromagnetic to paramagnetic. This is seen generally as a permanent

magnetization relaxing to a disordered, "non-magnetic" state due to thermal energy overcoming magnetic crystalline anisotropy. This mechanism affects longer wavelengths (1 µm to 50 µm) as the longer time that the electromagnetic (EM) field is in each polarization state allows the internal current generated by voltage of light to flow and be affected by the resistance change in the material. Increasing the MR increases the index of refraction (see Equation 1.13) and thus reflectivity (see Equation 1.20).

The second mechanism for MRE is suppression of Jahn-Teller electron polarization [49]. This polarization event is related to ultraviolet (UV) spectrum absorption due to electronic structure's resonance. This then affects wavelengths nearer the UV spectrum, from 2 µm to 0.3 µm or 300 nm more than longer wavelengths. Again, the peak response is found around the T_C. This mechanism is what allows the visible spectrum (800 nm to 450 nm) index of refraction to change with magnetic field. This mechanism decreases the reflectivity of the samples in a magnetic field, which indicates that the index of refraction is decreasing with the magnetic field. These two mechanisms, which influence the index of refraction in different directions, then counteract each other in their overlapping spectrum regions to create a spectrum of a null response, which is near 1500 nm for LSMO.

For this manuscript, the origin and theoretical physics oriented question of "why" have been put to the side, with the focus instead on the applied research question, "how can we use this?" So far no devices known to this thesis author has been made which cite MRE as its base effect.

Many uses for the MRE have been theorized, and Granovsky et al. [46] lists them well, covering non-contact sensors, lens, shutters, spin valves and many others. It is thought that Emmons et al. produced a sensor [30] using Fe_3O_4, which may work due to MRE, though they did not cite the effect, and his tests were performed well above the peak temperature for MRE in Fe_3O_4 [102]. It is upon that work and others' work that this manuscript builds and advances.

The MRE is agreed to drive the changes in the index of refraction of a material. Shifts in index may be perceived as changes in Bragg wavelength when the material is in an optical

fiber with an fiber Bragg grating (FBG) present (as described in section 2.5.1), or as changes in reflected intensity from a surface (as described in 1.7.1). As transmission is inversely dependent on reflection at a given boundary,

$$I = T + R \tag{4.1}$$

with I being the incident light, T being the transmitted light, and R being the reflected light. Thus, another MRE measurement technique is to measure transmission, magnetotransmission (MT). Both transmission and reflection can also have other optical changes related to magnetic field, but arising from other effects, such as Faraday rotation, Kerr rotation, second and third order rotations, and when these are combined with polarizers they are detected as changes in transmission or reflected intensity. Thus, the MRE is commonly studied in conjunction with the Kerr effect and other magneto-optical effects [51, 49, 45]. Rarely is the index of refraction back calculated [8], though it can be. What follows is the history of MREs advancements in literature, as researchers have sought larger changes, at higher temperatures, at smaller magnetic fields, in single phase materials, and in smaller physical size (grains or layer). A summary table of work by year, and an outline of the rest of this chapter's matter is seen in Table 4.1.

4.2 The seminal paper on MRE

The seminal work on MRE was done with a metal film multilayer of [$Ni_{80}Fe_{20/}$Cu/Co/Cu] in 1995 [54]. This was expected to and did show GMR. GMR was shown to theoretically give rise to the change in index of refraction at room temperature between 2 µm and 23 µm. This was shown to theoretically give rise to MRE and thus MT (see Equation 4.1). MT was experimentally shown and characterized. This seminal symposium proceeding, showed when the layers are thin enough to be on the order of the mean free path of the electrons then the charging by an optical EM wave, and the resulting current flow between layers is effected by MR between layers. This in turn is seen as the stack's complex permittivity changing (see Equation 1.10), and so its index of refraction (see Equation 1.13). This was demonstrated

Table 4.1: Summary of MRE materials of interest in the last 20 years.

Year	Material	Effect	Sensitivity (Δ/kOe)	T (K)	λ (μ m)	Ref.	Sec.
1995	$[Ni_{80}Fe_{20}/Cu/Co/Cu]$	MT	1.47	300	9	[54]	4.2
1996	$Nd_{1-x}Sr_xMnO_3$ (x=0.3)	MT	-2.81 E-3	180	1.37	[62]	4.3
1997	$La_{1-x}Sr_xMnO_3$ (x=0.1)	MT	1.88 E-2	132	4.85	[74]	4.4
2000	$Co_{46}Al_{22}O_{32}$	MRE	-3 E-2		10.3	[9]	4.6
2002	$La_{1-x}Ca_xMnO_3$ (x=0.33)	MT	-3.38 E-2	273	6.4	[108]	4.7
2005	$La_{1-x}Sr_xMnO_3$ (x=0.33)	MT	5.88 E-3	356	1.5	[109]	4.8
2009	$La_{1-x}Sr_xMnO_3$ (x=0.33)	MRE	-3.57 E-5	300	0.650	[49, 51]	4.9
2010	$La_{1-x}Ca_xMnO_3$ (x=0.33)	MRE	1.3 E-2	230	12.5	[110]	4.10
2010	$La_{1-x}Ca_xMnO_3$ (x=0.33)	MRE	-4.5 E-4	260	0.633	[50]	4.11
2010	$(Pr_{0.4}La_{0.6})_{0.7}Ca_{0.3}MnO_3$	MRE	-3.8 E-4	140	0.800	[11]	4.12
2010	Fe_3O_4	MRE	1 E-3	100	0.500	[10]	4.13
2012	$La_{1-x}Ag_xMnO_3$ (x=0.1)	MRE	-2.60 E-3	310	0.833	[111]	4.14
2014	$La_{1-x}Sr_xMnO_3$ (x=0.33)	MRE	-1.8 E-3	289	0.633		5

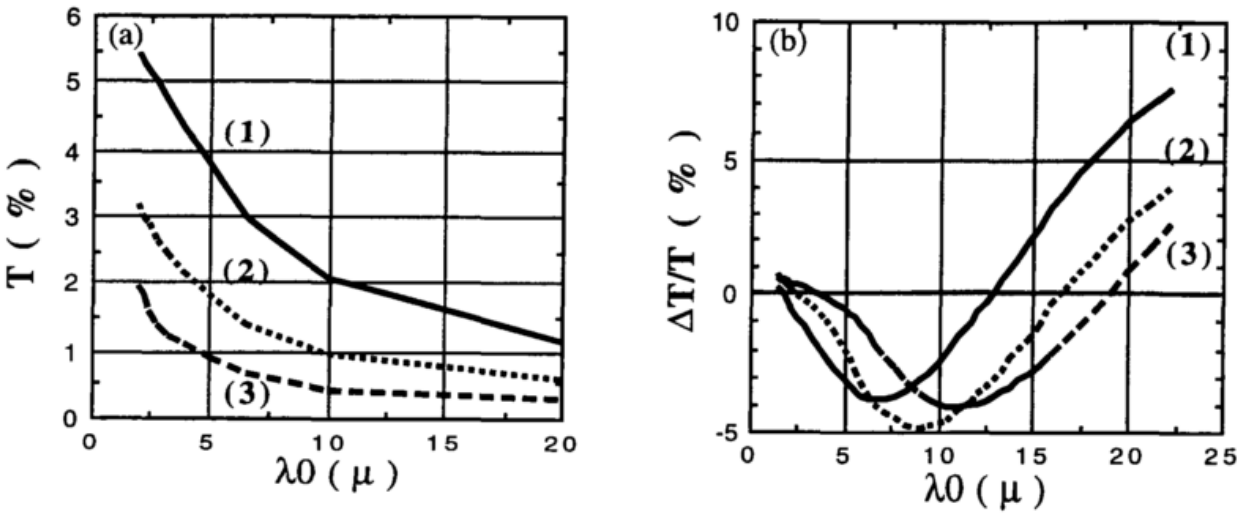

Fig.3 (a) The transmission T (b) and the relative change ΔT/T, measured as functions of λ0 the wavelength in vacuum, for the three [50 Å $Ni_{80}Fe_{20}$/tCu Cu/20 Å Co/tCu Cu]$_{x3}$ multilayer samples with tCu = 9.5 Å (1), 22 Å (2) and 34.5 Å (3).

Figure 4.1: Initial MT effect experimental data for metal thin film stacks by Jacquet and Valet [54].

by measuring the transmission through the stack for various wavelengths of light, to see MT seen in Figure 4.1.

The change in transmission was non-linear with magnetic field, due to the magnetic

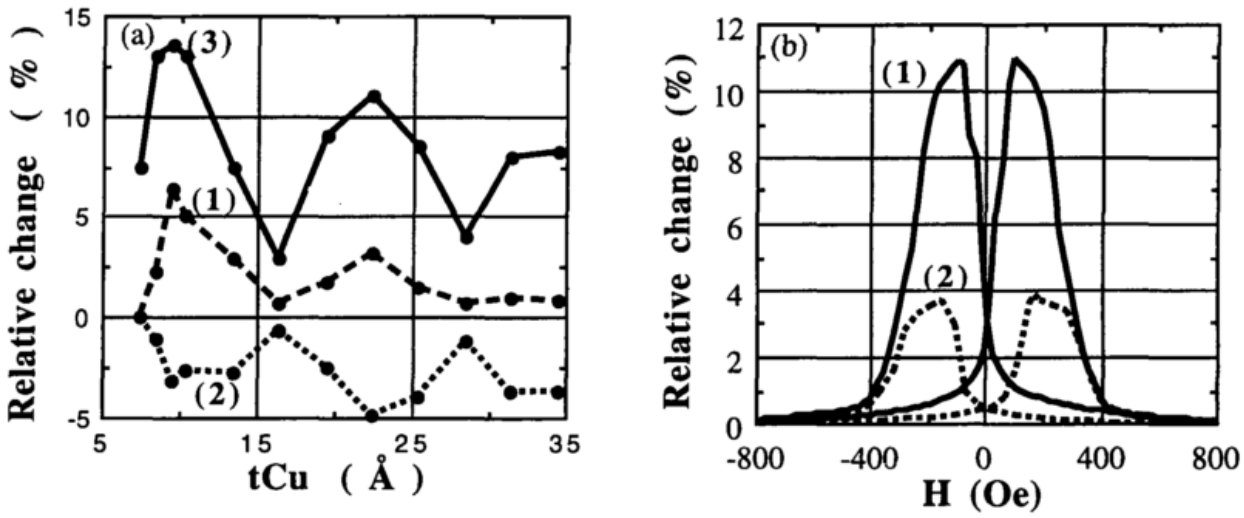

Fig.4 (a) $\Delta T/T_{sat}$ at two different wavelengths 9 μm **(1)** and 20 μm **(2)**, ploted with $\Delta\rho/\rho$ **(3)** as a function of tCu, for the multilayers [50 Å $Ni_{80}Fe_{20}$/tCu Cu/20 Å Co/tCu Cu]$_{x3}$.
(b) - $\Delta T/T(H) = - [T(H)-T(H_{sat})]/T(H_{sat})$ **(1)** measured at 10.6 μm of wavelength, ploted with $\Delta\rho/\rho(H)$ (2), for the sample [50 Å $Ni_{80}Fe_{20}$/22 Å Cu/20 Å Co/22 Å Cu]$_{x3}$.

Figure 4.2: Initial MRE experimental data for metal thin film stacks by Jacquet and Valet [54].

alignments of the multiple layers changing at different field intensities. Thus, the heightened resistance would die off as the magnetic field became large enough to re-polarize the "fixed" layer, and so "correct" the interlayer magnetic miss-alignment which led to the GMR and MRE. This multilayer was highly hysteretic, and its operation peaked at 75 Oe fields with 10 μm IR illumination. A temperature study of its response was not reported. The authors postulate that the change in transmission directly and inversely would relate to the reflectivity, but do not show experimental data of the MRE to compliment the MT. MT may arise due to the absorption in the material, and does not directly indicate a change in reflectivity though. As seen in Figure 4.2.

As seen in Figure 4.3, they reinforced experimental results using the mathematical model of Drude resistance changing reflectivity. These show good agreement between computational and experimental results. This is used as evidence that the principle behind the phenomenon is well modeled.

Jacquet and Valet's method is to approach the self averaging limit (SAL) of the GMR stack as one optical material with effective optical constants. It should be expected that

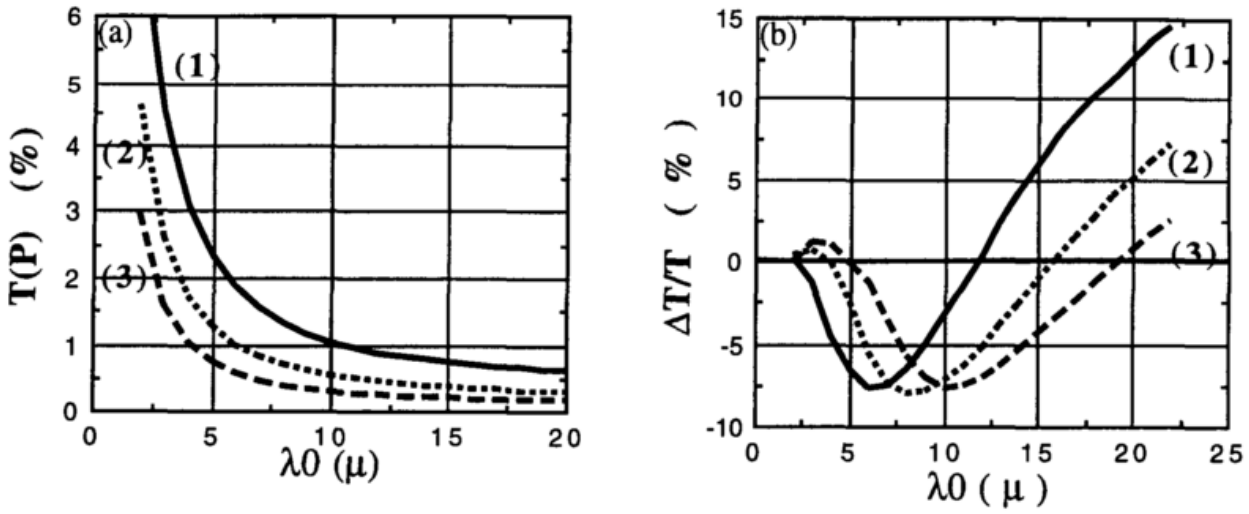

Fig.5 Calculated transmission $T^{(P)}$ (a), and relative change $\Delta T/T$ (b), as functions of $\lambda 0$ the wavelength in vacuum, for the three [50 Å $Ni_{80}Fe_{20}$/tCu Cu/20 Å Co/tCu Cu]$_{x3}$ multilayer samples with tCu = 9.5 Å (1), 22 Å (2) and 34.5 Å (3).

Figure 4.3: Calculated MT effect for metal thin film stacks of various copper thicknesses by Jacquet and Valet [54]. This is comparable to their experimental results in Figure 4.1.

this method will produce massive dispersion, as different wavelengths include different layer counts in their skin depths. Nonetheless, an effective material model was made and the index of refraction of the effective optical material is:

$$n_{SAL} = \sqrt{\epsilon_{SAL}} = \sqrt{\epsilon_{st} - \frac{i}{\epsilon_0 \omega}\left(\frac{\sigma^0_{SAL,+}}{1 + i\omega\tau_{SAL,+}} + \frac{\sigma^0_{SAL,-}}{1 + i\omega\tau_{SAL,-}}\right)} \tag{4.2}$$

with n_{SAL} the effective index of refraction of the self-averaging limited stack, ϵ_{SAL} the permittivity, σ^0_{SAL} as the conduction of electrons of different spins (designated by the - and +), ω as the frequency of the EM wave being examined, and finally ϵ_{st} is the residual, 'static' permittivity which is independent of frequency.

Their work has been accepted as the seminal paper on MRE, and as the paper on how MRE and MT arises from GMR. The same MR and SAL method works on the half-metal's manganites with spin dependent resistance.

4.3 Early MT in a magnetite film

In 1996, when studying $Nd_{1-x}Sr_xMnO_3$ (x=0.3), Kaplan et al. saw that the transmission dip with an applied magnetic field of 8.9 T. At 180 K this reached a nearly 25% dip in transmission at 0.65 eV. Thus they saw an MT of $-0.28\,\%$/kOe or $-0.0028\,\Delta$/kOe. The low temperature of the effect removed it as a candidate material for this thesis work.

4.4 LSMO absorption band shifting

Loshkareva reported in 1997 that the absorption band of various LSMO compositions shifted with temperature [74]. This was speculated to be due to the free carriers appearing with increasing temperature. In a sideline manner, the paper mentions "that magnetic field enhanced the effect."

Though seemingly not recognized at the time, this study moved the literature of MT (and MRE) from metal films and GMR, to CMR in oxide films. This experiment was similar to Jacquet's initial study, where a light source was shown onto a sample at a consistent angle, magnetic field applied, and the transmitted intensity measured. Though not stated to be the case in this study, many studies find absolute intensity via a silver mirror, and most studies vary the wavelength by use of a broad band source with a grating to split the light, then select the 'piece of the rainbow' to shine onto the sample. The low temperature of the effect in LSMO published here is due to the $X = 0.1$ compositional difference from the ideal, higher T_C, of $X = 0.33$.

Loshkareva et al.'s study though was focused on temperature effects and so only shows one magnetic field result of their three samples made. The phrase "Magnetorefractive Effect" is not mentioned in this paper, though these authors would go on to become the world experts on MRE and Lanthanum Manganites.

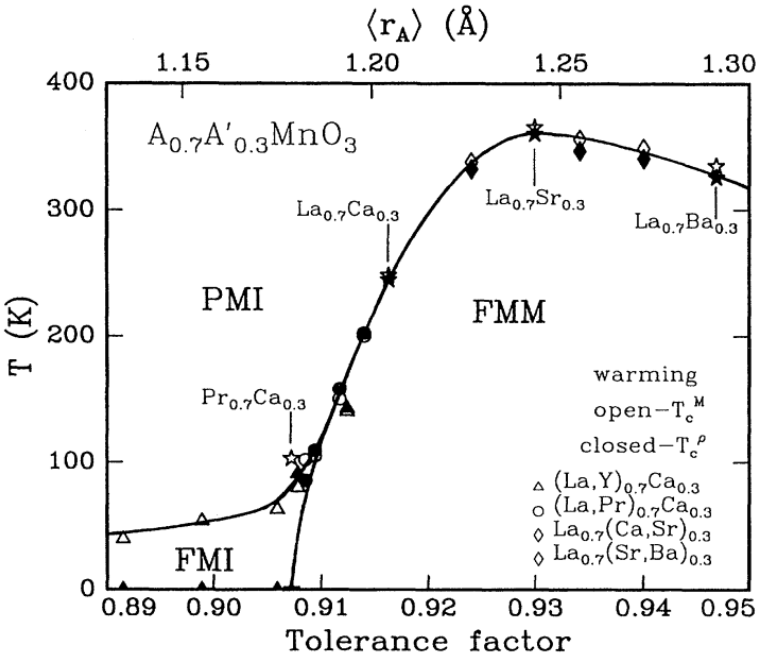

FIG. 4. Phase diagram of temperature vs tolerance factor for the system $A_{0.7}A'_{0.3}MnO_3$, where A is a trivalent rare earth ion and A' is a divalent alkali earth ion. Open symbols denote T_c^M measured at 100 Oe. Closed symbols denote T_c^ρ. Data taken while warming.

Figure 4.4: The T_C of various manganite compositions, reproduced from Hwang et al. [53].

4.5 Manganites and T_C

The T_C of many manganites is described well by Hwang et al.'s work [53], seen in Figure 4.4. While it omits the highest T_C, Silver-doped Lanthanum Manganite $La_{0.66}Ag_{0.33}MnO_3$ (LAMO), it does plot the rest and show LSMO's high T_C. Due to its room temperature T_C, LSMO was chosen to develop a room temperature magnetometer with, compared to other magnetites which may have MRE.

4.6 IR MRE in granular alloys with GMR

The next advancement in MRE research was with study of single phase materials in the mid-infrared (mid-IR) spectrum. Here again, GMR is the mechanism driving a Drude response, but now in a "Co-Al-O metal insulator magnetic films" [9]. The theory [45] was published

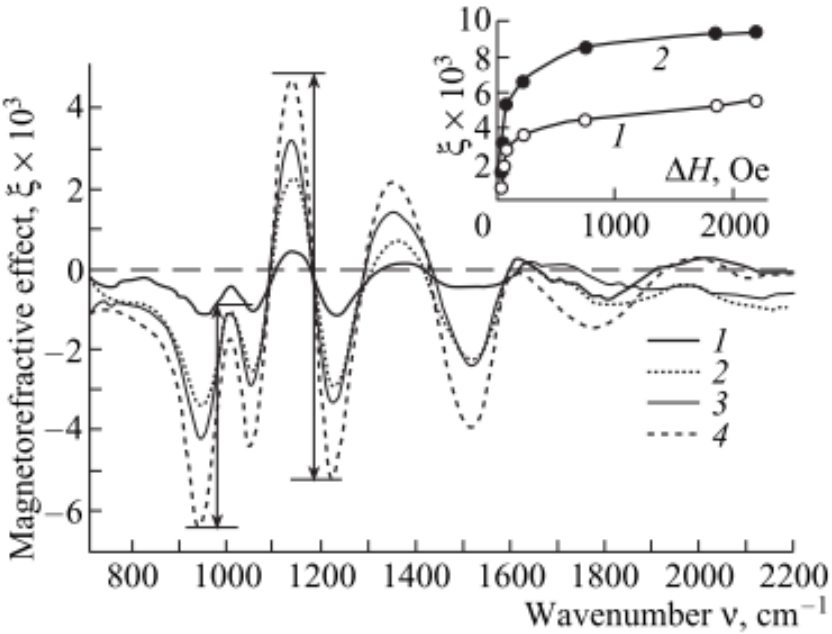

Fig. 3. Frequency response of the magnetorefractive effect of a $Co_{46}Al_{22}O_{32}$ film obtained for several magnetic fields, $\Delta H = H_{max} - H_i$; ΔH (Oe): (*1*) 50, (*2*) 100, (*3*) 250, and (*4*) 2200. The inset shows field dependences of the difference between the amplitude values of the magnetorefractive effect at (*1*) 970 and (*2*) 1180 cm^{-1}.

Figure 4.5: A single phase film test, the MRE is shown vs. wavenumber for 4 magnetic fields. The inset is the amplitude of the shift in MRE seen at (1) $970\,\mathrm{cm}^{-1}$ and (2) $1180\,\mathrm{cm}^{-1}$. Reproduced from Bykov et al. [9].

shortly before the experimental work [9] though the theoretical cited the experiment, as it was in the same group. Seen in Figure 4.5 is the experimental work showing the MRE from wavenumber $700\,\mathrm{cm}^{-1}$ to $2200\,\mathrm{cm}^{-1}$, corresponding to $14.3\,\mu\mathrm{m}$ to $4.54\,\mu\mathrm{m}$ respectively. MRE is represented by δ defined as

$$\delta = (R_H - R_0)/R_0 \tag{4.3}$$

with R_H the reflectivity with applied field, and R_0 the reflectivity without field applied. When comparing many MREs then the sign of the change in reflected intensity is sometimes dropped (and not always noted in papers between plots), and may be instead stated as:

$$\delta = |\Delta R|/R \tag{4.4}$$

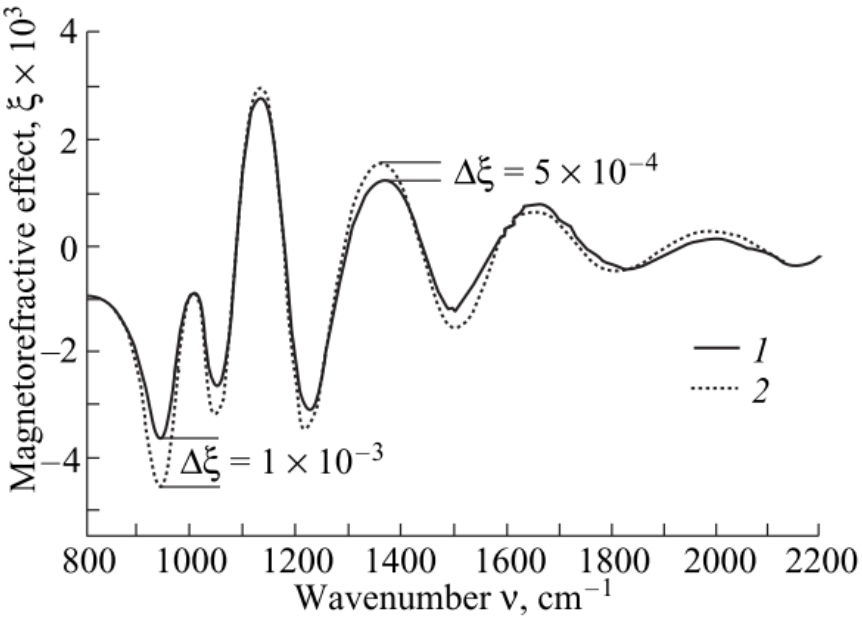

Fig. 5. Frequency response of the magnetorefractive effect of a $Co_{43}Al_{22}O_{35}$ film for the cases of equatorial and meridional magnetization: (*1*) the *H* vector is parallel to the plane of light incidence and (*2*) *H* is perpendicular to the plane of light incidence; $\Delta H = 2000$ Oe.

Figure 4.6: The dependence of MRE on wavelength, and magnetization direction to laser polarization for MRE reproduced from Bykov et al. [9].

Bykov et al. do not state the temperature of the experiment, so it is assumed to have been performed at ambient. As expected for the MRE derived from GMR, the MRE was experimentally found to die off as wavelength shortens. This is due to the frequency component in to denominator of Equation 4.2. Additionally, as the material fully magnetizes, then the MRE diminishes with more field. The inset in Figure 4.5 shows that the effect's sensitivity $\frac{\partial\delta}{\partial H}$ appears to peak near 80 Oe at $-0.28\,\%/80\text{Oe}$ (this should be negative judging by the main plot) and $\pm 0.54\,\%$ for 10.3 µm and 8.5 µm respectively for this $Co_{46}Al_{22}O_{32}$ oxide film.

This work [9] is the first to show impact of the direction of magnetic field with relation to incidence on the MRE. Seen in Figure 4.6, the perpendicular magnetization shift is up to 20 % more than the parallel magnetization study. This may be explained by magnetic anisotropy within the film, or it may be due to the GMR used in this work, vs. the CMR of other studies on MRE.

It may be that 2 kOe is not enough to fully magnetize the film, and with a hard axis out of plane, the in-plane magnetization does not fully rotate. It shows that a stronger response is seen when light is perpendicular to the applied magnetic field, up to 0.1 % more at the 10.3 µm wavelength and 2 kOe. This plane of light incidence is the plane made by the light incoming and reflected off the materials, not the plane of the sample.

4.7 Near room temperature MT

The next advancements were in 2002 when Sukhorukov et al. found Lanthanum Calcium Manganese Oxide $La_{0.66}Ca_{0.33}MnO_3$ (LCMO) possessed IR, near room temperature MT [108]. Using a fixed angle, variable wavelength and temperature setup, allowing only a few fixed magnetic fields (0 T, 0.8 T, 2.5 T and 5 T) to be applied while the opacity of the sample was measured. As the material was heated past 250 K it would suddenly become resistive and transparent. Both the resistance and transparency could be suppressed with applied magnetic field. The peak MR and MT were at the temperatures of most rapid resistance and transparency increases respectively. Sukhorukov et al. would revisit this material and check its MRE [110] in 2010, described further in section 4.10.

4.8 Above room temperature MT

Building on their study of LCMO, in 2005 Sukhorukov et al. found LSMO to possess MT. Using the same methods as before, they showed that the 50 nm and 300 nm thick films of LSMO on Strontium Titanate $SrTiO_3$ (STO) and Lanthanum Aluminate $LaAlO_3$ (LAO) substrates (4 samples) all showed MR and a correlated MT in the IR to mid-infrared (near IR) spectrum. The peak effect was seen in the thicker, 300 nm samples, with STO allowing the effect to continue until 1500 nm. This was the first example of an above room temperature effect found at a useful wavelength. As covered in section 2.4, 1550 nm is a common fiber optic wavelength with extensive off the shelf (OTS) components available for making devices to operate with. This material was later shown to also possess MRE by Hrabovsky et

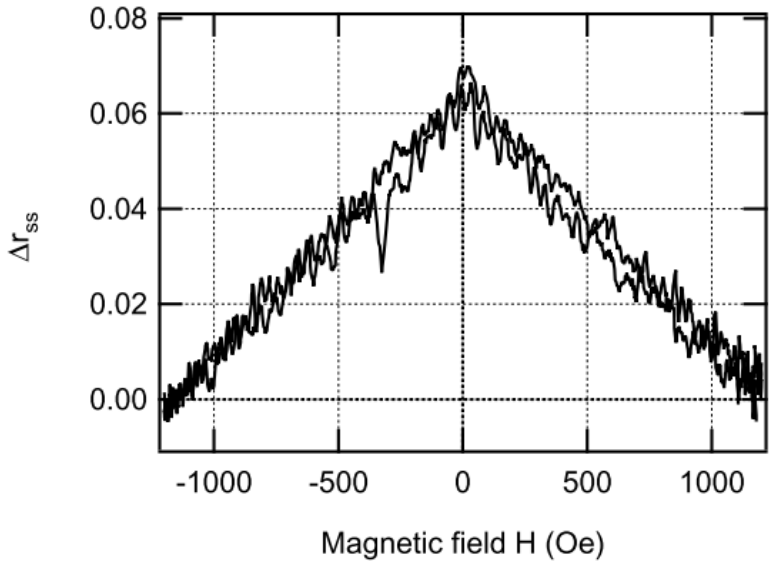

Figure 4.7: A LSMO film's reflectivity vs. applied magnetic field near room temperature. Reproduced from Hrabovsky et al. [51].

al. [49, 51] in 2009, as addressed in section 4.9.

4.9 Room temperature, visible spectrum MRE

A new group to MRE research in Spain was the next to advance the field. In 2009, Hrabovsky et al. showed that the raw reflectivity of a LSMO thin film was effected by applied magnetic field [51]. What was new is the temperature of the study, room temperature and then a sweep from 40 K to 320 K, combined with the wavelength, 650 nm [49]. Previous work had either been at that temperature or in the visible spectrum, but not both. These authors had previously spent much time examining the magneto optical Kerr effect (MOKE) results of films, and likely stumbled across the abnormal 'even' MRE effect in their data. Smartly, these researchers found that the effect was truly present and not an experimental error, ultimately finding the MRE to cite. They were not hampered by the pre-conceived notion that MRE cannot be seen in the visible spectrum, nor that reflectivity is harder to measure than MT. Figure 4.7 shows the reflectivity vs. field for the film at room temperature. Figure 4.8 shows how the even MRE effect scales with temperature, peaking as the odd traditional magneto-optical effect is falling off around 290 K.

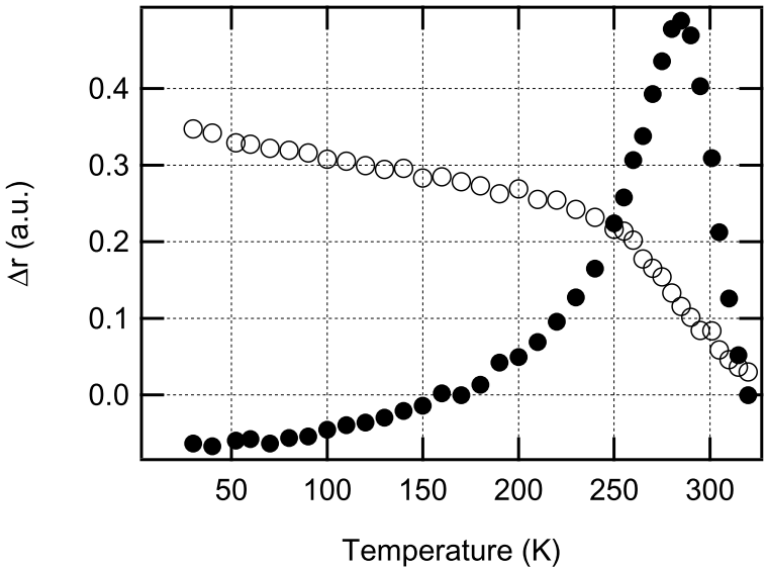

Figure 4.8: A LSMO film's even and odd effect's sensitivity vs. temperature. The solid symbols are the even MRE effect, while the empty symbols are the odd, MOKE signal. Reproduced from Hrabovsky et al. [51].

4.10 Low field MRE seen in LCMO

In 2010, a leader in MRE, Sukhorukov of the Ural Division of the Russian Academy of Sciences, Institute of Metal Physics showed that LCMO of $La_{0.7}Ca_{0.3}MnO_3$ could have a peak MRE of 3.9% at 230 K, with 12.5 µm light and 3 kOe of magnetic field. This is illustrated in Figure 4.9 [110]. This paper does not show an effect above the noise floor between 5 µm and 800 nm. This built on their previous 2002 work showing MT in LCMO [108].

Seen in Figure 4.10, the paper appears to need a field of at least 500 Oe to start the change in reflectivity, but the change in resistance begins before this. Such a lag may just be a signal to noise issue though as the work lacks error bars, and the data appears jumpy, as if there is a fixed noise component in the experimental setup. Once past 500 Oe, the MRE is relatively linear, as is the CMR effect with field. The correlation between MRE and CMR is otherwise strong, emphasizing the Drude effect's strong role in MRE at the 12.5 µm wavelength.

The T_C of the samples can be found by examining Figure 4.11. There in the sharp increase in MRE response is shown in sample 'No. 1' at the T_C of 230 K. This correlates to

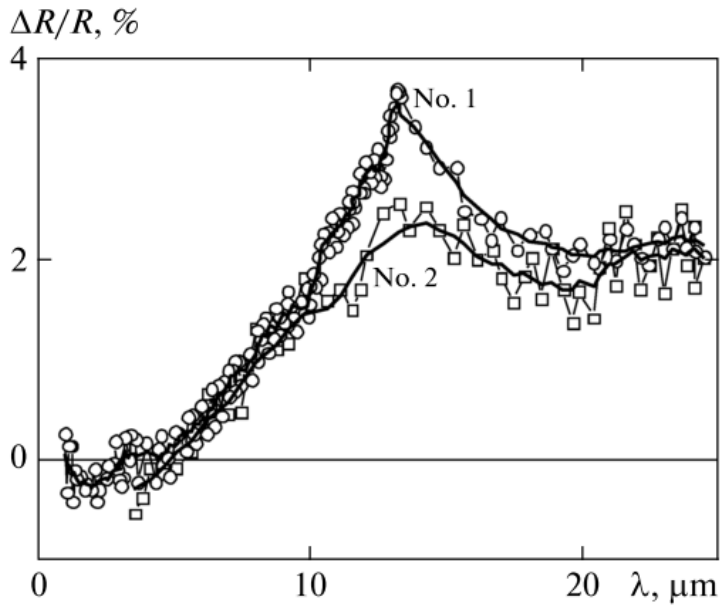

Fig. 5. Spectral dependences of the relative magnetic reflection $\Delta R/R$ in both samples in a magnetic field of 3 kOe at $T = 230$ K (the solid lines are plotted for clarity).

Figure 4.9: Two samples of LCMO which both show non-zero responses in the near visible spectrum, though substantially less significant the response in the mid IR. Reproduced from Sukhorukov et al. [110].

a relatively strong MR change too. Looking at the CMR study of the material though there appears to be a second key response at 260 K, the T_C reported in a study also published that year by Hrabovsky et al. [50] on LCMO also.

This is likely due to poor composition, as shown in the sample composition figure in the paper. As these samples are 5.5 mm by 4.0 mm by 0.5 mm pieces, they may also have a different bulk T_C than that of a film in sample, due to multiple phases being present in the sample, and surface [50].

4.11 Second visible spectrum MRE

In 2010, Hrabovsky et al. [50] showed that a 43 nm thick film of LCMO has MRE with 632 nm light. Results of this are seen in Figure 4.12. This was done at 160 K to 290 K. To isolate the MRE from Kerr effect on the MOKE setup, a quarter wave plate was added to the

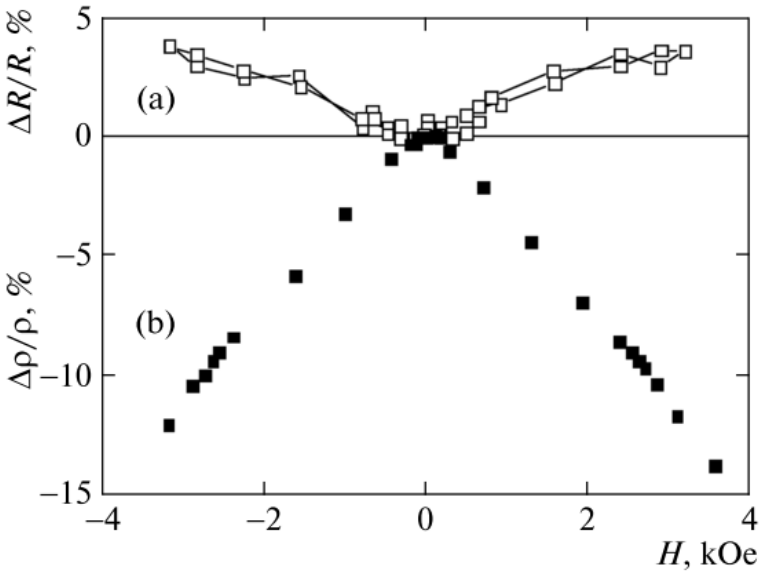

Fig. 4. Field dependences of the (a) relative magnetic reflection $\Delta R/R$ at $\lambda = 12.5$ μm and (b) relative colossal magnetoresistance $\Delta\rho/\rho$ for sample no. 1 at $T = 230$ K.

Figure 4.10: Plot of changes in reflected intensity on the top, compared to the change in resistance of the sample on the bottom. Convenient symmetry of the Figure should be noted, as the sample becomes less resistant, and more reflective with increasing absolute magnetic field. Reproduced from Sukhorukov et al. [110].

setup. When light rotated due to the Kerr effect, it would be observed in an 'odd' manner. MRE, as it changes the reflected intensity and not the polarization of the light, is perceived as an 'even' component to the shift.

Next, to better isolate the MRE signal from the MOKE signal, s-polarized light was used. This polarization will interact in a Kerr way with magnetizations that are perpendicular to the surface. As the solenoid for the study magnetizes in the plane of the film, there should be no out of plane magnetization for the light to interact with. This was seen in the following plots at 260 K with 632 nm light.

Unfortunately, while LCMO has a MRE response, it is dampened by 270 K, thus it is not a viable material for our room temperature project. This correlates to the T_C (260 K) for the material [50]. Still the 3.5% MRE effect at the T_C of 260 K with 632 nm light was an advancement in the search for this project's ideal material.

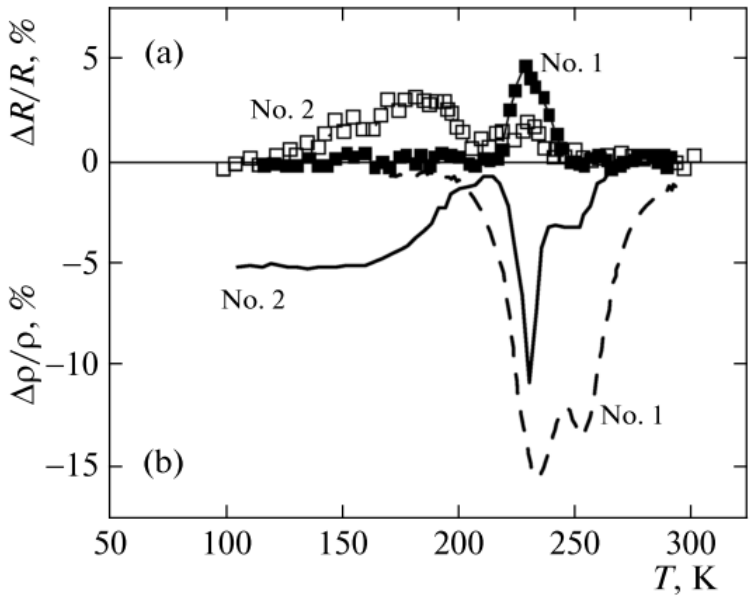

Fig. 3. Temperature dependences of the (a) relative magnetic reflection $\Delta R/R$ at $\lambda = 12.5$ μm and (b) relative magnetoresistance $\Delta\rho/\rho$ for the first and second samples in a magnetic field of 3 kOe.

Figure 4.11: The reflectivity and resistance changes in LCMO, induced by magnetic field, vs. temperature, reproduced from Sukhorukov et al. [110].

4.12 Green and blue spectrum MRE

In late 2010, Caicedo published a paper on lead doped LCMO $(Pr_{0.4}La_{0.6})_{0.7}Ca_{0.3}MnO_3$ (LPCMO) showing that with 400 nm and 500 nm light there is a linear MRE effect at 7 K and 140 K [11]. The film had a thickness of 100 nm using a pulse laser deposition (PLD) process from two targets, $Pr_{0.7}Ca_{0.3}MnO_3$ and $La_{0.7}Ca_{0.3}MnO_3$. The T_C is at 140 K and other properties were described in the paper's references 18 and 19. The LPCMO film was shown to be a CMR material, going from an insulator to conductor. The transverse Kerr signal is in Figure 4.13.

This response was shown to increase in intensity with longer wavelengths. Overall, LPCMO has a MRE effect, in the visible spectrum, but the effect is dissipated by room temperature (even by 210 K), eliminating the effect from being a candidate material for a room temperature MRE glass.

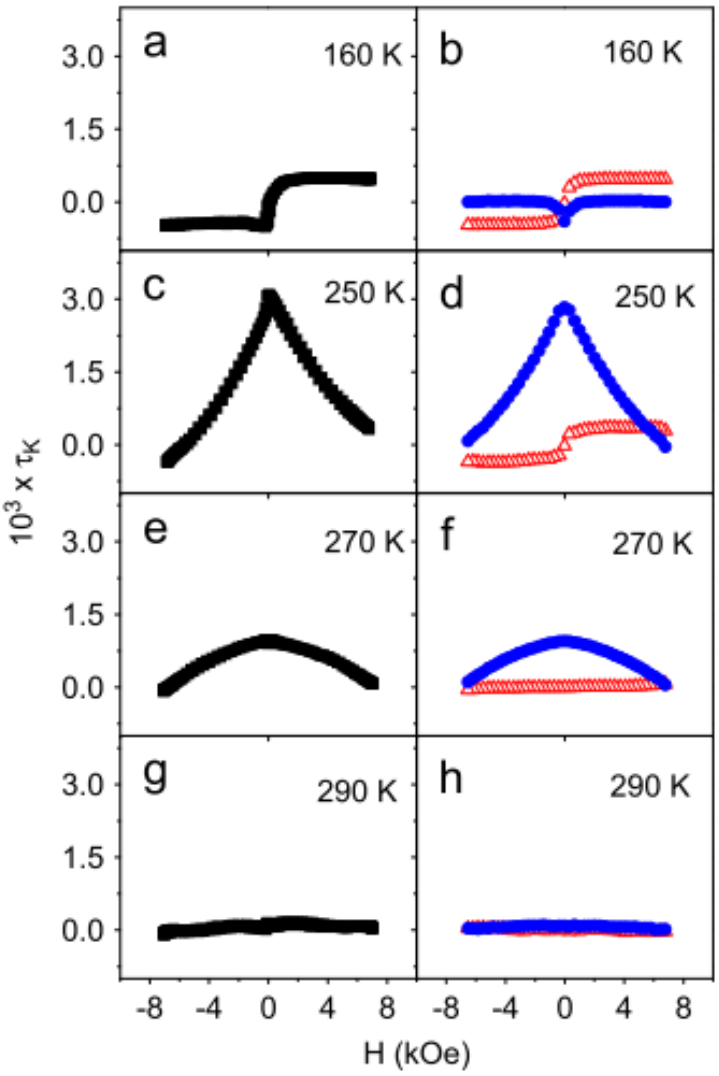

Fig. 1. Imaginary transverse Kerr signal τ_K measured at (a) 160 K, (c) 250 K, (e) 270 K and (g) 290 K. The odd and even in-field contributions to τ_K are are decomposed and plotted separately in (b), (d), (f) and (h) for every temperature (open and solids symbols respectively).

Figure 4.12: The MOKE signal from LSMO at four temperatures, and cycling field from $-8\,\mathrm{kOe}$ to $8\,\mathrm{kOe}$. Reproduced from Hrabovsky et al. [50].

4.13 MRE present in magnetite

In 2010, Fe_3O_4 was shown to have MRE [10]. The effect was present at wavelengths from 800 nm to 400 nm and from 8 K to 300 K. This supports that it is possible Emmons et al. saw FBG and MRE interactions [30]. This is seen in Figure 4.14.

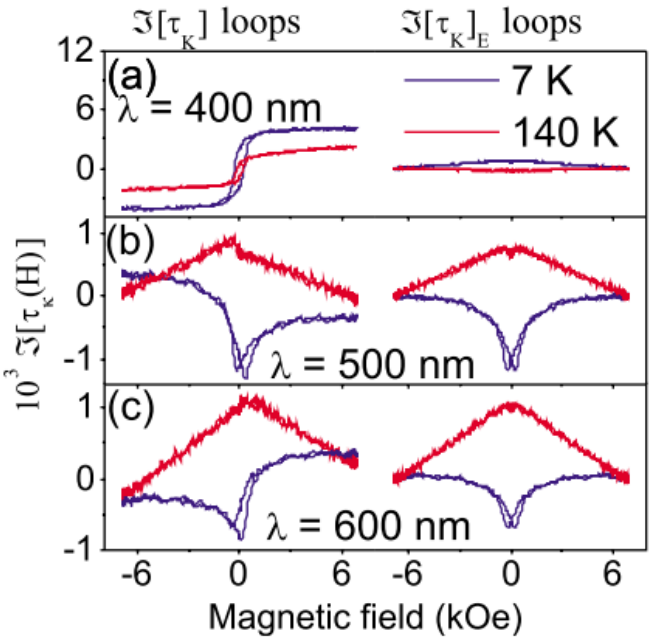

FIG. 1. (Color online) Left column: $\Im[\tau_K(H)]$ hysteresis loops measured at 7 and 140 K at wavelengths (a) λ=400 nm, (b) λ =500 nm, and (c) λ=600 nm. Right column: corresponding even-parity components $\Im[\tau_K(H)]_E$.

Figure 4.13: The MOKE signal from LCMO at two temperatures, three wavelengths, and cycling field from $-6\,\mathrm{kOe}$ to $6\,\mathrm{kOe}$. Reproduced from Caicedo et al. [11].

4.14 Visible, room temperature MRE reported in LAMO

Finally, an extensive publication on the MRE in the visible spectrum was published, now on LAMO and LCMO. In collaboration between two leading MRE research groups, LAMO was characterized. Shown in Figure 4.14 is the MRE of the sample at visible spectrum (from 300 nm to 900 nm) and at room temperature (310 K) [111]. These sputtered LAMO films showed a shift of $-3\,\%$ reflectivity at 11 kOe and at room temperature. MT was done for the longer wavelengths (longer than 1200 nm) for LAMO also.

Sukhorukov et al. also speaks of LCMO compositions, but all are tested at 265 K, thus below room temperature. Adding to this, a paper in 2003 on the CMR properties of LAMO by Pi et al. [93] shows that the ideal CMR 300 K material composition for LAMO is when $La_{1-x}Ag_xMnO_3$ $x = \frac{1}{6}$. This has a resistance change of -25%, vs. -2% for $x = 0.1$ at 1.2 T.

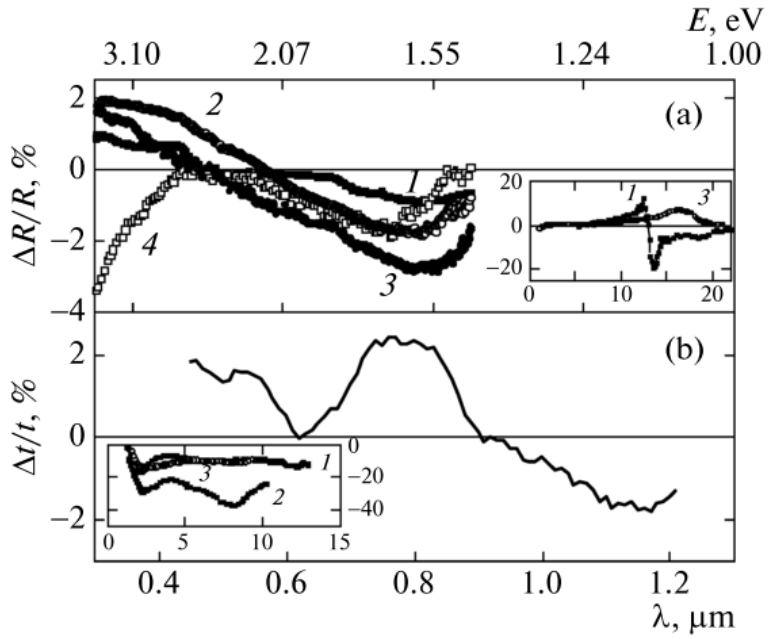

Fig. 1. (a) Spectra of magnetoreflectance $\Delta R/R$ measured in the magnetic field $H = 11$ kOe for (*1*, *2*) the $La_{0.7}Ca_{0.3}MnO_3$ films with thicknesses of (*1*) 50 and (*2*) 320 nm at the temperature $T = 265$ K and (*3*, *4*) the $La_{0.9}Ag_{0.1}MnO_3$ film at temperatures of (*3*) 310 and (*4*) 10 K. The inset in panel (a) shows the $\Delta R/R$ spectra of (*1*) the $La_{0.7}Ca_{0.3}MnO_3$ film with a thickness of 50 nm and (*3*) the $La_{0.9}Ag_{0.1}MnO_3$ film in the IR spectral region in the magnetic field $H = 3$ kOe. (b) Spectrum of magnetotransmittance $\Delta t/t$ measured for the $La_{0.7}Ca_{0.3}MnO_3$ film with a thickness of 180 nm at $T = 265$ K and $H = 2.8$ kOe. The inset in panel (b) shows the magnetotransmittance spectra of (*1*) the $La_{0.7}Ca_{0.3}MnO_3$ film with a thickness of 320 nm, (*2*) the $La_{0.7}Ca_{0.3}MnO_3$ film with a thickness of 180 nm, and (*3*) the $La_{0.9}Ag_{0.1}MnO_3$ film in the IR spectral region in the magnetic field $H = 8$ kOe.

Figure 4.14: MRE and MT of LAMO and LCMO at wavelengths from $0.3\,\mu m$ to $22\,\mu m$. Reproduced from Sukhorukov et al. [111].

This 10 times improvement in CMR may also be seen in the MRE, possibly allowing the film to have an improved response than previously reported, maybe up to -20% MRE instead (though this is unlikely, and quite large).

4.15 Goal

This research was sponsored to pursue and propel the development of a MRE material for inclusion in optical fiber as a novel magnetometer system. Thus, creating a magneto-refractive glass which is sufficiently optically transmissive to allow for inclusion, an optical fiber would be a viable result for the research to continue. Unfortunately, this was not achieved in the course of this work. Instead, it was ultimately found that LSMO's conductivity drives a high absorption, which will frustrate any inclusion into an optical fiber.

4.15.1 Magnetic fluids offer $n(H)$

Single magnetic FBGs have been achieved already. Dai et al. in 2011 created a magnetic FBG utilizing a magnetic fluid, magnetorheological fluid (MRF) with a sensitivity of 2.5 Gauss. This sensor is based off of tapering a FBG and sticking it in the MRF [17]. The MRF's particles moved and formed chains when in magnetic field, shifting the index of the fluid reversibly.

4.15.2 No glass yet possesses $n(H)$

Using a different mechanism, MRE, for a similar result, $n(H)$, this thesis initially set out to do similar experiments, but instead of packing Fe_3O_4 particles around an etched FBG core, it was proposed to make a glass that contains MRE particles and utilize this as a novel fiber optic cladding or core. So far, there exists no glass that possesses such magnetorefractive qualities ($n(H)$), though other magneto-optical glasses exist and are used in various optical systems. A new magneto-optical glass would open up designs for flat, adaptive lens whose optical shape is driven by the magnetic fields applied, as well as the magnetometers prompting this research. This early avenue of research proved so fruitless and frustrating as to not warrant a much place in this thesis. Two intermediary results achieved though were LSMO coated in SiO_2 seen in Figure 4.15, and a shattered overcoat of SiO_2 on a glass slide seen in Figure 4.16. The later only achieves entry in this thesis due to it being the most beautiful

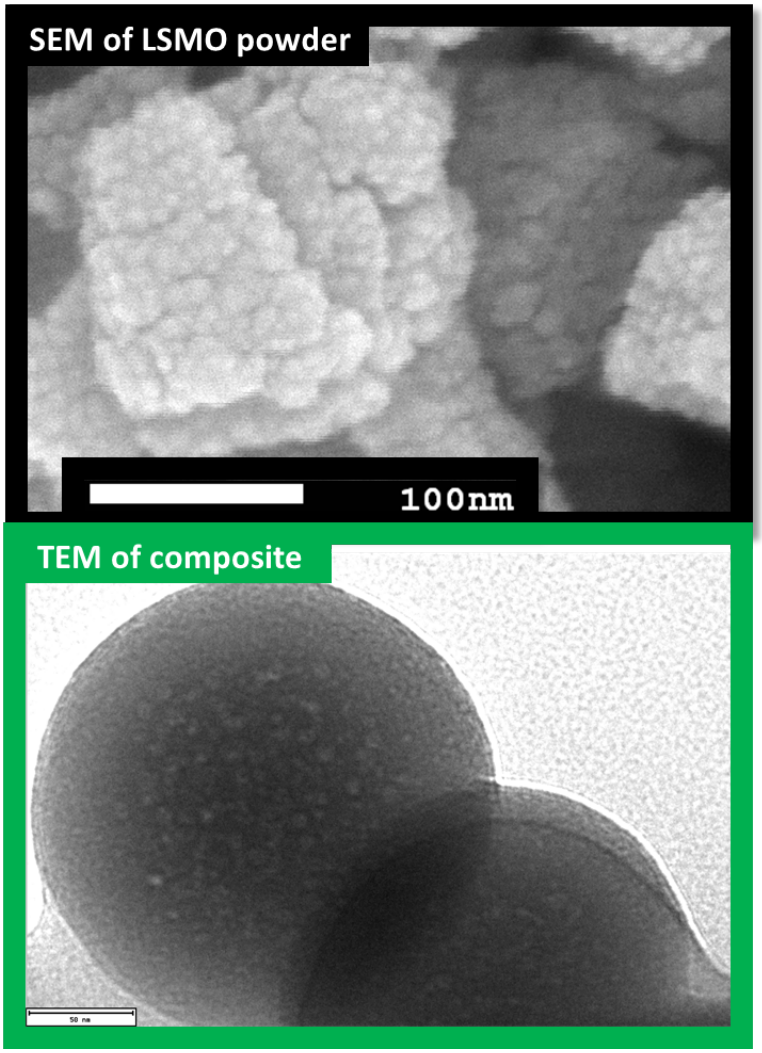

Figure 4.15: A scanning electron microscopy (SEM) of LSMO and a transmission electron microscopy (TEM) of a coreshell, LSMO@SiO_2, particle. The photos have the same scale, with the lower scale bar being $50\,\mathrm{nm}$ long. These were taken by Paul Nordeen and Laura Schelhas respectively, of samples prepared by the author.

image created in the course of this research... *May any future researcher reading this thesis remember that in every down moment and dead-ended feeling research attempt there can be beauty and joy found.* If this road had not been attempted I would have regretted the untrodden path and possible short cut to a quick answer.

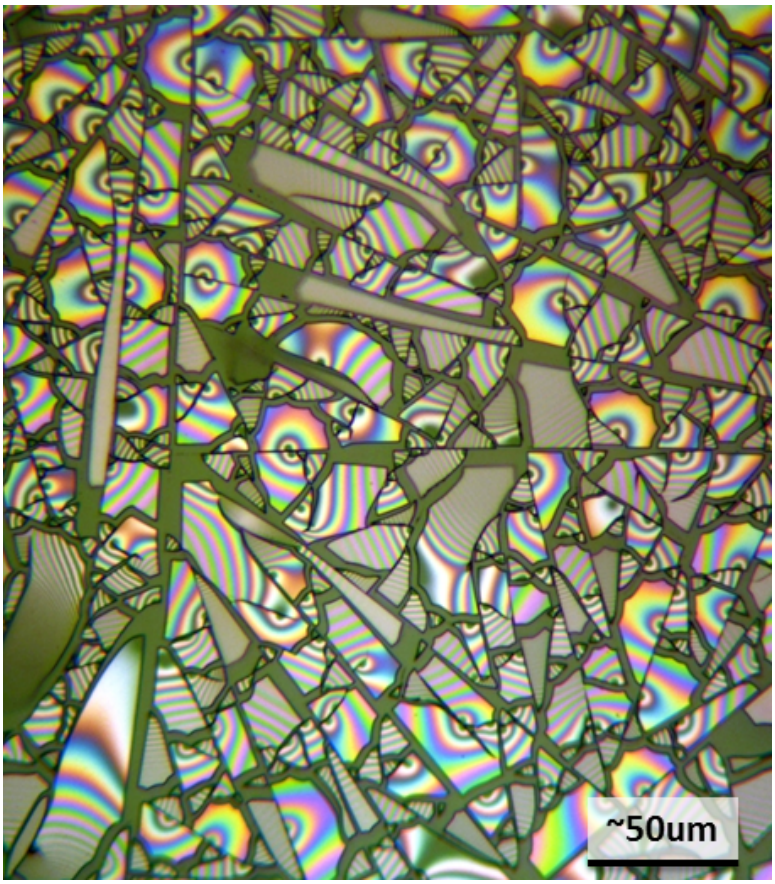

Figure 4.16: A shattered film of SiO_2 on a glass slide. Photo taken through a microscope, and the loose film was gone 24 hours later when a second image was attempted. This was the most beautiful image this research yeilded.

4.15.3 LSMO's expected index of refraction

LSMOs index of refraction varies by origin of the film, wavelength of light, temperature tested at, and, shown in this thesis, magnetic field applied. For LSMO films, their index can be calculated using diagonal dielectric tensor data shown in Figure 4.17 from Liu [72], gathered on magnetron sputtered films, yielding at 633 nm, 1.96 eV with dielectric values of $\epsilon_1 = 3.5$ and $\epsilon_2 = 2.5$. Given Equation 1.13, and that $\epsilon_2 = \frac{\sigma}{\omega}/\epsilon_0$ then,

$$n = \sqrt{(\sqrt{\epsilon_1^2 + \epsilon_2^2} + \epsilon_1/2)} \tag{4.5}$$

thus, the index n is 1.975. This is similar to the index of refraction found for sol-gel based electron beam resist LSMO [116] who found values around 2.08.

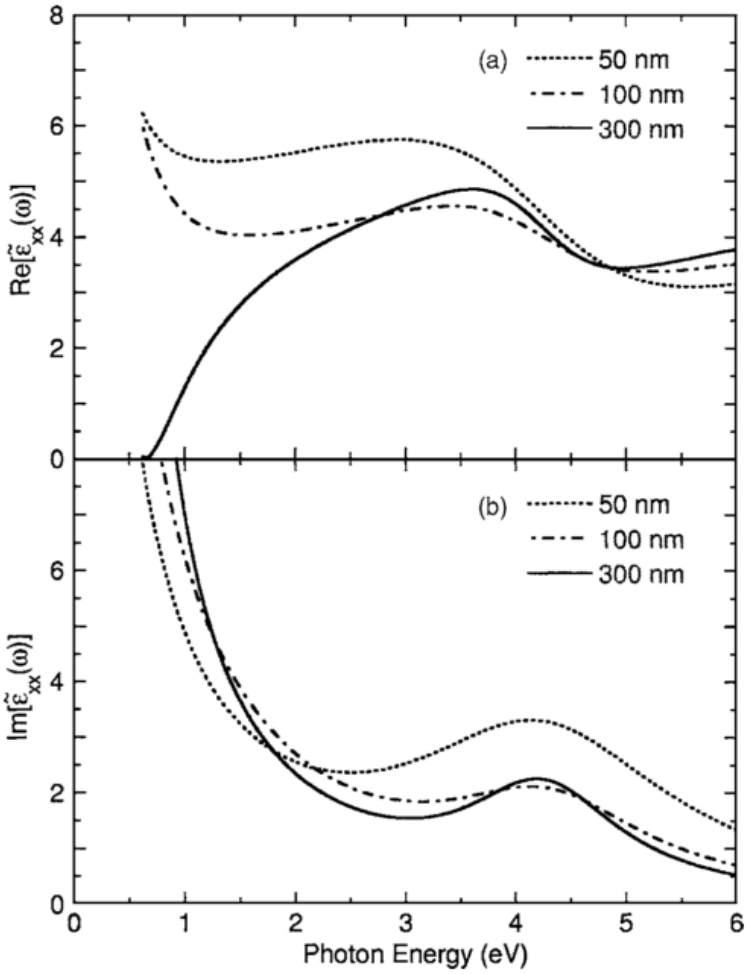

FIG. 3. The real and imaginary parts of the diagonal components of the dielectric tensor of the three LSMO films.

Figure 4.17: Permittivity of LSMO vs. photon energy, reproduced from Liu et al. [72].

4.16 Project hypothesis

UCLA proposed integrating a material exhibiting MRE, such as LSMO, with a FBG to create a magnetometer. A previous attempt to use optics and magnetic material to make a magnetometer was made at UCLA by Emmons et al. [30]. They used Fe_3O_4 powder and an FBG with its cladding mostly etched away. This is similar to the Fe_3O_4 ferro-fluid system studied by Dai et al. [17] tested. Ferro-fluids are colloids of magnetic nanoparticles suspended in a fluid such as silicon oil or water. Ferro-fluids coupled to an FBG is a common route for MFBG research, as ferro-fluids have been shown to exhibit changes of index of refraction under magnetic field due to particle movement. Such sensors require that the cladding

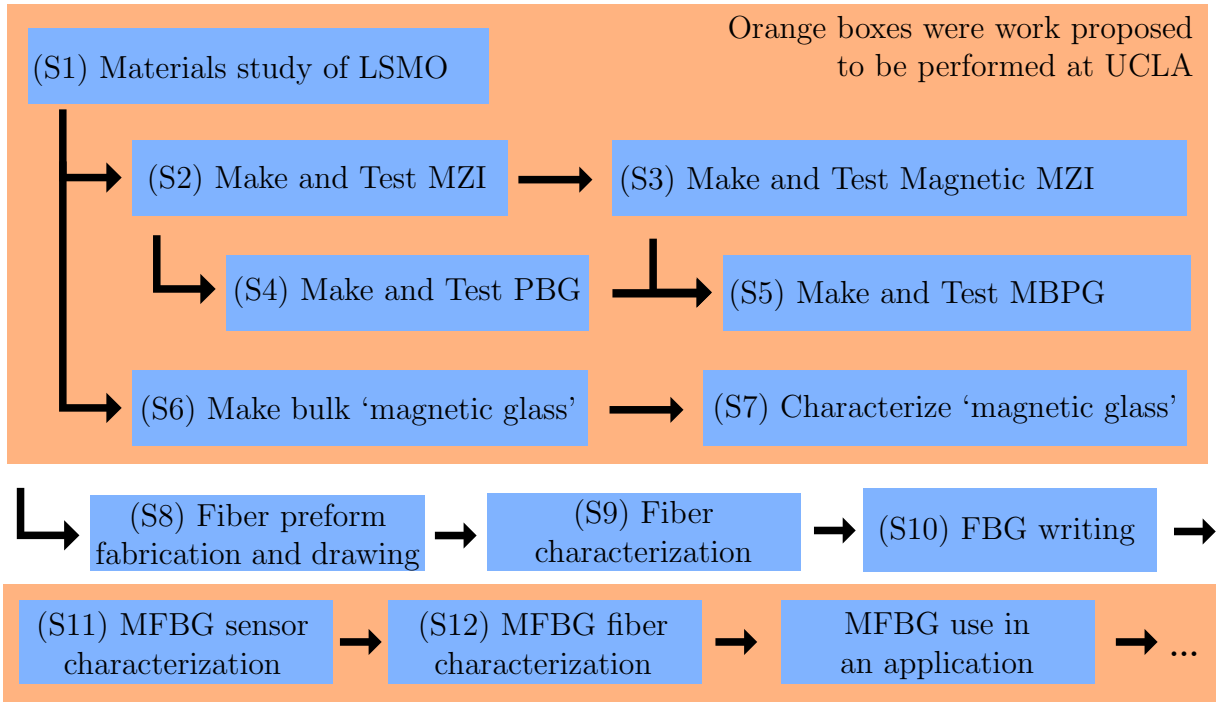

Figure 4.18: Proposed project road map for MFBG project. Orange boxes were work possible at UCLA.

of the FBG be etched away and exposed to a fluid. Both of these approaches produced single sensors, rather than distributed sensing systems. Here, we propose the development for integrating MRE materials into an optical fiber. This is covered by Emmons et al.'s patent US9274181 granted March of 2016. To achieve this goal, we proposed a series of developmental devices.

4.16.0.1 MFBG project road map

Illustrated in Figure 4.18 is a 13 step development plan to create this magnetometer array. Step 1 is a materials study (Chapter 6). Steps 2 (Chapter 7) and 3 (Chapter 8) are single point devices to validate the concept using an Mach Zehnder interferometer (MZI).

Following the development of the sensitive but inherently single point MZI device, step 4 proposed using a planar Bragg grating (PBG) setup. This next test device would be fabricated with the same methods and process as the interferometer, but would utilize the Bragg phenomenon of the FBG. Thus, it was expected to bridge the gap between the very

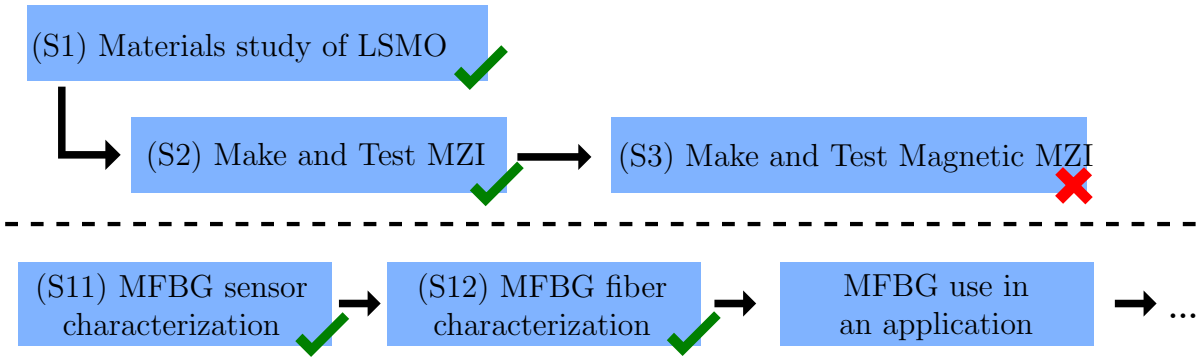

Figure 4.19: Progress on the project road map for MFBG project. Green checks mean successful achievement of exit criteria, and red crosses mean failure to reach exit criteria.

sensitive, single point MZI to the less sensitive, mulitpoint planar Bragg grating (PBG) sensor. This would further understanding of the MRE and how it interacts with a full FBG fiber. Step 5 as a magnetically sensitive PBG could be a stand-alone sensor. The PBG and MZI could operate in tandem on the same wafer. The two sensors would then be able to make absolute field measurements (via the PBG), and more sensitive relative field measurements (via the MZI).

In parallel to developing these optical devices, step 6 could have been undertaken to create a bulk glass embedded with LSMO to show the viability of making a fiber preform which incorporates LSMO. Once LSMO embedded glass is made, then shaping it into a fiber preform and drawing it into an optical fiber could take place. This fiber optic would then be written with Bragg gratings, creating the end result of an array of magnetically sensitive FBGs, each acting as independent, sensitive magnetometers. This magnetic FBG optical fiber would utilize similar electronics and the same multiplexing methods currently applied for state-of-the-art strain and temperature FBG arrays today.

4.17 Actual project progression

Illustrated in Figure 4.19 is the achieved project progress. As can be seen with the failure to achieve the exit criteria set for step 3, steps 4 through 10 were not attempted. Instead, a new method was found and tested for step 11. This method is introduced in Chapter 9, where

magnetic beads are strung onto an optical fiber with FBGs. The region responding to a single bead is one sensor. Arraying the devices is simple and was also achieved in Chapter 9, satisfying the goals of step 12.

CHAPTER 5

MRE of LSMO dependent on magnetic field and temperature

5.1 Introduction

The magneto-optics field studies the influence magnetic fields have on the interactions between light and materials. In 1995, Jacquet and Valet found a new magneto-optic effect where a magnetoresistive material's reflectivity and absorbency were influenced by an applied magnetic field [54] at room temperature. This magnetorefractive effect (MRE) was attributed to magnetic field induced conductivity changes influencing the index of refraction (i.e. through the Drude-Lorentz model), though the latter was not specifically measured. Subsequent research focused on magnetotransmission (MT) of magnetoresistive materials at shorter wavelengths [62], as contrasted with the original initial infrared study. Additional MRE experiments followed [49] using light in the visible spectrum [111]. While there is general agreement that conductivity changes influence index of refraction in the longer infrared spectrum, there is disagreement [46] on why the index changes in the shorter visible spectrum despite magneto-resistance not influencing the index of refraction. While several papers have stated that the applied magnetic fields [54, 62, 49, 111, 46] change the index of refraction, quantitative studies on the change of the index of refraction have not been conducted in the context of MRE or MT effects at any wavelengths.

5.1.1 Summary of UCLA's MRE results

In this study, we experimentally measure the index of refraction of Lanthanum Strontium Manganite $La_{0.66}Sr_{0.33}MnO_3$ (LSMO) as a function of magnetic field and temperature. The sample consists of epitaxially grown LSMO film on an Neodymium Gallate $NdGaO_3$ (NGO) substrate. MRE measurements were made using a 633 nm laser and show a near linear decrease in sample reflectivity by 0.95 % at 5.5 kOe measured at 288 K which is near Curie temperature (T_C). This is the strongest of the 4 wavelengths which were tested.

5.2 Experimental details

One sample and experimental setup were used in this study. A 70 nm thick film of LSMO was grown using reactive molecular-beam epitaxy (RMBE) on a 1 mm thick (110) oriented NGO substrate with the method described by Adamo et al. [3].

The sample was tested using the two setups shown in Figure 5.1 and later in Figure 6.1 for MRE and index of refraction measurements respectively. Figure 5.1 shows the main components of the fixed angle reflectivity setup, longitudinal fixed angle (LFA), [49], starting with a laser which shines light through a vertically oriented polarizer, into a cryostat with the sample oriented at roughly 5° with respect to the laser source. Two lasers of 1550 nm and 633 nm wavelength were used in this study. These MRE tests consist of ramping a magnetic field from 5.3 kOe to −5.3 kOe then back to 5.3 kOe for three cycles while sample reflectivity was measured with the photodiode. Magnetic field was measured with a Hall effect probe (not shown in figure) placed behind the cryostat and adjacent to the sample. Tests were conducted at fixed temperatures ranging from 275 K to 305 K using an integrated heater and thermal couple for sample temperature control within the cryostat.

$$MRE(\%) = \frac{R(H) - R(0)}{R(0)} \tag{5.1}$$

with $R(H)$ being the reflected intensity at a given field, and $R(0)$ being the reflected intensity at the null field.

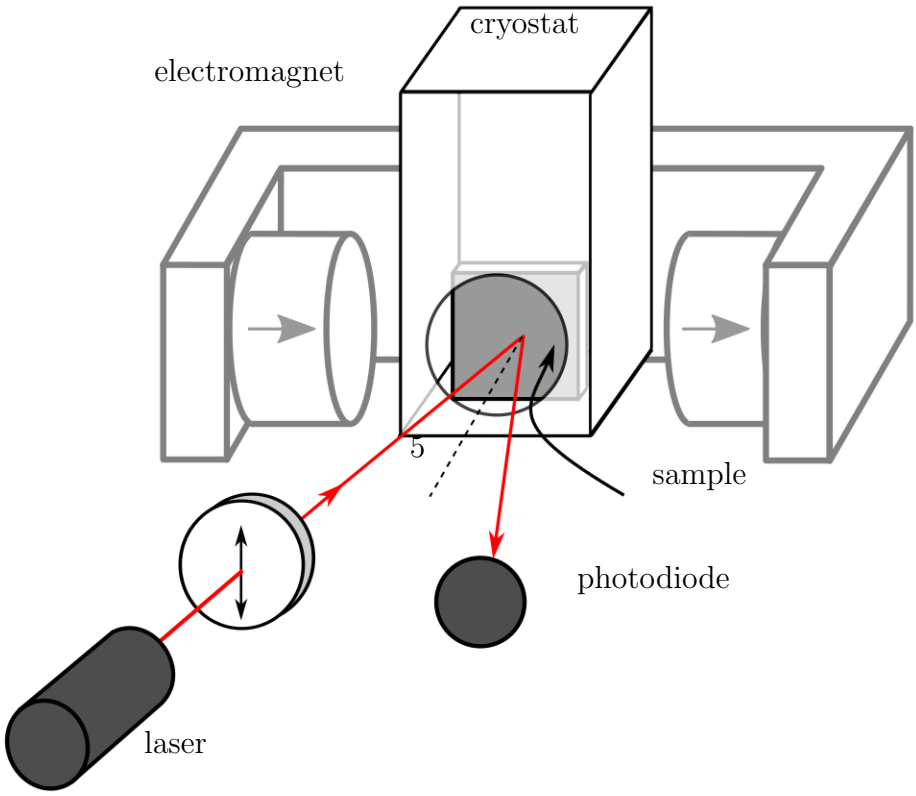

Figure 5.1: Experimental setup used for fixed angle characterization of MRE.

5.2.1 MRE vs. MOKE of RMBE LSMO

When the sample used in this was first received, initial studied to understand if there was angular dependence of the sample's crystal orientation to polarization in the responses. Previous characterization studies by Adamo et al. showed that these samples have a compressive strain state due to its crystal orientation with its substrate [3].

First, magneto optical Kerr effect (MOKE) characterization of the sample's magnetization using the experimental setup shown in Figure 5.1 were performed. The sample was mounted at the end of a rod able to be rotated in controlled fashion, instead of in a cryostat as pictured. A photo-elastic modulator (PEM) and second polarizer were added to the beam line very similar to as seen in [49], and a lock-in amplifier was connected to the PEM. Figure 5.2 shows MOKE intensity for magnetic field loops at various sample angles. There is clearly a magnetic anisotropy in the data, with the magnetic moment wanted to align in

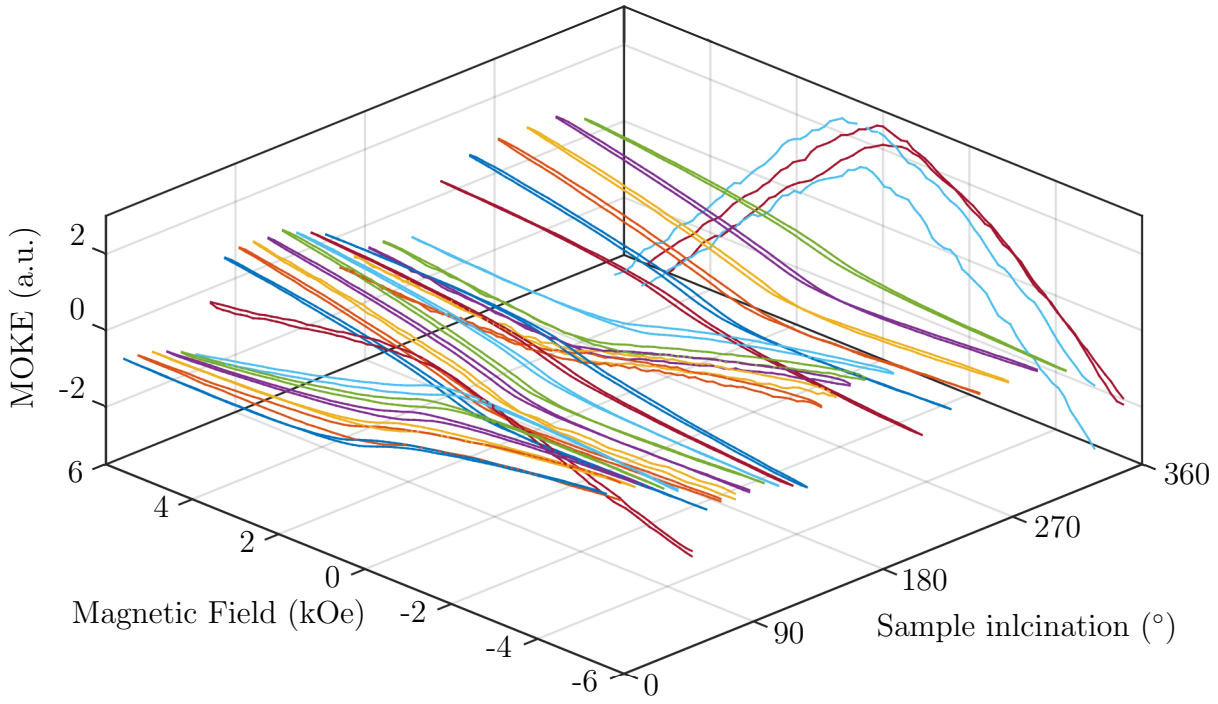

Figure 5.2: MOKE response vs. field applied and angle of the sample in a full 360° rotation.

two directions, 90° apart.

5.3 Experimental results and discussion

The LFA reflectometer showed that 633 nm had the largest response of the four available wavelengths, showing a peak response at 290 K. When fitting raw data using the correct thin film reflectivity equation, the index is found to change by −1.6 mRIU/kOe.

5.4 LFA ellipsometry for MRE

Figure 5.3 shows MRE vs. applied field for tests conducted at three temperatures, 275.7 K, 288.8 K and 298.0 K with a 633 nm laser on the experimental setup shown in Figure 5.1. The

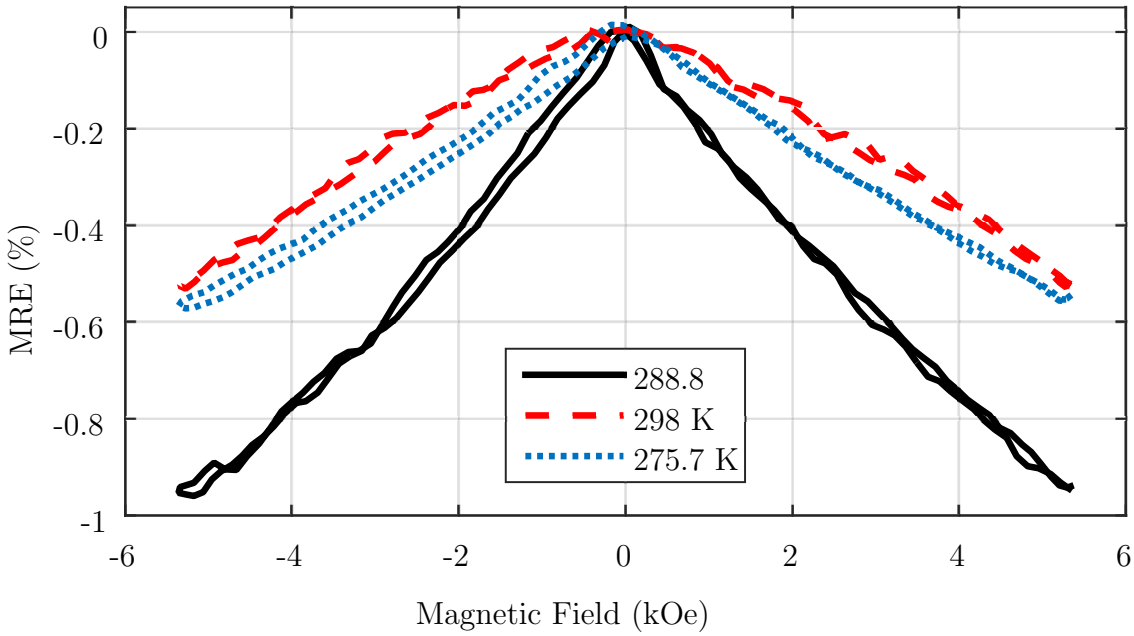

Figure 5.3: Reflectivity of 633 nm light vs. magnetic field for the sample at three temperatures, 275.7 K, 288.8 K and 298.0 K.

magnetorefractive effect is defined as

$$MRE(\%) = \frac{R(H) - R(0)}{R(0)} \tag{5.2}$$

where R(0) is the zero field reflectivity and R(H) is the reflectivity at the measured field [54]. The data shows a negative MRE value that decreases as magnetic field is increases for all temperatures measured. The negative reflectivity is due to UV absorption bands shifting as the electronic structure is effected by magnetic fields as explained by the Jahn-Teller interactions [49]. Comparing the data in Figure 5.3, the slope is approximately $-0.11\,\%$/kOe for 275.7 K, which increases to $-0.18\,\%$/kOe at 288.8 K and decreases to $-0.10\,\%$/kOe at 298.0 K. However, the data taken at 298.0 K shows a slight nonlinear response, i.e. the slope increases as the field increases. We attribute this nonlinearity to the applied magnetic field's influence on T_C [24] which is approximately 290 K [51]. These MRE data have similar trends to previous reports [49, 102], but with different magnitudes. The differences are attributed to dissimilarities in test setup such as angles of incidence and film thicknesses [44].

Figure 5.4 shows MRE test data for 633 nm light as a function of temperature for five

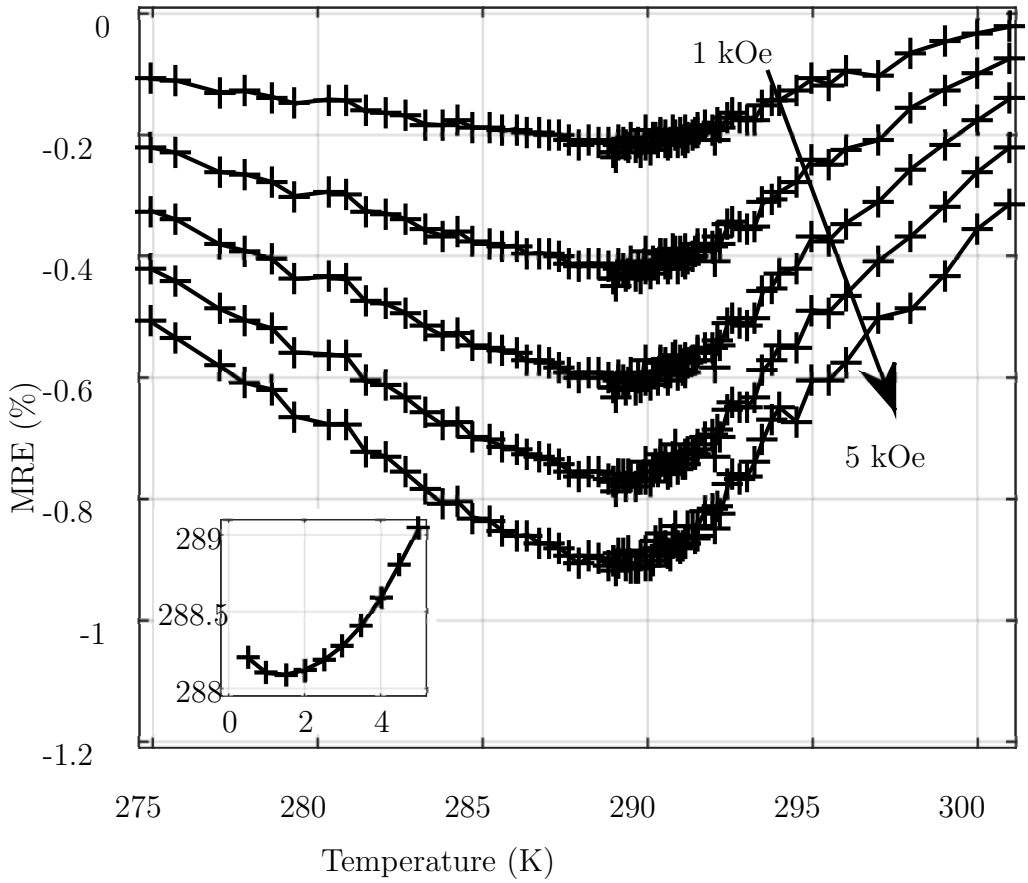

Figure 5.4: MRE of 633 nm light vs. temperature for five applied absolute field values. Inset tracks the temperature of maximum MRE, T_M, vs. applied field.

applied magnetic fields and the setup in Figure 5.1. The MRE first increases in absolute magnitude with increasing temperature followed by a decrease after 290 K for all fields studied [49]. The local effect maximums, T_M, observed in the figure at are attributable to the Jahn-Teller interactions directly related to the material's susceptibility. The susceptibility is maximal near T_C of the material and thus produces a maximum shift in the ultraviolet (UV) absorption bands. Shown in the Figure 5.1 inset is a plot of T_M versus applied field. As one can see, T_M increases as the field increases from 0 kOe to 5 kOe. We attribute this to the magnetic field's influence on T_C by stabilizing the spin states to remain ordered [24] until higher temperatures.

Figure 5.5 shows MRE results as a function of temperature for five applied magnetic fields using a 1550 nm light source and the setup in Figure 5.1. This test shows positive MRE for all

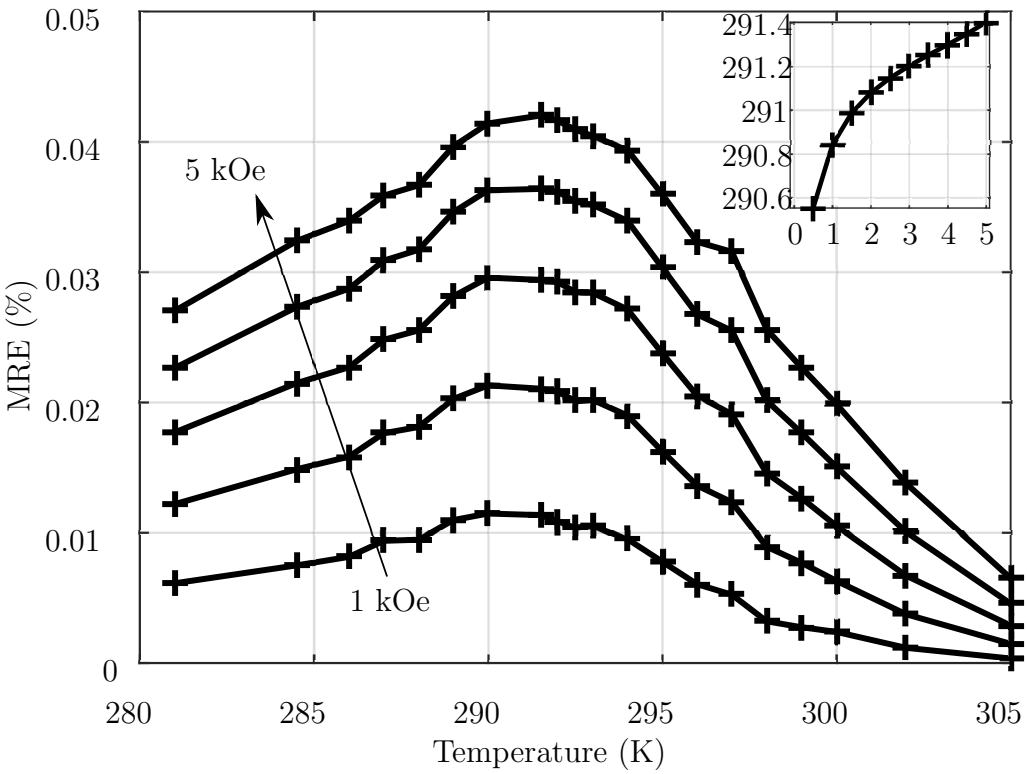

Figure 5.5: MRE of 1550 nm light vs. temperature for five applied absolute field values. Inset is the fitted peak MRE vs. temperature.

fields and temperatures as contrasted with the negative MRE values reported in Figure 5.3 and Figure 5.4. Also, while the trends are similar, the absolute value of the MRE shown in Figure 5.5 is an order of magnitude smaller than Figure 5.4. The reason for both of these (the magnitude decrease and sign inversion) is that there is now a second opposing MRE phenomenon, the Drude-Lorentz based MRE effect. This effect is related to the magneto-resistance of the material, which decreases with applied field. As the magneto-resistance decreases the reflectivity increases, increasing the MRE. The peak in T_M is caused by the fact that the magneto-resistance also peaks at T_C. The inset shows that the temperature at which peak MRE occurs (T_M) shifts with applied magnetic field with similar magnitude changes as reported in the inset of Figure 5.4. However, the concavity difference is likely attributed to the Drude-Lorentz effect present in the 1550 nm study but absent in the 633 nm study. As the 633 nm testing showed stronger MRE than the 1550 nm testing, it was used in the second part of this study.

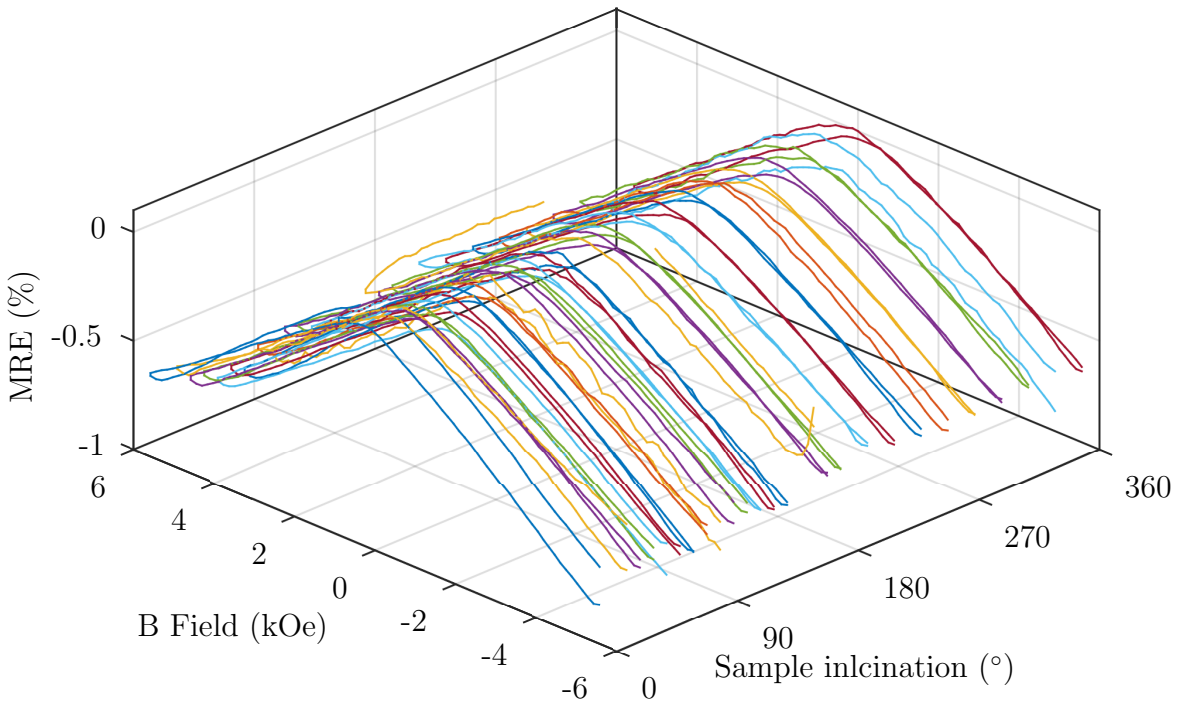

Figure 5.6: MRE response vs. field applied and angle of the sample in a full 360° rotation.

5.5 Examining peak wavelength for LSMO

In addition to the two wavelengths highlighted, two other wavelengths were also loosely studied. 1032 nm and 532 nm were also studied and are plotted in the composite plot in Figure 5.7. Of the four wavelengths tested, 633 nm shows the strongest response. Roque's thesis [102] also indicates that the strongest response in LSMO should be at 633 nm of the wavelengths tested.

Figure 5.7 illustrates the index of refraction sensitivity vs. magnetic field for 4 wavelengths. Each line shows the change in reflectivity due to the application of 4 kOe at various temperatures. These trends show peak changes in reflectivity near 289 K. All the trends have a max effect (characterized as the greatest absolute change in MRE (%) within 5 K of 289 K.

Roque showed in his Figure 4.24 [102] that the peak response is 590 nm in the 355 nm to 2000 nm spectrum (visible wavelengths to near IR). Of the four wavelengths examined in

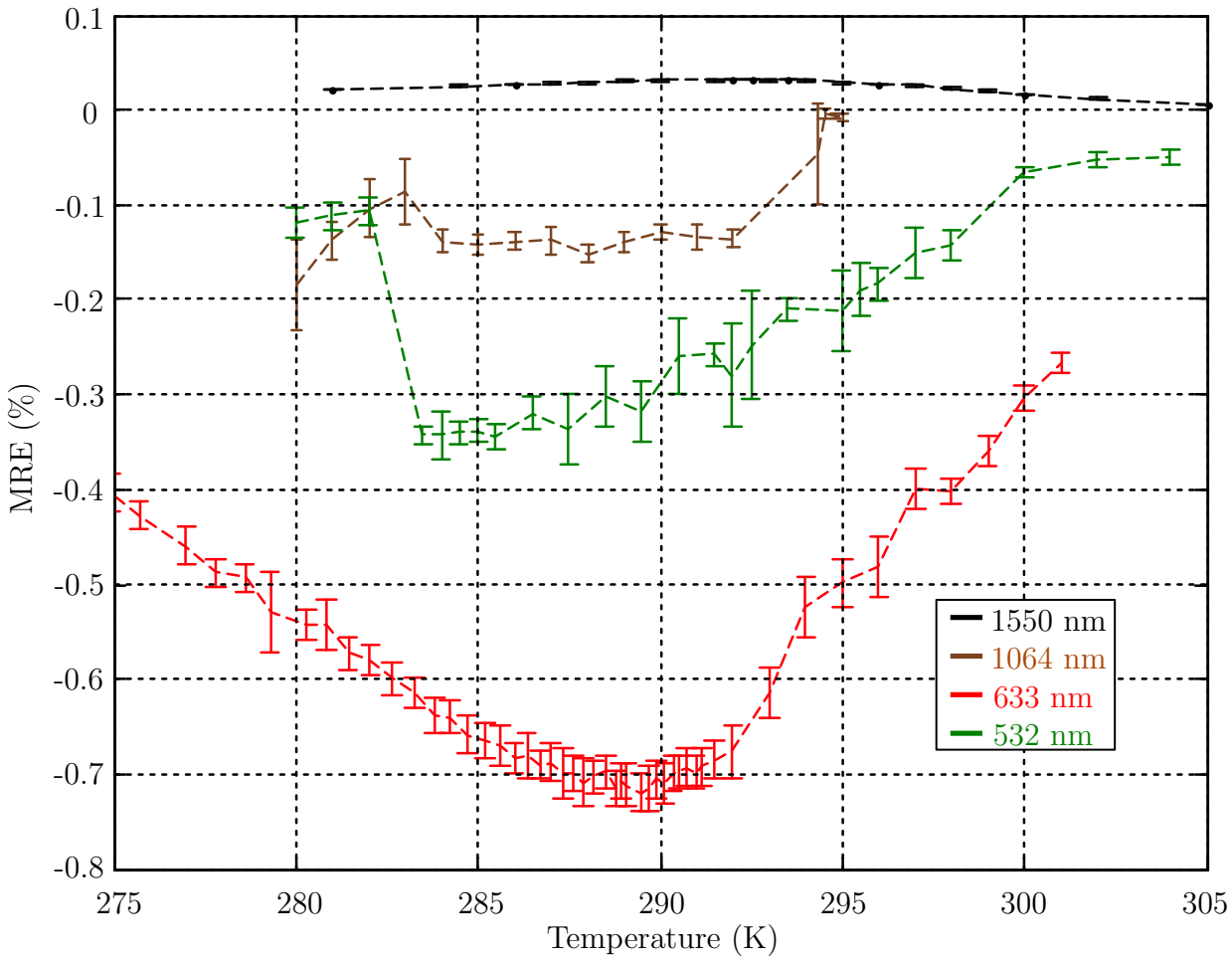

Figure 5.7: LFA study of LSMO on NGO at various wavelengths. This shows that the strongest response of the 4 wavelengths to magnetic fields is from 633 nm light for this sample.

Figure 5.7, 633 nm light had the strongest response, and is the wavelength closest to Roque's peak wavelength, although a higher peak performance wavelength likely exists. To identify the wavelength of absolute peak performance for a given sample would require a tunable laser or an array of lasers. Testing in the visible to near IR spectrum is important, as this is the region the majority of off the shelf (OTS) optical parts are designed for. Roque's work suggests that we may expect a 30% performance gain through further wavelength optimization.

5.6 Conclusion

This chapter introduced and examined the MRE. Base principles from this have been replicated and then understanding on this has been expanded on.

Acknowledgment

The authors would like to thank the AERO Institute and NASA Armstrong for supporting this work. The authors would also like to thank Kang Wang of Department of Electrical Engineering, University of California, Los Angeles for use of his MOKE setup and Darrell Schlom and Carolina Adamo of Cornell for the LSMO sample. Finally, the authors would like to thank NASA Kennedy Space Center for feedback and support of the follow-on steps in the magnetic fiber Bragg grating (MFBG) project.

CHAPTER 6

The index of refraction of LSMO dependent on magnetic field and temperature

6.1 Introduction

The magneto-optics field studies the influence magnetic fields have on the interactions between light and materials. In 1995, Jacquet and Valet found a new magneto-optic effect where a magnetoresistive material's reflectivity and absorbency were influenced by an applied magnetic field [54] at room temperature. This magnetorefractive effect (MRE) was attributed to magnetic field induced conductivity changes influencing the index of refraction (i.e. through the Drude-Lorentz model), though the latter was not specifically measured. Subsequent research focused on magnetotransmission (MT) of magnetoresistive materials at shorter wavelengths [62] as contrasted with the original initial infrared study. Additional MRE experiments followed [49] using light in the visible spectrum [111]. While there is general agreement that conductivity changes influence index of refraction in the longer infrared spectrum, there is disagreement [46] on why the index changes in the shorter visible spectrum despite magnetoresistance not influencing the index of refraction. While several papers have stated that the applied magnetic fields [54, 62, 49, 111, 46] change the index of refraction, quantitative studies on the change of the index of refraction have not been conducted in the context of MRE or MT effects at any wavelengths.

6.1.1 Summary of results

In this study, we experimentally measure the index of refraction of Lanthanum Strontium Manganite $La_{0.66}Sr_{0.33}MnO_3$ (LSMO) as a function of magnetic field and temperature. The sample consists of epitaxially grown LSMO film on an Neodymium Gallate $NdGaO_3$ (NGO) substrate. MRE measurements where made using a 633 nm laser and show a near linear decrease in sample reflectivity by 0.95 % at 5.5 kOe measured at 288 K which is near Curie temperature (T_C). Index of refraction measurements also show a linear decrease under magnetic field, decreasing by 8.25×10^{-3} RIU for an applied 3 kOe field at 290 K or a sensitivity of -2.75×10^{-3} RIU/kOe.

6.2 Experimental details

One sample and two experimental setups were used in this study.

6.2.1 Experimental sample

A 70 nm thick film of LSMO was grown using reactive molecular-beam epitaxy (RMBE) on a 1 mm thick (110) oriented NGO substrate with the method described by Adamo et al. [3].

6.2.2 Experimental setup

The sample was tested using the two setups shown in Figure 5.1 and Figure 6.1 for MRE and index of refraction measurements respectively.

Figure 6.1 shows the test setup to measure index of refraction. This test setup consists of a 633 nm laser shining light through a polarizer into a test chamber and onto the sample. The light is reflected off the sample and onto a photodiode detector enclosed within the chamber. The sample and electromagnet are mounted onto a rotating stage allowing the angle of incidence of the laser to be varied by Θ. The index of refraction test consisted of performing reflection measurements for (Θ) values between 66° and 55° in steps of 0.75°. The absolute positioning accuracy relative to 0° is ±1°, with the stage performing relative

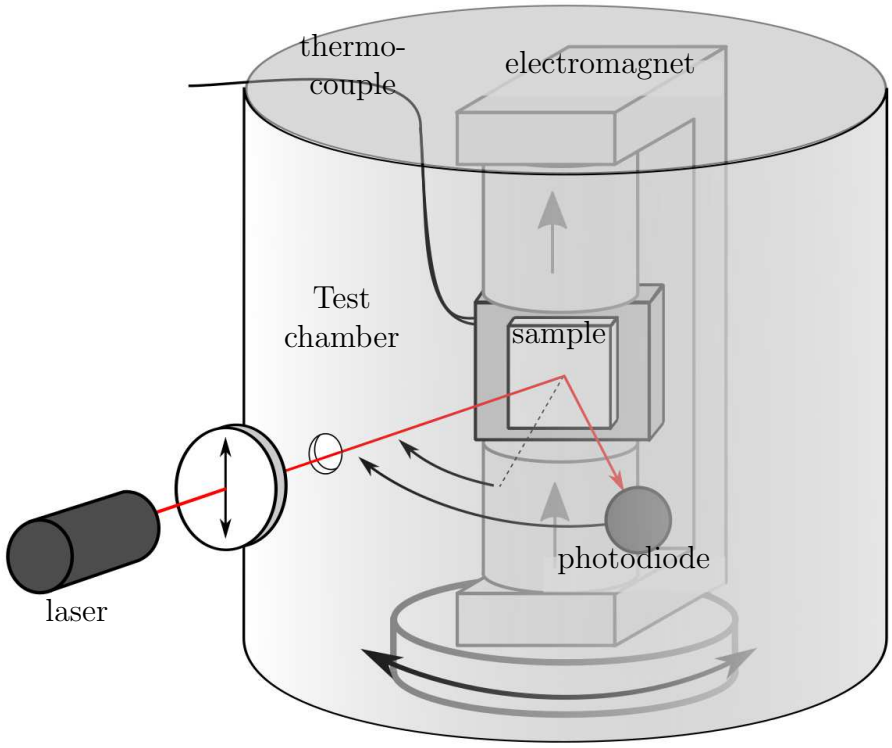

Figure 6.1: Experimental setup used for characterization of index of refraction under the influence of magnetic field and temperature.

positioning to $\pm 0.01^{\circ}$ between readings and index characterizations. This yields a $\pm 4\,\%$ uncertainty in base index measurements, but a $\pm 0.04\,\%$ relative uncertainty or $\pm 0.08\,\mathrm{mRIU}$. Before and during each index test, the electromagnet applied a constant magnetic field with values ranging from $-2.9\,\mathrm{kOe}$ to $2.9\,\mathrm{kOe}$. The sample's temperature was tracked using a surface mounted thermocouple attached to the sample's aluminum holder.

6.3 Modeling

As the experiment involved thin films, a modeling effort was conducted to understand thin film interference. An undergraduate engineering student, Adam Garcia, was engaged to lead this aspect of the research. The goal was to predict analytically how changes in the index of the thin film would manifest in the experimental setup, and mirror the experimental setup. Initially, a bulk reflectivity equation 6.1 was used for index fitting to the raw data, and this would help 'scale' the result of that study. The results shown for the experimental work in

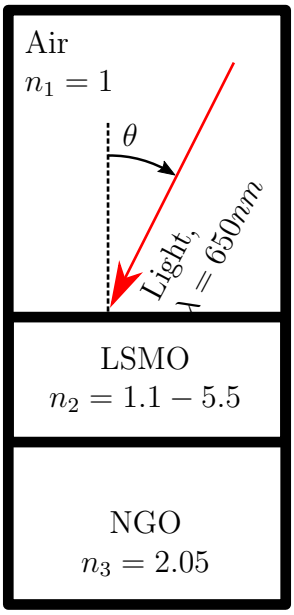

Figure 6.2: In the developed COMSOL Multiphysics FEA software (COMSOL) model, the reflection off of the model of LSMO film on NGO was modeled at different angles, θ. This was repeated as the index of the LSMO film was varied from 1.1 to 5.5, and the laser's angle of incidence was swept for each index condition.

this thesis now use the thin film and correct reflectivity equation 6.2 uncovered in literature over the course of this section of work.

6.3.1 Model development

Shown in Figure 6.2 is a modified reflectivity model which was created in the finite element software COMSOL. It is an adaptation of the "Fresnel Equations" model (COMSOL Application ID: 12407). This utilizes the RF module in COMSOL. A mesh refinement study was run. The LSMO layer's index was set to be variable. The angle of incidence was varied during tests to reflect the actual physical multiple-angle-of-incidence (MAI) setup. For optical modeling, the index of NGO at 633 nm was set to 2.05 [99].

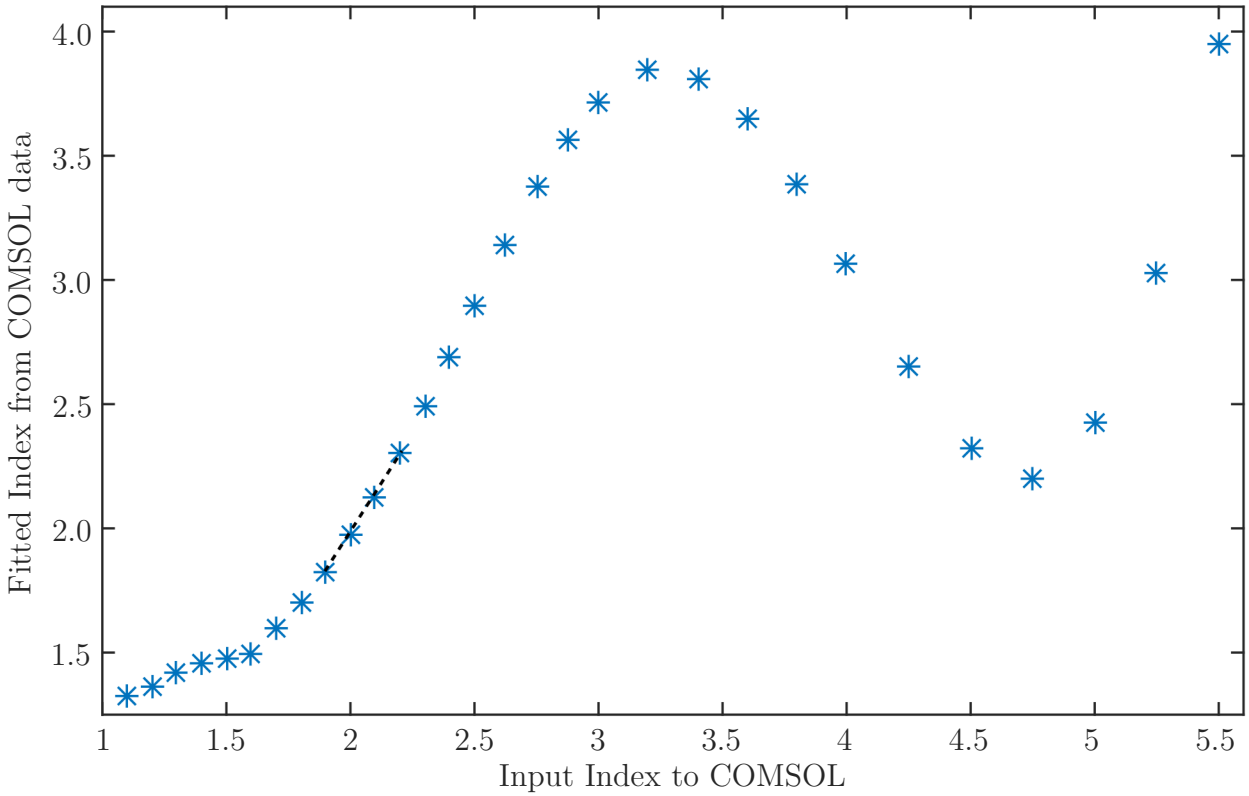

Figure 6.3: Using the resulting reflectivity vs. angle data from the COMSOL model shown in Figure 6.2 and the Eq. 6.1, the index of refraction of the film was then found, represented by the "Fitted Index" axis. This is plotted vs. the input index for n_2 (the LSMO layer). LSMO has a nominal index near 2.12 [72]

6.4 Modeling results and discussion

The results of the study are shown in Figure 6.3. The independent x-axis is the input index to the COMSOL model. The dependent variable is the fitted index of refraction from a bulk reflectivity equation. If our fitting equation was a perfect representation of the setup, then these points would fall on a straight line. As they do not, this shows that our simple bulk fitting equation, Eq. 6.1, is not representative of the system. This advanced our understanding of the test, showing clearly that thin film nature needed to be considered. While there is a non-linear correlation between the "fitted index" and the "input index", found by using the bulk reflectivity Eq. 6.1, in a given local 0.1 RIU region a linear correlation is valid. This allows for local correlation of a shift in detected index to shifts in real index if

the region of the real index is already known. The bulk reflectivity is given as,

$$R = \left(\frac{n_2^2 cos(\theta) - n_1 \sqrt{n_2^2 - n_1^2 sin(\theta)^2}}{n_2^2 cos(\theta) + n_1 \sqrt{n_2^2 - n_1^2 sin(\theta)^2}} \right)^2 \tag{6.1}$$

where n_k is the index of the k^{th} layer, starting with air, and assuming that there is just air and LSMO in the model. Thus, this is a two layer model of infinite thickness.

LSMO is expected to have an index around 2.12 [72] to 2.38 [13]. In the modeling data of Figure 6.3, the slope between detected change in index vs. the real change (which is inputted to the model) is 1.76 RIU/RIU for this region. This may be used as a conversion metric from data fitted using the bulk optics model to what the real change in index is. Thus, a detected sensitivity of $1\,\mathrm{refractiveindexunitperabsoluteGauss(RIU/G)}$ would really be $0.57\,\mathrm{RIU/G}$.

Given the experimental conditions of a thin film and variable angle laser incidence, the higher fidelity expression for reflectivity must be dependent on layer thickness as well as existing indices and angle of incidence. The general expression for this was developed by Cook in 1948 [15], and a modified version of it is Eq. 6.2,

$$R = \frac{r_{12} + r_{23} * e^{i2\phi_2}}{1 + r_{12} r_{23} * e^{i2\phi_2}} \tag{6.2}$$

with R being the net reflectivity off of the first boundary, that of air to LSMO. r_{kk+1} is the reflectivity from k to k+1, k being the layer number from the top, and defined in Eq. 6.3. ϕ_k is the phase lag and defined in Eq. 6.4. r_{kk+1} is similar to Eq. 6.1 but defined as,

$$r_{kk+1} = \frac{n_{k+1} c_k - n_k * c_{k+1}}{n_{k+1} c_k + n_k * c_{k+1}} \tag{6.3}$$

with n_k as the index of the k^{th} layer, and c_k is light's path, defined in Eq. 6.5. The ϕ_k from Eq. 6.2 is the phase lag induced in the material, defined by

$$\phi_k = -2\pi * n_k * c_k * d_k * \lambda^{-1} \tag{6.4}$$

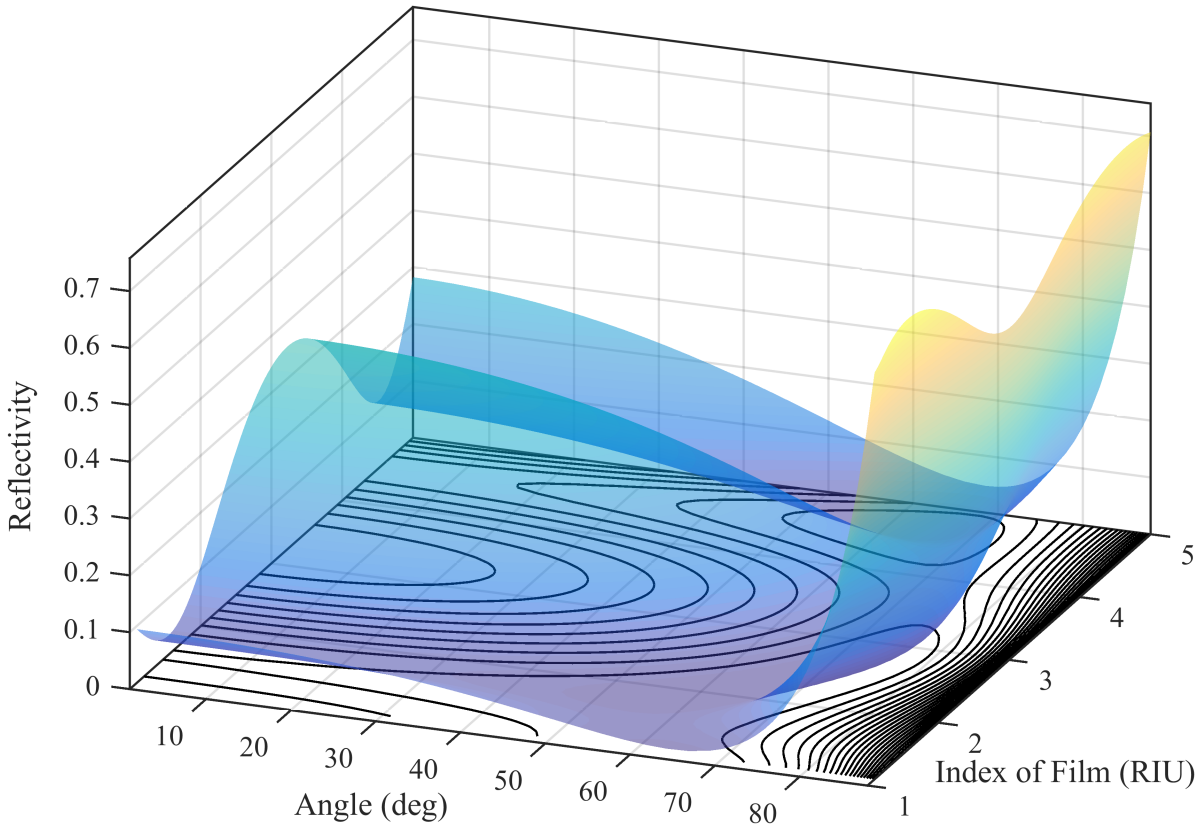

Figure 6.4: The reflectivity of a thin film on a substrate, given a varying angle of incidence, and film index of refraction. This is based on modeling the formula of Eq. 6.2 for angles 1 to 88 and indices from 1.1 to 5.

ϕ_k also utilizes the light's path, c_k, which is angle and index dependent,

$$c_k = -i\sqrt{(n_1 * sin(\theta)/n_k)^2 - 1} \tag{6.5}$$

where k=[1,2,3] represents air, LSMO and NGO respectively, while d_k are their respective thicknesses. λ is the wavelength of light, in the same units as d_k. Finally, θ is the angle of incidence from air onto the sample. The equations have been reduced by assuming that n_1 = 1.

Figure 6.4 plots the reflectivity for varying index and angle of incidence (the relevant variables for the experiment) using this Eq. 6.2. Interestingly, depending on the angle and film index (for a fixed thickness), increasing the index of refraction may increase or decrease

the sample's reflectivity. This is due to interference within the film, as both the top and bottom interfaces of the LSMO film reflect, and these two reflections interfere. The first reflection is from the film-air interface. The second reflection is off of the film-substrate interface. This second reflection of light passes through the film, and that passage adds a phase lag to that reflection. This lag is dependent on the optical path length. Optical path length is dependent on index of the material, thickness, and angle of the path through that thickness. Thus, the phase of the second reflection is dependent on the index and thickness of the material, and the angle of the light. When the two reflected electromagnetic (EM) waves meet again they may constructively or destructively interfere. This manifests as a higher or lower net reflectivity.

This new Eq. 6.2, which incorporates the thin film geometry, predicts the same reflectivity as seen in COMSOL. Using the equation to fit test data proved difficult, so test data was still fit to the bulk reflectivity value, and then the sensitivity was corrected with the bulk to thin film model correlations, as seen in Figure 6.3.

6.5 Experimental results

The MAI ellipsometer showed that LSMO changes its index with magnetic field. When fitting raw data using the correct thin film reflectivity equation, 6.2, the index is found to change by $-1.6\,\mathrm{mRIU/kOe}$.

6.5.1 Transverse MAI ellipsometry results

Figure 6.5 shows one set of data which will be focused on for the majority of this section. In it are displayed the field and temperature conditions of a given index of refraction characterization per characterization for over 1200 characterizations performed over many hours. The Index is seen to correlate with the temperature of the characterization. There are periodic outliers. The magnetic field does not at first seem to play a significant role in index of refraction. The magnetic field applied increases over time, seemingly with temperature, but actually drives the temperature.

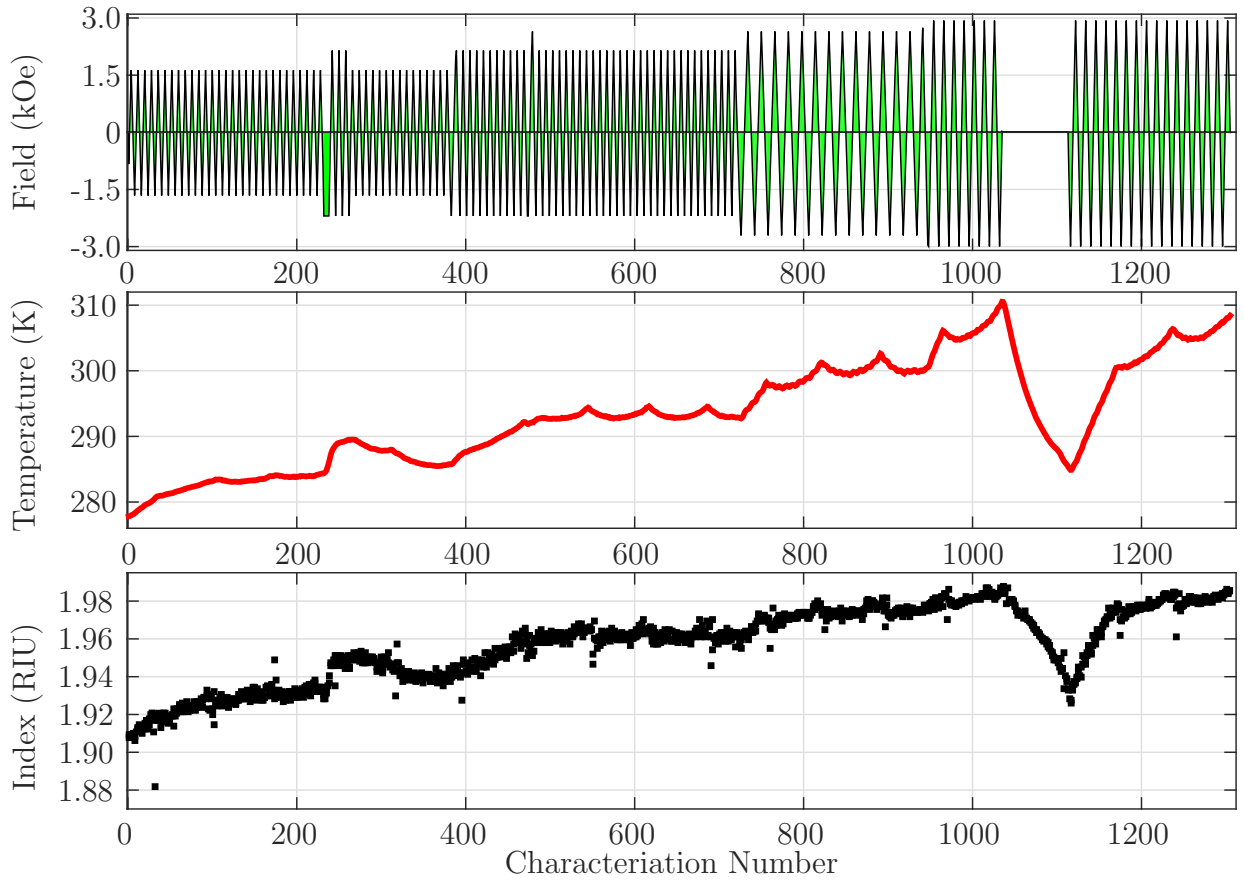

Figure 6.5: Magnetic field applied with temperature measured during the test, and the fitted index of each test over time.

The electromagnet at the center of the MAI setup, as seen in Figure 6.1, has 10 Ω resistance, allowing it to act as a joule heater while also applying magnetic field. The heat produced, W is proportional to the square of current, I, while the magnetic field H applied is proportional to current (as well as turns of the wire N and the permeability of the area μ).

$$W = R * I^2 \tag{6.6}$$

$$H = N * \mu * I \tag{6.7}$$

As seen in Figure 6.5, when reaching high fields, the setup readily heats up. This requires that any lower temperature (refrigerator-temp) testing be performed at low magnetic fields. A new thermal equilibrium is reached over time for each step in field strength. While using the commercial air conditioning unit (ACU) in this fashion, the restricted air flow causes

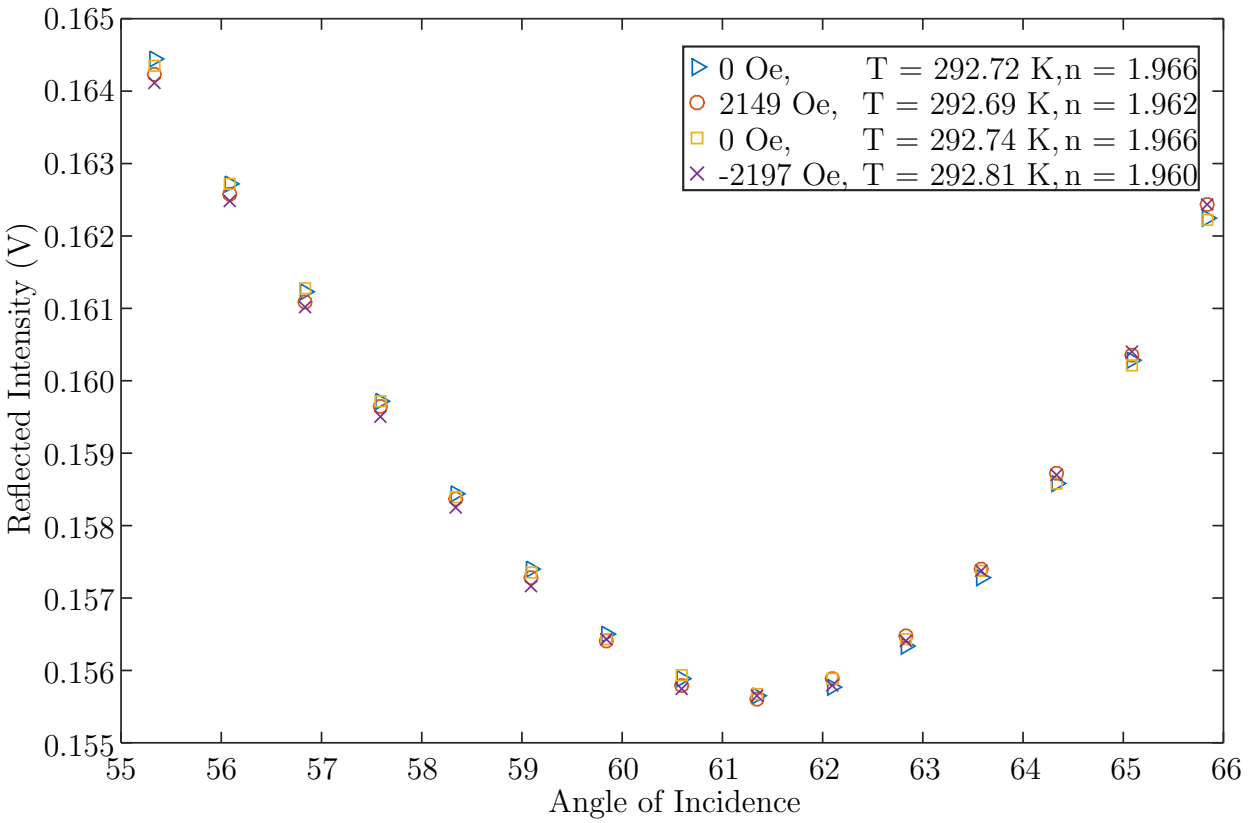

Figure 6.6: An example of three passes in sequence of testing, all at 293.3 K with various fields applied. When fitting, the indices listed on the legend where found.

the ACU intake to periodically ice over. This triggers the ACU to turn off, melting the ice, and then drawing very moist air into the setup. The 19 regions of the data when the ACU had this problem manifest in the data as a local peak in temperature. These icing events correlate to when the found index of LSMO is seen to dip or spike, approximately every 60 tests.

Figure 6.6 shows reflectivity vs. angle for four readings. This experiment was designed to understand the index of refraction's sensitivity to magnetic field. To measure the index of refraction, reflectivity measurements must be taken at various angles of incidence. To understand the effect of magnetic field on the sample's refractive index, the magnetic field is changed, and the index of refraction test is repeated. To confirm that there are no other 'odd' effects being measured (such as the Kerr effect, or erroneous mechanical phenomenon), the field is varied in both directions. The MRE is an 'even' phenomenon, and thus should

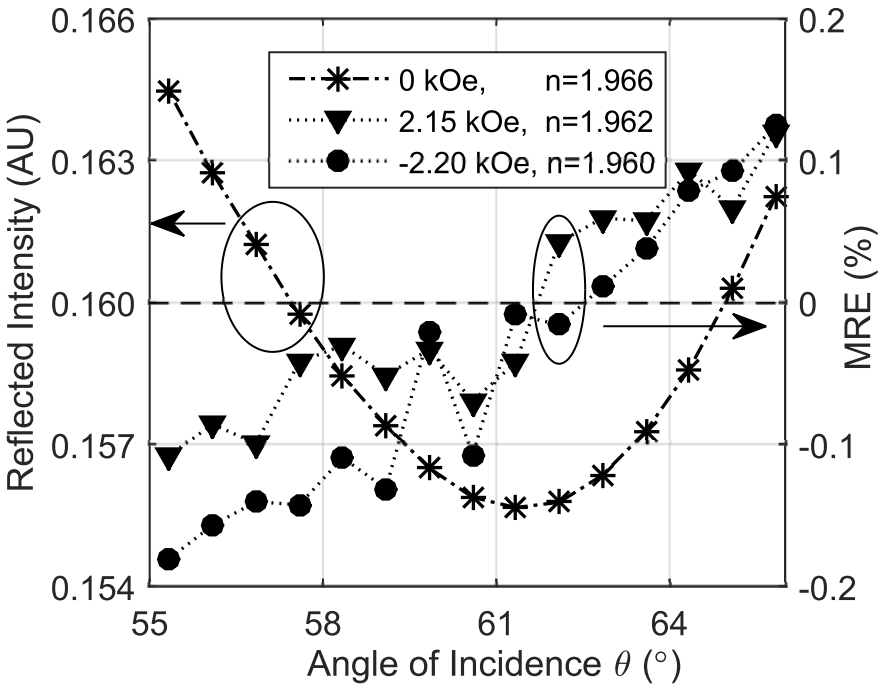

Figure 6.7: Reflected Intensity and MRE of 633 nm light vs. angle for three passes at different magnetic field conditions. The reflected intensity for no applied field is plotted using the left axis, and the change in reflectivity with applied field is quantified as MRE for the two applied field conditions, and plotted with the right axis.

respond to the absolute magnetic field strength, independent of field polarity [102]. It can be seen in Figure 6.6 that applying a magnetic field in either direction for a small angle of incidence reduces the sample's reflectivity.

Figure 6.7 shows room temperature data taken using a 633 nm light source with the test setup shown in Figure 6.1. The data represented with asterisks is the reflected intensity (i.e. left axis) vs. angle without an applied magnetic field. All tests were conducted near the Brewster's angle (61.5°) to improve the index of refraction measurements. The reflected intensity data shows a continuous and smooth reflectivity vs. angle relationship. The index of refraction is 1.966 RIU, determined from a fitting function using a mono-film reflectivity equation [15] using only real values. In this calculation, the substrate index was 2.12 RIU. The data represented by triangles and circles in the figure are MRE (i.e. right axis) vs. angle for applied magnetic fields of 2.15 kOe or −2.2 kOe respectively. These MRE values were calculated from reflected intensity measurements performed as a function of angle of inci-

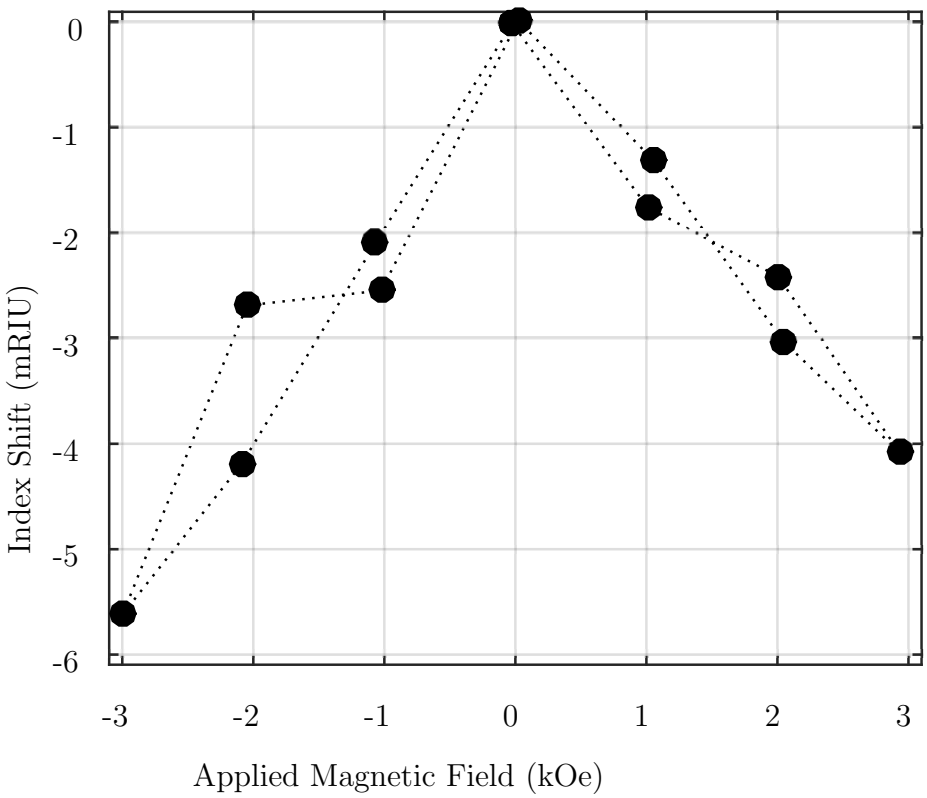

Figure 6.8: Index Shift vs. Applied Magnetic Field for 13 characterizations cycled from 0 kOe to −3 kOe, then 3 kOe to 0 kOe, with temperature rising from 288 K to 292 K during the cycle.

dence, i.e. similar to the asterisks' data. As can be seen, the MRE values follow a linear trend from negative values below the Brewster's angle to positive values above [44]. The calculated index of refraction is 1.962 RIU at 2.15 kOe while for −2.20 kOe it is 1.960 RIU. Both of these index of refraction values are smaller than that measured at 0 kOe.

Figure 6.8 shows index shift relative to the index measured at H=0 kOe as a function of magnetic field for the 633 nm light source at 290(2) K using similar test data to that presented in Figure 6.7. The index decreases in a linear manner for both positive and negative applied magnetic fields. The average slope in Figure 6.8 defines the index of refraction's magnetic sensitivity, which is calculated to be −1.58 mRIU/kOe for both positive and negative magnetic fields.

Figure 6.9 shows the index of refraction's magnetic sensitivity as a function of tempera-

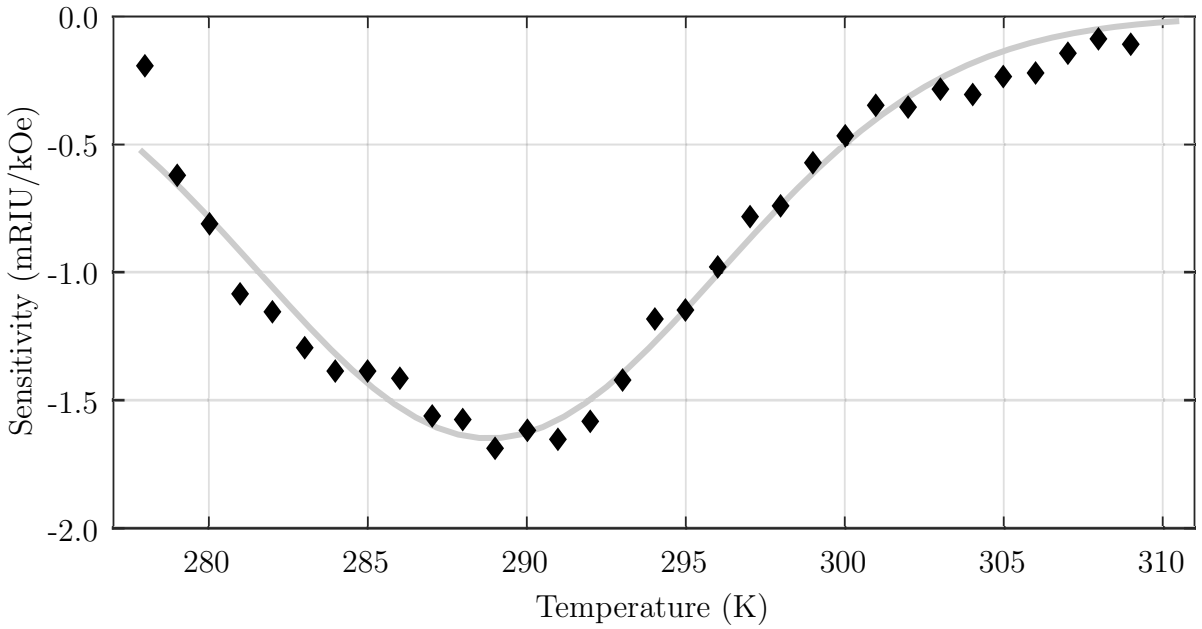

Figure 6.9: Sensitivity vs. Temperature, and fitted line using a Gaussian model for sensitivity.

ture. A Gaussian model defined by

$$\frac{dn}{dH} = \alpha \exp - \left(\frac{T_\alpha - T}{T_s} \right)^2 \tag{6.8}$$

can be fitted to the data producing values of peak sensitivity $\alpha = -1.6\,\text{mRIU/kOe}$, peak sensitivity temperature $T_\alpha = 288.8\,\text{K}$, and the temperature span $T_s = 10.2\,\text{K}$. The proximity of T_α to the materials T_M at this wavelength of light as identified in Figure 5.4 is expected since the MRE arises from index of refraction changes. Thus, the location of the maximum MRE should correspond to the maximum sensitivity of the index of refraction to an applied magnetic field as shown in Figure 8. The magnitude of the magneto-optical coefficient α in equation 6.8 is 120 times larger than and opposite in sign to that of water's, which is reported to be 0.013 mRIU/kOe for 633 nm light [48].

Figure 6.10 shows the index of refraction vs. temperature for tests performed at zero magnetic field. In general, the index of refraction increases with temperature, however there is a distinct change in slope. To better understand this slope change, a fitted index of

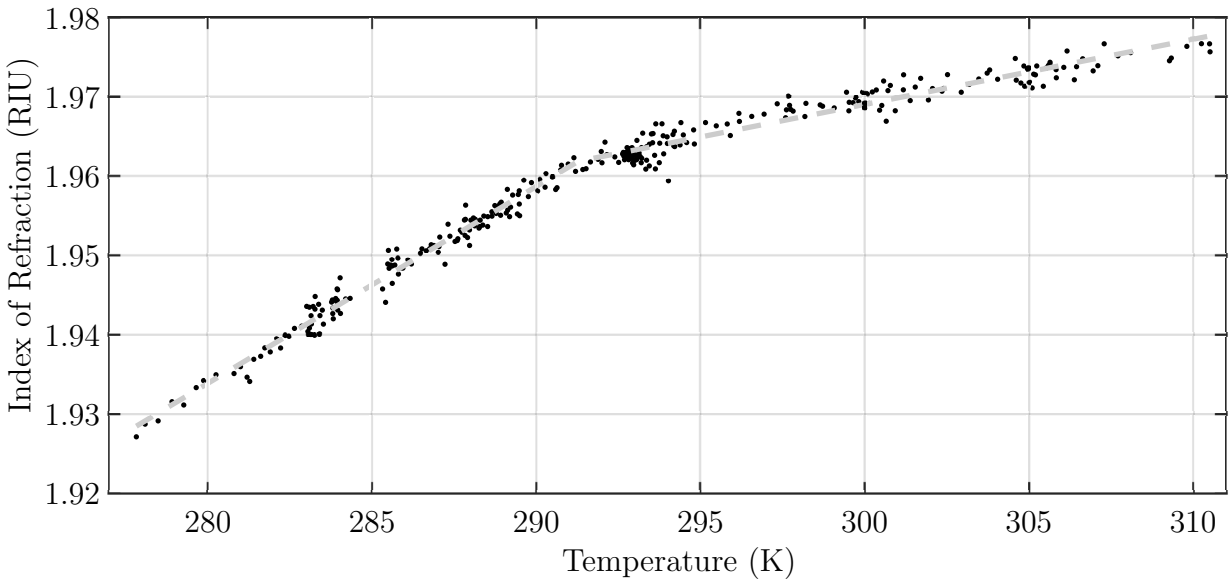

Figure 6.10: Index of refraction vs. temperature for characterizations performed with H=0 kOe.

refraction model is plotted over the points using an equation

$$n = n_T + (T - T_T)\frac{dn}{dT} \tag{6.9}$$

with transition temperature's index of refraction n_T=1.962(80) RIU, T_T is the transition temperature 291.3 K, and where the thermo-optic coefficient $\frac{dn}{dT}$ is defined as

$$\frac{dn}{dT} = \begin{cases} \beta_F & T < T_T \\ \beta_P & T \geq T_T \end{cases} \tag{6.10}$$

where β_F is the low temperature thermo-optic coefficient equaling 2.5 mRIU/K, and β_P is the higher temperature thermo-optic coefficient equaling 0.8 mRIU/K. This slope change at T_T aligns with the material's T_C. This indicates that the magnetic phase change, i.e. ferromagnetic β_F to paramagnetic β_P, influences the electronic structure and thermo-optic coefficient.

Table 6.1: Optical coefficients and temperatures for equation 6.11

Variable	Name	Value	Figure
n	Index of refraction		
n_T	Index of refraction at T_T	$1.962(80)\,\mathrm{RIU}$	6.10
α	MRE magneto-optic coefficient	$-1.6\,\mathrm{mRIU/kOe}$	6.9
T_s	Temperature span of MRE	$10.2\,\mathrm{K}$	6.9
T_α	Peak magneto-optic temperature	$288.8\,\mathrm{K}$	6.9
T_T	Thermo-optic transition temperature	$291.3\,\mathrm{K}$	6.10
β_F	Ferromagnetic thermo-optic coefficient	$2.5\,\mathrm{mRIU/K}$	6.10
β_P	Paramagnetic thermo-optic coefficient	$0.8\,\mathrm{mRIU/K}$	6.10

6.6 Discussion of results

Combining the magnetic and thermal effects correlations, a unified index of refraction function can be presented for LSMO for the first time.

$$n(H,T) = n_T + |H|\alpha \exp - \left(\frac{T_\alpha - T}{T_s}\right)^2 + (T - T_T) \begin{cases} \beta_F & T < T_T \\ \beta_P & T \geq T_T \end{cases} \tag{6.11}$$

with the values of each variable given in Table 6.1 for 633 nm light. It is expected that n_T, α, β_F, β_P, and T_s may shift with wavelength. It is not expected that T_α will drastically change with wavelength though. This work addressed the index of refraction of LSMO as only a real value. From literature there is an expectation that the index of refraction in LSMO is complex [72]. The index changes found here then may be shared by both the real and imaginary components. It is likely that the imaginary dielectric constant is the root of the shift characterized in this study.

The peak magneto-optic temperature, T_α, is nearly identical to T_M for 633 nm light, at 288.8 K and 288.3 K. Two separate thermocouples were used to find those experimental values on the same sample, and it is expected that in the material, $T_\alpha = T_M$ in practice. The point of maximum susceptibility and magnetic phase change, T_C, is enabling the electronic structure of LSMO to be strongly influenced by magnetic field via multiple mechanisms. As T_T divides the para- and ferro- phase's thermo-optic responses, it is not surprising that it aligns with T_M and T_α too. As these temperatures (T_M, T_α, and T_T) were all measured

to be nominally similar, and theorized to originate from the same thermally induced high susceptibility, these temperatures may all be the same, T_C. An average of 290 K could replace them to ease use of the index equation until further optical measurements can be made. Whichever mechanism is dominating at a given wavelength will still be localized around that T_C. Strongly applied magnetic fields may shift the T_C to complicate the above characterization, but this contribution will be on the 0.2 K/kOe scale. High applied fields may also increase the T_s in the material and appear to broaden the MRE results at a 1 K/kOe scale.

Though only one test (the largest conducted) has been highlighted here and carefully walked through, tests performed while developing this one showed similar results. Shown in Figure 6.11 is a characterization performed using a power supply only able to apply current in one direction, and using a liquid nitrogen based chiller instead of the ACU. It shows nearly the same α, -1.7 mRIU/kOe, a T_s of 8.9 K, and a T_α of 287.2 K.

Shown in Figure 6.12 is another characterization performed the same week as Figure 6.11. It shows nearly the same α, -1.5 mRIU/kOe, a T_s of 12.2 K, and a T_α of 285.0 K.

6.7 Conclusion

This chapter describes the index of refraction of LSMO under applied magnetic field and room temperature. Of note is the characterization of the MRE's role in affecting the index of refraction to decrease with applied magnetic field. The impact of the magnetic phase change on the thermo-optic coefficient was unexpected, but easily understood. Further research addressing the complex index of refraction of LSMO should be pursued.

The exit criteria for Step 1 of this magnetic fiber Bragg grating (MFBG) road map shown in Figure 4.18 was to characterize the index of refraction's sensitivity to magnetic field. This was done, and in the process, other working conditions such as peak wavelength to utilize and temperature region were identified. With the exit criteria for Step 1 achieved, the second step of the MFBG project was next perused.

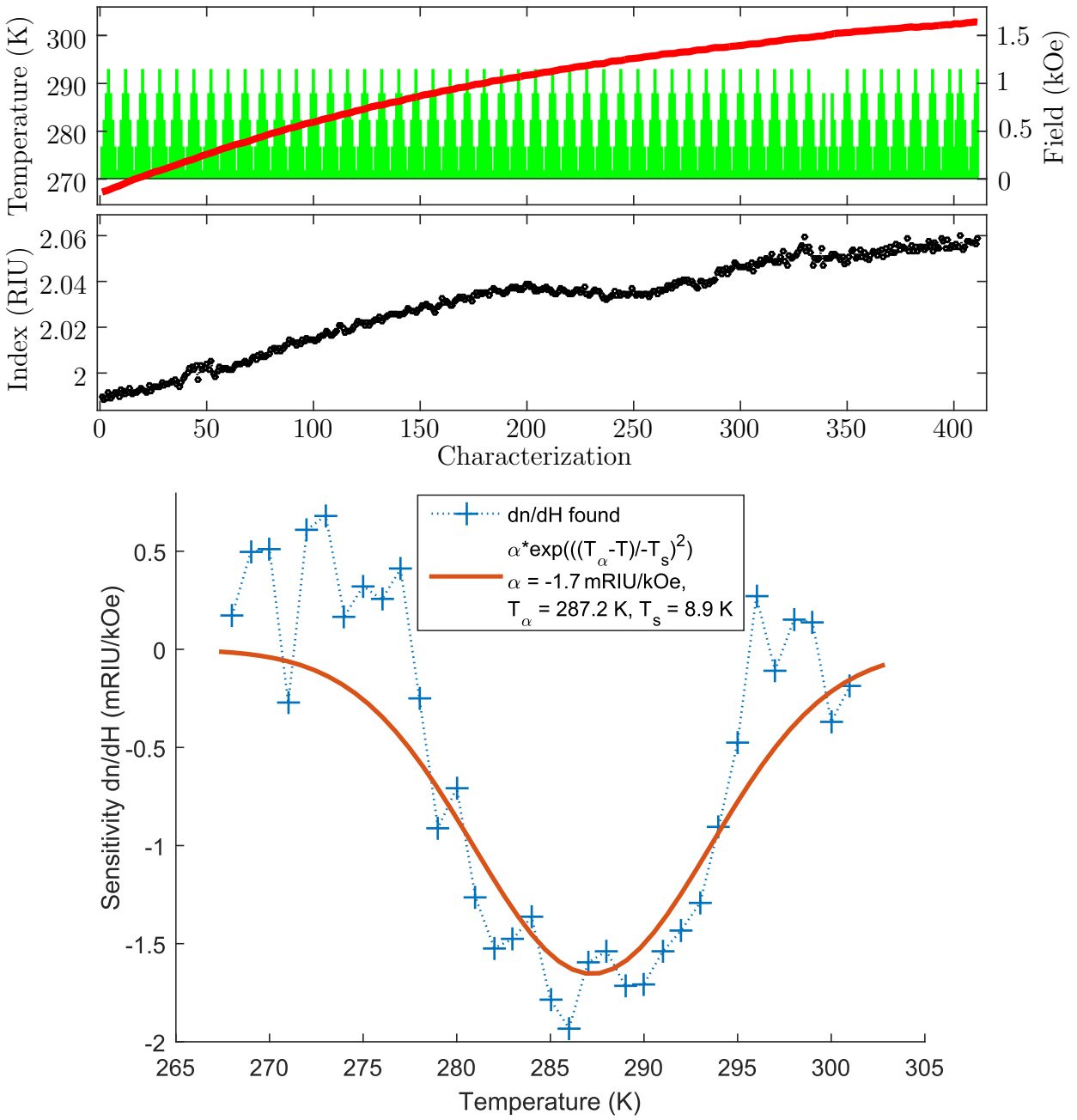

Figure 6.11: Top: Summary of Index of refraction found for various magnetic field conditions over a span of temperatures. Bottom: Sensitivity vs. temperature and Gaussian model fitting of the data showing a peak sensitivity α of $-1.7\,\mathrm{mRIU/kOe}$

Chapter acknowledgment

The author would like to thank the AERO Institute and NASA Armstrong for supporting this work. The author would also like to thank Kang Wang of Department of Electrical

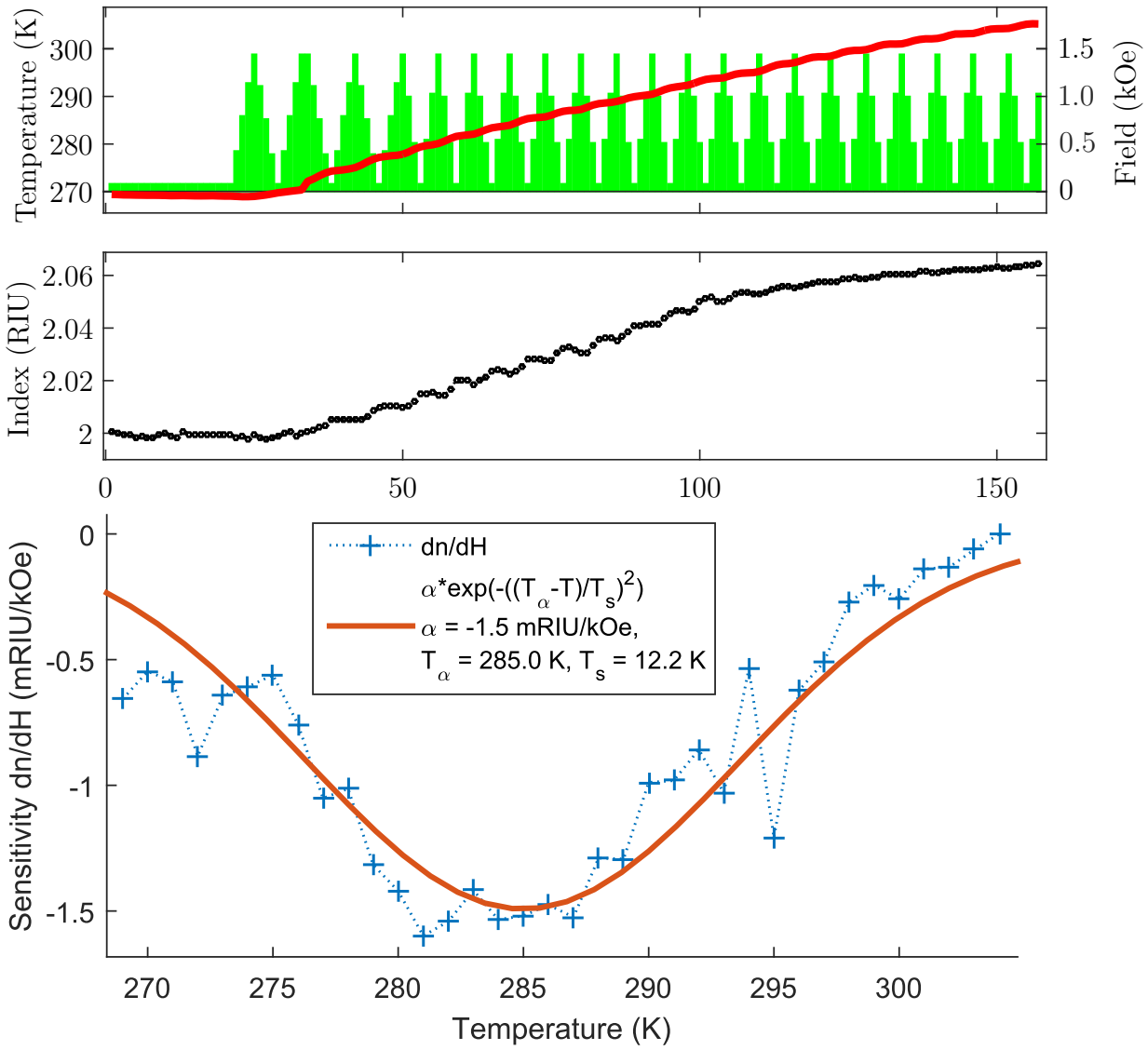

Figure 6.12: Top: Summary of Index of refraction found for various magnetic field conditions over a span of temperatures. Bottom: Sensitivity vs. temperature and Gaussian model fitting of the data showing a peak sensitivity α of $-1.5\,\mathrm{mRIU/kOe}$

Engineering, University of California, Los Angeles for use of his magneto optical Kerr effect (MOKE) setup. The author would like to thank Darrell Schlom and Carolina Adamo of Cornell for the LSMO sample. Finally, the author would like to thank NASA Kennedy Space Center for feedback and support of the follow-on steps in the MFBG project.

CHAPTER 7

MZI

7.1 Introduction

This chapter summarizes the progress of Step 2 of the magnetic fiber Bragg grating (MFBG) project supported by the NASA Kennedy Space Center (KSC)'s Launch Services Program (LSP). Step 2 of the MFBG project focused on fabricating and characterizing an MZI sensor to assess its sensitivity and potential use as a magnetometer. Experimental characterization indicates that the exit criteria have been achieved and that the stretch goal of the next step, 1 G sensitivity, could have been possible, if not for further issues encountered in that step.

7.1.1 Project's Goal

This report focuses on fabricating and testing an Mach Zehnder interferometer (MZI) sensor for potential use as a sensitive magnetometer based on index of refraction changes seen in Lanthanum Strontium Manganite $La_{0.66}Sr_{0.33}MnO_3$ (LSMO) and covered Chapter 6 and defined by Equation 6.11.

7.1.2 MZI Goal

The statement of work for this chapter was to create an MZI sensor sensitive enough to detect the magnetorefractive effect (MRE) present in LSMO when it is deposited onto the MZI in the next step of this project. Here it is important to remember and understand that the final goal of this project is to create an magnetic fiber Bragg grating (MFBG) sensor which can detect 0.1 G fields, the order of magnitude of Earth's magnetic field. However,

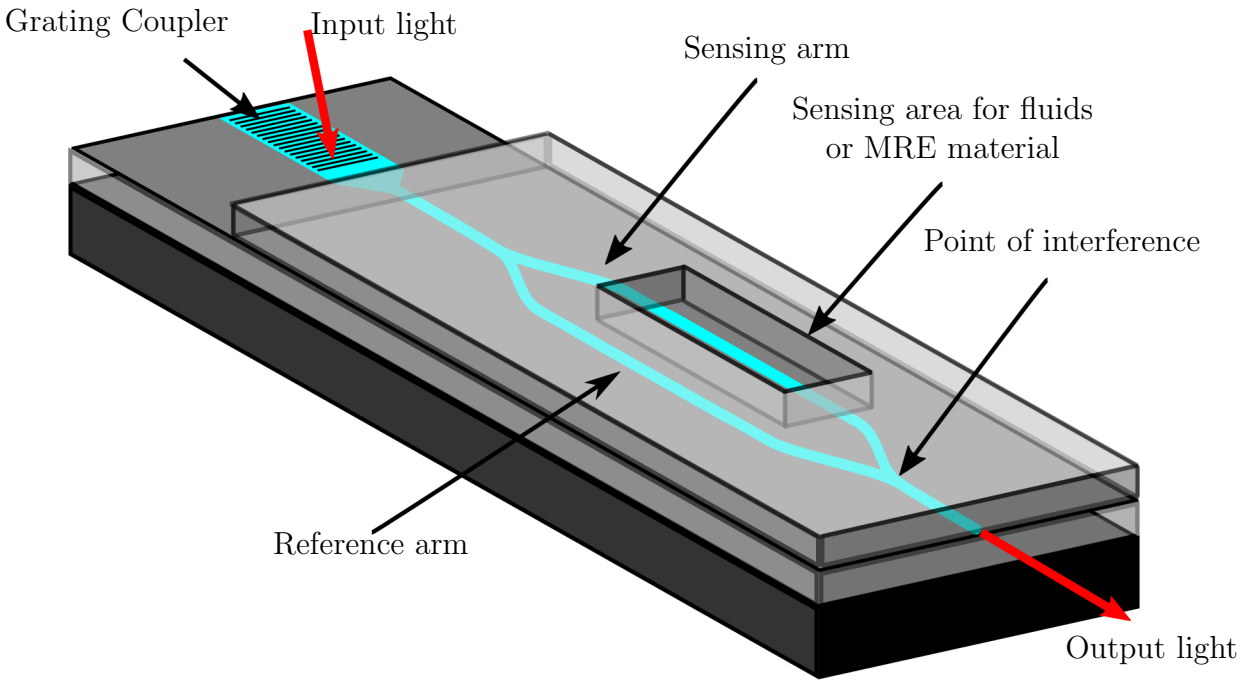

Figure 7.1: A diagram of the developed MZI.

prior to creating a fiber Bragg grating (FBG) sensor with LSMO in the core, we will first focus on demonstrating the concept using a MZI sensor. Thus, the MZI sensor has a different exit criteria than the planar or FBG sensor would later.

The exit criteria for step 2 were drafted, considering the needs of the magnetic MZI sensor. Assuming that the sensitivity of the LSMO is 1.6×10^{-6} RIU/G (i.e. index change per unit gauss), we can back calculate what is required to measure our MZI exit criteria, which is 1 G. This calculation consists of 1.6×10^{-6} RIU/G * 1 G and results in a required sensitivity of our MZI of 1.6×10^{-6} RIU. That is the MZI must be sufficiently sensitive to detect a change of index by 1.6×10^{-6} RIU.

7.1.3 MZI

Figure 7.1 shows an illustration of a typical MZI including grating coupler, sensing region and output region. The design shown in Figure 7.1 was previously developed by Prieto et al. [94]. The grating coupler shown in the figure increases the amount of light entering the MZI and produces a superior signal to noise ratio by a 10x factor. Once the light is introduced into

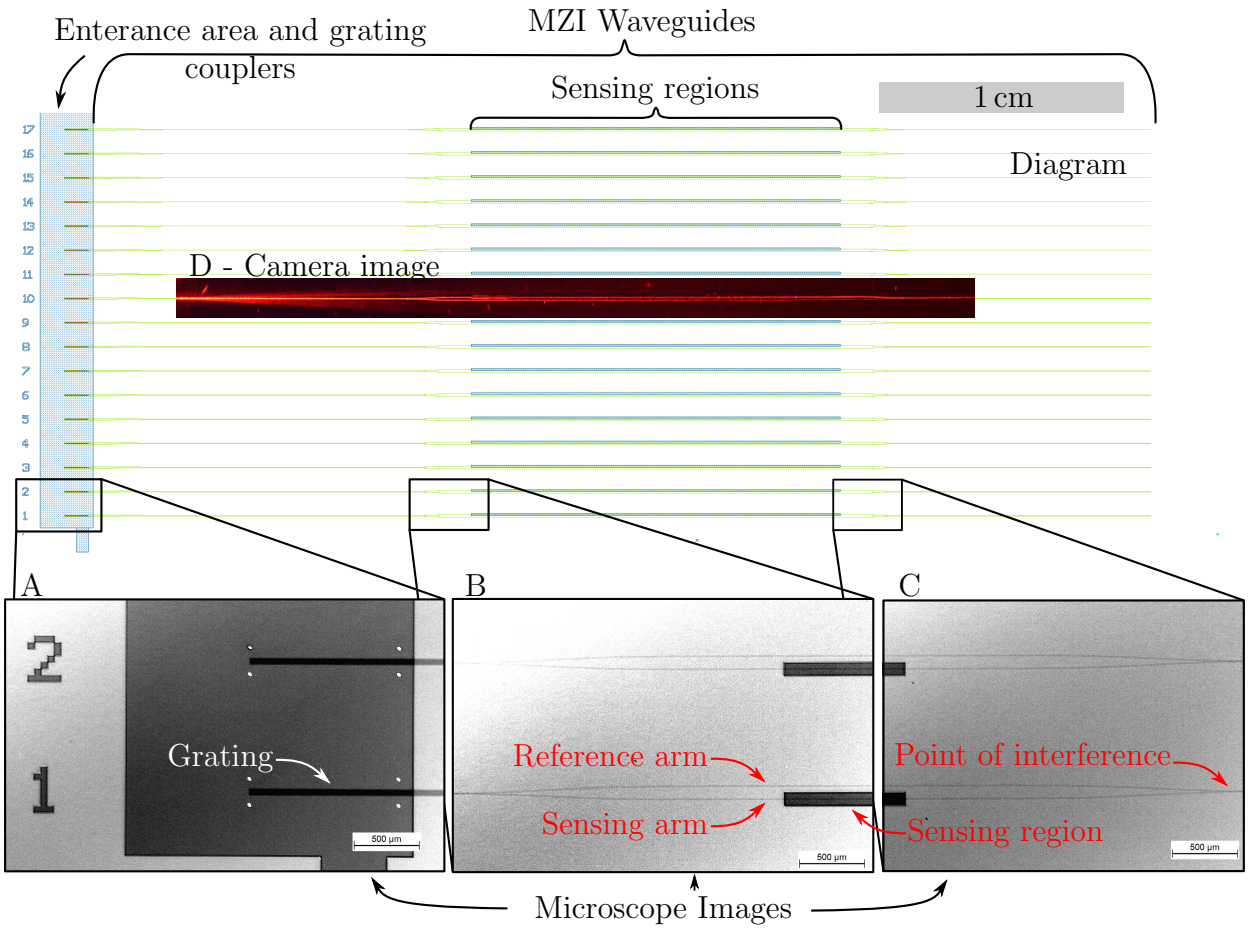

Figure 7.2: Diagram of the MZI with images of fabricated important regions.

the grating coupler, it travels toward the sensing and reference arm branches. After passing through these two branches it exits the MZI and is measured. Below, we provide a brief description of the operational principles of the MZI and its relationship to the magnetic field MZI we are working on.

The proposed MZI measures relative shift in phase between two light paths, referred to as the sensing arm and reference arm shown in the figure. Since the two arms split from a single input source, the light in each arm initially has the same phase. The light that travels through the sensing arm experiences a relative optical path length change due to the light interacting with fluids or materials in the region marked "sensing area for fluids or MRE material" in the figure. The optical path length change is directly related to the effective optical index produced by the material in the sensing region. The effective optical length is a function of what is in the sensing area due to light's evanescent field interacting with

it. When the light traveling along the two paths recombine at the "point of interference" as shown in the figure, they may have a different phase from one another. This produces either a constructive or destructive interference, when the light exits the "output light" regions shown in the figure.

In this step, the MZI is fabricated without LSMO. The purpose of this step is to create a base MZI device and measure its sensitivity (see previous section exit criteria). This measurement provides proof of principle to continue with the LSMO based sensing later. For this step, we use fluids as the medium in the sensing area to modify the effective path length described in the preceding paragraph. In these tests, we measure the output light's intensity oscillations as a function of time and the fluid added. From these measurements, we can determine the MZI sensor's sensitivity and relate it to the exit criteria described in the preceding section.

7.2 MZI fabrication, test setup, and test fluids and modeling

This section describes the fabrication, and characterization, for the MZI. The MZI was made in the UCLA clean room facilities and the characterization setup was built in the Active Materials Lab on an optical table. The test fluids were common glycerin (from a local drug store) and water. The model of the MZI's waveguides was developed in the Active Materials Lab using COMSOL's "Electromagnetic Waves, Frequency Domain" package. The next section 7.2.1 describes the fabrication which is followed by section 7.2.2 which describes the characterization setup, and section 7.2.4 which describes the model of the waveguide.

7.2.1 MZI wafer fabrication

MZIs were fabricated in UCLA's Integrated Systems Nanofabrication Cleanroom (ISNC) class 100/1000 clean room, part of UCLA's California NanoSystems Institute (CNSI).

Figure 7.3 overviews the fabrication process for the MZI. The first stage was to obtain Si wafers with 2 µm SiO_2 and 250 nm Si_3N_4. The second main stage is to etch a 3(1) nm tall rib

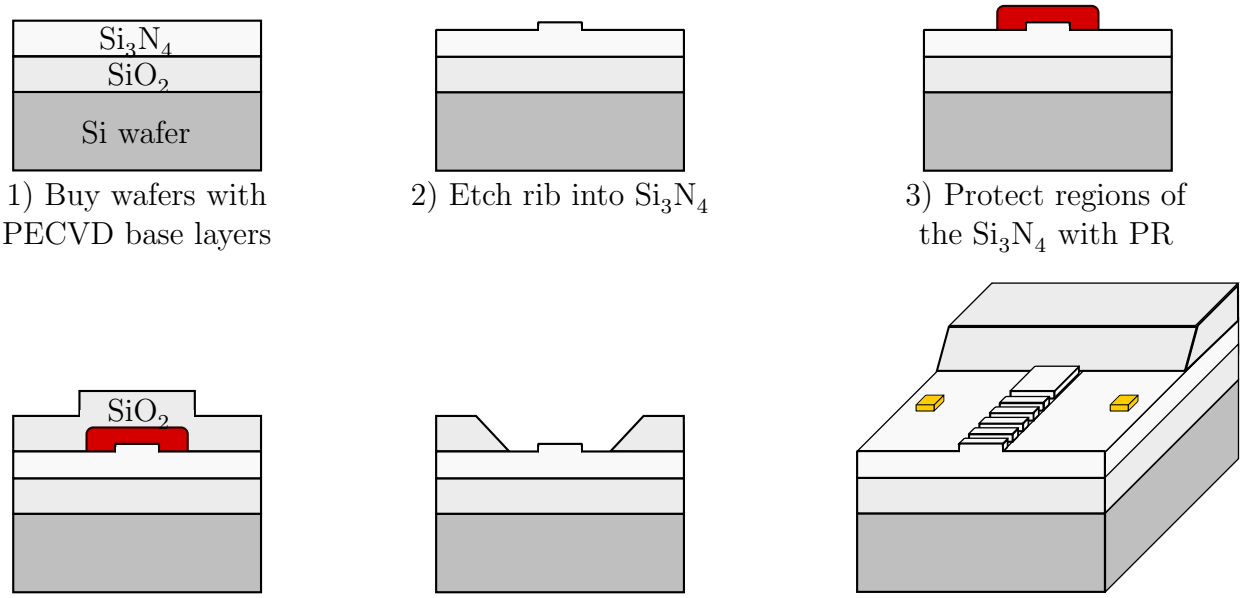

Figure 7.3: Diagram of key fabrication stages for making the MZI. The first six stages show the cross section of the sensing region of the waveguide, as seen in the right edge of the inset B, or the left edge of inset C of Figure 7.2. The last step shows the view of the entrance grating area, which is the region above the scale bar of the A inset of Figure 7.2.

waveguide into the Si_3N_4 top layer. The third stage is to selectively protect the waveguide with a photo resist (PR) pattern to prevent inadvertent etching in stage five. Stage four is to deposit a second SiO_2 layer of 1.5 µm onto the rib waveguide with protectivePR. This top SiO_2 layer is selectively etched away to reveal the PR coated areas of the Si_3N_4 rib waveguide in stage five. These SiO_2 etched regions can be seen in Figure 7.2 as the large dark area and the blocky numbers in inset A, as well as the right dark bars in inset B, and the left dark squares of inset C. The final stage is to add the entrance gratings to couple laser light efficiently into the devices. After removing the protective PR of stage 3, Au is evaporated onto the wafer and patterned with a lift-off process to produce a series of alignment markers for the final lithography step. The markers can be seen in Figure 7.2, inset A as the very small, bright white squares, 20 µm by 20 µm. Electron-beam lithography is used to write a pattern of 400 nm spaced gratings at half intensity. These gratings are etched 55 nm to 75 nm into the Si_3N_4 at the start of the waveguides. After removing the e-beam lithography resist,

the wafers are ready for testing. Further fabrication details are given in the Appendix.

This fabrication process had three significant obstacles that had to be overcome. First, the 3 nm etch to form the rib waveguide was a very shallow etch. Common Si_3N_4 dry etching processes etch rapidly, at nm/s, and are optimized for thick etching steps. To reduce the etching rate and offer finer control, the Oxford etcher's power was reduced from 200 W to 50 W, slowing the etch rate to $0.16\,\mathrm{nm\,s^{-1}}$ and this resolved the first problem. The second obstacle that we encountered was the thick top SiO_2 layer produced a low yield, flacking off wafers. While we could not overcome this issue on every wafer, the approach was to fabricate a sufficient number of wafers to produce useful sensor systems. During this phase, the process yielded 2 functional wafers for every 5 wafers fabricated. Here it is important to point out that the remaining 3 wafers could be rerun through the process. Thirdly, etching through the thick SiO_2 layer to the Si_3N_4 without damaging the waveguide ridge was a problem. A gold layer was tried initially, but this did not resolve the problem. To resolve this problem we used a protective photoresist layer as a barrier to stop etching, which offered an acceptable solution to this problem. While there were other issues that had to be overcome, for the sake of simplicity we have only highlighted the three most critical problems.

Figure 7.2 shows the wafer layout diagram, microscope images, and a camera image of the MZI device with light coupled into it. The wafer layout diagram shows 17 MZI sensors numbered on the far left with a 1 cm scale bar in the upper right for scale. To the right of these numbers (1-17) is the entrance area consisting of the grating couplers, as was previously shown in Figure 7.1. Inset A on the lower left shows a microscope image of the grating area, which is approximately 1 mm long and 50 µm tall. A 500 µm scale bar is provided for the three microscope images (A-C) at the bottom.

Inset B shown in Figure 7.2 are zoomed image of the waveguides splitting into the reference and sensing arms. The upper arm in the image is the "reference arm," and is covered with SiO_2. The lower arm is the "sensing arm" and the SiO_2 layer has been removed from it, which creates the "sensing region" labeled in the figure. Inset C shows images of the two arms joining at "the point of interference." The MZI continues to the right, where the wafer is cleaved to allow light to escape out of the waveguide. Finally, inset D is a camera image of

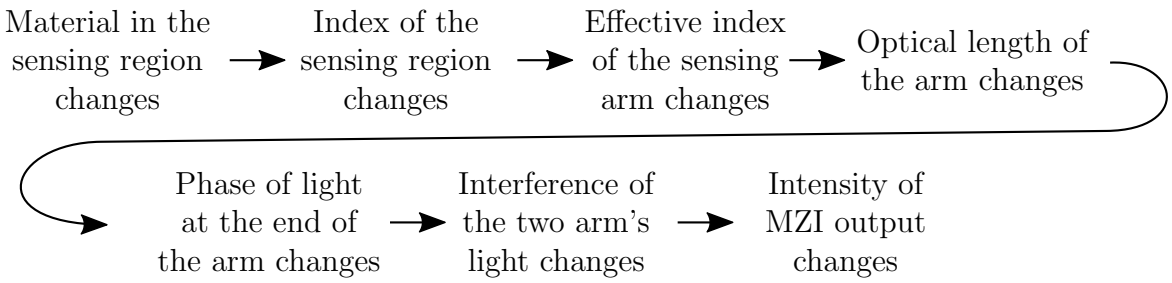

Figure 7.4: Conceptual effect flow of how the fluid in the sensing region effects the output intensity of the MZI.

the MZI with light coupled into it. The thin red line shows the device is in operation. The red light indicates that successful coupling is being achieved within the waveguide. Thus, we have operational MZI structures that we can now test to determine their sensitivity.

7.2.2 MZI testing setup

The MZIs were characterized to evaluate their sensitivity to changes in the index of refraction. Figure 7.4 shows the progression of how changing the material in the sensing region leads to changes in the intensity of the output of the MZI.

Figure 7.5 shows the MZI testing setup with a wafer. The test setup consists of a wafer with MZI, focusing lens, a 45° mirror, an alignment stage of two micrometers, and a photodiode. The general operating principle is to direct light into a single MZI via its grating coupler, and then measure the output intensity from the wafer edge with a photodiode. During this measurement, fluid is introduced into the sensing region to measure the change in signal at the photodiode. Details on the test setup are described below.

The first step in testing is to input the light into an MZI through its input grating. This requires focusing the 5 mW 633 nm laser using the two focusing lens shown in the figure. The lenses are adjusted to maximize the incident light intensity hitting the active area of the grating. These focusing lenses reduce the spot size of the laser light to approximately a 1 mm by 0.2 mm spot size. During this focusing step it is imperative that the laser spot shine

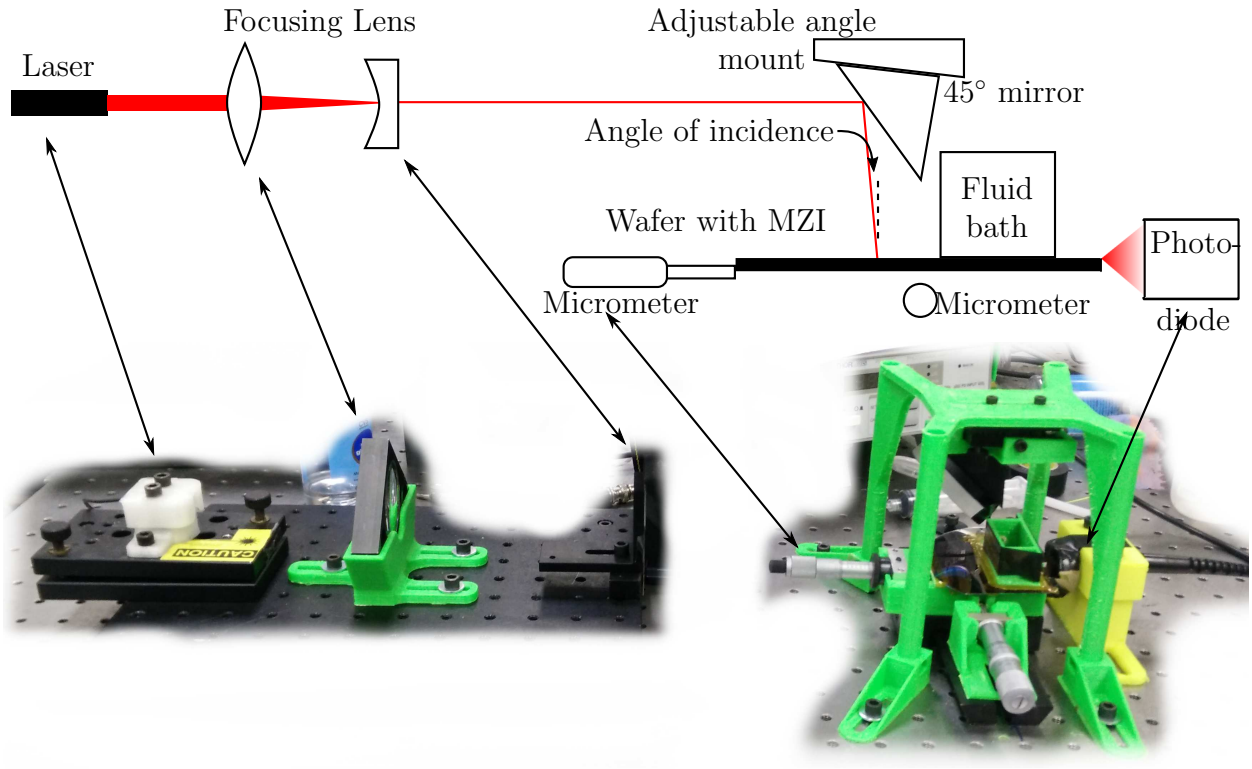

Figure 7.5: The diagram correlates to the image below it. The green structural parts are not represented in the diagram. Light is coupled into the MZI and then emitted from the edge of the wafer into the photodiode.

on the grating in a 50 µm by 50 µm. Next, finding an acceptable coupling angle between the laser was a significant challenge due to the relatively small acceptable angle that allows light to couple into the MZI. To aid in this process, the beam is reflected off a 45° mirror which has been pre-angled to shine onto the wafer. To further adjust the input angle, a dual axis leveling plate is placed between the mirror and its mount. To improve positioning we added two micrometers, allowing fine movement of the grating. While this all took a considerable amount of time, we were able to successfully couple the laser light into the grating.

Once coupled into the MZI grating, the light splits into the two arms (as shown in inset D of Figure 7.2). As stated previously, one is a reference arm while the other is a sensing arm. The sensing arm interacts with fluid or other material in the sensing region. During the experiment conducted in this report, a small amount of fluid is poured into the fluid path seen in Figure 7.5, such that it will interact with the sensing region shown in Figures 7.1 and 7.2. When the fluid is first poured into the fluid bath, it rapidly changes the output of the

sensor. Subsequent fluids added create smaller changes as they must displace that first fluid. In these tests, we utilized 2 base fluids, water and common glycerin. These were mixed to make a third fluid which was 3:1 water to glycerin. Each of these filling the sensing region of the MZI will lead to a different optical path length. Thus, after passing through the two arms, when light interferes it will do so differently, and after it travels to the edge of the wafer, it will shine out with a different intensity.

Once the laser light passes through the two arms of the sensor, it recombines and exits the edge of the wafer. Upon exiting the edge, a photodiode is positioned to measure the light intensity exiting. To minimize background signals, all other light sources are blocked. Local light is sufficient, while a black curtain around the optics table during testing removes lab lighting. The photodiode used is a Thorlabs cathode grounded Silicon wide aperture photodiode, part number SM1PD1A. It has approximately a 0.33 A/W sensitivity to 633 nm light. The photodiode is connected to a bench-top photodiode amplifier, Thorlabs part number PDA200C, which amplifies the photodiode current. The output of the amplifier is connected to either an oscilloscope or National Instruments Data Acquisition Unit to record the signal verses time. If the index of reflection changes in the sensing region, the light intensity is modulated and can be measured by the photodiode.

After a fluid step has been tested, the "fluid bath" and "sensing regions" must be cleaned by flushing them with first water, and then DI water. This cleaning can be confirmed to be completed by monitoring for interference cycles, because adding more water to a perfectly cleaned area will not induce any change in the index of refraction, and thus should not induce interference cycles. During this step, 5 tests were conducted. While other tests were evaluated, they are not described in this report unless useful data was produced.

7.2.3 Materials tested

Sensitivity of the MZI's were tested with multiple fluids having differenct index of refraction fluids. The fluids consisted of de-ionized water and 99% pure glycerin, and a mixture of the two. They have indices of refraction of 1.330 and 1.473 respectively, and varying index fluids

will be formed depending on their mixing, as when mixed they may be made to have fluids of varying index. Index of refraction of a certain medium is defined by the speed of light in a free space divided by the speed of light in the medium.

$$n = \frac{c}{v} \tag{7.1}$$

Index of refraction is a unit-less quantity. For ease of use though, we shall adopt the literature method of noting measurements of index of refractions as having 'refractive index units' (RIU) hence forth. To create smaller index of refraction steps, the two liquids are mixed in various ratios. The resulting solution index follows the volume averaging ratio, and is represented as n_{fluid} in

$$n_{\text{fluid}} = n_{\text{water}} \text{f}_{\text{water}} + n_{\text{glycerin}}(1 - \text{f}_{\text{water}}) \tag{7.2}$$

where n_{water} is the index of water at 1.330 RIU, n_{glycerin} is the index of glycerin at 1.473 RIU, and f_{water} is the volume fraction of water in a solution.

7.2.4 Waveguide Model

The cross section of the MZI's rib waveguide was modeled in COMSOL using the "Electromagnetic Waves, Frequency Domain" package available in version 5.0. This model did a "Mode Analysis" study, finding the resonant modes of the waveguide. The effective index of each mode was found by the program. Understanding how the effective index of the primary TM mode was affected by the material above the ridge waveguide, as it would change in the sensing region over the course of the test, was the goal of this subsection. The results are reported in Table 7.1.

Seen in Figure 7.6 is the 2D model of the waveguide. The scale of the design is in µm. As can be seen, the model assumes three layers. The bottom layer is fixed as SiO_2, with an index of 1.5 RIU. The middle layer (shown in blue) is Si_3N_4 with an index of 2.0 RIU. Finally, the upper layer is variable, and represents the fluid in the sensing region (or air,

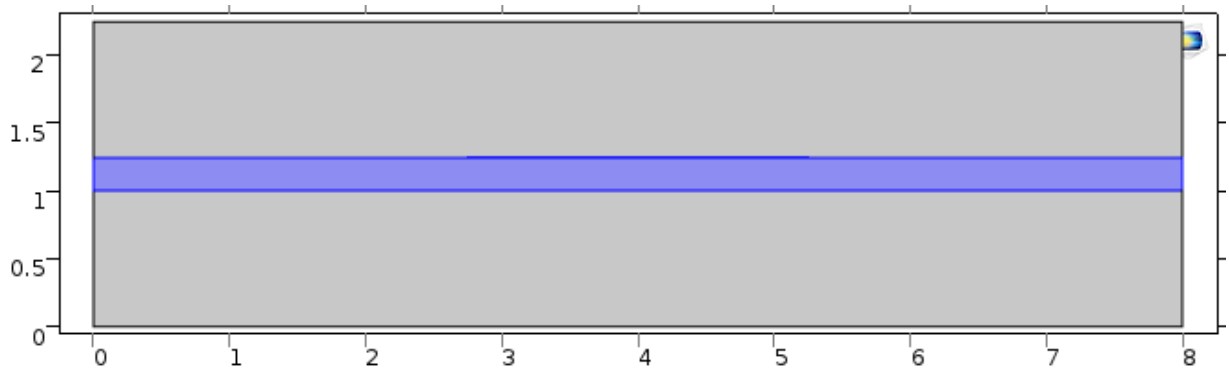

Figure 7.6: Image of the 2D waveguide model.

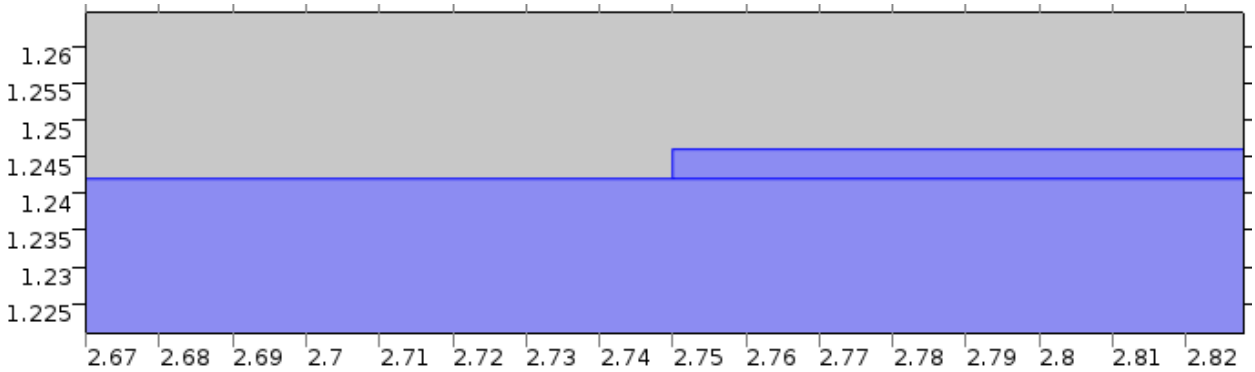

Figure 7.7: Closer image of the 2D waveguide model's ridge's left corner.

before testing, or SiO_2 to model the reference arm.

Figure 7.7 shows just the right corner of the 4 nm ridge in the waveguide. Again, the blue area is the Si_3N_4, and the gray region above it is the variable upper layer. This 4 nm tall ridge is what confines the light in the waveguide and runs from 2.75 µm to 5.25 µm.

Finally, Figure 7.8 shows the model meshed with triangular elements, with a maximum mesh size at the ridge small enough to capture its nature. A meshing size study was done to define the mesh size for the different regions of the model.

7.3 Experimental results and discussion

The MZI's were characterized to evaluate their sensitivity to changes in index of refraction. Analytical modeling results aid in understanding the experimental results. Figure 7.4 shows the progression of how changing the material in the sensing region leads to changes of the

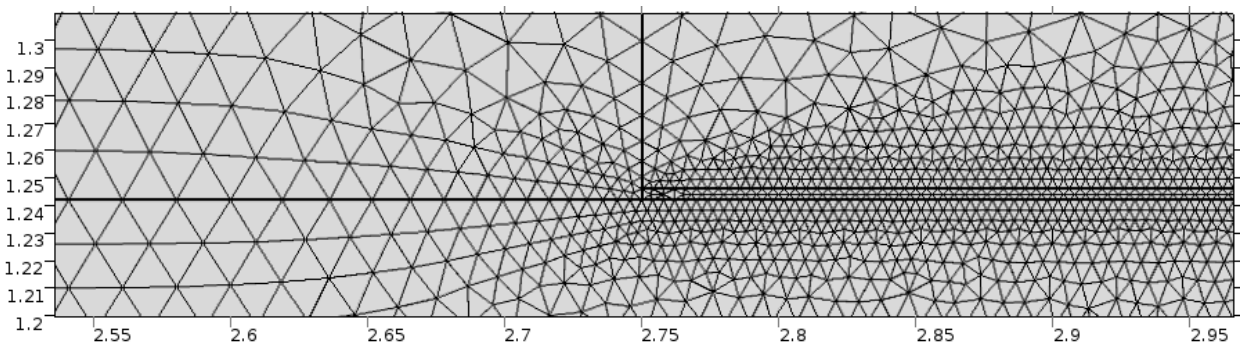

Figure 7.8: Closer image of the 2D waveguide model's ridge's left corner, now meshed with triangular elements.

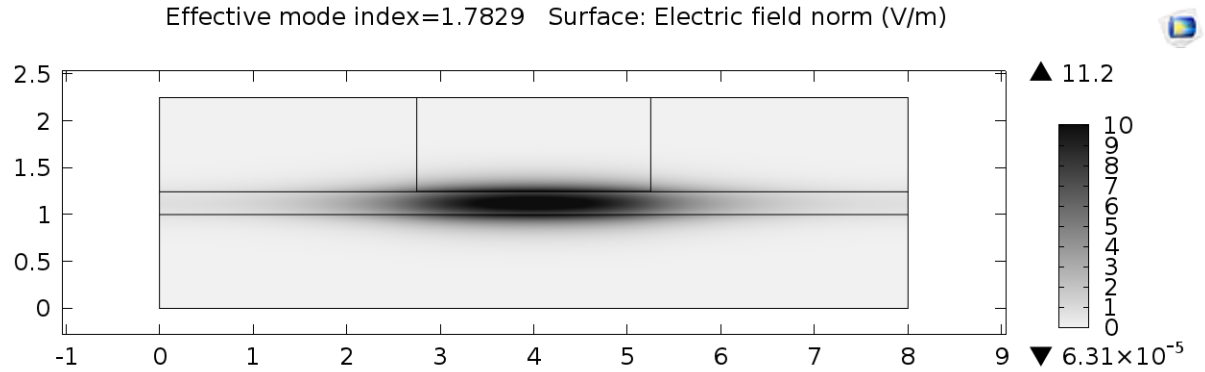

Figure 7.9: COMSOL model of the primary TM optical mode present in the MZI's sensing arm when glycerin is in the sensing region.

intensity of the output of the MZI. Thus, first we will look at the results of the model, effective optical index, and use them in discussing the experimental results.

7.3.1 Modeling results

Shown in Table 1 are the results of the model in Figure 7.9, when the top layer of the analytical model has been varied. The effective index of the sensing arm changes when the material interacting with the MZI's waveguides is changed. Further, the effective index of the sensing arm will be different to transverse electric (TE) modes vs. transverse magnetic (TM) modes of light. When working experimentally, we couple the light into the waveguide as a TM mode.

When the MZI's sensing region is bare, it has a TM mode effective index of 1.7381 RIU

Table 7.1: Effective indices of sensing arm

Sensing area material	Material's index (RIU)	Effective sensing arm index	
		TE (RIU)	TM (RIU)
Air	1.0003	1.8252	1.7381
Water	1.330	1.8343	1.7656
3:1 Glycerin	1.3657	1.8358	1.7695
Glycerin	1.473	1.8410	1.7829
SiO_2	1.500	1.8426	1.7867

due to air filling the region. When water is added to cover the MZI it induces a great number of interference cycles, due to the 0.0275 RIU step in the 15.3 mm long sensing region. Water to glycerin similarly has a large change of index, 0.0173 RIU, but it may be metered to happen slower, allowing that response to be counted. Finally, it should be noted that most of the MZI has SiO_2 on top of the rib waveguides, leading to an effective index of 1.7867 RIU throughout much of the device.

An expected sensitivity of the device to effective index changes may be calculated by

$$\frac{\lambda}{l} = \Delta n_{\text{effective index}} \tag{7.3}$$

$$\frac{633\,\text{nm}}{15.3\,\text{mm}} = 4.1373 \times 10^{-5}\,\text{RIU} \tag{7.4}$$

with l being the length of the sensing region, 15.3 mm, and λ the wavelength of light. Thus, when the sensing arm experiences a 4.14×10^{-5} RIU change in effective optical index, a cycle will be seen.

The useful definition of sensitivity for an MZI though is the change in the index of refraction of material in the sensing region divided by the number of cycles seen in the intensity of the MZI output. The sensitivity of an MZI is characterized by

$$\text{Sensitivity} = \frac{n_{\text{finish}} - n_{\text{start}}}{\text{cycles}} = \frac{\Delta n}{\text{cycles}} \tag{7.5}$$

More cycles per a fixed change in index represents a better sensor, and smaller sensitivity'. Sensitivity can be increased with a longer sensing region, or more light interacting with the

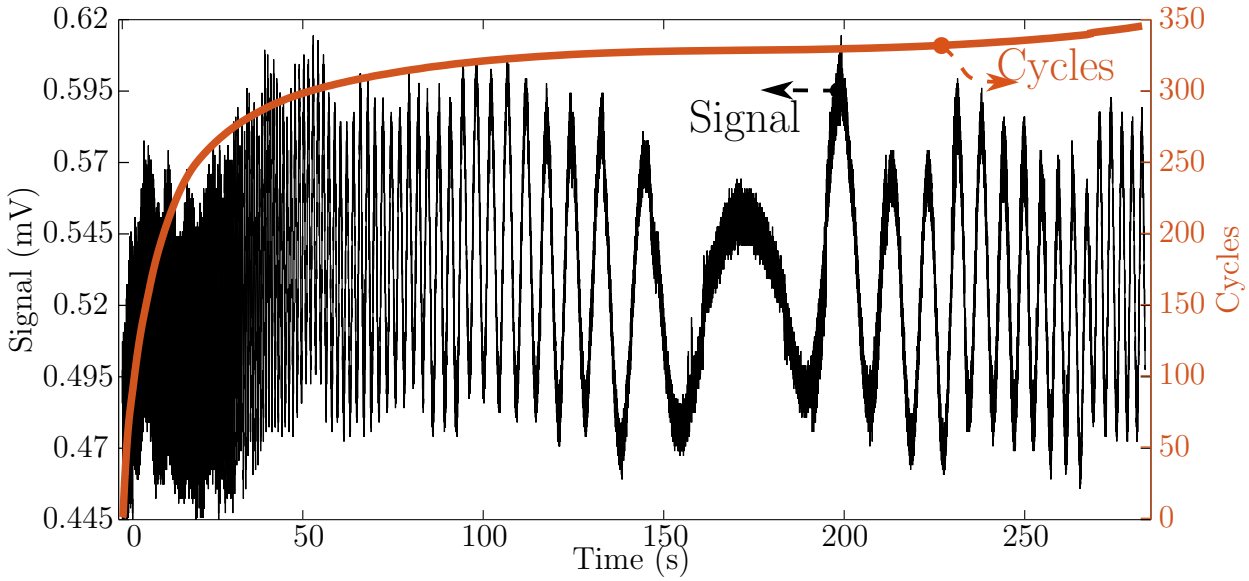

Figure 7.10: Plot of signal output obtained from amplifier verses time for glycerin added to an MZI coated with a film of water. Also shown on the plot is the number of cycles verses time. The signal reverses after 171 s, when the glycerin begins being diluted by the water dissolving into the glycerin layer.

sensed material.

7.3.2 MZI performance with fluids

The MZI's were characterized by changing the index in the sensing region via addition of pure glycerin, or a quarter glycerin solution to a starting water film. This created index changes of 0.143 RIU and 0.0357 RIU respectively in the sensing area material. Such materials lead to 0.0173 RIU and 0.0039 RIU, effective optical index changes in the TM mode in the sensing arm. While the glycerin solution provides four times the index change, there is a greater than proportional effective index change. When the index of the material above the rib waveguide changes, so does the intensity of interaction with the sensed material. The higher index glycerin 'pulls' light into its index more than the lower index quarter glycerin solution does. This makes the sensitivity of the device increase some with increasing index of the sensing region. It is expected that the characterization with quarter glycerin would have less than a quarter of the response of the pure glycerin test. The first tests performed were the full glycerin tests. These were followed by the quarter glycerin testing.

Figure 7.10 graphs signal versus time and cycles versus time. The signal is obtained from the amplifier attached to the photodiode measuring the intensity of the light exiting the MZI. The data in Figure 7.10 represents an MZI initially containing water in the sensing region to which glycerin was added at $t = 0s$. As can be seen, the signal oscillates with time. This is caused by the effective index of the sensing arm's region changing when the glycerin is added. The oscillations observed in the recorded signal represent interference cycles. Specifically, one interference cycle corresponds to a 2π phase change in the sensing arm. This first 2π shift occurs when the effective index of the sensing arm's light changes by 4.1373×10^{-5} RIU, as found in equation 7.3. Initially the oscillations are rapid, indicating the system is experiencing a rapid change of index. This rapid change from 0 s to 10 s is caused by glycerin quickly entering and spreading across part of the sensing area. As can be seen, from 48 s to 171 s the rate of oscillations decreases with time, as glycerin completely fills the sensing region.

The second curve in Figure 7.10 is cycles (corresponding to the vertical axis on the right) and represents the number of 2π oscillations determined from the signal. As can be seen from 0 s to 10 s the number of cycles rapidly increases from 0 cycles to 200 cycles. From 48 t to 171 the number of cycles increases to and eventually plateaus at ∼328 cycles. Given that each cycle corresponds to a 4.1373×10^{-5} RIU change of effective index, the 328 cycles represents an effective index change in the sensing arm of

$$4.3173 \times 10^{-5}\,\text{RIU} * 328 = 0.0135\,\text{RIU} \tag{7.6}$$

This value compares reasonably well with the expected change of 0.0173 RIU from glycerin displacing water. The difference between the expected change and the measured change is due to a difference in device sensitivity that was modeled. It is not due to any mixing between the water and glycerin. Such mixing happened after the 180 s mark.

To confirm the above conclusion was correct, another test was conducted by adding a dilution of 25% glycerin solution to the sensing region rather than pure glycerin (i.e. 99.9%).

Figure 7.11 plots both signal versus time and cycles versus time. In the first 3 seconds

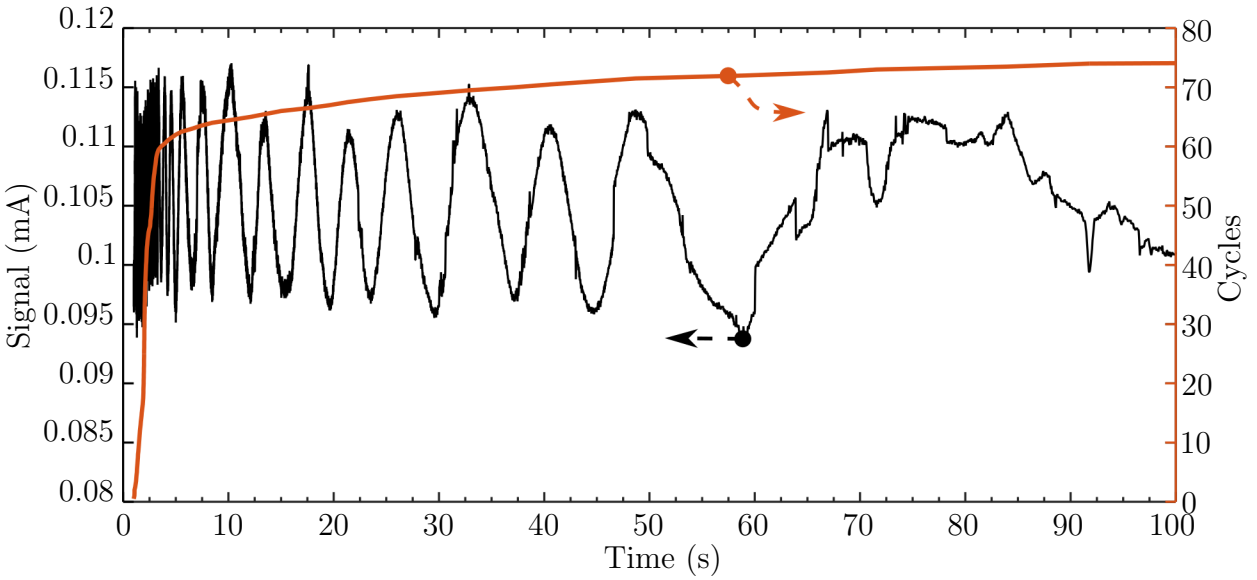

Figure 7.11: In this test, initially the bath contained a thin film of water which was filled the sensing regions, which was displaced as the 3:1 water:glycerin was added.

there is a rapid 2π change in signal which slows down as the test ends at 100 seconds. This is in sharp contrast to the data presented in Figure 7.10 with the difference attributed to the mixture of water + glycerin being added as compared to pure glycerin. In Figure 7.11, the number of 2π cycles that the signal oscillates increases to 60 rapidly followed by slow ramp to $\sim$72 cycles. Given that each cycle corresponds to a 4.3173×10^{-5} RIU change of effective index, the 72 cycles represent an effective index change in the sensing arm of

$$4.3173 \times 10^{-5}\,\text{RIU} * 72 = 0.002\,98\,\text{RIU} \tag{7.7}$$

This value compares reasonably well with the expected change of 0.0039 RIU represented by a 25% glycerin solution. The measured response is 77% of the expected response, which also compares reasonably well with the 78% found in the preceding test. Therefore, this data supports the conclusion that the MZI is working.

During this study, a number of tests were performed. In Table 7.2, five characterizations' data are presented on 2 different interferometers. The first column represents the interferometer number tested. The second column represents the percent of glycerin added in the solution. The third column represents the measured number of cycles (i.e. the right verti-

Table 7.2: Summary of testing results for index of refraction

MZI	Test Fluid	Cycles	Sensitivity $*10^{-4}\ \frac{\lvert RIU \rvert}{cycle}$
8	100 % Glycerin	328.5	4.35
8	100 % Glycerin	168.0	8.51
8	100 % Glycerin	323.5	4.42
8	25 % Glycerin	130.0	2.75
20	25 % Glycerin	72.5	4.92

cal axis of Figures 7.10 and 7.11) observed during the test. The fourth column represents the sensitivity (i.e. using Equation 7.5), which represents the fluid's influence on the index change per cycle. The data presented in the first and last rows of Table 7.2 are representative of Figure 7.10 and Figure 7.11 data respectively.

As can be seen in Table 7.2, the devices showed an average sensitivity of 4.99×10^{-4} |RIU|/cycle with a standard deviation of 2.13×10^{-4} |RIU|/cycle. The two outlier points in the table (i.e. 8.51 and 2.75×10^{-4} |RIU|/cycle) that contribute strongly to the large standard deviation are attributable to sloshing of fluid due to poor introduction of the fluid in the cavity and excessive noise in the data. If these two data points are removed, the sensitivity ranges from 4.92 to 4.35×10^{-4} |RIU|/cycle. The results presented here are comparable to those of Duval et al. and their 4.0×10^{-4} |RIU|/cycle sensitivity [25]. These data clearly show that the UCLA fabricated MZI devices successfully detect changes of index. With a quarter cycle resolution, this means that the sensor has a 1.25×10^{-4} |RIU| resolution. This exceeds the exit criteria of 1×10^{-3} |RIU| for step 2. In the next section, we relate these measured index changes produced by adding fluids to an MZI magnetic field sensor utilizing LSMO film.

7.3.3 Projected performance of next step

In this section we predict the performance of the MZI interferometer with LSMO film deposited on the sensing arm. LSMO is a magnetic material whose index of refraction changes with the application of a magnetic field. Thus, as the fluid did in the preceding section, the magnetic field will produce index changes causing 2π oscillations like those seen in the signal response of Figure 7.10. The proposed metric for this program was the ability to sense a

magnetic field of 1 G. Below, we use the experimental data from the preceding section along with measurements of the change in index of LSMO when exposed to a magnetic field to estimate magnetic field sensitivity of a MZI containing LSMO. This calculation provides motivation to continue the work on the next phase of the program and confirms the required exit criteria for this phase.

The MZI magnetic sensitivity is calculated as follows. The measured MZI's average sensitivity shown in Table 7.2 is 4.99×10^{-4} |RIU|/cycle. The index of refraction change experimentally measured at UCLA for LSMO is -1.86×10^{-6} |RIU|/G of magnetic field applied, as documented in the Step 1 report and is included in an upcoming AIP publication by Strutner et al. This data was measured at UCLA using an ellipsometer system and measured at room temperature. Additionally, historical data shows that a quarter cycle of the 2π oscillations previously shown in Figure 7.10 and 7.11 can be resolved. This $2\pi/4$ defines the lower experimental data limit that can be determined in terms of signal measurements as a function of time. To calculate the magnetic field measurable with the proposed MZI device, we divide the sensitivity by the LSMO index change per gauss and multiply by $2\pi/4$ as below. As can be seen, this provides a resolution limit of 67 G for magnetic sensing in the present MZI design.

$$\text{Step3}_{\text{Resolution}} = \frac{\text{MZI}_{\text{Sensitivity}}}{n_H} * \frac{\pi}{2} \tag{7.8}$$

$$\text{Step3}_{\text{Resolution}} = \frac{4.99 \times 10^{-4}\,|\text{RIU}|/2\pi}{-1.86 \times 10^{-6}\,\text{RIU/G}} * \frac{\pi}{2} = \ 67\,|\text{G}| \tag{7.9}$$

The stretch goal for step 3 is to develop a design for an MZI with a magnetic sensitivity of 1 G. There are two paths to reach the 1 G goal from the current 67 G prediction. First, the sensing arm can be made longer, which increases the sensitivity because the EM wave is in contact with the LSMO for longer distances. This would require an increase in length from a 15.3 mm long sensing arm to a 1 m long sensing arm. As a point of reference, a 10 m long spiral waveguide was tested by Srinivasan et al. of UCSB [105] and a 9 m long spiral

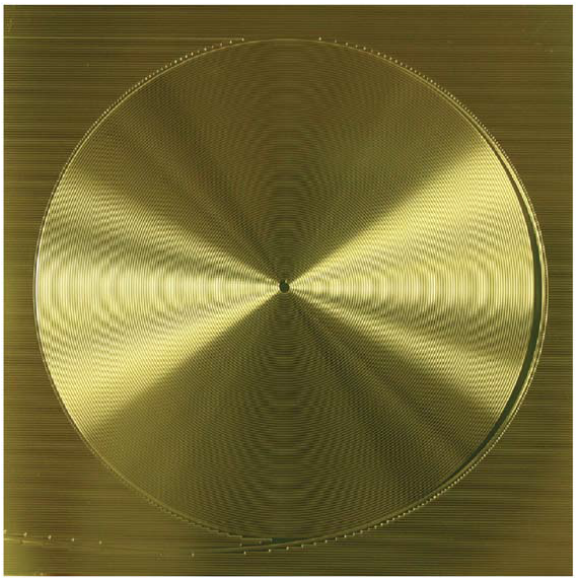

Figure 7.12: A 9 m long planar waveguide made by Lee et al. of CalTech, reproduced from [68].

waveguide was tested by Lee et al. of CalTech [68], shown in Figure 7.12.

Another approach to increase sensitivity is to change materials to Lanthanum Calcium Manganese Oxide $La_{0.66}Ca_{0.33}MnO_3$ (LCMO) instead of LSMO. The magnetorefractive effect in LCMO is 70x that of LSMO [49]. Using the current UCLA 15.3 mm long sensing arm, this would produces a 1G sensitivity. If the sensing arm is increased and the material changed, the magnetic field sensitivity could approach 0.0014 G for a 10 m long arm with LCMO.

7.4 Chapter conclusion

An MZI device was designed, fabricated, and characterized. Characterizations show it has an average sensitivity of 4.99×10^{-4} |RIU|/cycle. With a quarter cycle resolution, this means that the sensor has a 4.99×10^{-4} |RIU| resolution. This exceeds the exit criteria of 1×10^{-3} |RIU| for step 2. In terms of magnetic field sensitivity, this correlates to 67 G for LSMO or 1 G for LCMO. The next and third step of the MFBG project consists of depositing LSMO onto the MZI sensor and measuring response. We anticipate a 67 G magnetic field detection. The stretch goal of 1 G can be achieved by either increasing the sensor arm's

length or by changing the active material to be LCMO.

Chapter acknowledgment

The authors would like to thank the NASA KSC's LSP for supporting this work. The authors would also like to thank AERO Institute of Palmdale and NASA Armstrong for their feedback. We acknowledge the use of the ISNC at the CNSI of UCLA in this work.

CHAPTER 8

Magnetic MZI

8.1 Introduction

This document summarizes the work to create a magnetic Mach Zehnder interferometer (MZI) as step 3 of the magnetic fiber Bragg grating (MFBG) project supported by the NASA Kennedy Space Center (KSC)'s Launch Services Program (LSP). Step 3 of the MFBG project was to fabricate a developmental device and characterize its sensitivity. Shown in Figure 8.1 is the device concept built on the previous MZI concept shown in Figure 7.1.

This study fabricated the magnetometer and encountered a lack of signal when testing. Not all exit criteria were achieved for this step.

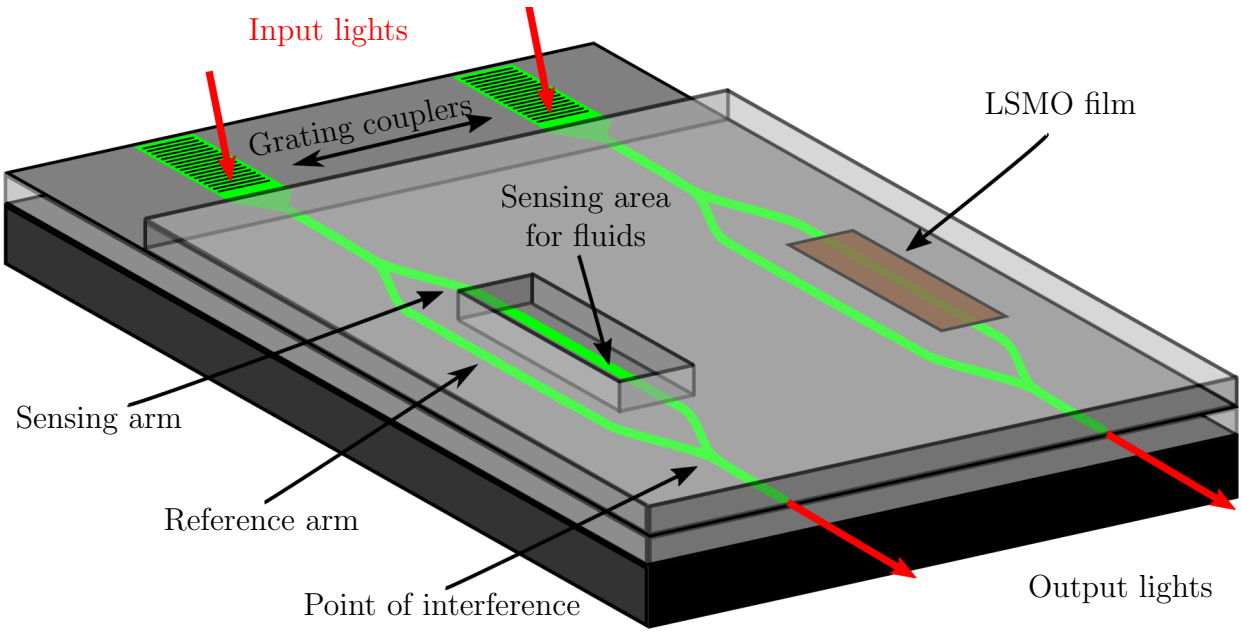

Figure 8.1: A diagram of two MZI's, one sensitive to fluids, and one to magnetic fields, integrated onto the same substrate.

8.1.1 Project's problem statement

During six months, a proof of concept magnetometer was developed, fabricated and tested at UCLA, which could have led to the distributed magnetic field measurement device, but instead brought to light an unwanted materials characteristic. This was step 3 of the larger MFBG project with the goal of creating a distributed magnetic field sensor. To achieve this goal, we first proposed a series of developmental devices. Each device had a series of steps in their development which have go/no-go exit criteria. This step reached a "no-go" ending.

Figure 4.18 shows the 13 step development plan to create the magnetometer array. Step 1 was a materials study. Step 2 entailed creating an optical device, the Mach Zehnder interferometer (MZI), which is sensitive to index of refraction changes. Step 3 is transforming this optical device into a single point magnetic field sensor device. National Air and Space Administration (NASA) LSP at Kennedy Space Center identified that this magnetically sensitive MZI could be used as a standalone device. They proposed packaging it as a portable standalone device at the end of step 3 with increased financial support for external electronics and thermal control.

8.1.2 Step 3 exit criteria

Prior to beginning step 3, when the project was being laid out, we laid out exit criteria for step 3. The criteria focuses on creating a sensor sensitive enough to detect the magnetorefractive effect (MRE) effect, which was expected to be present in Lanthanum Strontium Manganite $La_{0.66}Sr_{0.33}MnO_3$ (LSMO). As fiber Bragg gratings (FBGs) have a core sensitivity of 2.4×10^{-6} RIU/pm, and Emmons et al. [30] showed a FBG system has 5 pm, we expect the final MFBG to have a 1.2×10^{-5} RIU sensitivity. LSMO needed a magnetic field sensitivity of 1.2×10^{-6} RIU/G. It has a measured sensitivity of 1.6×10^{-6} RIU/G, 30% higher.

To detect and confirm the LSMO magnetic sensitivity would require a sensor that could see multiple cycles of interference in a 3000 G field. 3 cycles in a 3000 G field, is 1000 G/cycle sensitivity. This step ended with a device that did not have a signal, due to the LSMO film.

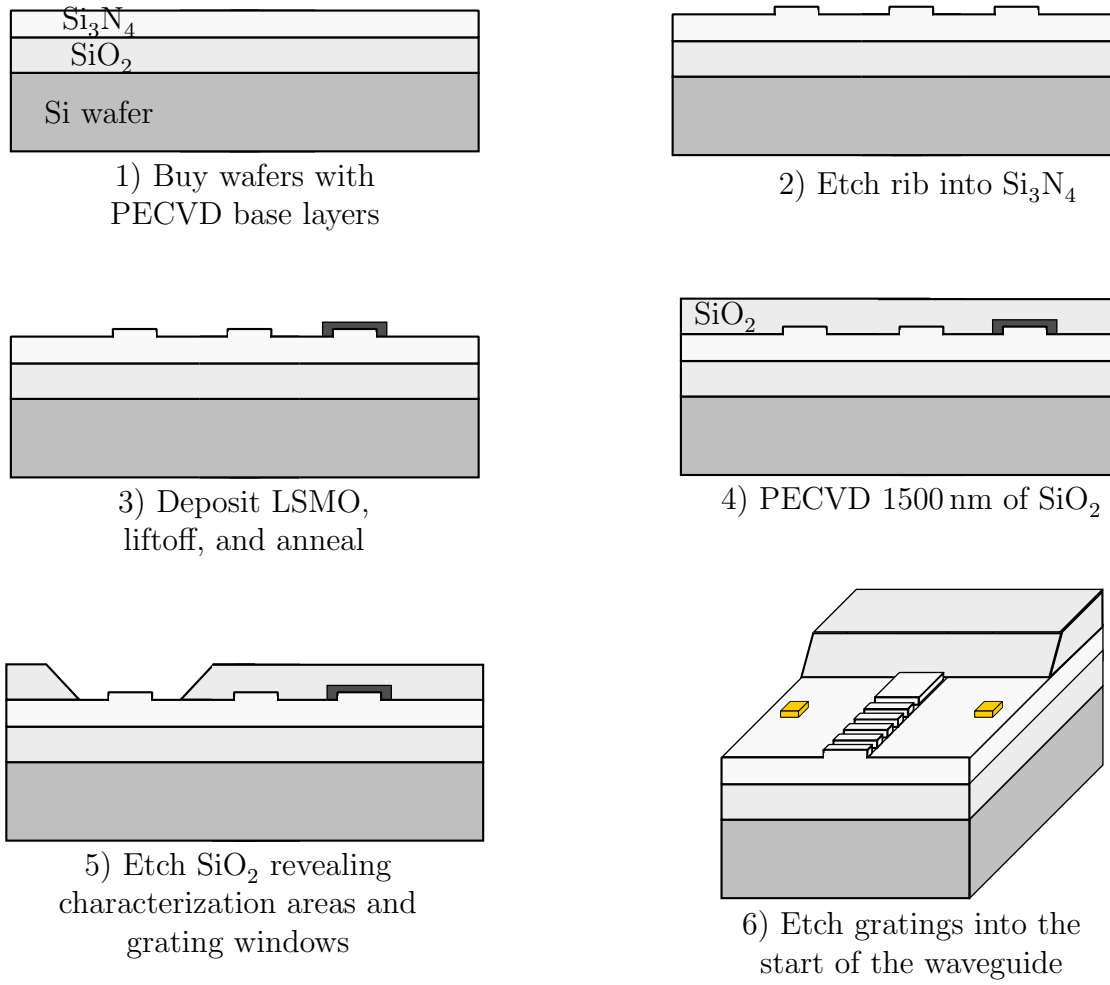

Figure 8.2: Diagram of key fabrication stages for making the MZI. The first five stages show the cross section of the sensing regions of the waveguide, as seen the right edge of the inset B, or left edge of inset C of Figure 7.2. The last step shows the view of the entrance grating area, which is the region above the scale bar of the A inset of Figure 7.2.

8.1.3 Introduction to the magnetic MZI

Illustrated in Figure 8.1 is a pair of MZIs able to sense fluids and magnetic fields. The fluid sensor has had its top SiO_2 layer etched away over the sensing arm as discussed in Chapter 7, while the magnetic sensor has had a new LSMO layer deposited before the top SiO_2 layer.

8.2 Magnetic MZI wafer fabrication

The wafer of MZI's was fabricated in UCLA's Integrated Systems Nanofabrication Cleanroom (ISNC) class 100/1000 clean room, part of UCLA's California NanoSystems Institute (CNSI). Figure 8.2 overviews the fabrication process for the magnetic MZI. There were a few minor changes made to the MZI fabrication process as introduced in section 7.2.1. After the waveguide ridges are etched, instead of selectively protecting regions of the wafer, photo resist (PR) was used to pattern via lift off an LSMO film which was deposited via sputtering. This patterned film was then annealed at 800 °C for 2 h. This was done such that the SiO_2 upper layer applied after would have to undergo the annealing, which was a development issue. The SiO_2 layer was deposited via chemical vapor deposition (CVD). This layer was then only etched away in 2/3rds of the device's sensing regions, instead of all sensing regions. This top SiO_2 layer is selectively etched away to reveal the Si_3N_4 rib waveguide. This was found to not damage the ridge if done using a 10:1 BHF/BOE wet etch. The final stage is to add the entrance gratings as before. Further fabrication details are given in the Appendix again.

Illustrated in Figure 8.3 is a picture of a section of the wafer, with both types of MZI'ss mid-fabrication. On the left is the entrance region of the wafer. The dark strips in the middle of the image (in sets of 6) are each an area of LSMO for magnetic MZI devices. The lighter regions of the same shape (in sets of 3) are where SiO_2 has been removed from the top of wafer for fluid-sensitive MZI of the type characterized in Chapter 7.

8.3 Experimental setup

The new magnetic MZI could be optically connected using the same setup as described in section 7.2.2, but applying a magnetic field must be incorporated. Illustrated in Figure 8.4 is an attempt to couple light into the wafer using the fluid setup's optics but not its fluid application features.

To aid testing, the device array on the wafer was diced down to 6 device sets lettered A

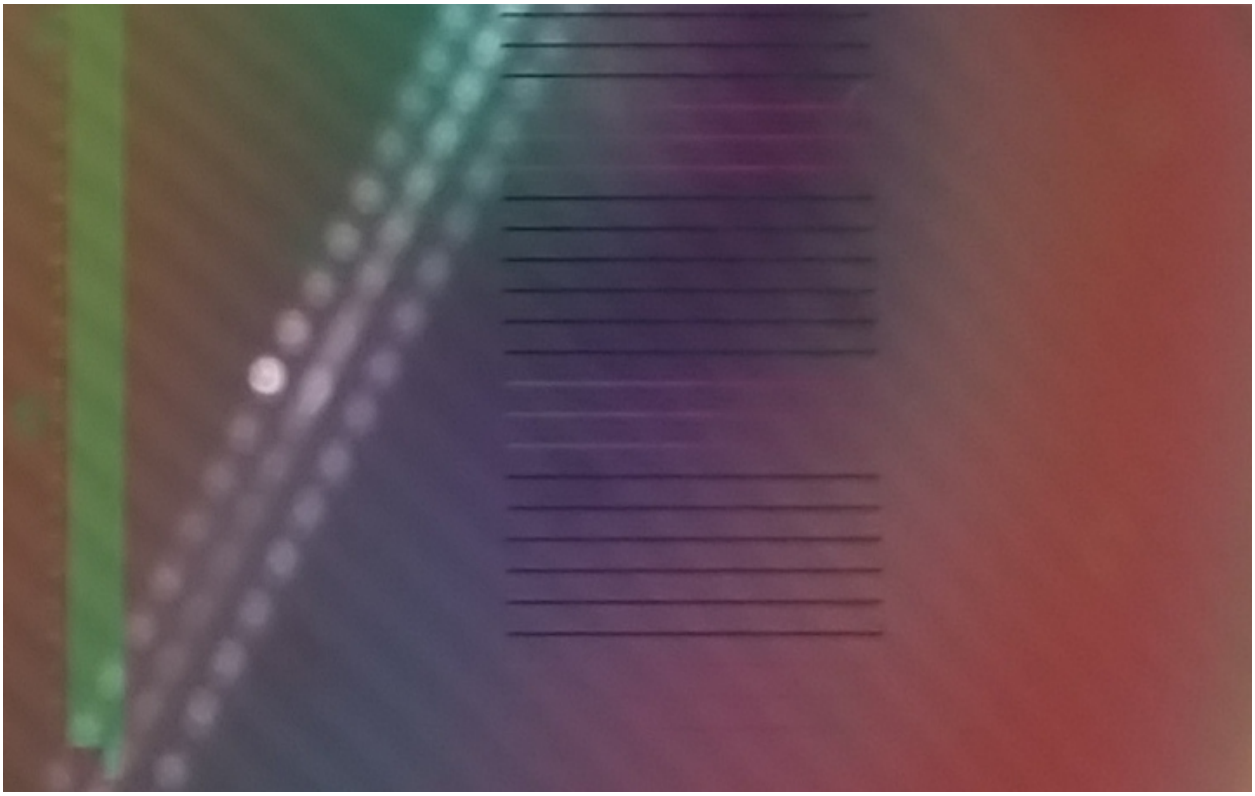

Figure 8.3: An image of a section of the wafer, before Au markers have been placed, with two types of MZI's, one sensitive to fluids, and one to magnetic fields, integrated onto the same substrate.

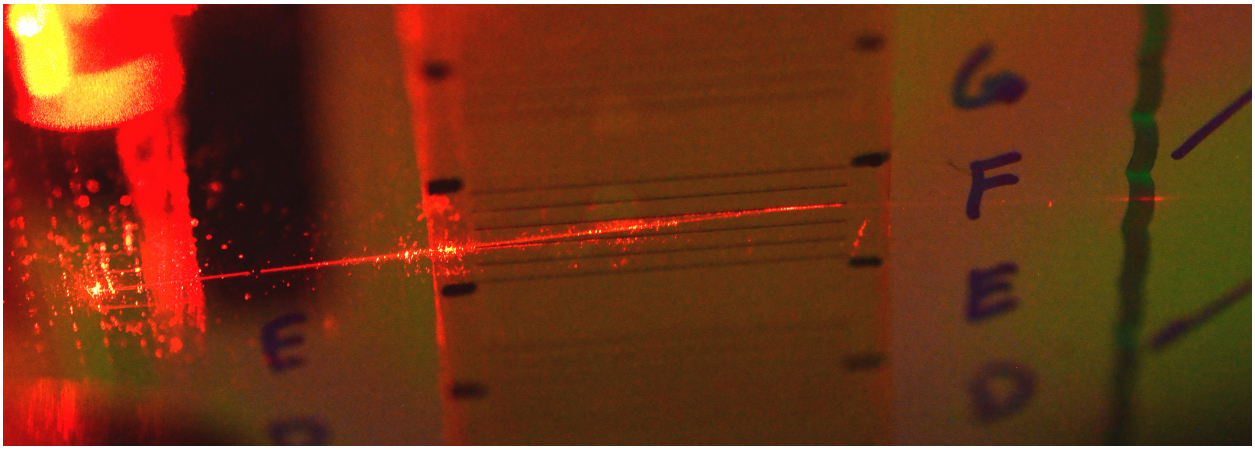

Figure 8.4: An image of a section of the wafer with light not yet properly coupling into the optical waveguides.

through L. Illustrated in Figure 8.5 is a fully fabricated dual device wafer with dicing marks to aid the dicing saw operator. Undergraduate intern Sabina Ula worked on creating a test setup for the diced MZI chips as seen in Figure 8.6, which would allow light to be properly

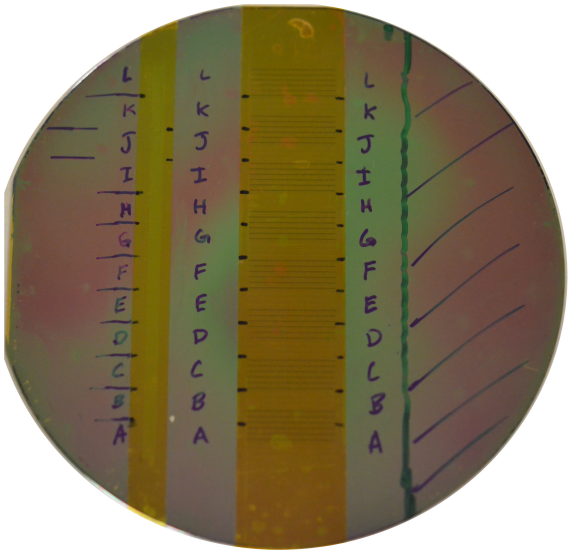

Figure 8.5: An image of the wafer fully fabricated and ready for dicing down to chips. Protective tape has been applied to exposed regions to protect them. Dicing lay-out has been marked out to aid the dicing operator.

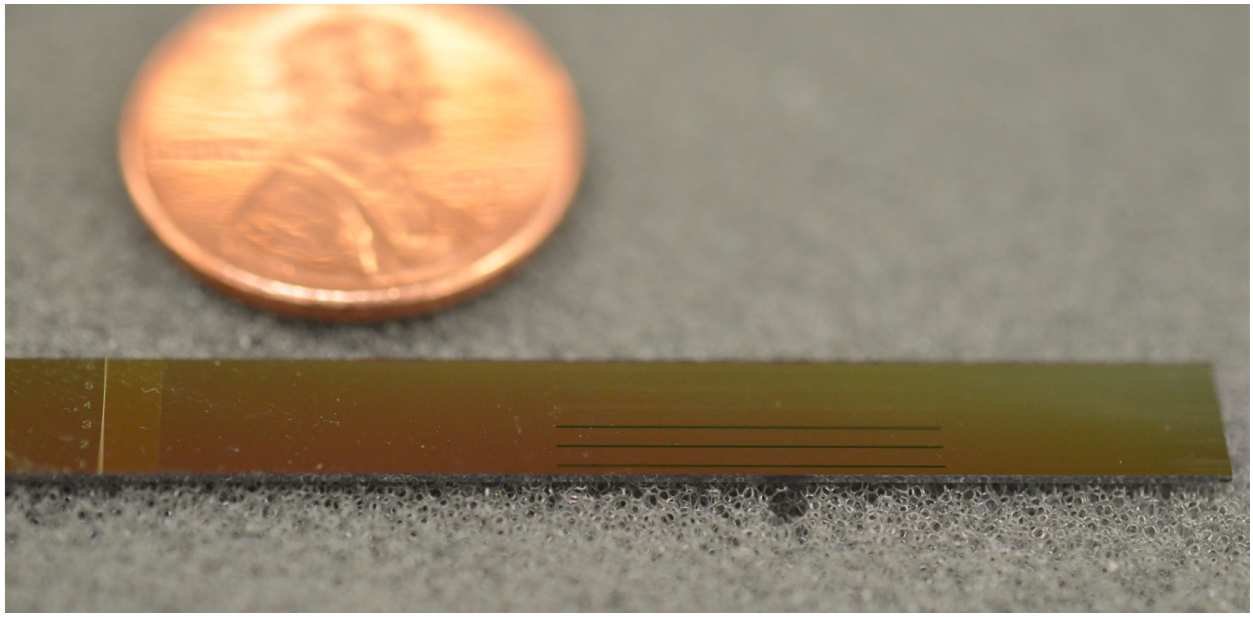

Figure 8.6: An image of the device diced next to a penny for scale.

coupled into the grating couplers consistently, and a magnetic field applied.

Finally, to improve the optical connection, the device was submitted to 3rd party fiber pig-tailing, where optical fibers were connected above the entrance gratings and at the edge of the wafer chip. This is seen in Figure 8.7.

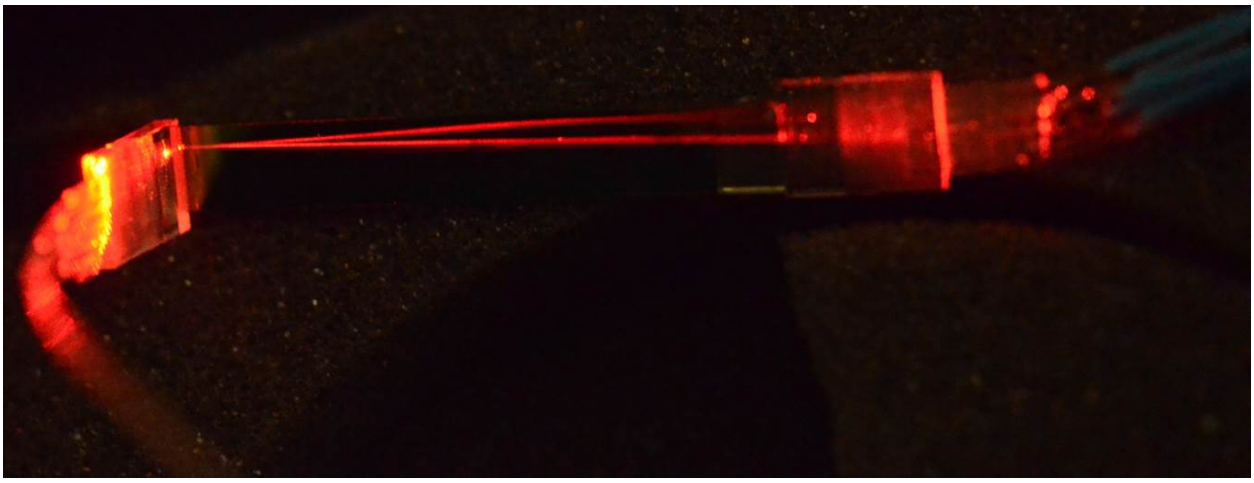

Figure 8.7: An image of the device chip with fiber optics attached, and light scattering towards the exit fiber optics.

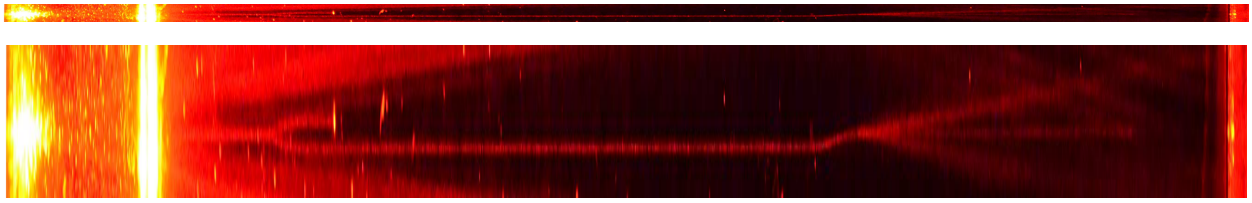

Figure 8.8: Images of the illumination of the MZI waveguide due to light coupled in. The top image strip is the actual dimensions. The bottom image has had its aspect ratio adjusted to improve visibility of the light path and lack of light in the LSMO region.

8.3.1 Magnetic MZI testing setup

A test setup was developed to apply high magnetic field across a 5 mm gap between two square iron poles of 25 cm^2 area. This was not used for characterization though, as the fabricated device after pig-tailing was found to not produce a signal despite strong illumination.

8.4 Experimental results and discussion

As shown in Figure 8.8, light entering the device could be well coupled into the device, but upon striking the LSMO film, would not continue.

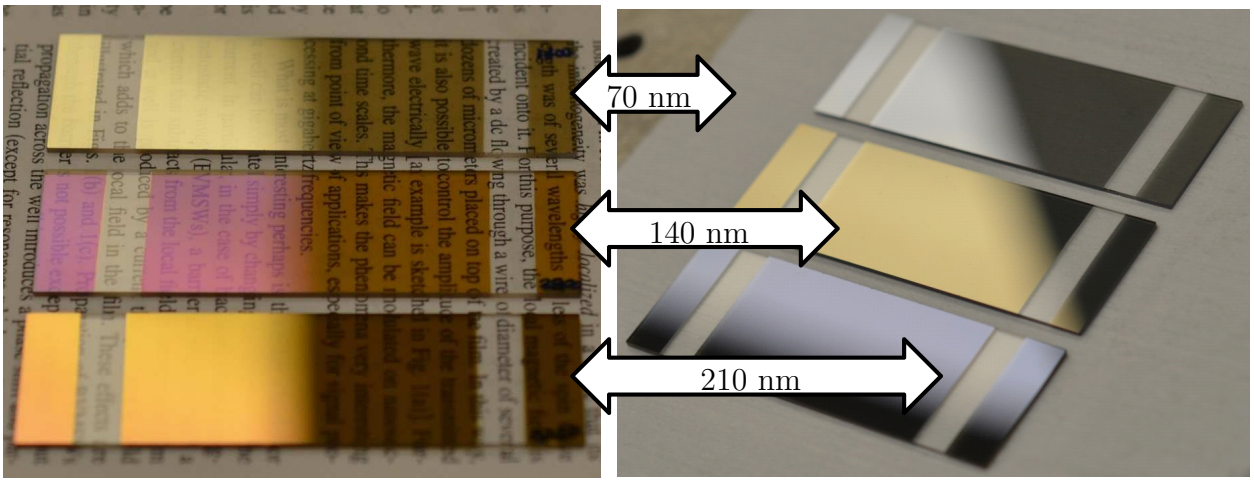

Figure 8.9: Images of the three LSMO films on quartz. The left images are pre-annealing, and the right images post-annealing. The film thicknesses are 70 nm, 140 nm and 210 nm from top to bottom as noted.

8.5 Absorption

With a lack of light transmitting through the LSMO region in Figure 8.8, samples of LSMO on quartz were deposited by Ted Lee. Shown in Figure 8.9 are those samples. It is easily apparent that the films are not transmitting light un-effected. In testing the films via passing a laser through them and watching the photodiode current dip, it was found that the annealed films blocked 51 %, 66 % and 77 % of 633 nm light respectively. Thus, in only 1 µm of the 15.3 mm long LSMO region, only 0.06 % of light would have been transmitted. To recover the device, it was thought that there may be an optical band of lower absorption. Figure 8.10 shows the absorption spectrum of the LSMO samples from 400 nm to 3000 nm

Taking these films and re-testing them for MRE and magnetotransmission (MT) using the setup shown in Figure 5.1, we find that they do possess the desired qualities as shown in Figure 8.11.

8.6 Conclusion

The high absorption by LSMO must be overcome before it will be used for transmitting optical material in this work or others. Unfortunately, the origin of its high absorption and

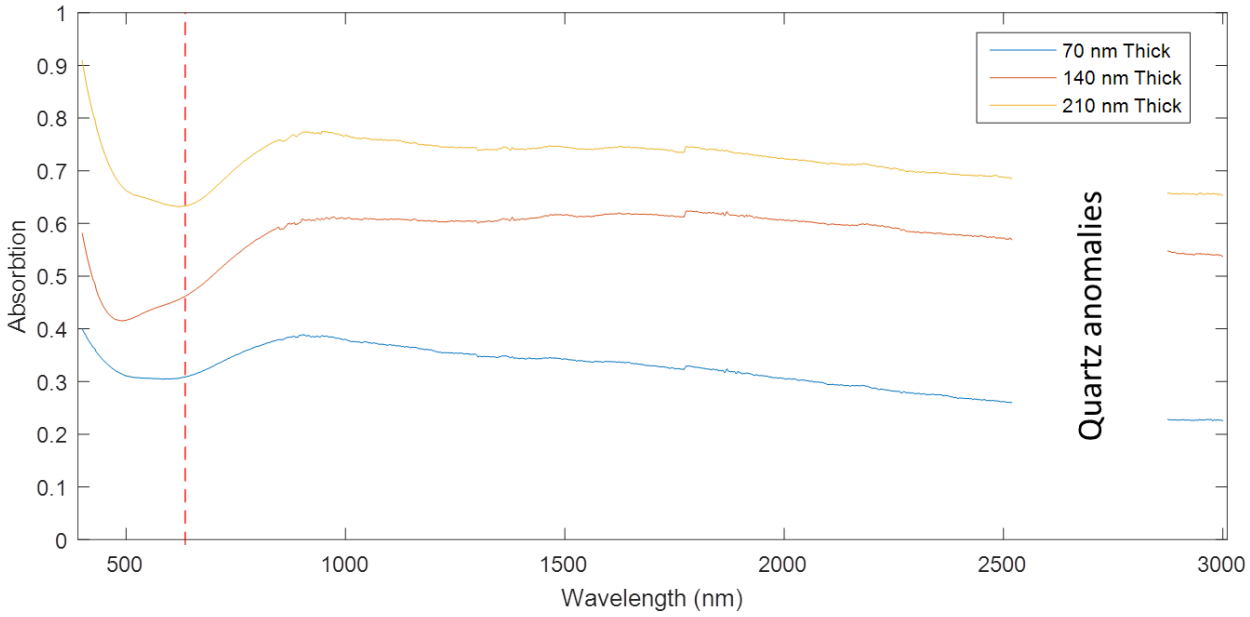

Figure 8.10: The absorption spectrum vs. wavelength for the three samples of LSMO after annealing as shown on the right side of Figure 8.9. The red dashed line denotes 633 nm.

interesting optical qualities are linked. The changes in resistance which drive long-wavelength index changes and MRE may also be stated as conductivity changes. Conductivity in optical materials drives large absorption. At shorter wavelengths, the movement of ultraviolet (UV) **absorption** bands with applied magnetic field impact the index of refraction and absorption in the material plays a large role in its MRE response.

Section acknowledgment

The author would like to thank the NASA KSC's LSP for supporting this work. The author would also like to thank AERO Institute of Palmdale and NASA Armstrong for their feedback. The author acknowledges the use of the ISNC at the CNSI of UCLA in this work.

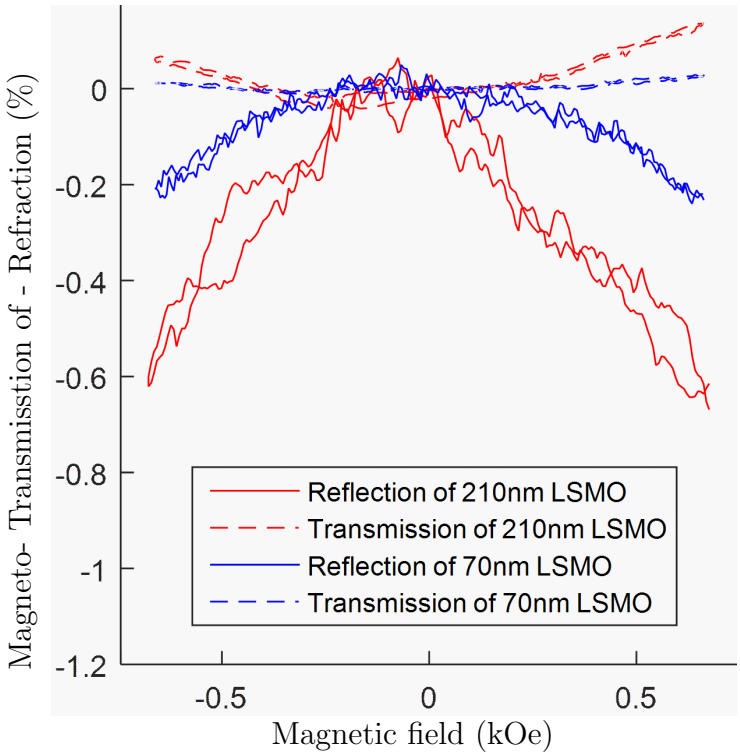

Figure 8.11: MRE and MT of two of the three annealed LSMO films on quartz vs. field. The dashed lines are MT and the solid lines are MRE for the samples.

CHAPTER 9

MFBG Array

In the waning weeks of the Ph.D. degree, a simple, elegant method to make an fiber Bragg grating (FBG) array was conceptualized, rapidly fabricated, tested, and is now under-going patenting and further work.

9.1 Introduction

The mechanism is not entirely new, but its multiplexibility and higher sensitivity than previous FBG magnetic sensors are new. The concept is to use magnetic attraction to strain an FBG in a fiber, instead of using magneto-optics to modify the index of material in an FBG that light interacts with.

9.2 Concept

Magnetic fields have been shown to strain an FBG before, such as when a magneto-strictive material (i.e. Terfenol-D) is attached onto an FBG [20]. Figure 9.1 shows the method Davino et al. used. This is but one of many different methods and modifications to this principle that are frequently patented. Attaching magneto-strictive materials to the FBG generally makes for a hysteretic, thermally sensitive sensor which must be overcome with additional algorithms [20].

Additionally, as seen in Figure 9.2, a magnet may be attached to the end of an optical fiber to strain an FBG [87]. The optical fiber in Figure 9.2 performs as a mechanical element (spring) and a sensing element (tension sensor due to the FBG). The tension, T, in the

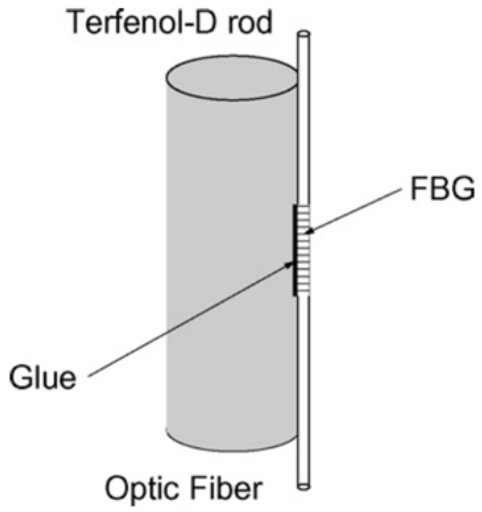

Figure 9.1: A Terfenol-D piece possessing magneto-strictive properties has may be attached to a FBG. This is reproduced from Davino et al. [20].

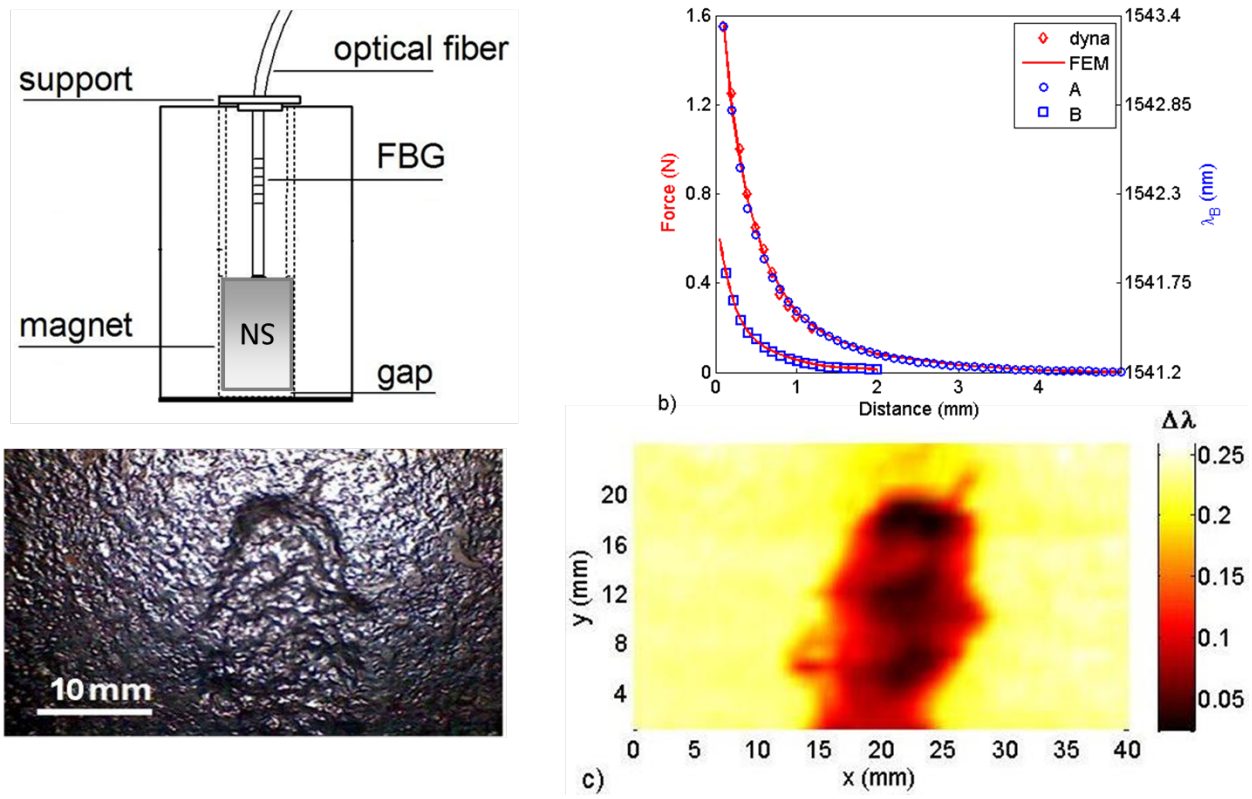

Figure 9.2: A magnet has been attached to an FBG, then the force of the magnetic attraction as the magnet is moved near an iron piece shifts the Bragg wavelength of the FBG. This is used to detect the corrosion pit in an iron sample. This figure is a composite of other figures reproduced from Pacheco and Bruno [87].

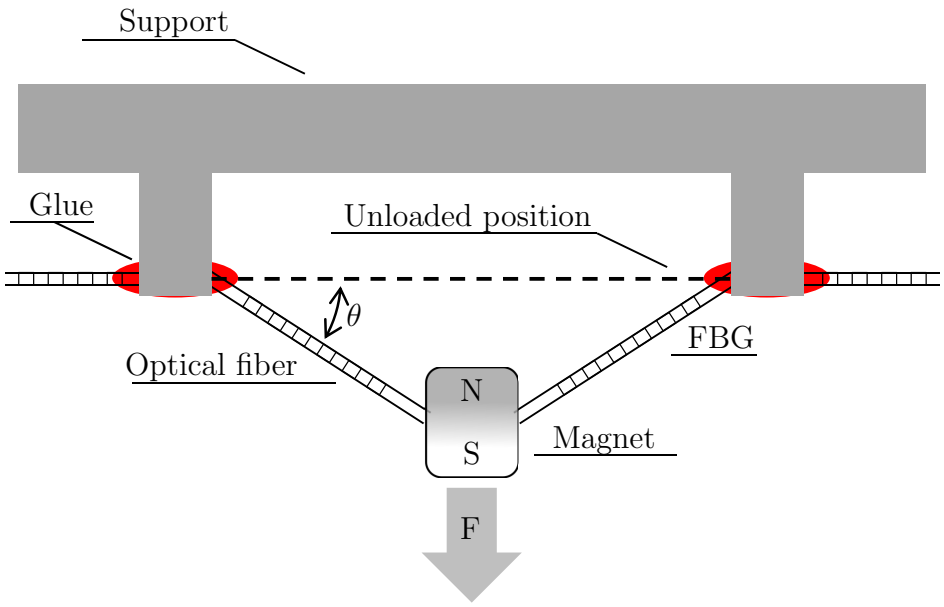

Figure 9.3: A design for a MFBG device using a magnet strung onto a FBG fiber, which is held in place by supports.

optical fiber and FBG is equal to the force, F, applied by the magnet.

$$T = F \tag{9.1}$$

But, these either showed poor magnetic sensitivity [20] or only single point sensing [87]. Instead, this chapter introduces using magnetic material strung along the fiber, like pearls on a necklace, and then the fiber selectively mounted to a frame to isolate induced tension and strain to only a region at a time and thus allow the fiber to act as a series of magnetic fiber Bragg gratings (MFBGs).

9.3 Device design and theoretical sensitivity

This thesis proposes and tests for the first time a new design of sensor.

Figure 9.3 shows a magnet, magnetized perpendicular to the optical fiber which it is strung on. As it encounters a magnetic field gradient, such as due to iron which is magnetized by the field, then the magnet is attracted with a force 'F'. This induces a tension in the optical

fiber, which can be solved for as

$$T = \frac{F}{2\sin\theta} \tag{9.2}$$

Thus, while the angle θ is less than 30° then the suspended bead will offer a mechanical advantage to the sensing of applied forces. To solve for θ, we can use the triangle made by the original length from the edge of the magnet to the edge of the support l, which strains by ϵ as it is forced down.

$$\cos(\theta) = \frac{l}{l(1+\epsilon)} = (1+\epsilon)^{-1} \tag{9.3}$$

$$\theta = \cos^{-1}((1+\epsilon)^{-1}) \tag{9.4}$$

Substituting Eq. 9.4 into Eq. 9.2 and solving for T,

$$F = 2T\sin(\cos^{-1}((1+\epsilon)^{-1})) \tag{9.5}$$

This can be simplified with a trigonometric trick to

$$F = 2T\sqrt{1-(1+\epsilon)^{-2}} \tag{9.6}$$

Now tension T can be solved for as a strain on the spring nature k of the fiber

$$T = k\epsilon \tag{9.7}$$

with k as a stiffness of the optical fiber, which can be measured but should equal

$$k = AE \tag{9.8}$$

with A as the cross sectional area, and E as the Young's modulus. For the fiber used in testing, the manufacturer's product video states it yields when loaded with 49 N at 5 % strain [34] and 50 nm of $\Delta\lambda_B$, so the fiber has a k of roughly 1000 N.

$$F = 2k\epsilon\sqrt{1-(1+\epsilon)^{-2}} \tag{9.9}$$

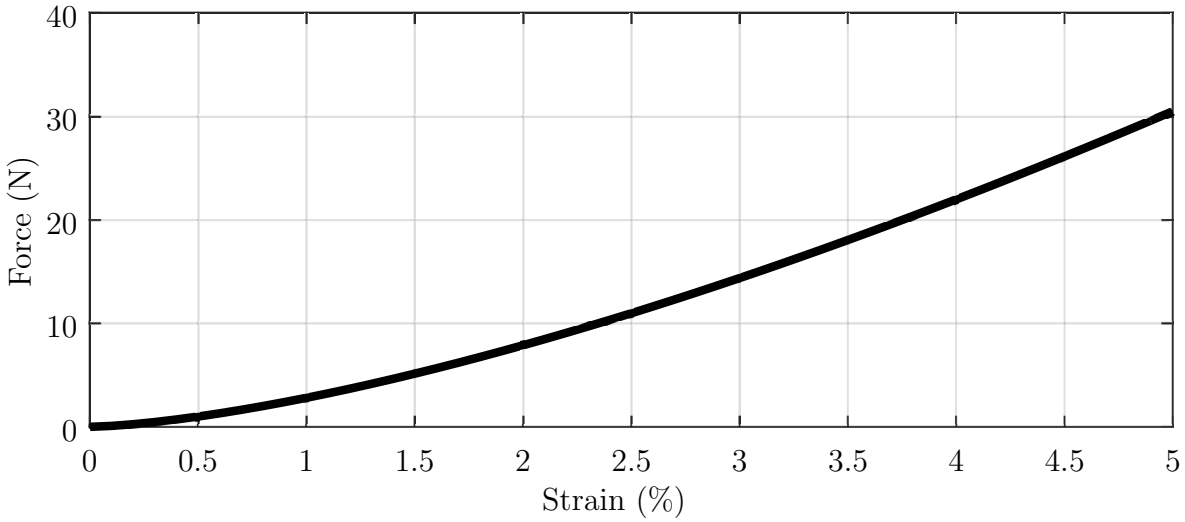

Figure 9.4: The strain to force relationship for a device with a loose magnetic bead, as shown in Figure 9.3

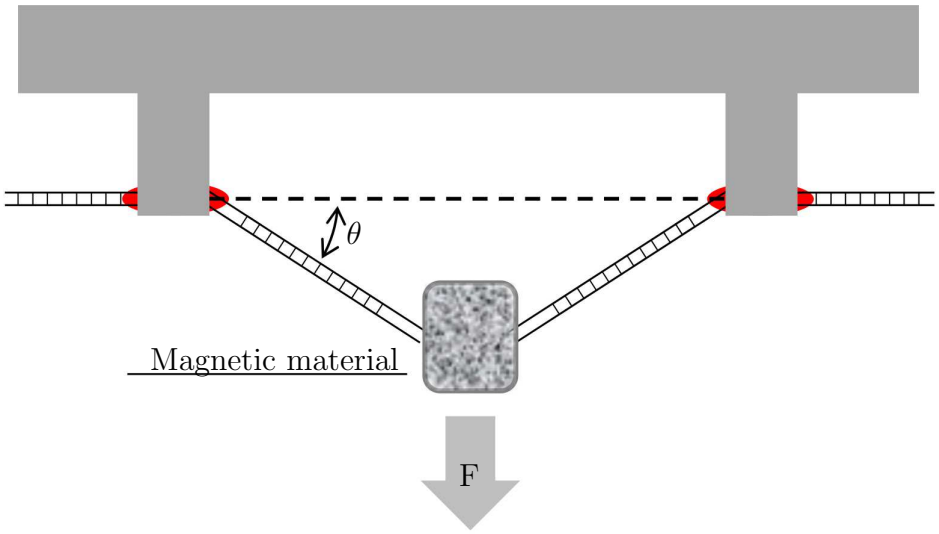

Figure 9.5: A design for a MFBG device using a magnetic material bead strung onto a FBG fiber, which is held in place by supports. A substantiation of this design is shown in Figure 9.10.

Figure 9.4 plots Equation 9.9 for a k of 1000 N. A relatively large strain (2.3%) is found from a 10 N force. Using Equation 9.4, it can be seen that at 5 % the deflection θ is only 17.75°.

Figure 9.5 shows the concept of a bead of magnetic material strung on the optical fiber. As it encounters a magnetic field gradient, such as due to an approaching magnet, the bead

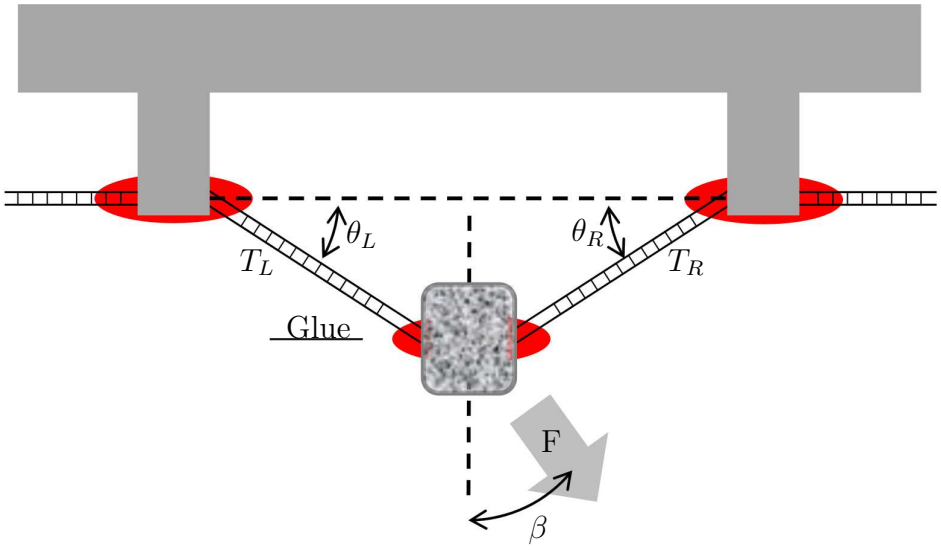

Figure 9.6: A design for a MFBG device using a magnetic material bead strung onto a FBG fiber, which is held in place by supports.

is magnetized and then it is attracted with a force 'F.' This induces a tension in the optical fiber shown in Equation 9.2 and uses the same strain to force the relationship of Equation 9.9. This MFBG was made and is discussed in the Experimental section of this chapter.

Figure 9.6 shows a bead of magnetic material strung on the optical fiber and glued in place. As it encounters a magnetic field gradient, it is attracted with a force 'F'. If this field is not the in the plane perpendicular to the fiber's axis, then there is an angle β between the force and the fiber axis. This induces a tension in the optical fiber. As the glue keeps the bead from sliding, it may also imbue a lateral force onto the fiber, essentially breaking the right and left parts of the fiber into two sensors. Now, when finding the force in the device, F_{down} is

$$F_{down} = T_L * \sin(\theta_L) + T_R * \sin(\theta_R) \tag{9.10}$$

and F_{right} is

$$F_{right} = T_L * \cos(\theta_L) - T_R * \cos(\theta_R) \tag{9.11}$$

As F is

$$F = \sqrt{F_{right}^2 + F_{down}^2} \tag{9.12}$$

then it can be seen that

$$F = \sqrt{(T_L * \cos(\theta_L) - T_R * \cos(\theta_R))^2 + (T_L * \sin(\theta_L) + T_R * \sin(\theta_R))^2} \tag{9.13}$$

which simplifies to

$$F = \sqrt{T_L^2 + T_R^2 - 2\cos(\theta_L + \theta_R) T_L T_R} \tag{9.14}$$

Which using Equation 9.4 and Equation 9.7 can be restated in terms of strain ϵ of each side

$$F = k\sqrt{\epsilon_L^2 + \epsilon_R^2 - 2\cos(\cos^{-1}((1+\epsilon_L)^{-1}) + \cos^{-1}((1+\epsilon_R)^{-1}))\epsilon_L \epsilon_R} \tag{9.15}$$

and β of the force direction can be solved for as

$$\beta = \tan^{-1}\frac{F_{right}}{F_{down}} = \tan^{-1}\frac{T_L * \cos(\theta_L) - T_R * \cos(\theta_R)}{T_L * \sin(\theta_L) + T_R * \sin(\theta_R)} \tag{9.16}$$

using Equation 9.4 and Equation 9.7 to restate this in terms of strain ϵ of each side

$$\beta = \tan^{-1}\frac{\epsilon_L * \cos(\cos^{-1}((1+\epsilon_L)^{-1})) - \epsilon_R * \cos(\cos^{-1}((1+\epsilon_R)^{-1}))}{\epsilon_L * \sin(\cos^{-1}((1+\epsilon_L)^{-1})) + \epsilon_R * \sin(\cos^{-1}((1+\epsilon_R)^{-1}))} \tag{9.17}$$

which simplifies down to

$$\beta = \tan^{-1}\frac{\epsilon_L * (1+\epsilon_L)^{-1} - \epsilon_R * (1+\epsilon_R)^{-1}}{\epsilon_L * \sqrt{1-(1+\epsilon_L)^{-2}} + \epsilon_R * \sqrt{1-(1+\epsilon_R)^{-2}}} \tag{9.18}$$

Figure 9.7 shows a bead of magnetic material strung and glued on the optical fiber. As it encounters a magnetic field gradient, such as due to a void in magnetic material under the sensor which is magnetized by the two magnets pictured in the Figure. This causes a fringing field which attracts the magnetic material with a force 'F'. This may be measured using Equation 9.9 if assumed to be perfectly perpendicular, and Equation 9.15 when the force is non-perpendicular.

Figure 9.8 shows a magnet strung on the optical fiber. As it encounters a magnetic field gradient, the magnet will both spin to face the magnet, as well as attract towards the

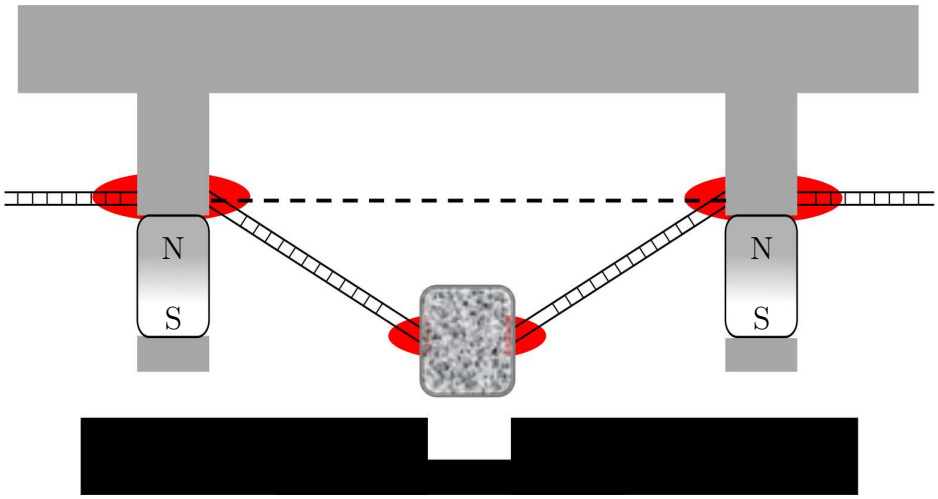

Figure 9.7: A design for a MFBG device similar to the one in Figure 9.6 with side magnetics, such that it can perform magnetic flux leakage (MFL) testing on a sample, such as the iron piece placed beneath it.

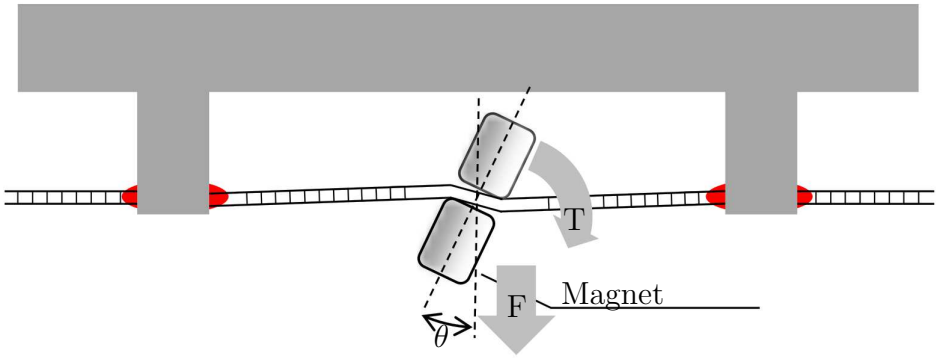

Figure 9.8: A design for a MFBG device using a magnetic material bead strung onto a FBG fiber, which is held in place by supports.

gradient. This will produce a force 'F' and torque 'T'. This induces a tension in the optical fiber as will be measured in the Experimental section.

9.4 Device fabrication

To make an array of MFBGs, a multi-bay support piece was designed and 3D printed out of ABS plastic. A rendering of the support is shown in Figure 9.9.

Figure 9.10 shows the fabricated device. The four gray objects are ferrite choke toroids with a permeability of 550, and dimensions of 3.18 mm thick, an outer diameter of 9.65 mm

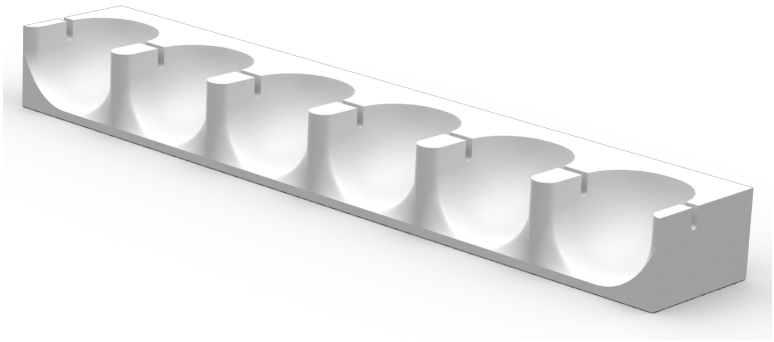

Figure 9.9: The rendering of the support backing used to array MFBGs devices. The bays are spaced with a $2\,\mathrm{cm}$ pitch.

Figure 9.10: The substantiation of an MFBGs array of the type shown in Figure 9.5. The ruler in the picture is in inches.

and inner diameter of 4.78 mm. The specification sheet for this C055276A2 Mag Inc. product states it has a mass of 1.5 g and volume of 164 mm^3. The fiber is glued with cyanoacrylate based super glue, whose drying was accelerated with Insta-Dry (a mixture of Naphtha (Petroleum) Hydrotreated Heavy and N,N Dimethyl-P-Toluidine) by Bob Smith Industries. The fiber was glued to the supporting structure each time it crossed it.

Figure 9.11 shows a second fabricated device. The six tilted silver objects are Neodymium-Iron-Boron magnets, grade N42, and dimensions of 1.5875 mm thick, an outer diameter of 6.35 mm and inner diameter of 1.5875 mm. The specification sheet for this R411 K and J Magnetics product states it has pull force of 5 N. This array has been specifically arrayed such that the north faces face each other, and south faces face each other. This creates strong repulsion between each magnet, keeping them separate and rotating them away from each other. On the right three magnets in the image, there are small spacers (cut pieces of

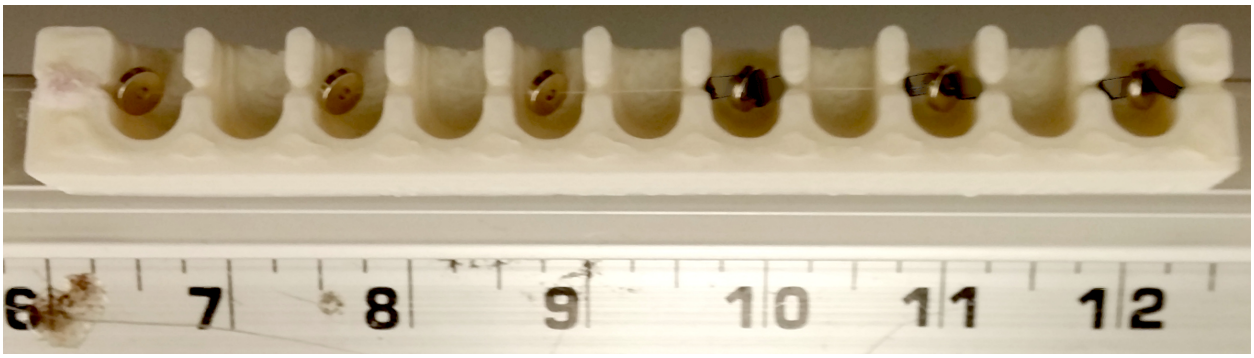

Figure 9.11: The substantiation of an MFBGs array of the type shown in Figure 9.8. The ruler in the picture is in inches.

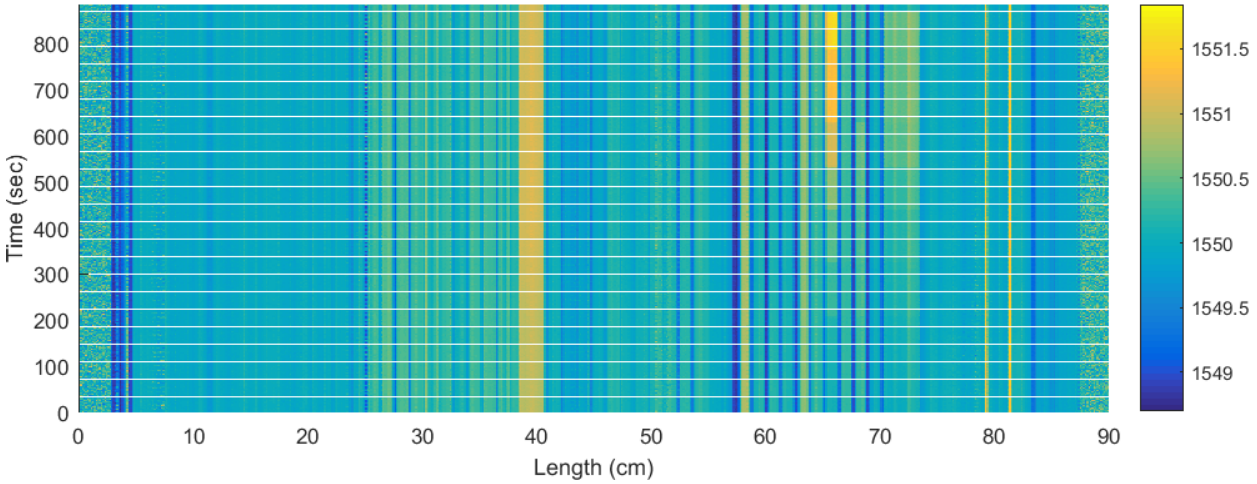

Figure 9.12: Raw FBG wavelength over time, along the length of 90 cm with 1.5 mm resolution used to de-multiplex. The color of the patch may be compared to the color bar on the right for the wavelength in nm.

coffee stir straws) which helped to center the magnets on the fiber.

9.5 Experiment and results

Figure 9.12 shows the raw reflected wavelength of the fiber optic. The x-axis is the length along the reflection data, which has been interrogated of fiber. The y-axis is time progression of the test. The Bragg imbued region of the fiber optic is 84 cm long. The first 3 cm of the data is free fiber, as well as the last 2.7 cm of the data. The region from 3 cm to 15 cm is loose FBG fiber and may be assumed at a neutral state. There is a pattern of thin regions of lower wavelength data, representing slight compression from gluing the fiber to the structure

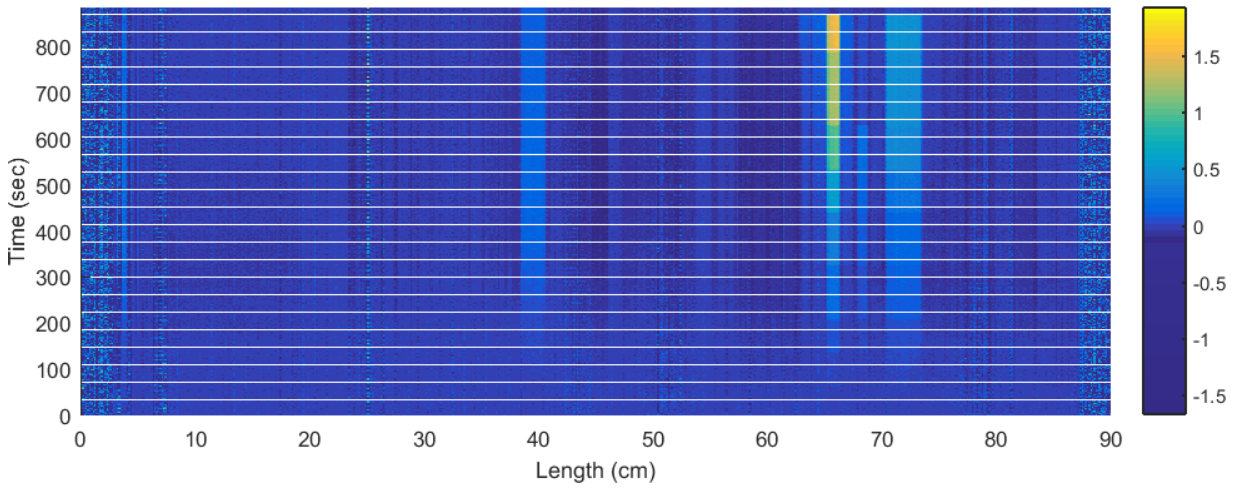

Figure 9.13: FBG wavelength shift over time, by subtracting the time 0 s in Figure 9.12 from the rest of the data at each point. The color of the patch may be compared to the color bar on the right for the wavelength shift in nm.

and also longer tension regions induced between these points. This is due to the glue used to adhere the fiber also compressing, simultaneously mildly straining the fiber between hold points. The region from 58 cm to 70 cm is where the magnetics were strung, as shown in Figure 9.11. Over time, a large test magnet was moved progressively closer towards a magnet strung at 67 cm in the data. This attracted the magnet, straining the fiber and shifting the Bragg wavelength to a longer λ_B.

Figure 9.13 shows the shift of reflected wavelength along the fiber over time from the data showed in Figure 9.12. The shift in wavelength as the magnet is moved closer to the strung magnet is quite apparent. The tension and strain due to this is clearly isolated from the two non-magnetic fiber sections on either side of the magnet. The magnets further over do not respond to the applied magnetic gradient. The data in the first 3 cm and last 2.7 cm of the plot is noise due to the lack of Bragg gratings to reflect back a consistent wavelength, leaving that spectrum to merely be determined by fiber aberrations and quite random.

Figure 9.14 shows this shift in Bragg wavelength vs. the magnetic field. The field was found by measuring it at the fiber for that distance between the large magnet and FBG magnetometer. Inset is the low field sensitivity. As the fiber optic system can distinguish shifts down to 10 pm, the device thus has a 2.3 Oe resolution. This is roughly 10x the earth's

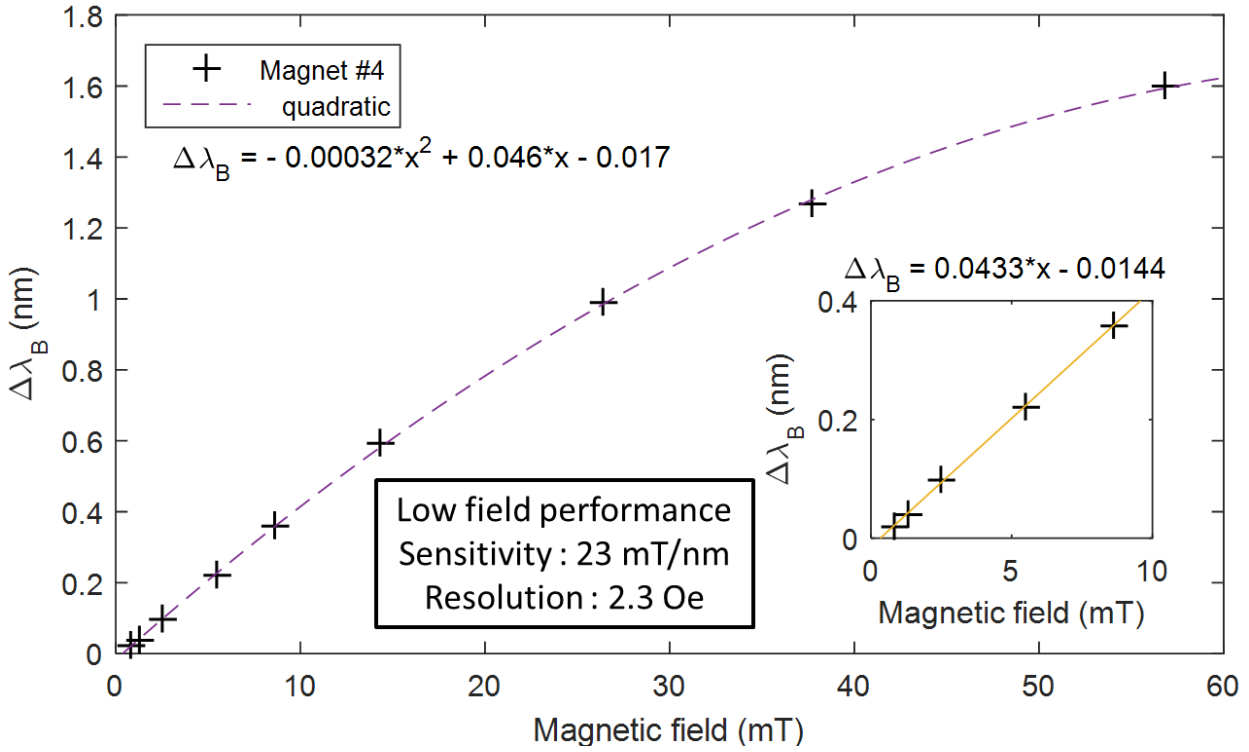

Figure 9.14: FBG wavelength shift vs. applied field at the point in the fiber where the magnet responded in Figure 9.13. Inset is the low field response enlarged. Both have polynomial fits included.

magnetic field (0.3 Oe), and on the order of a Hall Effect sensor's resolution. The sensor does not truly respond to magnetic fields, but instead magnetic field gradients.

Figure 9.15 shows this shift in Bragg wavelength vs. the magnetic field gradient. The gradient was found by taking the field measurements used in Figure 9.14, fitting an equation as a function of distance, and taking a derivate to use as the gradient at each test point. There is a sensitivity in the low gradient measurements of $0.91\,\mathrm{T\,m^{-1}}$. As the fiber optic system can distinguish shifts down to 10 pm, the device thus has a $0.0091\,\mathrm{T\,m^{-1}}$ resolution.

9.6 Future improvements

There are three directions for MFBG improvement: sensitivity of the device, directional (vector) sensing, and density of readings of arrayed devices.

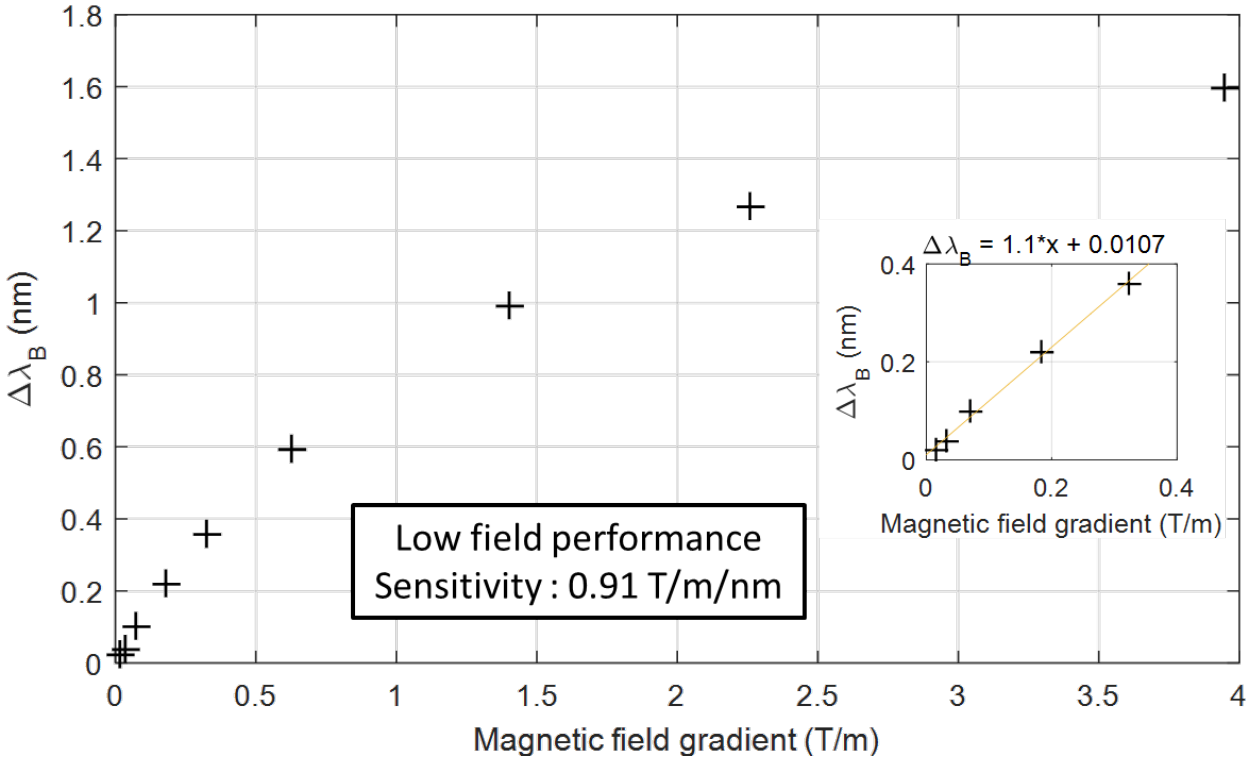

Figure 9.15: FBG wavelength shift vs. magnetic field gradient at the point in the fiber where the magnet responded in Figure 9.13 and Figure 9.14. Inset is the low gradient response enlarged with a linear fit included.

9.6.1 Sensitivity improvements

The sensitivity of this MFBG method is limited by the mechanical stiffness of the optical fiber, as well as the intensity of the magnetic moment. In this study, the fiber's 'force sensitivity' was $1\,\mathrm{nm\,N^{-1}}$. A $30\,\mu\mathrm{m}$ diameter tapered plastic optical fiber with a FBG has been made with a 'force sensitivity' of $643\,\mathrm{nm\,N^{-1}}$ [96]. This would proportionally increase the magnetic sensitivity of the sensor to be $643x$. Increasing the magnetic material and that magnetic material's permeability would proportionally increase the sensitivity. Metglas based beads would offer higher permeability than the ferrite toroid cores this work was done with.

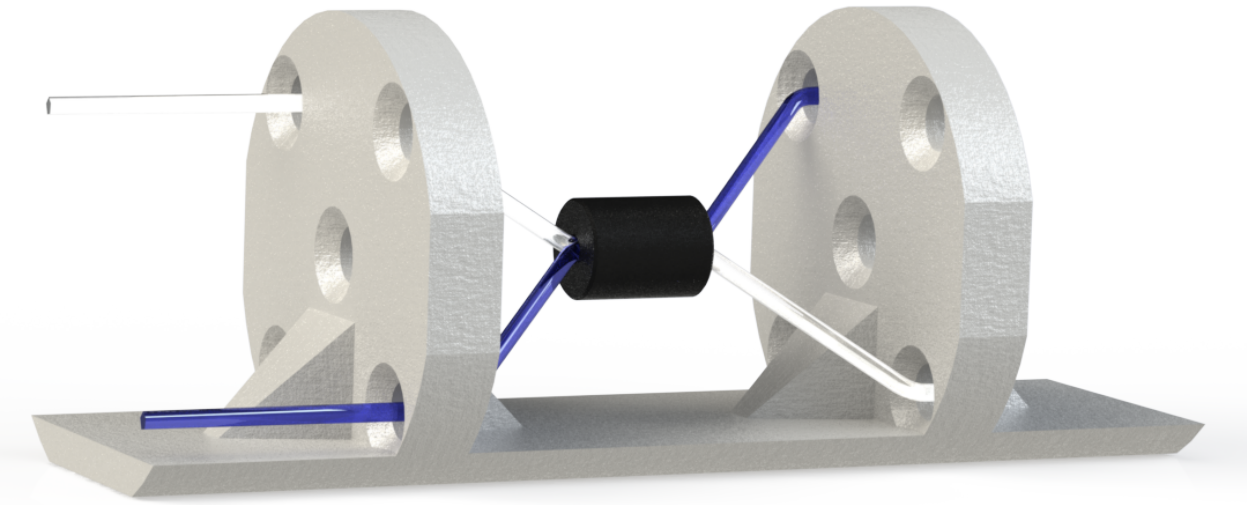

Figure 9.16: A magnetic bead or magnet may be strung with two fiber optics to offer a multi-dimensional gradient field reading. The two vertical supports are 1 in from front face to front face.

9.6.2 Directional sensitivity

While gluing the magnetic mass onto the fiber as proposed in Figure 9.6 will offer a directional sensitivity, it may be that the added complexity of this is harder than having two isolated sensing fibers. A dual fiber method was proposed prior to the glued ferrite idea's origination.

Collaborator Tony Barra proposed a 2D MFBG sensor of the style shown in Figure 9.16. In this CAD rendering, the optical fiber's diameter and color have been amplified for visibility. Two fibers 'perpendicular' to each other allow for in-plane vector sensitivity. The force of the bead in the X-Y plane is captured in the clear and blue optical fiber. While this proposal does not need the gluing of the bead as proposed in Figure 9.6, the sensitivity could be enhanced by gluing the magnetic mass on to the fiber at its middle location. Glue would prevent the mass from shifting laterally on the fibers. Now the mass will induce some direct tension in the fiber most parallel to the magnetic field gradient. The mechanical advantage

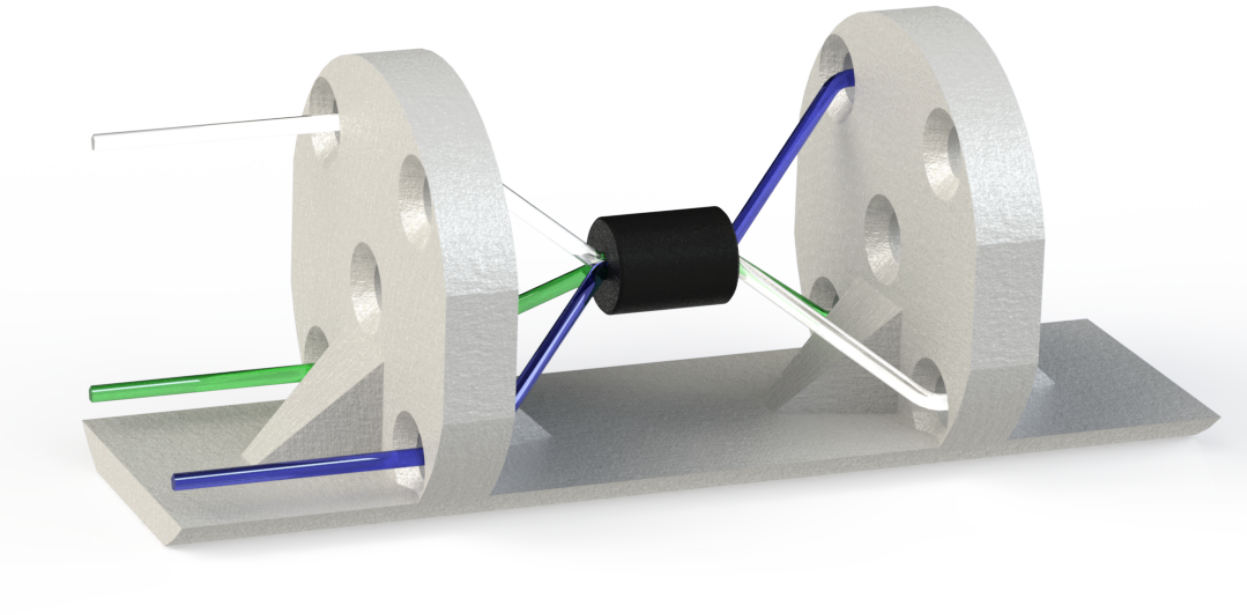

Figure 9.17: A magnetic bead or magnet may be strung with three fiber optics to offer a multi-dimensional gradient field reading.

of bending the fiber to induce tension over the directly attached magnet of Pacheco and Bruno [87] will be eliminated.

An extension of the 2D MFBG is a third fiber added out of plane for 3D field sensing. Figure 9.17 shows the method. The force of the bead in the X-Y plane is captured in the bead's clear and blue fibers. The new green fiber captures the bead's out of plane contribution. This methodology allows each fiber to be a separate X, Y, and Z measurement, easing a distributed measurement of a largely distributed field gradient. No glue is needed in this model.

An extension of the 3D MFBG is a 3D method with only two fibers. Figure 9.18 shows the method. The red caps on either side of the middle mass are glued, firmly attaching the magnetic bead to both fibers. The force of the bead in the X-Y plane is captured in the bead's clear and blue fibers on the left side of the mass. The right side fibers of the mass allows for measuring the Z vector contribution by the difference in force between the blue

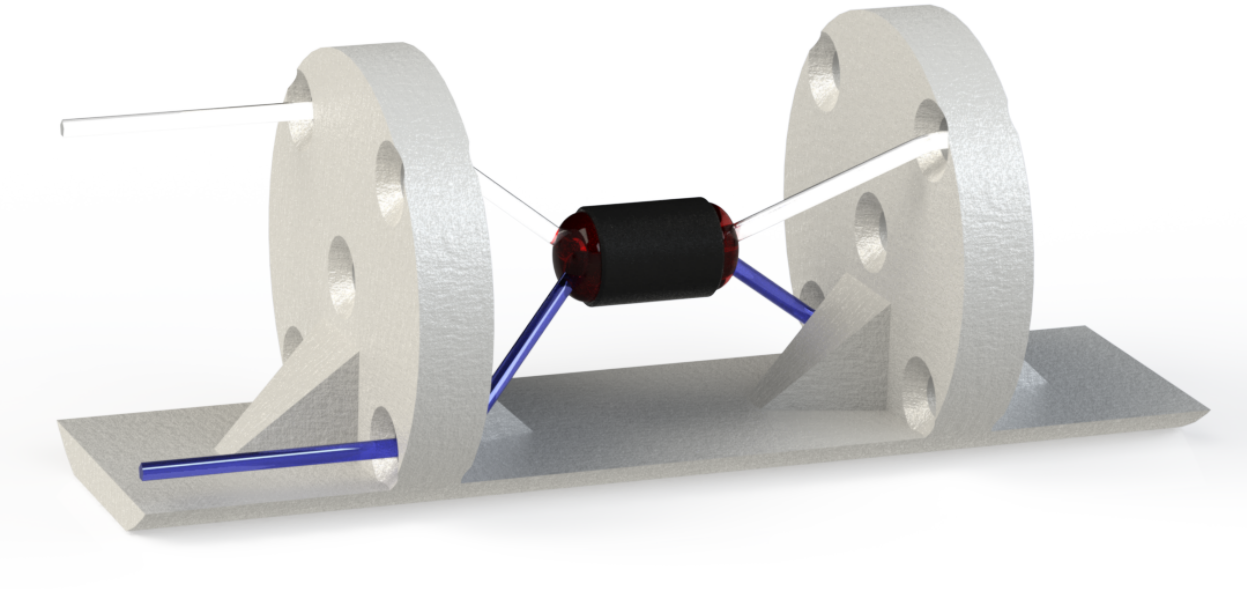

Figure 9.18: A magnetic bead or magnet may be strung with two fiber optics to offer a multi-dimensional gradient field reading.

and clear fibers. The new orientation of the fibers replaces the need for the green optical fiber in Figure 9.17.

This work will continue to develop past what is covered here and is the active extension of this Ph.D. thesis at time of publication.

9.6.3 Density of sensors

There are a few limitations to the density of sensors achievable. First, the demultiplexing limit of FBGs has been shown to exist below 500 µm in Chapter 3. Next, in constructing the sensor, 1 mm of support structure, 1 mm of magnetic material, and 1 mm of fiber optic on either side of the mass will total to a 4 mm sensor limit. This is only for the 1D sensor. 2D and 3D sensors function based on a fiber bent and twisting between mass and posts. The bending radius achievable is the limited factor as sensor densities of 0.75 in on the type shown in Figure 9.18 have been found to break optical fiber in fabrication of the device with

4 mm long masses strung. A 1 in spaced fiber array is the current expected limit for vector field sensing.

9.7 Conclusion

Introduced here is a simple and 'clean' way to sense magnetic gradients, and the fields which create them. This method relies on off-the-shelf components instead of fancy magneto-optic materials such as Lanthanum Strontium Manganite $La_{0.66}Sr_{0.33}MnO_3$ (LSMO). To enable magnetic field sensing in the next decade, this method and its derivatives will be the most practical, economical method. The main draw-back of this method vs. other MFBG sensors are the vibrational sensitivity and larger size than a small optical fiber. Both fluid and magneto-strictive sensors could be smaller and vibrationally isolated from a structure.

Chapter acknowledgment

The author would like to specifically thank Frank Pena of NASA and the AERO institute for lending his time and resources to test these devices using the fiber optic interrogator at the AERO institute, and collaborator Tony Barra for 'shooting the shit' in the later afternoons together which led to this idea's germination. Thank you Tony for also continuing this research. Thank you Professor Carman for being both proud enough of your students and humble enough yourself to say on numerous occasions that you did not think this idea was worth researching yet allowing us to anyways. Finally, thank you to AERO Institute and NASA LSP whose co-mingled funding sponsored this work in the waning weeks of this Ph.D.

CHAPTER 10

Conclusions and discussion

This Ph.D.'s aim was to advance the fiber Bragg grating (FBG) field and it has modestly done so. This spatial resolution able to be demultiplexed was shown to be improved, showing down to 500 µm FBG regions and strain concentrations from structural microcracks. This recovered the signal from an otherwise unreadable, multi-fringent FBG sensor into an understandable reading. Next, two paths for introducing magnetic sensing to make a magnetic fiber Bragg grating (MFBG) were pursued. These were a 'sexy' magneto-optical method, and a mundane but effective 'engineering' solution.

The magnetorefractive effect (MRE) was reviewed, and a candidate material (Lanthanum Strontium Manganite $La_{0.66}Sr_{0.33}MnO_3$ (LSMO)) which could change strongly in index of refraction with applied magnetic field was identified. The reflectivity of a sample was studied, and then the index of refraction of the material was characterized under various magnetic fields and temperatures to create a novel index of refraction function for LSMO. A proof of concept optical device was devised, fabricated and characterized to detect index of refraction changes. This had LSMO incorporated and revealed the high absorption of LSMO. This showed that while the index is changing, the material should not be used in any transmission mode.

Next, a short 'engineering' method of MFBG device experimentation was pursued. By stringing magnetic materials onto a mounted fiber of FBGs then the magnetic field applied to the bead was transduced into tension and strain in the fiber. Fabrication of this concept and testing revealed a very strong response, similar to that of Hall effect sensors.

10.1 Answering the Research Questions

The research questions at the outset of this Ph.D. were:

1. Why are some (many) FBGs reporting back peaks when attached to a composite overwrapped pressure vessel (COPV)?
2. What structural health monitoring (SHM) can be done with these FBGs?
3. How can magnetic sensitivity be added to a FBG improving on Emmons et al.'s work?

The first question was answered by the presence of microcracks in the composite structure loading a 5 mm grating with a strain state ranging from 6 mϵ to 17 mϵ and so creating a chirped grating reflecting a broad spectrum. The second question was answered by it will be possible to calculate microcrack density, which in corner cases of composites (those exposed to fluids and icing cycles) can expose a structure vulnerable to future failure. The third question was answered by MRE being a probable method to enhance solid materials whose index of refraction is influenced by applied magnetic field. This will require overcoming high absorption in those materials.

In the process of this Ph.D. further research questions developed:

1. Why did LSMO possessing MRE not make a successful MFBG?
2. How else could an MFBG be made?
3. How could one use an MFBG?

The high absorption of light by LSMO limits its use, especially in an Mach Zehnder interferometer (MZI) or FBG method as these require it to conduct light with low loss. Next, an MFBG may be made via magnetic field transduction to strain, and then strain detection. Finally, an MFBG may be used in magnetic flux leakage (MFL) inspections, as well as eddy current monitoring applications and magnetic exposure monitoring (akin to dye tilt sensors on a package, but monitoring magnetic exposure).

10.2 Connections and conclusions

FBGs are highly multiplexable and seeking broader commercial usage. While they may be made sensitive to many phenomena via novel optical materials, it may be easiest to instead transduce many phenomena into strain effects, which can then be measured by the FBG's strongest detection method.

10.3 Theoretical implications and recommendations for further research

If the absorption of light by MRE materials can be overcome, a novel optical material would be introduced to the broader optics community, which could have impactful use. In particular, adaptive optics systems would embrace a way to add continuous instead of discrete adapting of lens and mirror surfaces. When working on a new magneto-optical material, the two most important qualities are its transparency and magnetic nature. Secondly, its interaction of the two: strong interactions are most useful in materials that are already good at both fields they are bridging.

APPENDIX A

MZI fabrication

This fabrication process details refer to the process performed for the MZI device discussed in Chapter 7.

A.1 Fabrication steps

Fabrication of the wafers was performed in the Integrated Systems Nanofabrication Cleanroom (ISNC) at the California NanoSystems Institute (CNSI) of UCLA. The steps of the process are detailed in Table A.1 and the exact machines are in Table A.2.

Table A.1: Detailed fabrication flow

	Process Flow	Tool	Time or dose	Recipe
Alignment marks	Coat wafer with PR	Track Coater		Positive PR
	Expose 0° marks	Stepper	$150\,\mathrm{mJ\,s^{-1}}$	A-Zero
	Expose 90° marks	Stepper	$150\,\mathrm{mJ\,s^{-1}}$	D-Zero
	Develop	Track Developer		Positive PR
	Inspect	Microscope		
	Etch Si_3N_4	RIE Etcher	8 min	Nitride-Fast
	Strip/Clean	Asher	3 min	240 °C
	Wash	Wafer Washer		
	Clean	Asher	1 min	50 °C

Continued on next page

Table A.1 – continued from previous page

	Process Flow	Tool	Time or dose	Recipe
Waveguides	Coat wafer with PR	Track Coater		Negative PR
	Expose Top	Stepper	$150\,\mathrm{mJ\,s^{-1}}$	A - Top
	Expose Bottom	Stepper	$150\,\mathrm{mJ\,s^{-1}}$	B - Bottom
	Develop	Track Developer		Negative PR
	Inspect	Microscope		
	Measure film thickness	Nanospecs		Si_3N_4 on SiO_2
	Etch Si_3N_4	RIE Etcher	18 s	Nitride-Slow-WG
	Measure film thickness	Nanospecs		Si_3N_4 on SiO_2
	Strip PR	AZ 300T Bath	30 min	80 °C
	Wash	Wafer Washer		
	Strip/Clean	Asher	3 min	240 °C
SiO_2 top layer	Coat wafer with PR	Track Coater		Negative PR
	Expose Center	Stepper	$150\,\mathrm{mJ\,s^{-1}}$	C - Center
	Expose Entrance	Stepper	$150\,\mathrm{mJ\,s^{-1}}$	D - Entrance Bar
	Develop	Track Developer		Negative PR
	Inspect	Microscope		
	Evaporate	CHA	15 000 Å	$5\,\mathrm{Å\,s^{-1}}$ of SiO_2
Etch sensing window	Coat wafer with PR	Track Coater		Positive PR
	Expose Center	Stepper	$150\,\mathrm{mJ\,s^{-1}}$	C - Center
	Expose Entrance	Stepper	$150\,\mathrm{mJ\,s^{-1}}$	D - Entrance Bar
	Develop	Track Developer		Positive PR
	Inspect	Microscope		
	Etch SiO_2	RIE Etcher	40 min	Oxide-Slow
	Etch SiO_2	RIE Etcher	14 min	Oxide-Fast
	Strip PR	AZ 300T Bath	30 min	80 °C
	Wash	Wafer Washer		
	Strip/Clean	Asher	3 min	240 °C
E-Beam alignment markers	Coat wafer with PR	Track Coater		Positive PR
	Expose Global	Stepper	$150\,\mathrm{mJ\,s^{-1}}$	Ebeam - 60 µm
	Expose Local	Stepper	$150\,\mathrm{mJ\,s^{-1}}$	Ebeam - 20 µm
	Develop	Track Developer		Positive PR
	Inspect	Microscope		
	Evaporate	CHA	0.050 kÅ to 0.300 kÅ	$1\,\mathrm{Å\,s^{-1}}$ to $2\,\mathrm{Å\,s^{-1}}$ of Ti
	Evaporate	CHA	1.000 kÅ to 3.600 kÅ	$3\,\mathrm{Å\,s^{-1}}$ of Au
	Lift off	Acetone bath	12 h	Oscillating Table
	Rinse	DI water	until Au removed	
	Wash	Wafer Washer		
	Inspect	Microscope		
	Check marker height	Profilometer		

Continued on next page

Table A.1 – continued from previous page

	Process Flow	Tool	Time or dose	Recipe
Entrance gratings	Clean	Asher	1 min	50 °C
	HMDS Prime	HMDS Tank	10 min	
	Apply PR	Wafer Spinner	60 s	3000 RPM
	Bake	Hot Plate	2 min	180 °C
	E-beam Lithography	E-beam Writer	180 µC/cm^2	50 µm x 50 µm gratings
	Develop	ZED-N50 bath	60 s	IPA rinse, blow dry
	Inspect	Microscope		
	Etch Si_3N_4	RIE Etcher	90 s	Nitride-Slow
	Strip	NMP bath	12 h	35 °C
	Wash	Wafer Washer		
	Inspect	Microscope		
	Check grating height	Profilometer		

A.2 Fabrication step process details

A.2.1 PR details

Positive PR is SPR 700, and is developed with MF 26. Negative PR is AZ NLOF 2020, and is developed with MF319.

The positive SPR 700 PR track coater process is 60 s HMDS vapor chamber at 120 °C. Cool for 30 s. Then the wafer is moved to the spinner. There it is spun for 5 s at 2000 RPM as the SPR 700 PR is applied. Then the wafer is spun for 25 s at 4500 RPM, followed by 10 s at 750 RPM, and then 15 s at 2000 RPM. The wafer is moved to the hot plate, and soft baked for 60 s at 95 °C.

The positive SPR 700 PR track developer process is 60 s pre-bake at 115 °C. Cool for 30 s. Then the wafer is moved to the spinner. There it is spun for 6 s at 75 RPM as the MF 26 developer is applied. Then the wafer is left to sit for 55 s (so spun at 0 RPM), followed by 15 s at 1000 RPM, and then 12 s at 500 RPM as DI is used to flush the wafer, and then finally this is spun off for 20 s at 3000 RPM. The wafer is moved to the hot plate, and hard baked for 60 s at 155 °C.

Table A.2: Listing of the full names of machines and short-hand names

Short Name	Full Name
Stepper	ASML 550 Stepper
Track Coater	SVG 8800 Track Coater
Track Developer	SVG 8800 Track Developer
Asher	Matrix 105 Asher
RIE Etcher	Oxford Plasmalab 80 Plus RIE
Microscope	Leica DM2500M
Wafer Washer	Verteq Auto-Washer
E-beam Writer	Vistec EBPG 5000+ES
Profilometer	Vecco DEKTAK 150 Profilometer
AFM	Bruker Dimension Icon AFM
CHA	Solution Process Development System
Nanospecs	Nanospec AFT 2100

The negative AZ NLOF 2020 PR track application process is 60 s HMDS vapor chamber at 120 °C. Cool for 25 s. Then the wafer is moved to the spinner. There it is spun for 5 s at 200 RPM as the AZ NLOF 2020 PR is applied. Then the wafer is spun for 25 s at 3100 RPM, followed by 15 s at 750 RPM, and then 15 s at 2000 RPM. The wafer is moved to the hot plate, and soft baked for 60 s at 110 °C.

The positive AZ NLOF 2020 PR track developer process is 60 s pre-bake at 110 °C. Cool for 30 s. Then the wafer is moved to the spinner. There it is spun for 5 s at 75 RPM as the MF 319 developer is applied. Then the wafer is left to sit for 55 s (so spun at 0 RPM), followed by 15 s at 1000 RPM as DI is used to flush the wafer, and then finally this is spun off for 15 s at 3000 RPM. The wafer is moved to the hot plate, and hard baked for 60 s at 115 °C.

A.2.2 RIE details

There are 5 recipes used on the Oxford Plasmalab 80 Plus RIE. They are listed in Table A.3.

A.2.3 Asher details

Asher 240 °C recipe is 500 W for 3 min with 45% O_2.

Table A.3: Listing of RIE recipes

Recipe	RF power	Pressure	Gas 1	Gas 2
Nitride-Slow	200 W	0.035 torr	25 sccm Ar	25 sccm CHF_3
Nitride-Slow-WG	50 W	0.035 torr	25 sccm Ar	25 sccm CHF_3
Nitride-Fast	200 W	0.055 torr	3 sccm O_2	30 sccm CHF_3
Oxide-Slow	200 W	0.035 torr	25 sccm Ar	25 sccm CHF_3
Oxide-Fast	200 W	0.15 torr	3 sccm O_2	35 sccm CF_4

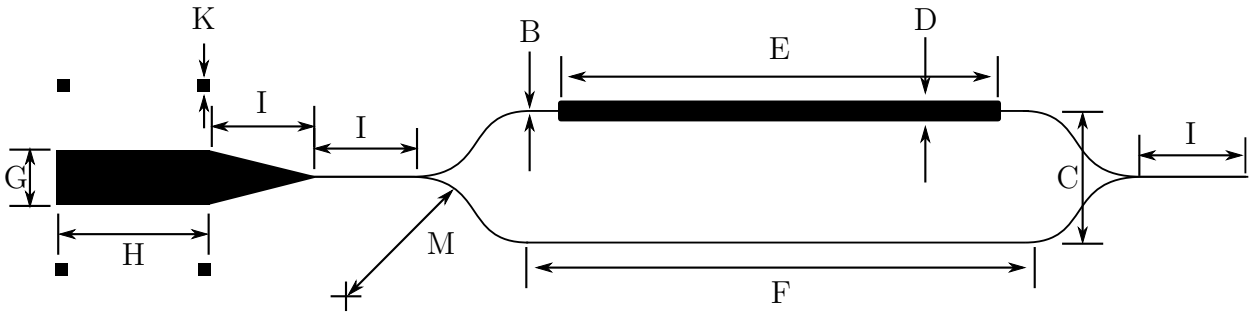

Figure A.1: A diagram of the MZI for the dimensions in Table A.4. Note that the diagram is not to scale.

Table A.4: Listing of MZI dimensions

Dimension	Value	Reference	Figure
Wafer Diameter	101.6 mm or 4 inch	A	
Waveguide Width	2.5 µm	B	A.1
arm separations	100 µm	C	A.1
LSMO width	100 µm	D	A.1
LSMO Length	15.3 mm	E	A.1
Straight Arm Length	17 mm	F	A.1
Entrance flag width	50 µm	G	A.1
Entrance flag Length	5 mm	H	A.1
Entrance to Arm split	10 mm	I	A.1
E-Beam Litho Global Marker	60 µm	J	
E-Beam Litho local Marker	20 µm	K	A.1
Device Array Pitch	1 mm	L	
S-bend Radius	80 mm	M	A.1

Asher 50 °C recipe is 80 W for 1 min with 45% O_2.

A.3 MZI device geometry details

APPENDIX B

Magnetic MZI Fabrication

B.1 Fabrication steps

Fabrication of the wafers was performed in the ISNC at the CNSI of UCLA. The steps of the process are detailed in Table B.1 and the exact machines are in Table A.2. Recipes and design layout are detailed in the previous Chapter.

Table B.1: Detailed fabrication flow

	Process Flow	Tool	Time or dose	Recipe
Alignment marks	Coat wafer with PR	Track Coater		Positive PR
	Expose 0° marks	Stepper	$150\,\mathrm{mJ\,s^{-1}}$	A-Zero
	Expose 90° marks	Stepper	$150\,\mathrm{mJ\,s^{-1}}$	D-Zero
	Develop	Track Developer		Positive PR
	Inspect	Microscope		
	Etch Si_3N_4	RIE Etcher	8 min	Nitride-Fast
	Strip/Clean	Asher	3 min	240 °C
	Wash	Wafer Washer		
	Clean	Asher	1 min	50 °C
Waveguides	Coat wafer with PR	Track Coater		Negative PR
	Expose Top	Stepper	$150\,\mathrm{mJ\,s^{-1}}$	A - Top
	Expose Bottom	Stepper	$150\,\mathrm{mJ\,s^{-1}}$	B - Bottom
	Develop	Track Developer		Negative PR
	Inspect	Microscope		
	Measure film thickness	Nanospecs		Si_3N_4 on SiO_2
	Etch Si_3N_4	RIE Etcher	18 s	Nitride-Slow-WG
	Measure film thickness	Nanospecs		Si_3N_4 on SiO_2
	Strip PR	AZ 300T Bath	30 min	80 °C
	Wash	Wafer Washer		
	Strip/Clean	Asher	3 min	240 °C

Continued on next page

Table B.1 – continued from previous page

	Process Flow	Tool	Time or dose	Recipe
Etch sensing window LSMO regions and SiO_2 top	Coat wafer with PR	Track Coater		Positive PR
	Expose Center	Stepper	$150\,mJ\,s^{-1}$	C - Center 2/3rds
	Develop	Track Developer		Positive PR
	Strip/Clean	Asher	1 min	50 °C
	Sputter		200 nm	
	Lift off	Acetone bath	1 h	Oscillating Table
	Strip/Clean	Asher	3 min	240 °C
	Anneal	Oven	2 h	800 °C
	Inspect	Microscope		
	Grow SiO_2	PECVD	1500 nm	$10\,nm\,min^{-1}$ of SiO_2
	Coat wafer with PR	Track Coater		Positive PR
	Expose Center	Stepper	$150\,mJ\,s^{-1}$	C - Center 1/3rds
	Expose Entrance	Stepper	$150\,mJ\,s^{-1}$	D - Entrance Bar
	Develop	Track Developer		Positive PR
	Inspect	Microscope		
	Etch SiO_2	10:1 BHF/BOE	about 210 s	$550\,nm\,min^{-1}$
	Wash	Wafer Washer		
	Strip/Clean	Asher	3 min	240 °C
E-Beam alignment markers	Coat wafer with PR	Track Coater		Positive PR
	Expose Global	Stepper	$150\,mJ\,s^{-1}$	Ebeam - 60 µm
	Expose Local	Stepper	$150\,mJ\,s^{-1}$	Ebeam - 20 µm
	Develop	Track Developer		Positive PR
	Inspect	Microscope		
	Evaporate	CHA	0.050 kÅ to 0.300 kÅ	$1\,Å\,s^{-1}$ to $2\,Å\,s^{-1}$ of Ti
	Evaporate	CHA	0.600 kÅ to 3.600 kÅ	$3\,Å\,s^{-1}$ of Au
	Lift off	Acetone bath	12 h	Oscillating Table
	Rinse	DI water	until Au removed	
	Wash	Wafer Washer		
	Inspect	Microscope		
	Check marker height	Profilometer		

Continued on next page

Table B.1 – continued from previous page

	Process Flow	Tool	Time or dose	Recipe
Entrance gratings	Clean	Asher	1 min	50 °C
	HMDS Prime	HMDS Tank	10 min	
	Apply PR	Wafer Spinner	60 s	3000 RPM
	Bake	Hot Plate	2 min	180 °C
	E-beam Lithography	E-beam Writer	180 µC/cm^2	50 µm x 50 µm gratings
	Develop	ZED-N50 bath	60 s	IPA rinse, blow dry
	Inspect	Microscope		
	Etch Si_3N_4	RIE Etcher	90 s	Nitride-Slow
	Strip	NMP bath	12 h	35 °C
	Wash	Wafer Washer		
	Inspect	Microscope		
	Check grating height	Profilometer		

Glossary

T_C Curie temperature. xv, 58, 59, 60, 65, 66, 65, 71, 72, 73, 85, 89, 90, 95, 108, 109

AC alternating current. 9

ACU air conditioning unit. 103, 110

CMR colossal magnetoresistance. 59, 65, 68, 71, 73, 76

CNSI California NanoSystems Institute. 116, 132, 135, 141, 163, 168

COMSOL COMSOL Multiphysics FEA software. xviii, 98, 102

COPV composite overwrapped pressure vessel. xiii, xiv, xv, 1, 3, 29, 37, 38, 40, 41, 42, 43, 44, 45, 46, 51, 53, 54, 53, 161

CTE coefficient of thermal expansion. 29

CVD chemical vapor deposition. 25, 135

DAQ data acquisition unit. 31

DC direct current. 6, 9

DP data points. 48, 50

EM electromagnetic. xiii, 6, 7, 9, 10, 11, 14, 59, 61, 64, 101

FBG fiber Bragg grating. xiii, xiv, xv, xxi, xxii, 3, 12, 14, 22, 25, 26, 27, 28, 29, 30, 31, 33, 34, 35, 37, 38, 40, 41, 42, 43, 44, 45, 44, 46, 45, 46, 47, 48, 47, 48, 50, 52, 53, 54, 52, 60, 74, 78, 80, 82, 83, 113, 134, 143, 145, 143, 147, 148, 149, 152, 153, 154, 158, 160, 161

FFT fast Fourier transformation. 35

FOID fiber optic interrogation device. xiv, 42

FWHM full width half max. 47

GMR giant magnetoresistance. 59, 61, 62, 63, 64, 65, 66, 67, 68

IR infrared. xvi, 9, 10, 15, 58, 62, 69, 71

ISNC Integrated Systems Nanofabrication Cleanroom. 116, 132, 135, 141, 163, 168

KSC Kennedy Space Center. 113, 132, 133, 141

LAMO Silver-doped Lanthanum Manganite $La_{0.66}Ag_{0.33}MnO_3$. xvi, 65, 75, 76

LAO Lanthanum Aluminate $LaAlO_3$. 69

LCMO Lanthanum Calcium Manganese Oxide $La_{0.66}Ca_{0.33}MnO_3$. xvi, 69, 70, 71, 72, 73, 72, 73, 74, 75, 76, 131, 172

LFA longitudinal fixed angle. xvii, 86, 88, 91

LPCMO lead doped Lanthanum Calcium Manganese Oxide $La_{0.66}Ca_{0.33}MnO_3$ (LCMO) $(Pr_{0.4}La_{0.6})_{0.7}Ca_{0.3}MnO_3$. 73, 74

LSMO Lanthanum Strontium Manganite $La_{0.66}Sr_{0.33}MnO_3$. xvi, xvii, xviii, xxi, 19, 31, 58, 60, 65, 69, 70, 73, 77, 78, 79, 80, 83, 85, 86, 92, 91, 94, 95, 96, 98, 100, 101, 102, 103, 108, 109, 110, 113, 114, 116, 129, 130, 131, 134, 135, 136, 139, 140, 159, 160, 161

LSP Launch Services Program. 113, 132, 133, 134, 141

MAI multiple-angle-of-incidence. 98, 102

MFBG magnetic fiber Bragg grating. xvii, xxi, xxii, 22, 58, 80, 82, 83, 94, 110, 113, 131, 133, 134, 145, 147, 148, 147, 149, 150, 151, 154, 156, 157, 159, 160, 161

MFL magnetic flux leakage. xiii, xxii, 2, 5, 149, 161

mid-IR mid-infrared. 66

MO magneto-optical. 12, 59

MOKE magneto optical Kerr effect. xvi, xvii, 70, 72, 73, 74, 87, 94, 110

MR magnetoresistance. 58, 59, 61, 64, 69, 71

MRE magnetorefractive effect. xv, xvi, xvii, xviii, xxi, xxiv, 9, 19, 58, 59, 60, 61, 63, 62, 64, 65, 66, 67, 66, 67, 68, 67, 68, 69, 70, 71, 72, 73, 74, 75, 76, 77, 78, 80, 82, 85, 86, 89, 90, 89, 90, 91, 90, 91, 93, 95, 104, 105, 109, 110, 113, 134, 140, 160, 161, 162

MRF magnetorheological fluid. 78

MT magnetotransmission. xv, xvi, xxi, 61, 62, 61, 62, 63, 64, 65, 69, 70, 75, 76, 85, 95, 140

MZI Mach Zehnder interferometer. xix, xx, xxi, xxiii, 82, 113, 114, 113, 114, 115, 116, 118, 119, 118, 119, 120, 121, 122, 123, 124, 123, 124, 125, 126, 128, 129, 130, 131, 133, 134, 135, 134, 135, 136, 139, 161, 163, 167

NASA National Air and Space Administration. 3, 37, 134

near IR mid-infrared. 69

NGO Neodymium Gallate $NdGaO_3$. xvii, xviii, 85, 86, 91, 95, 96, 98, 101

OFDR optical frequency domain reflectometery. xiii, 35, 37, 41, 42, 47

OTS off the shelf. 69, 92

PBG planar Bragg grating. 82

PE photo-elasticity. 32

PEM photo-elastic modulator. 87

PLD pulse laser deposition. 73

POF plastic optical fibers. 22

PR photo resist. 116, 135

RIU/G refractive index unit per absolute Gauss. 100

RMBE reactive molecular-beam epitaxy. 86, 96

ROI return on investment. 3

SAL self averaging limit. 63, 64

SEM scanning electron microscopy. xvii, 78

SHM structural health monitoring. 37, 38, 40, 41, 161

STO Strontium Titanate $SrTiO_3$. 69

TE transverse electric. 124

TEM transmission electron microscopy. xvii, 78

TM transverse magnetic. xx, 124, 126

UV ultraviolet. xiii, 15, 25, 27, 33, 34, 60, 89, 140

WDM wavelength domain multiplexing. 35, 42

References

[1] Corning Optical Fiber — Forty Years of Fiber Overview, 2013. [22]

[2] 4DSP-LLC. NASA Grants 4DSP License for Sensing Technology. 1(775):12–13, 2011. [42]

[3] C. Adamo, X. Ke, H. Q. Wang, H. L. Xin, T. Heeg, M. E. Hawley, W. Zander, J. Schubert, P. Schiffer, D. a. Muller, L. Maritato, and Darrell G. Schlom. Effect of biaxial strain on the electrical and magnetic properties of (001) La[sub 0.7]Sr[sub 0.3]MnO[sub 3] thin films. *Applied Physics Letters*, 95(11):112504, 2009. [86, 87, 96]

[4] Richard J. Black, David Zare, Levy Oblea, Yong-Lae Park, Behzad Moslehi, and Craig Neslen. On the Gage Factor for Optical Fiber Grating Strain Gages. *Proceedings of Society for the Advancement of Materials and Process Engineering (SAMPE'08)*, 2008. [30]

[5] LC Boles and KJ Lohmann. True navigation and magnetic maps in spiny lobsters. *Nature*, 421(January), 2003. [2]

[6] N F Borrelli and R a Miller. Determination of the individual strain-optic coefficients of glass by an ultrasonic technique. *Applied Optics*, 7(5):745–50, may 1968. [15]

[7] David Brewster. Depolarisation of light as exhibited by various mineral, animal, and vegetable bodies, with a reference of the phenomena to the general principles of polarisation. *Philosophical Transactions of the Royal Society*, 105:29–53, jan 1815. [14]

[8] I.V. Bykov and Elena Alexandrovna Ganshina. Magnetorefractive effect in granular alloys with tunneling magnetoresistance. *Physics of the Solid State*, 47(2):281–286, 2005. [61]

[9] IV Bykov, Elena Alexandrovna Ganshina, Alexander B. Granovsky, and V. S. Gushchin. Magnetorefractive effect in granular films with tunneling magnetoresistance. *Physics of the Solid State*, 42(3):498–502, 2000. [xvi, 62, 66, 67, 68]

[10] J. M. Caicedo, S. K. Arora, R. Ramos, I. V. Shvets, J. Fontcuberta, and G. Herranz.

Large magnetorefractive effect in magnetite. *New Journal of Physics*, 12(10):103023, oct 2010. [62, 75]

[11] J. M. Caicedo, M. C. Dekker, K. Dörr, J. Fontcuberta, and G. Herranz. Strong magnetorefractive and quadratic magneto-optical effects in (Pr0.4La0.6)0.7Ca0.3MnO3. *Physical Review B*, 82(14):140410, oct 2010. [xvi, 62, 74, 76]

[12] William D. Callister. *Materials Science and Engineering: An Introduction*. John Wiley & Sons, 7th edition, 2007. [2]

[13] Chih-Min Chuang, Ming-Chung Wu, Yu-Ching Huang, Kuo-Chung Cheng, Ching-Fu Lin, Yang-Fang Chen, and Wei-Fang Su. Nanolithography made from water-based spin-coatable LSMO resist. *Nanotechnology*, 17:4399–4404, 2006. [100]

[14] D. Colladon. On the reflections of a ray of light inside a parabolic liquid stream. *Comptes Rendus*, 15:800–802, 1842. [22, 23]

[15] AW Crook. The reflection and transmission of light by any system of parallel isotropic films. *JOSA*, 38(11):954–964, 1948. [19, 100, 105]

[16] B. D. Cullity and C. D. Graham. *Introduction to magnetic materials*. IEEE Press, Piscataway, New Jersey, second edition, 2009. [2]

[17] Jixiang Dai, Minghong Yang, Xiaobing Li, Hongliang Liu, and Xinglin Tong. Magnetic field sensor based on magnetic fluid clad etched fiber Bragg grating. *Optical Fiber Technology*, 17(3):210–213, may 2011. [78, 81]

[18] Isaac Daniel and Ori Ishai. *Engineering Mechanics of Composite Materials*. Oxford University Press, New York, New York, 2nd edition, 2006. [1, 38, 51, 54]

[19] Ramzy Daou, Franziska Weickert, Michael Nicklas, Frank Steglich, Ariane Haase, and Mathias Doerr. High resolution magnetostriction measurements in pulsed magnetic fields using fiber Bragg gratings. *The Review of scientific instruments*, 81(3):033909, mar 2010. [27]

[20] D. Davino, C. Visone, C. Ambrosino, S. Campopiano, a. Cusano, and a. Cutolo. Compensation of hysteresis in magnetic field sensors employing Fiber Bragg Grating and magneto-elastic materials. *Sensors and Actuators A: Physical*, 147(1):127–136, sep 2008. [xxi, 27, 143, 144, 145]

[21] Claire Davis, Silvia Tejedor, Ivan Grabovac, James Kopczyk, and Travis Nuyens. High-Strain Fiber Bragg Gratings for Structural Fatigue Testing of Military Aircraft. *Photonic Sensors*, 2(3):215–224, jul 2012. [38, 47]

[22] René Descartes. *Le Monde, ou Traite de la lumiere*. Abaris Books, New York, New York, 1979. [6]

[23] Mark E Deutschlander, John B Phillips, and S Chris Borland. The case for light-dependent magnetic orientation in animals. *Journal of Experimental Biology*, pages 891–908, 1999. [2]

[24] J. F. Ding, O. I. Lebedev, S. Turner, Y. F. Tian, W. J. Hu, J. W. Seo, C. Panagopoulos, W. Prellier, G. Van Tendeloo, and T. Wu. Interfacial spin glass state and exchange bias in manganite bilayers with competing magnetic orders. *Physical Review B*, 87(5):054428, feb 2013. [89, 90]

[25] D. Duval, J. Osmond, S. Dante, C. Dominguez, and Laura M. Lechuga. Grating couplers integrated on Mach-Zehnder interferometric biosensors operating in the visible range. *IEEE Photonics Journal*, 5(2):3700108–3700108, apr 2013. [129]

[26] Michael C. Emmons. *Development of Fiber Bragg Grating Strain, Thermal, and Magnetic Sensors for Smart Structure Applications*. Phd disertation, UCLA, 2012. [12, 15, 27]

[27] Michael C. Emmons, Gregory P. Carman, Kotekar Mohanchandra, and W. Lance Richards. Characterization and birefringence effect on embedded optical fiber Bragg gratings. In Tribikram Kundu, editor, *Proceedings of SPIE*, volume 7295, pages 72950C–72950C–11. Spie, mar 2009. [33, 41, 46]

[28] Michael C. Emmons, Sunny Karnani, Kotekar Mohanchandra, Gregory P. Carman, Stefano Trono, and W. Lance Richards. Characterization of Optical Fiber Bragg Gratings as Strain Sensors Considering Load Direction. In *ASME Conference on Smart*

Materials, Adaptive Structures and Intelligent Systems, pages 1–5, Ellicott City, Maryland, USA, 2008. [41]

[29] Michael C. Emmons, Sunny Karnani, Stefano Trono, Kotekar Mohanchandra, W. Lance Richards, and Gregory P. Carman. Strain Measurement Validation of Embedded Fiber Bragg Gratings. *International Journal of Optomechatronics*, 4(1):22–33, jan 2010. [41, 42]

[30] Michael C. Emmons, Hyungsuk K.D. Kim, Gregory P. Carman, and W. Lance Richards. Magneto-optic field coupling in optical fiber Bragg gratings. *Optical Fiber Technology*, pages 2–5, mar 2012. [27, 60, 75, 81, 134]

[31] Jayantha A Epaarachchi, Gayan Rathnaweera, John Canning, and Michael Stevenson. Response Fibre Bragg Grating (FBG) strain sensors embedded at different locations through the thickness around a delamination in a composite lamina. In *7th Asian-Australasian Conference on Composites (ACCM7)*, pages 1–4, Taipei, Taiwan, 2010. [38, 47]

[32] T. Erdogan. Fiber grating spectra. *Journal of Lightwave Technology*, 15(8):1277–1294, 1997. [27]

[33] K. M. Evenson, J. S. Wells, F. R. Petersen, B. L. Danielson, G. W. Day, R. L. Barger, and J. L. Hall. Speed of Light from Direct Frequency and Wavelength Measurements of the Methane-Stabilized Laser. *Physical Review Letters*, 29(19):1346–1349, nov 1972. [7]

[34] FBGS Draw Tower Gratings. ADVANTAGES DTG, 2013. [146]

[35] M. H. Fizeau. Sur une expérience relative à la vitesse de propagation de la lumière. *Comptes Rendus de l'Académie des Sciences*, 29:90–92, 1849. [7]

[36] Gerta Günther Fleissner, Elke Holtkamp-Rötzler, Marianne Hanzlik, Michael Winklhofer, Nikolai Petersen, and Wolfgang Wiltschko. Ultrastructural analysis of a putative magnetoreceptor in the beak of homing pigeons. *The Journal of comparative neurology*, 458(4):350–60, apr 2003. [2]

[37] Tom Fowler and Daniel Gilbert. Oil-Pipeline Cracks Evading Robotic 'Smart Pigs'. *The Wall Street Journal*, 2013. [xiii, 5, 6]

[38] GR Fowles. *Introduction to modern optics*. Dover, Mineola, New York, 2nd edition, 1975. [6, 7]

[39] RB Frankel and RP Blakemore. Navigational compass in magnetic bacteria. *Journal of Magnetism and Magnetic Materials*, 1980. [2]

[40] O Frazão, J P Carvalho, L a Ferreira, F M Araújo, and J L Santos. Discrimination of strain and temperature using Bragg gratings in microstructured and standard optical fibres. *Measurement Science and Technology*, 16(10):2109–2113, 2005. [27]

[41] Mark Froggatt. Distributed measurement of the complex modulation of a photoinduced Bragg grating in an optical fiber. *Applied Optics*, 35(25):5162–4, sep 1996. [28]

[42] Mark Froggatt and Jason Moore. Distributed measurement of static strain in an optical fiber with multiple Bragg gratings at nominally equal wavelengths. *Applied Optics*, 37(10):1741–1746, 1998. [36]

[43] Mark Froggatt and Jason Moore. High-spatial-resolution distributed strain measurement in optical fiber with Rayleigh scatter. *Applied Optics*, 37(10):1735–1740, 1998. [27]

[44] Alexander B. Granovsky, M. Inoue, and J. P. Clerc. Magnetorefractive effect in nanocomposites: Dependence on the angle of incidence and on light polarization. *Physics of the Solid State*, 46(3):498–501, 2004. [89, 106]

[45] Alexander B. Granovsky, M. V. Kuz'michev, and J. P. Clerc. Optical and magnetooptical properties of granular alloys with giant magnetoresistance in the IR region of the spectrum. *Journal of Experimental and Theoretical Physics*, 89(5), 1999. [61, 66]

[46] Alexander B. Granovsky, Yurii P. Sukhorukov, Elena Gan, and Andrey V. Telegin. Magnetorefractive Effect in Magnetoresistive Materials. In Mitsuteru Inoue, Miguel Levy, and Alexander V. Baryshev, editors, *Magnetophotonics: From Theory to Appli-*

cations, volume 178 of *Springer Series in Materials Science*, pages 107–133. Springer Berlin Heidelberg, Berlin, Heidelberg, 2013. [59, 60, 85, 95]

[47] K.O. Hill, Y. Fujii, DC Johnson, and BS Kawasaki. Photosensitivity in optical fiber waveguides: Application to reflection filter fabrication. *Applied Physics Letters*, 32(May 1978):647–649, 1978. [14, 34]

[48] Haruki Hosoda, Haruki Mori, Norihito Sogoshi, Akira Nagasawa, and Seiichiro Nakabayashi. Refractive Indices of Water and Aqueous Electrolyte Solutions under High Magnetic Fields. *The Journal of Physical Chemistry A*, 108(9):1461–1464, mar 2004. [59, 107]

[49] D. Hrabovský, J. M. Caicedo, G. Herranz, I. C. Infante, F. Sánchez, and J. Fontcuberta. Jahn-Teller contribution to the magneto-optical effect in thin-film ferromagnetic manganites. *Physical Review B*, 79(5):052401, feb 2009. [58, 60, 61, 62, 70, 85, 86, 87, 89, 90, 95, 131]

[50] D. Hrabovský, G. Herranz, J.M. Caicedo, I.C. Infante, F. Sánchez, and J. Fontcuberta. Strong magnetorefractive effect in epitaxial La2/3Ca1/3MnO3 thin films. *Journal of Magnetism and Magnetic Materials*, 322(9-12):1481–1483, may 2010. [xvi, 62, 72, 73, 75]

[51] D. Hrabovský, G. Herranz, K. Postava, I. C. Infante, F. Sánchez, and J. Fontcuberta. Optical sensing of magnetic field based on magnetorefractive effect in manganites. In Francesco Baldini, Jiri Homola, and Robert A. Lieberman, editors, *Proceedings of SPIE*, volume 7356, pages 73560R–73560R–10. SPIE, may 2009. [xvi, 58, 61, 62, 70, 71, 89]

[52] S. Huang, M. M. MM Ohn, M. LeBlanc, and Raymond M Measures. Continuous arbitrary strain profile measurements with fiber Bragg gratings. *Smart Materials and Structures*, 7:248–256, 1997. [42, 47]

[53] H. Y. Hwang, S-W. Cheong, P. G. Radaelli, M. Marezio, and B. Batlogg. Lattice Effects on the Magnetoresistance in Doped LaMnO3. *Physical Review Letters*, 75(5):914–917, jul 1995. [xv, 66]

[54] JC Jacquet and T. Valet. A new magnetooptical effect discovered on magnetic mul-

tilayers: the magnetorefractive effect. In *Materials Research Symposium Proceedings*, volume 384, pages 477–490, 1995. [xv, 58, 59, 61, 62, 63, 64, 85, 89, 95]

[55] Brian Jenkins, Peter Joyce, Deborah Mechtel, Kyle Milden, Kyle Elam, and Joe Watkins. Highly localized thermal response measurements in composites using embedded fiber Bragg grating temperature sensors. *SPIE*, 8693:869308–869308–10, apr 2013. [27]

[56] Sönke Johnsen and Kenneth J Lohmann. The physics and neurobiology of magnetoreception. *Nature Reviews Neuroscience*, 6(9):703–712, sep 2005. [2]

[57] Ian Johnson. Polymer-fiber grating sensors. *SPIE Newsroom*, (Dic):2–4, 2010. [xiii, 35]

[58] JPL. COPV Propellant Tank Failure on the Dawn Spacecraft. Technical Report 1, JPL. [4]

[59] Gayan C. Kahandawa, Jayantha A Epaarachchi, and K. T. Lau. Indexing damage using distortion of embedded FBG sensor response spectra. In Jayantha A. Epaarachchi, Alan Kin-tak Lau, and Jinsong Leng, editors, *Fourth International Conference on Smart Materials and Nanotechnology in Engineering*, volume 8793, pages 87930K1–6, aug 2013. [47]

[60] Hyun-Kyu Kang, Jae-Sung Park, Dong-Hoon Kang, Cheol-Ung Kim, Chang-Sun Hong, and Chun-Gon Kim. Strain monitoring of a filament wound composite tank using fiber Bragg grating sensors. *Smart Materials and Structures*, 11:848–853, 2002. [30, 42, 46]

[61] K.C. Kao and G.A. Hockham. Dielectric-fibre surface waveguides for optical frequencies. *Proceedings of the Institution of Electrical Engineers*, 113(7):1151, 1966. [13, 22]

[62] S. G. Kaplan, M. Quijada, H. D. Drew, D. B. Tanner, G. C. Xiong, R. Ramesh, C. Kwon, and T. Venkatesan. Optical Evidence for the Dynamic Jahn-Teller Effect in Nd0.7Sr0.3MnO3. *Physical Review Letters*, 77(10):2081–2084, sep 1996. [62, 85, 95]

[63] A F Kravets, Yu. I. Dzhezherya, V. G. Kravets, and E. S. Klimuk. Specific features of

the reflection of infrared radiation by crystalline dielectrics in a magnetic field. *Journal of Experimental and Theoretical Physics*, 99(6):1189–1192, dec 2004. [59]

[64] V. G. Kravets, L. V. Poperenko, I. V. Yurgelevych, a. M. Pogorily, and A F Kravets. Optical and magneto-optical properties and magnetorefractive effect in metal-insulator CoFeAl[sub 2]O[sub 3] granular films. *Journal of Applied Physics*, 98(4):043705, 2005. [59]

[65] Barbara M. Kreutz. Mediterranean Contributions to the Medieval Mariner's Compass. *Technology and Culture*, 14:367–383, 1973. [2]

[66] K. S. C. Kuang, S. T. Quek, C. G. Koh, W. J. Cantwell, and P. J. Scully. Plastic Optical Fibre Sensors for Structural Health Monitoring: A Review of Recent Progress. *Journal of Sensors*, 2009:1–13, 2009. [22, 27]

[67] D. K. W. Lam and B. K. Garside. Characterization of single-mode optical fiber filters. *Applied Optics*, 20(3):440–445, 1981. [28]

[68] Hansuek Lee, Tong Chen, Jiang Li, Oskar Painter, and Kerry J. Vahala. Ultra-low-loss optical delay line on a silicon chip. *Nature Communications*, 3(May):867, 2012. [xx, 131]

[69] Mark R Leifeste. Interrelationship Of Nondestructive Evaluation Methodolologies Applied To Testing Of Composite Overwrapped Pressure Vessels. Technical report, NASA Johnson Space Center White Sands Test Facility, Las Cruces, NM, USA, 2007. [38]

[70] JE Lenz. A review of magnetic sensors. *Proceedings of the IEEE*, 78(9036163), 1990. [2]

[71] Hugo F Lima, Romeu da Silva Vicente, Rogério N Nogueira, Ilda Abe, Paulo Sérgio De Brito André, Catarina Fernandes, Hugo Rodrigues, Humberto Varum, Hypolito José Kalinowski, Aníbal Costa, and João De Lemos Pinto. Structural Health Monitoring of the Church of Santa Casa da Misericórdia of Aveiro Using FBG Sensors. *IEEE Sensors Journal*, 8(7):1236–1242, 2008. [30]

[72] H L Liu, K S Lu, M X Kuo, L Uba, S Uba, L M Wang, and H-T Jeng. Magneto-optical

properties of La0.7Sr0.3MnO3 thin films with perpendicular magnetic anisotropy. *Journal of Applied Physics*, 99:043908, 2006. [xvii, xviii, 80, 81, 99, 100, 109]

[73] Ting Liu, Xianfeng Chen, Ziyun Di, Junfeng Zhang, Xinwan Li, and Jianping Chen. Tunable magneto-optical wavelength filter of long-period fiber grating with magnetic fluids. *Applied Physics Letters*, 91(12):121116, 2007. [27]

[74] N. N. Loshkareva, Yurii P. Sukhorukov, B. a. Gizhevskii, A. A. Samokhvalov, V. E. Arkhipov, V. E. Naish, S. G. Karabashev, and Ya. M. Mukovskii. Red Shift of Absorption Edge and Nonmetal-Metal Transition in Single Crystals La1-xSrxMnO3 (x= 0.1, 0.2, 0.3). *Physica Status Solidi (a)*, 164(2):863–867, 1997. [62, 65]

[75] Tadamichi Mawatari and Drew Nelson. A multi-parameter Bragg grating fiber optic sensor and triaxial strain measurement. *Smart Materials and Structures*, 17(3):035033, jun 2008. [27, 30]

[76] Pat B. McLaughlan and Scott C. Forth. Composite Overwrapped Pressure Vessels, A Primer. Technical Report March, NASA, Houseton, TX 77058, 2011. [1, 38, 40]

[77] G Meltz, W W Morey, and W H Glenn. Formation of Bragg gratings in optical fibers by a transverse holographic method. *Optics letters*, 14(15):823–5, aug 1989. [27]

[78] Scott Miller and Frank Sander. Pipeline Technology Conference 2008 Advances in Feature Identification using Tri-Axial MFL Sensor Technology. In *Pipeline Technology Conference 2008*, pages 1–13, 2008. [3]

[79] Tadahito Mizutani, Yoji Okabe, and Nobuo Takeda. Crack identification in CFRP laminates using small-diameter FBG sensors. In Daniele Inaudi and Eric Udd, editors, *Smart Structures and Materials 2002: Smart Sensor Technology and Measurement Systems*, volume 4694, pages 330–340. SPIE, jul 2002. [38, 47, 54]

[80] W. W. Morey, G Meltz, and W. H. Glenn. Fiber Optic Bragg Grating Sensors. pages 98–107, Boston, feb 1990. [15]

[81] John A Nairn. Matrix Microcracking in Composites. In R. Talreja and J.-A. E. Månson, editors, *Polymer Matrix Composties*, volume 2, chapter 13. Elsevier Science,

2000. [54]

[82] Isaac Newton. A Letter of Mr . Isaac Newton ... containing his New Theory about Light and Colors. *Philosophical Transactions of the Royal Society*, 80:3075–3087, 1671. [6]

[83] Isaac Newton. Hypothesis explainig the properties of light. In Thomas Birch, editor, *The History of the Royal Society vol.3*, pages 247–305. London, 1757. [6]

[84] Yoji Okabe, Shigeki Yashiro, Tatsuro Kosaka, and Nobuo Takeda. Detection of transverse cracks in CFRP composites using embedded fiber Bragg grating sensors. *Smart Materials and Structures*, 9(6):832–838, dec 2000. [38, 47, 54]

[85] Andreas Othonos. Fiber Bragg gratings. *Review of Scientific Instruments*, 68(12):4309, 1997. [40]

[86] C. J. Pacheco and A. C. Bruno. The effect of shape anisotropy in giant magnetostrictive fiber Bragg grating sensors. *Measurement Science and Technology*, 21(6):065205, jun 2010. [27]

[87] Clara J. Pacheco and Antonio C. Bruno. A noncontact force sensor based on a fiber Bragg grating and its application for corrosion measurement. *Sensors (Basel, Switzerland)*, 13(9):11476–11489, 2013. [xxi, 143, 144, 145, 157]

[88] J Palaniappan, H Wang, S.L. Ogin, a Thorne, G T Reed, S.C. Tjin, and L N McCartney. Prediction of the reflected spectra from chirped fibre Bragg gratings embedded within cracked crossply laminates. *Measurement Science and Technology*, 17(6):1609–1614, jun 2006. [46, 54]

[89] Chun Park and Kara Peters. Comparison of damage measures based on fiber Bragg grating spectra. *Measurement Science and Technology*, 23(2):025105, feb 2012. [27]

[90] Francisco Pena, Scott M. Strutner, W. Lance Richards, Anthony Piazza, and Allen R. Parker. Evaluation of Embedded FBGs in Composite Overwrapped Pressure Vessels for Strain Based Structural Health Monitoring. In Kevin M. Farinholt, editor, *SPIE:*

Industrial and Commercial Applications of Smart Structures Technologies VIII, volume 9059, page 90590G, mar 2014. [41, 45]

[91] Kara Peters. Polymer optical fiber sensors - a review. *Smart Materials and Structures*, 20(1):013002, jan 2011. [40]

[92] John B Phillips and O Sayeed. Wavelength-dependent effects of light on magnetic compass orientation in Drosophila melanogaster. *Journal of Comparative Physiology A*, pages 303–308, 1993. [2]

[93] L Pi, M Hervieu, A Maignan, C Martin, and B Raveau. Structural and magnetic phase diagram and room temperature CMR effect of La1-xAgxMnO3. *Solid State Communications*, 126(4):229–234, apr 2003. [76]

[94] F Prieto, B Sepulveda, A Calle, A Llobera, C Dominguez, A Abad, A Montoya, and L M Lechuga. An integrated optical interferometric nanodevice based on silicon technology for biosensor applications. *Nanotechnology*, 14(8):907–912, 2003. [114]

[95] Shengli Pu, Xianfeng Chen, Yuping Chen, Yonghao Xu, Weijun Liao, Lijun Chen, and Yuxing Xia. Fiber-optic evanescent field modulator using a magnetic fluid as the cladding. *Journal of Applied Physics*, 99(9):093516, 2006. [27]

[96] Ginu Rajan, Bing Liu, Yanhua Luo, Eliathamby Ambikairajah, and Gang-Ding Peng. High Sensitivity Force and Pressure Measurements Using Etched Singlemode Polymer Fiber Bragg Gratings. *IEEE Sensors Journal*, 13(5):1794–1800, may 2013. [155]

[97] R Rashed, Chicago Press, The History, and Science Society. A pioneer in anaclastics: Ibn Sahl on burning mirrors and lenses. *Isis*, 81(3):464–491, 1990. [5, 16]

[98] P. Saidi Reddy, R. L. N. Sai Prasad, D. Sen Gupta, M. Sai Shankar, K. Sriman-narayana, and P. Ravinder Reddy. Quasi-distributed fiber bragg grating array sensor for furnace applications. *Photonic Sensors*, (December 2011), may 2012. [29]

[99] Ali Hussain Reshak, M Piasecki, S Auluck, I V Kityk, R Khenata, B Andriyevsky, C Cobet, N Esser, A Majchrowski, M. Świrkowicz, R Diduszko, and W Szyrski. Effect

of U on the Electronic Properties of Neodymium Gallate (NdGaO 3): Theoretical and Experimental Studies. *Journal of Physical Chemistry B*, 113:15237–15242, 2009. [98]

[100] Lance Richards, Allen R Parker, William L Ko, and Anthony Piazza. Fiber Optic Wing Shape Sensing on NASA ' s Ikhana UAV. Technical report, NASA, Edwards, CA, 2008. [3]

[101] T Ritz, S Adem, and K Schulten. A model for photoreceptor-based magnetoreception in birds. *Biophysical journal*, 78(2):707–18, feb 2000. [2]

[102] Jose Manuel Caicedo Roque. *Magneto-Optical Spectroscopy of Complex Systems: Magnetic Oxides and Photonic Crystals*. PhD thesis, Universitat Autonoma de Barcelona, 2012. [58, 60, 89, 92, 105]

[103] Alison Sider. The Trouble With Inspection Tools for Oil Pipelines. *The Wall Street Journal*, jul 2015. [5]

[104] G Sines and YA Sakellarakis. Lenses in antiquity. *American Journal of Archaeology*, 91(2):191–196, 1987. [5]

[105] Sudharsanan Srinivasan, Renan Moreira, Daniel Blumenthal, and John E Bowers. Design of integrated hybrid silicon waveguide optical gyroscope. *Optics express*, 22(21):24988–93, 2014. [130]

[106] Donald J. Jr. Sterling. *Technician's Guide To Fiber Optics*. Delmar Publishers Inc., Albany, New York, second edition, 1993. [13, 22, 26, 27]

[107] Yang Su, Yong Zhu, Baofu Zhang, Jianhua Li, and Yuquan Li. Use of the polarization properties of magneto-optic fiber Bragg gratings for magnetic field sensing purposes. *Optical Fiber Technology*, 17(3):196–200, may 2011. [27]

[108] Yurii P. Sukhorukov, Elena Alexandrovna Ganshina, B. I. Belevtsev, N. N. Loshkareva, a. N. Vinogradov, K. D. D. Rathnayaka, a. Parasiris, and D. G. Naugle. Giant change in infrared light transmission in La[sub 0.67]Ca[sub 0.33]MnO[sub 3] film near the Curie temperature. *Journal of Applied Physics*, 91(7):4403, 2002. [62, 69, 71]

[109] Yurii P. Sukhorukov, a. P. Nosov, N. N. Loshkareva, E. V. Mostovshchikova, Andrey V. Telegin, E. Favre-Nicolin, and L. Ranno. The influence of magnetic and electronic inhomogeneities on magnetotransmission and magnetoresistance of La[sub 0.67]Sr[sub 0.33]MnO[sub 3] films. *Journal of Applied Physics*, 97(10):103710, 2005. [62]

[110] Yurii P. Sukhorukov, Andrey V. Telegin, Alexander B. Granovsky, Elena Alexandrovna Ganshina, S. V. Naumov, N. V. Kostromitina, L. V. Elokhina, and J. Gonzalez. Magnetorefractive effect in La0.7Ca0.3MnO3 in the infrared spectral range. *Journal of Experimental and Theoretical Physics*, 111(3):355–362, nov 2010. [xvi, 62, 69, 71, 72, 73, 74]

[111] Yurii P. Sukhorukov, Andrey V. Telegin, Alexander B. Granovsky, Elena Alexandrovna Ganshina, A. Zhukov, J. Gonzalez, G. Herranz, J. M. Caicedo, A. N. Yurasov, V. D. Bessonov, Kaul' a. R., O. Yu. Gorbenko, and I. E. Korsakov. Magnetorefractive effect in manganites with a colossal magnetoresistance in the visible spectral region. *Journal of Experimental and Theoretical Physics*, 114(1):141–149, feb 2012. [xvii, 58, 62, 76, 77, 85, 95]

[112] Marcel Urban, François Couchot, Xavier Sarazin, and Arache Djannati-Atai. The quantum vacuum as the origin of the speed of light. *The European Physical Journal D*, 67(3):58, mar 2013. [7]

[113] M. Ussorio, H. Wang, S.L. Ogin, A.M. Thorne, G.T. Reed, S.C. Tjin, and R. Suresh. Modifications to FBG sensor spectra due to matrix cracking in a GFRP composite. *Construction and Building Materials*, 20(1-2):111–118, feb 2006. [38, 47]

[114] Mike Wall. European Satellite, Out of Fuel, Will Plunge to Earth Next Month. *Space.com*, oct 2013. [xiii, 4, 5]

[115] Bao-Jian Wu, Ying Yang, and Kun Qiu. Magneto-optic fiber Bragg gratings with application to high-resolution magnetic field sensors. *2008 1st Asia-Pacific Optical Fiber Sensors Conference*, pages 1–3, aug 2008. [27]

[116] Ming-Chung Wu, Chih-Min Chuang, Yang-Fang Chen, and Wei-Fang Su. Fabrication and optical properties of periodical structures based on a water-developable and tunable La0.7Sr0.3MnO3 resist. *Journal of Materials Chemistry*, 18:780, 2008. [80]

[117] M. G. Xu, J.-L. Archambault, L. Reekie, and J. P. Dakin. Discrimination between strain and temperature effects using dual-wavelength fibre grating sensors. *Electronics Letters*, 30(13):1085–1087, jun 1994. [30]

[118] Minghong Yang, Jixiang Dai, Xiaobin Li, and Junjie Wang. Side-polished fiber Bragg grating refractive index sensor with TbFeCo magnetoptic thin film. *Journal of Applied Physics*, 108(3):033102, 2010. [27]

[119] Huugh D. Young and Roger A. Freedman. *Sears and Zemansky's university physics : with modern physics*. Pearson Education, San Fransico, 12th edition, 2008. [18]

[120] Yong Zhao, Qing-yao Meng, and Kun Chen. Novel current measurement method based on fiber Bragg grating sensor technology. *Sensors and Actuators A: Physical*, 126(1):112–116, jan 2006. [27]